공학박사학위논문

광대역 에너지 국부화 및 수확을 위한 압전 결함 인가 음향양자 결정의 모델링 및 설계

Modeling and Design of a Phononic Crystal with Piezoelectric Defects for Broadband Energy Localization and Harvesting

2021 년 2 월

서울대학교 대학원

기계항공공학부

조 수 호

광대역 에너지 국부화 및 수확을 위한 압전 결함 인가 음향양자 결정의 모델링 및 설계

Modeling and Design of a Phononic Crystal with Piezoelectric Defects for Broadband Energy Localization and Harvesting

지도교수 윤 병 동

이 논문을 공학박사 학위논문으로 제출함

2020 년 10 월

서울대학교 대학원

기계항공공학부

조 수 호

조수호의 공학박사 학위논문을 인준함

2020 년 12 월

위 원 장 : 김 윤 영 (인)

부위원장 : 윤 병 동 (인)

위 원 : 김 도 년 (인)

위 원 : 신 용 대 (인)

위 원 : 김 흥 수 (인)

Abstract

Modeling and Design of a Phononic Crystal with Piezoelectric Defects for Broadband Energy Localization and Harvesting

Soo-Ho Jo
Department of Mechanical and Aerospace Engineering
The Graduate School
Seoul National University

Energy harvesting (EH) technology, which converts ambient, otherwise wasted, energy into usable electricity, has attracted much attention as a solution to ultimately eliminate the replacement cost of the chemical batteries in wireless sensor networks (WSNs). Depending on energy sources and conversion mechanisms, a wide range of technology has been actively researched including wind, solar, thermal, and mechanical energy harvesting. Among them, piezoelectric energy harvesting (PEH) is recognized as a promising solution due to its advantages of (1) high power density and (2) ease of miniaturization for use in WSNs.

Recently, the incorporation of phononic crystals (PnCs) into PEH systems (so-

called PnC-based PEH systems) has emerged as a breakthrough technology to amplify the amount of input mechanical energy fed into PEH devices by tailoring wave propagation, thus dramatically enhancing energy conversion efficiency. A PnC, an artificially engineered structure that consists of periodically repetitive unit cells, exhibits unusual phenomena that have not been observed in nature, such as a band gap. If single or multiple defects are introduced into a PnC by breaking the periodicity of unit cells, defect bands are formed in a band gap regime. Near defect band frequencies, waves inside the PnC become localized in the vicinity of the defects. By attaching PEH devices to the defects of the PnC, the output electric power can be thus remarkably amplified.

In terms of reducing the mechanical impedance mismatching between solid medium and solid PEH devices, elastic waves with PnCs might be more favorable than acoustic waves for PEH purposes. However, most of the existing studies have focused on only phenomena of improvement of PEH performance under elastic waves. The following two issues of fundamental importance arise: (1) there is no design rationale for a PnC with single or double defects for high dense PEH and (2) defect mode-enabled energy localization has inherently narrowband characteristics for output performances of PEH. In order to bridge the domains of the defect-mode-enabled elastic wave localization and PEH, this doctoral dissertation aims at advancing two essential and one co-related research areas: Research Thrust 1 - parametric studies on structural and electrical circuit designs of a PnC with piezoelectric defects; (2) Research Thrust 2 - new design concepts of a PnC with piezoelectric defects for broadband PEH; and (3) Appendix - an analytical model for a PnC with piezoelectric defects for the formation and splitting of defect bands.

Research Thrust 1: When designing a two-dimensional PnC with single or double piezoelectric defects, this thrust aims to provide guidelines and rationales for key design parameters for the purpose of maximizing the harvestable electric power. Here, design parameters include: the supercell size, defect location, and relative position between double defects in the mechanical domain and the electrical circuit connection between double defects in the electrical domain. First, the selection of a target defect mode shape is elucidated from the perspective of avoiding voltage cancellation. Second, mechanical and electrical responses of several two-dimensional PnCs with a piezoelectric defect are thoroughly investigated for two following cases: (1) various supercell sizes with a fixed defect location and (2) various defect locations with a fixed supercell size. Lastly, for several two-dimensional PnCs with double piezoelectric defects, mechanical and electrical responses are thoroughly investigated for two following cases: (1) various distances and arranging directions between the double defects in an independent connection and (2) five electrical circuit connection types (i.e., one independent connection, two series connections, and two parallel connections) with the fixed distance and direction.

Research Thrust 2: Due to inherent narrowband characteristics of defect mode-enabled energy localization, the objective of this thrust is to propose new design concepts of a PnC with piezoelectric defects that can realize broadband energy localization and harvesting. One is a PnC with L-shape arranged triple defects. It plays a key role in superposing PnC-based PEH systems with a single defect and with double defects to make use of the advantages of each system. A PnC-based PEH system with a single defect can harvest high output electric power at a certain defect band frequency with narrow bandwidth. A PnC-based PEH system with double defects can obtain

relatively broad bandwidth can be obtained at two split defect band frequencies with low output electric power. Thus, superposing two systems enables broadband piezoelectric energy harvesting. The other is a graded PnC with decoupled double defects. Since the defect band frequency is determined based on the mass and stiffness of the lattices surrounding the relevant defect, the combination of decoupling and graded characteristics allows to separately design defect band frequencies corresponding to each of the double defects. It leads to localizing elastic waves near each defect at the designed different defect band frequencies; thus, the graded PnC can successfully achieve broadband PEH.

Appendix: One is a lumped-parameter model (i.e., a multi-degree-of-freedom (M-DOF) mass-spring system) of a one-dimensional PnC with single or double defects to fundamentally elucidate the underlying principles of the formation and splitting of defect bands. When asymptotic approaches are applied into defect band analysis, the limiting behaviors of defect bands and corresponding defect mode shapes provide important keys to what the physical meaning of defect-mode-enabled energy localization is. The other is an electroelastically coupled analytical model of a one-dimensional PnC with a single defect to predict defect bands and output performance of PEH. Newton's 2nd law and Gauss's law are used to derive a mechanical equation of motions and electrical circuit equation, respectively. By solving these coupled equations with the help of Green's function, the electroelastically coupled transfer matrix is derived in an explicit manner. Finally, based on the transfer matrix method (TMM) and S-parameter method (SPM), band structures and output performance of PEH are obtained.

Keywords: Piezoelectric energy harvesting (PEH)
Self-powered wireless sensor networks (WSNs)
Phononic crystal (PnC)
Band gap
Defect mode
Energy localization

Student Number: 2016-20715

Table of Contents

Abstract ..... **i**

List of Tables ..... **xiii**

List of Figures ..... **xvii**

Nomenclatures ..... **xxix**

Chapter 1 Introduction **1**

1.1 Motivation 1

1.2 Research Scope and Overview 7

1.3 Dissertation Layout 11

Chapter 2 Single Defect Mode of a Phononic Crystal for Energy Localization and Harvesting – From the Perspective of Supercell Size and Defect Location **13**

2.1 System Description of a Phononic Crystal with a Single Defect 15

2.2 Band Structure Analysis for a Phononic Crystal with a Single Defect 22

2.3 Effects of the Supercell Size on Energy Localization and Harvesting Performance 32
2.3.1 Mechanical Output Performance with Different Supercell Sizes ... 32
2.3.2 Electrical Output Performance with Different Supercell Sizes 37

2.4 Effects of the Defect Location on Energy Localization and Harvesting Performance 43
2.4.1 Mechanical Output Performance with Different Defect Locations 43
2.4.2 Electrical Output Performance with Different Defect Locations 48

2.5 Effects of the Supercell Size on the Optimal Defect Location 55

2.6 Summary and Discussion 57

Chapter 3 Double Defect Modes of a Phononic Crystal for Energy Localization and Harvesting – From the Perspective of Relative Position and Electrical Circuit Connection 60

3.1 System Description of a Phononic Crystal with Double Defects 62

3.2 Defect Band Analysis for a Phononic Crystal with a Single Defect 67

3.3 Defect Band Analysis for a Phononic Crystal with Double Defects 71

3.4 Effects of the Relative Position between Double Defects on Energy Localization and Harvesting Performance 77
3.4.1 Mechanical and Electrical Output Performances with Different

Distances under the Open-circuit Condition 78
3.4.2 Mechanical and Electrical Output Performances with Different Arranging Directions under the Open-circuit Condition 87
3.4.3 Experimental Validation of the Splitting of Defect Bands under Elastic Waves 93

3.5 Effects of the Electrical Circuit Connection between Double Defects on Energy Localization and Harvesting Performance 106
3.5.1 Five Scenarios for Electrical Circuit Configuration 106
3.5.2 Effects on Shift Patterns of the Split Defect Bands 111
3.5.3 Effects on Mechanical and Electrical Performances under the Open-circuit Condition 115
3.5.4 Effects on the Maximum Output Electric Power and Optimal External Electrical Resistance 123

3.6 Summary and Discussion 130

Chapter 4 L-Shape Arranged Triple Defects for Broadband Piezoelectric Energy Harvesting – Superposition of Phononic Crystals with Single and Double Defects 134

4.1 System Description of a Phononic Crystal with L-Shape Arranged Triple Defects 136

4.2 Energy Localization and Harvesting Analyses for the Phononic Crystal with L-shape Arranged Triple Defects 140

4.2.1 The Maximum Output Voltage under the Open-circuit Condition 140
4.2.2 The Maximum Output Electric Power under the Optimal External Electrical Resistance 144

4.3 Summary and Discussion 147

Chapter 5 A Graded Phononic Crystal with Decoupled Double Defects for Broadband Piezoelectric Energy Harvesting . 149

5.1 Band Gap Analysis of a Graded Phononic Crystal without Defects 151

5.2 Defect Band Analysis of a Graded Phononic Crystal with a Single Defect 154

5.3 Defect Band Analysis of a Graded Phononic Crystal with Decoupled Double Defects 165

5.4 Energy Localization and Harvesting Analyses for the Graded Phononic Crystal with the Decoupled Double Defects 172
5.4.1 Setting for Harmonic Analysis 172
5.4.2 The Maximum Output Voltage under the Open-circuit Condition 174
5.4.3 The Maximum Output Electric Power under the Optimal External Electrical Resistance 177

5.5 Summary and Discussion 183

Chapter 6 Conclusion 186

6.1 Contributions and Significance 186

6.2 Suggestions for Future Research 189

Appendix A A Lumped-parameter Model of Phononic Crystals with Single and Double Defects for Formation and Splitting of Defect Bands under Longitudinal Waves 196

A.1 System Configuration and Modeling Assumption for a Lumped-parameter Model 198

A.2 Eigenvalue Problems of Phononic Crystals for Dispersion Analysis 202

A.2.1 A Phononic Crystal without Defects 202

A.2.2 A Phononic Crystal with a Single Defect 203

A.2.3 A Phononic Crystal with Double Defects 204

A.2.4 Planning for Band Structure Analysis 205

A.3 Band Gap Analysis for a Phononic Crystal without Defects 209

A.4 Principles of Formation of Defect Bands for a Phononic Crystal with a Single Defect 210

A.4.1 Formation of Defect Bands within Band Gaps and Corresponding Defect Mode Shapes 211

A.4.2 Asymptotic Analysis of the Formation of Defect Bands 212

A.4.3 Formation of Fixed-like Boundary Conditions by Band Gaps 215

A.5 Principles of Splitting of Defect Bands for a Phononic Crystal with Double

Defects 218
A.5.1 Splitting of Defect Bands within Band Gaps and Corresponding Defect Mode Shapes 218
A.5.2 Asymptotic Analysis of the Splitting of Defect Bands 219
A.5.3 Formation of Fixed-like Boundary Conditions by Band Gaps 221

A.6 Summary and Discussion 225

Appendix B An Electroelastically Coupled Analytical Model for a Phononic Crystal with a Piezoelectric Defect for Energy Harvesting under Longitudinal Waves 228

B.1 System Configuration and Modeling Assumption for an Electroelastic Coupled Analytical Model 231

B.2 Derivation of an Electroelastically Coupled Transfer Matrix 233
B.2.1 Mechanical Equation of Motions 234
B.2.2 Electrical Circuit Equation 236
B.2.3 Electroelastically Coupled Transfer Matrix 238

B.3 Methods for Output Performance Prediction 243
B.3.1 Band Structure Calculation Based on Transfer Matrix Method 244
B.3.2 Output Voltage Calculation Based on S-Parameter Method 245

B.4 Evaluation of Model Predictive Capability 247
B.4.1 Evaluation Planning 247

B.4.2 Band Structure Evaluation 251
B.4.3 Energy Localization Performance Evaluation 257
B.4.4 Electrical Output Performance Evaluation 260

B.5 Application of the Proposed Model: Design Optimization of a Phononic Crystal for Maximizing Output Electric Power at a Target Frequency 265
B.5.1 Design Optimization Formulation and Procedure..... 265
B.5.2 Design Optimization Results 270

B.6 Summary and Discussion..... 275

References 277

국문 초록 303

List of Tables

Table 2-1 Geometric dimensions of the unit cell and PEH device for a PnC with a single defect. 20

Table 2-2 Mechanical properties of aluminum. 20

Table 2-3 Mechanical and electrical properties of PZT-4D. 21

Table 2-4 Defect band frequencies under the external electrical resistances of 0 Ω (short-circuit) and 100 MΩ (open-circuit) when **k**=(0, 0). 31

Table 2-5 Output performances under external electrical resistances of 0 Ω (short-circuit) and 100 MΩ (open-circuit) for different supercell sizes. 41

Table 2-6 The maximum output electric power at the optimal external electrical resistance for different supercell sizes. 42

Table 2-7 Output performances under external electrical resistances of 0 Ω (short-circuit) and 100 MΩ (open-circuit) at different defect locations. 53

Table 2-8 The maximum output electric power at the optimal external electrical resistances at different defect locations. 54

Table 3-1 Geometric dimensions of the unit cell and PEH device for a PnC with double defects. 66

Table 3-2 Comparison between numerical and experimental results for the effects

of the distance between double defects on the splitting of defect bands. 105

Table 3-3 Shift patterns of the frequencies of the split defect bands that correspond to the monopole-like defect mode shape for five electrical circuit connections. 114

Table 3-4 Mechanical and electrical output performances at peak frequencies under the external electrical resistance of 100 MΩ (open-circuit) for five electrical circuit connections..... 122

Table 3-5 The maximum output electric power across the optimal external electrical resistance for five electrical circuit connections..... 129

Table 5-1 Defect band frequencies for the graded PnC with the single defect under the external electrical resistances of 0 Ω (short-circuit) and 100 MΩ (open-circuit) when **k**=(0, 0). 164

Table 5-2 Defect band frequencies for Cases I, II, and III under external electrical resistances of 0 Ω (short-circuit) and 100 MΩ (open-circuit) when **k**=(0, 0). 169

Table 5-3 The maximum output voltage at each peak frequency for Cases I, II, and III under the external electrical resistance of 100 MΩ. 181

Table 5-4 The maximum output electric power at each peak frequency for Cases I, II, and III across the optimal external electrical resistance. 182

Table A-1 Geometric dimensions of aluminum and steel stacks. 207

Table A-2 Material properties of aluminum and steel stacks. 208

Table B-1 Geometric dimensions of the unit cell and PEH device. 249

Table B-2 Mechanical and electrical properties of PZT-5H. 250

Table B-3 Information about design variables of the one-dimensional PnC with the piezoelectric defect. 273

Table B-4 Design optimization results of the one-dimensional PnC with the piezoelectric defect. 274

List of Figures

Figure 1-1 Electric polarization in response to the applied mechanical strain. 2

Figure 1-2 A brief concept of a PnC-based PEH system. 3

Figure 1-3 A brief concept of defect-mode-enabled energy localization.....5

Figure 2-1 A schematic view of the two-dimensional PnC-based PEH system with a single defect: (a) the PEH system with excitation source and perfectly matched layers, (b) a cylindrical stub-type unit cell, and (c) the 5×7 supercell with the PEH device. 17

Figure 2-2 Band structure analysis for a 5×7 supercell with a single defect under the external electrical resistance 0 Ω (short-circuit): (a) the 1st irreducible Brillouin zone (M→Γ→X→M→Y→Γ) and (b) formation of six defect bands within the full band gap, ranging from 53.36 to 66.31 kHz (54.20 kHz (A), 55.62 kHz (B), 55.83 kHz (C), 58.62 kHz (D), 64.45 kHz (E), and 65.83 kHz (F)).....29

Figure 2-3 Various defect mode shapes (z-directional displacement fields) for a 5×7 supercell with a single defect under the external electrical resistance of 0 Ω (short-circuit): (a) 54.197 kHz (A), (b) 55.618 kHz (B), (c) 55.825 kHz (C), (d) 58.617 kHz (D), (e) 64.446 kHz (E), and (f) 65.834 kHz (F). 30

Figure 2-4 Operating deflection shapes (z-directional displacement fields) under

the external electrical resistance of 0 Ω (short-circuit) at each peak frequency when the defect is introduced in: (a) 5×4 supercell, 55.73 kHz, (b) 5×5 supercell, 55.78 kHz, (c) 5×6 supercell, 55.81 kHz, and (d) 5×7 supercell, 55.82 kHz. 33

Figure 2-5 Mechanical displacement FRFs for different supercell sizes under the external electrical resistances of (a) 0 Ω (short-circuit) and (b) 100 MΩ (open-circuit). 34

Figure 2-6 Output voltage FRFs for different supercell sizes under the external electrical resistance of 100 MΩ (open-circuit). 37

Figure 2-7 Electrical output performances with respect to the external electrical resistance for different supercell sizes: (a) output voltage at an open-circuit resonance frequency, (b) output electric power at a short-circuit resonance frequency, and (c) output electric power at an open-circuit resonance frequency. 40

Figure 2-8 Operating deflection shapes (z-directional displacement fields) under the external electrical resistance of 0 Ω (short-circuit) at each peak frequency when the defect is introduced at: (a) 2nd layer, 55.74kHz, (b) 3rd layer, 55.82 kHz, (c) 4th layer, 55.83 kHz, (d) 5th layer, 55.81 kHz, and (e) 6th layer, 55.76 kHz. 47

Figure 2-9 Mechanical displacement FRFs at different defect locations under the external electrical resistances of (a) 0 Ω (short-circuit) and (b) 100 MΩ (open-circuit). 48

Figure 2-10 Output voltage FRFs at different defect locations under the external electrical resistance of 100 MΩ (open-circuit).....49

Figure 2-11 Electrical output performances with respect to the external electrical resistance at different defect locations: (a) output voltage at an open-circuit resonance frequency, (b) output electric power at a short-circuit resonance frequency, and (c) output electric power at an open-circuit resonance frequency. 52

Figure 2-12 Output voltage FRFs for different supercell sizes and defect locations under the external electrical resistance of 100 MΩ (open-circuit): (a) 2nd and 3rd layers in 5×4 supercell, (b) 2nd and 3rd layers in 5×5 supercell, (c) 2nd and 3rd layers in 5×6 supercell, and 2nd and 3rd layers in 5×7 supercell. 56

Figure 3-1 A schematic view of the two-dimensional PnC-based PEH system with double defects: periodic boundary condition and perfectly matched layers as the boundary conditions and transversely polarized A0 Lamb wave as the excitation condition. 64

Figure 3-2 Defect band analysis for a 17×17 supercell with a single defect under the external electrical resistance 0 Ω (short-circuit): (a) the 1st irreducible Brillouin zone (Γ→X→M→Y) and (b) formation of six defect bands within the full band gap, ranging from 56.55 kHz to 62.51 kHz (57.04 kHz (A), 57.20 kHz (B), 57.55 kHz (C), 59.94 kHz (D), 61.62 kHz (E), and 62.39 kHz (F)). 69

Figure 3-3 Various defect mode shapes (z-directional displacement fields) for a 17×17 supercell with a single defect under the external electrical resistance of 0 Ω (short-circuit): (a) 57.04 kHz (A), (b) 57.20 kHz (B), (c) 57.55 kHz (C), (d) 59.94 kHz (D), (e) 61.62 kHz (E), and (f) 62.39 kHz (F). 70

Figure 3-4 Defect band analysis for a 17×17 supercell with double defects under the external electrical resistance 0 Ω (short-circuit): (a) the 1st irreducible Brillouin zone (Γ→X→M→Y) and (b) formation of twelve defect bands within the full band gap (57.03 kHz (A), 57.05 kHz (B), 57.13 kHz (C), 59.28 kHz (D), 57.41 kHz (E), 57.70 kHz (F), 59.79 kHz (G), 60.11 kHz (H), 61.59 kHz (I), 61.65 kHz (J), 62.11 kHz (K), and 62.78 kHz (L)). 74

Figure 3-5 Various defect mode shapes (z-directional displacement fields) for a 17×17 supercell with double defects under the external electrical resistance of 0 Ω (short-circuit): (a) 57.03 kHz (A), (b) 57.05 kHz (B), (c) 57.13 kHz (C), (d) 57.28 kHz (D), (e) 57.41 kHz (E), (f) 57.70 kHz (F), (g) 59.79 kHz (G), (h) 60.11 kHz (H), (i) 61.59 kHz (I), (j) 61.65 kHz (J), (k) 62.11 kHz (K), and (l) 62.78 kHz (L). 76

Figure 3-6 Operating deflection shapes (z-directional displacement fields) under the external electrical resistance of 100 MΩ (open-circuit) at each peak frequency when the defect is introduced in: (a) the 4th layer in the case of the single defect, (b) the 4th layer and (c) the 7th layer in the case of the double defects 80

Figure 3-7 A schematic configuration of a PnC with double defects with four different distances. 81

Figure 3-8 Mechanical displacement FRFs for four different distances of double defects under the external electrical resistances of 100 MΩ (open-circuit): (a) (4, 7), (b) (4, 8), (c) (4, 9), and (d) (4, 10)..... 85

Figure 3-9 Output voltage FRFs for four different distances of double defects under the external electrical resistances of 100 MΩ (open-circuit): (a) (4, 7), (b) (4, 8), (c) (4, 9), and (d) (4, 10)..... 86

Figure 3-10 A schematic configuration of a PnC with double defects with four different arranging directions. 88

Figure 3-11 Mechanical displacement FRFs for four different arranging directions of double defects under the external electrical resistances of 100 MΩ (open-circuit): (a) (4, 7-⓪), (b) (4, 6-①), (c) (4, 5-②), and (d) (4, 4-③). 91

Figure 3-12 Output voltage FRFs for four different arranging directions of double defects under the external electrical resistances of 100 MΩ (open-circuit): (a) (4, 7-⓪), (b) (4, 6-①), (c) (4, 5-②), and (d) (4, 4-③). 92

Figure 3-13 A schematic illustration of elastic wave localization using a two-dimensional PnC with double defects, relative incident waves. 94

Figure 3-14 A schematic illustration of an aluminum plate with a PnC having double defects (4, 7) under the finite domain condition. 96

Figure 3-15 Normalized out-of-plane displacement FRF results under the (a) infinite and (b) finite domain conditions. 97

Figure 3-16 Experimental setup for elastic wave generation system and visualization system. 100

Figure 3-17 Measured out-of-plane displacements in the time domain for (a) the single defect and those for double defects in (b) 4th and (c) 7th layers. 101

Figure 3-18 Comparison between numerical and experimental results for the single defect, double defects (4, 7), (4, 8), and (4, 9): numerically calculated out-of-plane displacement FRFs in (a) to (d); experimentally measured out-of-plane displacement FRFs in (e) to (h); and experimentally visualized mode shapes in (i) to (l). 103

Figure 3-19 Effects of the (a) density, (b) Young's modulus, (c) diameter of the circular hole, and (d) thickness of the unit cell on the defect band frequencies that correspond to in and out-of-phase monopole-like defect mode shapes. 104

Figure 3-20 Electrical circuit configurations for two PEH devices, colored in dark-blue: (a) an enlarged side view of the PnC-based PEH system with double defects; (b) Independent, (c) Series-Type A, (d) Series-Type B, (e) Parallel-Type C, and (f) Parallel-Type D connections. 109

Figure 3-21 Electrical circuit diagrams between two PEH devices: (a) Independent

connection, (b) in-phase and (c) out-of-phase electric current generation in the Series-Types A and B connections, (d) in-phase and (e) out-of-phase electric current generation in the Parallel-Types C and D connections. 110

Figure 3-22 Cancellation of electric current (or voltage) generated by two PEH devices for the out-of-phase defect mode shape in the Parallel-Type C connection and in-phase defect mode shape in the Parallel-Type D connection. 112

Figure 3-23 Mechanical displacement FRFs for five electrical circuit connections under the external electrical resistances of 100 MΩ (open-circuit): (a) Independent, Series-Types A and B, (b) Parallel-Types C and D connections 115

Figure 3-24 Output voltage FRFs for five electrical circuit connections under the external electrical resistances of 100 MΩ (open-circuit): (a) Independent, (b) Series-Types A and B, Parallel-Type C and D connections 117

Figure 3-25 Zero electric potential difference between the external electrical resistance for the out-of-phase defect mode shape in the Series-Type A connection and in-phase defect mode shape in the Series-Type B connection. 118

Figure 3-26 Output voltage and electric power across the external electrical resistance at peak frequencies for five electrical circuit connections: (a)

output voltage and (c) output electric power at 59.87 kHz for the Independent, Series-Type A, and Parallel-Type C connections, (b) output voltage and (d) output electric power at 60.19 kHz for the Independent, Series-Type B, and Parallel-Type D connections. 127

Figure 3-27 Output electric power FRFs across the optimal external electrical resistance for five electrical circuit connections: (a) Independent (120.2 kΩ), (b) Independent (95.50 kΩ), (c) Series-Types A (239.9 kΩ) and B (190.6 kΩ), and (d) Parallel-Types C (60.26 kΩ) and D (47.86 kΩ) connections..... 128

Figure 4-1 A schematic view of the two-dimensional PnC-based PEH system with L-shape arranged triple defects: periodic boundary condition and perfectly matched layers as the boundary conditions and transversely polarized A_0 Lamb wave as the excitation condition. 139

Figure 4-2 Operating deflection shapes (z-directional displacement fields) under the external electrical resistance of 100 MΩ (open-circuit) at (a) 60.01 kHz, (b) 60 kHz, and (c) 60.03 kHz. 142

Figure 4-3 Output voltage FRFs for a PnC with L-shape arranged triple defects, a PnC with a single defect, and a PnC with double defects under the external electrical resistance of 100 MΩ (open-circuit)..... 143

Figure 4-4 Output voltage and electric power FRFs for the PnC with L-shape arranged triple defects across optimal external electrical resistances: (a) output voltage and (b) electric power in Case I, and (c) output voltage

and (d) electric power in Case II. 146

Figure 5-1 Configuration of the supercell of the graded PnC consisting of 14 unit cells: (a) a schematic view and (b) a side view. 153

Figure 5-2 Calculated dispersion curves for the graded PnC without defects in the 1st irreducible Brillouin zone (M→Γ→X→M→Y→ Γ)..... 154

Figure 5-3 Defect band analysis for a graded PnC with a single defect imposed in (3, 4) under the external electrical resistance 0 Ω (short-circuit): (a) configuration of the graded PnC and (b) formation of five defect bands, labeled from A to E, within the full band gap ranging from 50.79 to 68.94 kHz. 160

Figure 5-4 Various defect mode shapes (z-directional displacement fields) of a graded PnC with a single defect under the external electrical resistance of 0 Ω (short-circuit): (a) 53.63 kHz (A), (b) 55.17 kHz (B), (c) 63.24 kHz (C), (d) 66.62 kHz (D), and (e) 67.47 kHz (E). 161

Figure 5-5 Trends of the defect band frequency that correspond to the monopole-like defect mode shape with respect to the defect location along the y-direction for the uniform PnC ((a) and (b)) and graded PnC ((c) and (d)) under external electrical resistances of 0 Ω (short-circuit, (a) and (c)) and 100 MΩ (open-circuit, (b) and (d))..... 162

Figure 5-6 Results of a different graded PnC with a single defect where the height of circular stubs hN is expressed as 13.00 mm+2.00 mm×sin{2π(N-

1)/14}: (a) a schematic of the graded PnC, (b) a side view of the graded PnC under periodic boundary conditions, and (c) trends of the defect band frequency with respect to the defect location under the external electrical resistance of 0 Ω (short-circuit). 163

Figure 5-7 Configuration of graded PnCs with: (a) the double defects imposed at (3, 4) and (3, 11) (Case I); (b) the single defect imposed at (3, 4) (Case II); and (c) the single defect imposed at (3, 11) (Case III). 165

Figure 5-8 Defect band analysis for a graded PnC with decoupled double defects (Case I): (a) defect bands of 55.15 kHz and 55.17 kHz under the external electrical resistance of 0 Ω (short-circuit), (b) defect bands of 55.72 kHz and 55.74 kHz under the external electrical resistance of 100 MΩ (open-circuit), monopole-like defect mode shapes at (c) 55.15 kHz (PEH Device 2) and (d) 55.17 kHz (PEH Device 1)..... 170

Figure 5-9 Defect band analysis for a uniform PnC with double defects of which the height of circular stubs is 13.45 mm under the external electrical resistance of 0 Ω (short-circuit): (a) configuration of the uniform PnC, (b) five defect bands within the band gap, and (c) monopole-like defect mode shape at 55.17 kHz. 171

Figure 5-10 System configuration of the graded PnC-based PEH system with the decoupled double defects. 173

Figure 5-11 Output voltage FRFs for Cases I, II, and II under the external electrical resistance of 100 MΩ (open-circuit). 176

Figure 5-12 Operating deflection shapes (z-directional displacement fields) in Case I under the external electrical resistance of 100 MΩ (open-circuit) at: (a) 55.72 kHz and (b) 55.74 kHz.....176

Figure 5-13 Output electric power for Cases I, II, and III with respect to external electrical resistances at each peak frequency. 180

Figure 5-14 Output electric power FRFs for Cases I, II, and III across the optimal external electrical resistance. 180

Figure A-1 Configuration of PnCs with defects: a PnC with (a) a single defect and (b) double defects, a M-DOF mass-spring system for a PnC with (c) a single defect and (d) double defects.....201

Figure A-2 Formation of band gaps with complex dispersion curves that are obtained from a lumped-parameter model of a one-dimensional PnC without defects under longitudinal elastic waves.....210

Figure A-3 Defect band analysis for a PnC with a single defect: (a) the formation of two defect bands within the first band gap; corresponding defect mode shapes at frequencies of (b) $f_{\mathrm{sd},1}$ and (c) $f_{\mathrm{sd},2}$. 212

Figure A-4 Asymptotic analysis for a PnC with a single defect: (a) the limiting behaviors of passbands and two defect bands; normalized displacement fields at frequencies of (b) $f_{\mathrm{sd},1}^{\mathrm{lim}}$, (c) $f_{\mathrm{sd},2}^{\mathrm{lim}}$, and (d) $f_{\mathrm{pb},3}^{\mathrm{lim(sd)}}$.....216

Figure A-5 Absolute normalized displacement fields a PnC with a single defect at frequencies of (a) $f_{\mathrm{sd},1}$ and (b) $f_{\mathrm{sd},2}$.....217

Figure A-6 Defect band analysis for a PnC with double defects: (a) the splitting of two defect bands into four defect bands; corresponding defect mode shapes at frequencies of (b) $f_{dd,1}$, (c) $f_{dd,2}$, (d) $f_{dd,3}$, and (e) $f_{dd,4}$. 222

Figure A-7 Asymptotic analysis for a PnC with double defects: (a) limiting behaviors of passbands and four defect bands; normalized displacement fields at frequencies of (b) $f_{pb,2}^{lim(dd)}$, (c) $f_{dd,1}^{lim}$, (d) $f_{dd,2}^{lim}$, (e) $f_{dd,3}^{lim}$, (f) $f_{dd,4}^{lim}$, (g) $f_{pb,4}^{lim(dd)}$, and (h) $f_{pb,5}^{lim(dd)}$.....224

Figure A-8 Absolute normalized displacement fields at frequencies of (a) $f_{dd,1}$, (b) $f_{dd,2}$, (c) $f_{dd,3}$, and (d) $f_{dd,4}$. 225

Figure B-1 A PnC-based PEH system with a defect: (a) a schematic view and (b) an enlarged view of a piezoelectric defect, with an electrical circuit configuration. 233

Figure B-2 Formation of defect bands within the band gap for the three cases (Cases I, II, and III). 251

Figure B-3 Defect mode shapes (normalized strain fields): (a) the 1st defect mode shape at 15.20 kHz (Case I); the 2nd defect mode shape (b) at 24.89 kHz (Case I), (c) at 22.08 kHz (Case II), and at 22.32 kHz (Case III). 256

Figure B-4 Effects of the external electrical resistance on the 2nd defect band frequency. 257

Figure B-5 Operating deflection shapes (strain fields) in and out of the PnC having

the piezoelectric defect at 22.08 kHz (Case II). 259

Figure B-6 PEH performance FRFs across various external electrical resistances of 50 Ω, 436 Ω, 4,571 Ω, and 50,000 Ω: (a) output electric power, (b) output voltage, and (c) output current. 264

Figure B-7 The flowchart of design optimization of a PnC with a piezoelectric defect for target frequency matching. 267

Figure B-8 Comparison of initial and optimal designs: (a) band gap and (b) output electric power FRFs. 271

Nomenclatures

PnC	phononic crystal
PEH	piezoelectric energy harvesting
PVEH	piezoelectric vibration energy harvesting
M-DOF	multi degree-of-freedom
FEM	finite element method
TMM	transfer matrix method
SPM	S-parameter method
SQP	sequential quadratic programming
FRF	frequency response function
P wave	longitudinal wave
SV wave	shear-vertical wave
SH wave	shear-horizontal wave
wd	without defect
sd	single defect
dd	double defects
pb	passband
lim	limiting behaviors
Ind	independent connection
Ser	series connection
Par	parallel connection
λ, μ	the 1st and 2nd Lame's constants of solids
∇	gradient operator
δ_{ij}	Kronecker delta
$S_A \times S_B$	supercell size of a PnC

a	lattice constant of a two-dimensional unit cell
t	thickness of a two-dimensional unit cell
d_{s}	diameter of a cylindrical stub
h_{s}	height of a cylindrical stub
d_{p}	diameter of a disc-type PEH device
h_{p}	height of a disc-type PEH device
$\mathbf{a}_x$, $\mathbf{a}_y$	component of a lattice vector
$\mathbf{b}_x$, $\mathbf{b}_y$	component of a reciprocal vector
$\mathbf{r}$	spatial vector
$\overline{\mathbf{r}}$	lattice vector
$\mathbf{k}$	reciprocal wavevector in the 1st irreducible Brillouin zone
$\mathbf{K}(\mathbf{k})$	stiffness matrix of a two-dimensional PnC
$\mathbf{M}$	mass matrix of a two-dimensional PnC
$\mathbf{q}$	eigenvector of a two-dimensional PnC
$\mathbf{u}$	three-dimensional vector of particle displacement fields
Γ , X , M , Y	points of the 1st irreducible Brillouin zone
d_{h}	diameter of a circular hole
$\upsilon_{\mathrm{Ind}}(t)$, $\upsilon_{\mathrm{Ser}}(t)$, $\upsilon_{\mathrm{Par}}(t)$	output voltage for several electrical circuit connections
$I_{\mathrm{Ind}}(t)$, $I_{\mathrm{Ser}}(t)$, $I_{\mathrm{Par}}(t)$	electric current for several electrical circuit connections
R_{Ind} , R_{Ser} , R_{Par}	external electrical resistance for several electrical circuit connections
$\varepsilon_{ij}^{\mathrm{Ind}}$, $\varepsilon_{ij}^{\mathrm{Ser}}$, $\varepsilon_{ij}^{\mathrm{Par}}$	second-rank strain tensor for several electrical circuit connections
$\lvert\boldsymbol{P}\rvert_{\mathrm{Ind}}$, $\lvert\boldsymbol{P}\rvert_{\mathrm{Ser}}$, $\lvert\boldsymbol{P}\rvert_{\mathrm{Par}}$	amplitude of the maximum output electric power for several electrical circuit connections
h_N	height of a cylindrical stub in the N-th unit cell of a graded PnC

l_{a} , l_{b}	length of a one-dimensional stack
w_{a} , w_{b}	width of a one-dimensional stack
h_{a} , h_{b}	height of a one-dimensional stack
ρ_{a} , ρ_{b}	density of a one-dimensional stack
Y_{a} , Y_{b}	Young's modulus of a one-dimensional stack
ν_{a} , ν_{b}	Poisson's ratio of a one-dimensional stack
l_{unit}	lattice constant of a one-dimensional unit cell
l_{defect}	length of a one-dimensional defect
N	number of one-dimensional unit cells
K	K-th unit cell where an initial one-dimensional defect is introduced
T	number of unit cells between one-dimensional double defects
m_{a} , m_{b}	lumped mass of a one-dimensional stack
s_{a} , s_{b}	lumped stiffness of a one-dimensional stack
$s_{\mathrm{eq}}^{\mathrm{unit}}$	equivalent lumped stiffness of a one-dimensional unit cell
m_{defect}	lumped mass of a one-dimensional defect
s_{defect}	lumped stiffness of a one-dimensional defect
$s_{\mathrm{eq}}^{\mathrm{defect}}$	equivalent lumped stiffness of a one-dimensional defect
$u_{\mathrm{a},n}(t)$, $u_{\mathrm{b},n}(t)$	longitudinal displacement of a one-dimensional stack
$u_{\mathrm{sd}}(t)$	longitudinal displacement of a one-dimensional single defect
$u_{\mathrm{dd1}}(t)$, $u_{\mathrm{dd2}}(t)$	longitudinal displacement of one-dimensional double defects
$U_{\mathrm{a},n}$, $U_{\mathrm{b},n}$	displacement amplitude of a one-dimensional stack
U_{sd}	displacement amplitude of a one-dimensional single defect
U_{dd1} , U_{dd2}	displacement amplitude of one-dimensional double defects
k_{wd} , k_{sd} , k_{dd}	reciprocal wavenumber in the 1st Brillouin zone ($\Gamma \rightarrow \mathrm{X}$)
$\mathbf{K}_{\mathrm{wd}}$, $\mathbf{K}_{\mathrm{sd}}$, $\mathbf{K}_{\mathrm{dd}}$	stiffness matrix for a lumped-parameter model
$\mathbf{M}_{\mathrm{wd}}$, $\mathbf{M}_{\mathrm{sd}}$, $\mathbf{M}_{\mathrm{dd}}$	mass matrix for a lumped-parameter model

$\omega_{\mathrm{wd}}, \omega_{\mathrm{sd}}, \omega_{\mathrm{dd}}$	eigenfrequency for a lumped-parameter model
$\mathbf{U}_{\mathrm{wd}}, \mathbf{U}_{\mathrm{sd}}, \mathbf{U}_{\mathrm{dd}}$	eigenvector for a lumped-parameter model
$f_{\mathrm{bg},1}^{\mathrm{lower}}$, $f_{\mathrm{bg},1}^{\mathrm{upper}}$	lower and upper edges of the 1st band gap for a lumped-parameter model
$f_{\mathrm{bg},2}^{\mathrm{lower}}$	lower edge of the 2nd band gap for a lumped-parameter model
$f_{\mathrm{pb},i}^{\mathrm{lim(sd)}}$	limiting behavior of passbands for a lumped-parameter model
$f_{\mathrm{sd},i}$	defect band frequency for a single defect
$f_{\mathrm{sd},i}^{\mathrm{lim}}$	limiting behavior of a defect band frequency for a single defect
$f_{\mathrm{dd},i}$	defect band frequency for double defects
$f_{\mathrm{dd},i}^{\mathrm{lim}}$	limiting behavior of a defect band frequency for double defects
l_{p}	length of a PEH device
w_{p}	width of a PEH device
h_{p}	height of a PEH device
R_{load}	external electrical resistance
m_{eff}	mass of an effective medium per unit length
s_{eff}	stiffness of an effective medium per unit length
$u(x,t)$	longitudinal displacement
$f(x,t)$	axial force
ρ_{p}	density of a piezoelectric material
c_{ij}^{E}	second-rank elastic modulus tensor at a constant electric field
s_{ij}^{E}	second-rank elastic compliance tensor at a constant electric field
E	electric field in the poling direction
d_{31}	piezoelectric strain coefficient
e_{31}	piezoelectric constant
ε_{33}^{T}	dielectric permittivity at a constant stress
ε_{33}^{S}	dielectric permittivity at a constant strain
σ_{m}	normal stress of an isotropic and homogeneous medium

σ_{p}	normal stress of a PEH device
$H(\cdot)$	Heaviside unit step function
$\delta(\cdot)$	Dirac delta function
$\upsilon(t)$	output voltage
$i(t)$	electric current
S_{p}	top surface area of a PEH device
dS	infinitesimal surface area
C_{p}	capacitance of a PEH device
$\boldsymbol{U}(x)$	longitudinal displacement with time-harmonic assumptions
$\boldsymbol{A}$, $\boldsymbol{B}$	displacement amplitude of right-going and left-going waves
$\boldsymbol{F}(x)$	axial force with time-harmonic assumptions
$\boldsymbol{V}(\omega)$	output voltage with time-harmonic assumptions
$\mathbf{P}_{\mathrm{l}}$, $\mathbf{P}_{\mathrm{r}}$	2×2 matrix relating a vector of velocity and force and displacement amplitudes of an effective medium
$\mathbf{T}_{\mathrm{eff}}$	electroelastically coupled transfer matrix
ω	an arbitrary angular frequency
k_{eff}	wavenumber of an effective medium
Z_{eff}	mechanical impedance of an effective medium
η	loss factor (structural damping)
θ	electroelastical coupling coefficient
$\mathbf{T}_{\mathrm{m}}$, $\mathbf{T}_{\mathrm{M}}$	transfer matrix of an isotropic and homogeneous medium
k_{m} , k_{M}	wavenumber of an isotropic and homogeneous medium
Z_{m} , Z_{M}	mechanical impedance of an isotropic and homogeneous medium
$\mathbf{I}$	identity matrix
$\mathbf{P}_{\mathrm{m}}$, $\mathbf{P}_{\mathrm{M}}$	2×2 matrix relating a vector of velocity and force and displacement amplitudes of an isotropic and homogeneous medium

$\mathbf{T}_{\text{rem}}$	transfer matrix of a defect where PEH devices are not attached
$\mathbf{T}_{\text{PEH}}$	transfer matrix for a PnC with a piezoelectric defect
$\mathbf{S}_{\text{PEH}}$	scattering matrix for a PnC with a piezoelectric defect
$\mathbf{u}_{\text{eff}}$	longitudinal displacement of an effective medium
$\boldsymbol{A}_{\text{eff}}$, $\boldsymbol{B}_{\text{eff}}$	displacement amplitude of an effective medium
$\boldsymbol{A}_{\text{in}}$	displacement amplitude of incident waves
$\boldsymbol{B}_{\text{in}}$	displacement amplitude of reflected waves
$\boldsymbol{A}_{\text{out}}$	displacement amplitude of right-going transmitted waves
$\boldsymbol{B}_{\text{out}}$	displacement amplitude of left-going transmitted waves
$\boldsymbol{A}_{\text{s}}$, $\boldsymbol{B}_{\text{s}}$	displacement amplitude in a stack
$\mathbf{u}_{\text{s}}$	longitudinal displacement of a stack
$\mathbf{d}$	vector of design variables in design optimization
$\mathbf{d}_{\text{L}}$, $\mathbf{d}_{\text{U}}$	lower and upper bounds of design variables $\mathbf{d}$
$\mathbf{d}_{\text{re}}$	regularized design variables
$\mathbf{d}_{\text{re, L}}$, $\mathbf{d}_{\text{re, U}}$	lower and upper bounds of regularized design variables $\mathbf{d}_{\text{re}}$
f_{target}	a target frequency
$f_{\text{bandgap,lower}}$	lower edge frequency of a band gap calculated by TMM
$f_{\text{bandgap,upper}}$	upper edge frequency of a band gap calculated by TMM
$\lambda_{\text{m, target}}$, $\lambda_{\text{M, target}}$	wavelength of an isotropic and homogeneous medium at the target frequency f_{target}
$P\left(\mathbf{d}, f_{\text{target}}\right)$	output electric power at the target operating frequency f_{target} for the design variables $\mathbf{d}$
$f_{\text{res,short}}$, $f_{\text{res,open}}$	peak frequency under the short-circuit and open-circuit conditions
f_{peak}	peak frequency in the FRF of output physical quantities

Chapter 1

Introduction

1.1 Motivation

Innovation in the manufacturing industry through the 4th Industrial Revolution based on the industrial internet of things (IIoT) has emerged as a very notable topic in line with the recent rapid development of information and communication technology (ICT). An important issue for the advent of IIoT is to build sustainable wireless sensor networks (WSNs) for acquiring high and good quality data [1, 2]. A prerequisite for sustainable WSNs is to establish stable and economical power supply systems. However, there are physical limitations to connect wires with a myriad of remotely located sensors. Moreover, supplying electric power with chemical batteries, which should be periodically replaced, requires temporary power shutdown as well as incurs large maintenance costs.

With this motivation, energy harvesting (EH), which converts ambient, otherwise wasted, energy into usable electricity, has attracted much attention as an alternative solution to ultimately eliminate the replacement cost of the chemical batteries in WSNs. Depending on energy sources and conversion mechanisms, a wide range of technology has been actively researched including wind, solar, thermal,

and mechanical energy harvesting. Among them, conversion of mechanical energy source (e.g., vibrations and waves) into electrical power using piezoelectric [3, 4], electromagnetic [5, 6], electrostatic [7, 8], or magnetostrictive transduction [9, 10] mechanisms is capable of providing micro- to mill-watts of power, potentially satisfying the power level of WSNs for both industry and everyday life applications. Especially, piezoelectric energy harvesting (PEH) is recognized as a promising solution due to its advantages of (1) high power density and (2) ease of miniaturization for use in WSNs [11-18]. An important principle of PEH is that piezoelectric materials can produce an electric charge in response to applied mechanical strain; this is called the direct piezoelectric effect [19-21] as shown in Figure 1-1. When electric circuits are connected to piezoelectric materials [22-24], the generated electric power can be stored and used for charging low-power electronics. In practice, since most engineered systems induce vibrations during operation, PEH offers an attractive potential option to sustainably supply a power source to WSNs.

To date, the development of highly efficient piezoelectric materials [25, 26], electrical circuit designs [27, 28], electroelastic modeling [29, 30], and structural

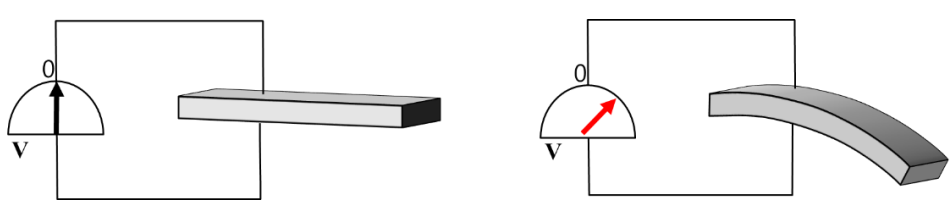

Figure 1-1 Electric polarization in response to the applied mechanical strain.

optimization [31, 32] of devices has been the key research approaches in order to enhance PEH performance. Optimal device designs allow efficient mechanical-to-mechanical energy coupling by allowing the absorption of mechanical energy into the PEH device as much as possible. High-performance piezoelectric materials along with a proper selection of electrode and structural materials increase the conversion efficiency of mechanical-to-electrical energy while circuit design with high efficiency reduces loss in the process of generated electrical power management and transfer to WSNs. However, conventional PEH has inherent limitations. That is, from the perspective of energy conservation, the harvestable electric power is inevitably small when the input mechanical energy transferred to the PEH device is small.

A possible solution to help improve the output electric power is to increase the input mechanical energy fed into the PEH device. In this context, a concept of phononic crystals (PnCs) has been recently incorporated into PEH systems to amplify the amount of input mechanical energy fed into PEH devices by tailoring

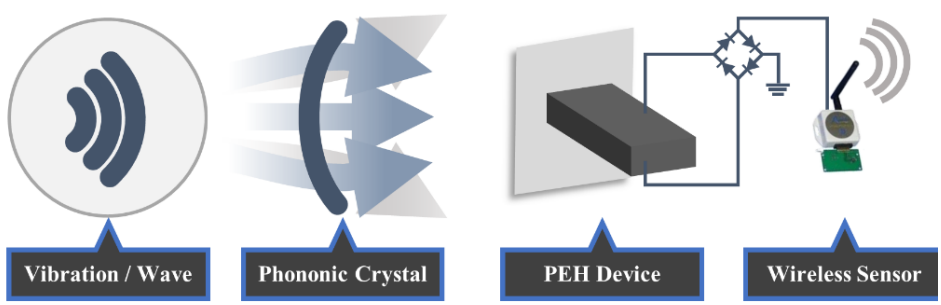

Figure 1-2 A brief concept of a PnC-based PEH system.

the wave propagation, before any conversion process is involved, as shown in Figure 1-2 [33-37]. It is a way of active energy harvesting in that the input mechanical energy is amplified by actively controlling it rather than passively harvesting and converting the given energy from the environment. In this doctoral dissertation, a PEH system where a PnC is incorporated is called a PnC-based PEH system.

A PnC, analogous to photonic crystals used in optics, refers to an artificially engineered structure that can be built by periodically modulating the density and Young's modulus of repetitive unit cells in line with the permeability and permittivity of the photonic crystal, respectively, under acoustic and/or elastic waves [38-45]. Due to the periodic characteristics, PnCs exhibit unusual phenomena that have not been observed in nature, such as a band gap [46, 47]. A PnC's band gap is a certain range of frequencies in which incident waves are prohibited from being transmitted while the PnC oscillates with a form of evanescent waves [48, 49]. In dispersion curves which represent the relationships between the frequency and wavenumber, band gaps are in the realm of frequencies that correspond to non-real complex wavenumbers. From the viewpoint of PEH, a great benefit of the band gap is to focus, guide, or localized the mechanical waves at the desired position for the purpose of achieving highly dense input mechanical energy [50]. The main concern of the research described in this doctoral dissertation is energy localization that induced by a defect mode of a PnC that possesses band gaps.

When a defect is introduced into a PnC by breaking the periodicity of unit cells such as eliminating one unit cell that is not arranged at borders of the PnC or replacing it with other unit cell having different material properties and/or geometrical dimensions [51-54], it is known that flat passbands (so-called defect

bands) are formed in a band gap regime [55, 56]. Furthermore, once an additional defect is introduced at a location away from the initial defect, the defect band of the single-defect case is split into two bands [57-60]. Here, the flatness of the bands indicates that the energy transport velocity (group velocity) is nearly zero [61]. Thus, when the PnC is exposed to waves whose excitation frequencies are close to defect band frequencies, evanescent waves inside the PnC become confined/trapped inside and in the vicinity of the defect. Figure 1-3 depicts a brief concept of defect-mode-enabled energy localization. By attaching PEH devices to the single or multiple defects of the PnC, the output electric power can be remarkably amplified as compared with a case in the absence of PnCs. When a conventional cantilever-type PEH device is used to convert ultrasonic waves induced by industrial applications such as power transformers or rotating machinery [62, 63] into electricity, it should be manufactured at a micro-scale for resonance [64, 65]. On the other hand, one can attach a macro-scale PEH device to the defect of a PnC, thereby enabling to generate the output electric power of a few mill-watts even under ultrasonic waves [66, 67].

Many prior research efforts have been made to enhance the output performance

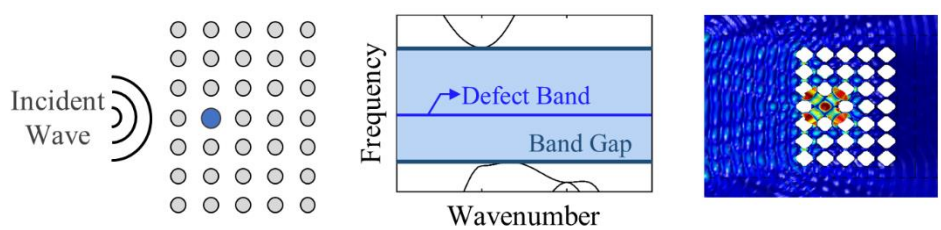

Figure 1-3 A brief concept of defect-mode-enabled energy localization.

of PEH by leveraging a defect mode of a PnC under acoustic waves [68-72]. In terms of reducing the mechanical impedance mismatching between solid medium and solid PEH devices, it should be emphasized that elastic waves with PnCs might be more favorable than acoustic waves for PEH purposes. Indeed, referring to the existing studies, it can be found that the amplification ratio of PEH can be remarkably high, but the absolute amount of the output electric power approaches near a few nano-Watts. With this motivation in mind, several research efforts have been made to exploit energy localization using defects of a PnC under elastic waves through numerical simulations and experiments [50, 66, 67, 73-76]. However, most of the existing studies have focused on only phenomena of improvement of PEH performance.

When bridging the domains of the defect-mode-enabled energy localization and PEH, little attention has been paid to the following two design issues that can arise. First, despite the successful enhancement of output performance PEH via a defect mode of a PnC, there have been very few attempts to provide any rationale for key design parameters (e.g., supercell size, defect location, and number of defects). Since the band gap characteristics, as well as amplitudes of evanescent waves, highly depend on both supercell size and defect location, there is a great need to investigate their effects on PEH performance for maximizing the harvestable electric power. Furthermore, the prior works limited their examination to a single defect. It should be emphasized that the incorporation of a PnC with double or multiple defects into PEH has not been touched yet. Second, since a PnC with a defect inherently possesses narrowband characteristics, the energy localization and harvesting performance could worsen under realistic environments. For instance, should an

excitation frequency be away from defect band frequencies, there could be a significant drop in the output electric power. Therefore, there is a great need to develop a new design concept of a PnC with defects which enables to broaden the bandwidth for PEH. Therefore, the above two issues should be properly addressed to make the best use of a PnC-based PEH system with defects in reality.

Furthermore, whereas several papers have presented numerical parametric studies of effects of material properties and geometric dimensions of a unit cell and/or a defect on defect band frequencies, there are few attempts to demonstrate (1) the fundamental principles of the formation and splitting of defect bands at certain frequencies and (2) why the existence of band gap is the precondition for defect-mode-enabled energy localization. Moreover, no further investigation has been made of elucidating the inertia, stiffness, and electroelastic coupling effects of PEH devices on defect bands even though attaching PEH devices to the defect may lead to changing the defect band frequencies, thereby resulting in a change to the output electric power. Therefore, there is a need to address the above-mentioned issue that emphasizes the physical interpretation of a PnC with piezoelectric defects.

1.2 Research Scope and Overview

This doctoral dissertation aims at advancing two essential and one co-related research areas to bridge the domains of defect-mode-enabled energy localization of a PnC and PEH: (1) Research Thrust 1 - parametric studies on structural and electrical circuit designs of a PnC with piezoelectric defects; (2) Research Thrust 2 - new design concepts of a PnC with piezoelectric defects for broadband PEH; and

(3) Appendix - an analytical model for a PnC with piezoelectric defects for the formation and splitting of defect bands.

Research Thrust 1: Parametric Studies on Structural and Electrical Circuit Designs of a Phononic Crystal with Piezoelectric Defects

Research Thrust 1 makes a step forward towards a deep understanding of the defect mode-enabled energy localization and its application to PEH for a two-dimensional PnC from the viewpoint of design issues. Research Thrust 1 proposes the following two topics under bending waves. First, when designing a two-dimensional PnC with a piezoelectric defect, an important issue that comes to mind is the number of unit cells that surround a defect (i.e., supercell size) and defect location within the supercell. Through examining the degree of the shifting of defect band frequencies when switching electric boundary conditions from short-circuit to open-circuit conditions, the selection of a target defect mode shape is elucidated for a two-dimensional PnC that can avoid voltage cancellation. Mechanical and electrical output performances of several two-dimensional PnCs with a piezoelectric defect are thoroughly investigated for two following cases: (1) various supercell sizes having a fixed defect location and (2) various defect locations having a fixed supercell size. Second, when designing a two-dimensional PnC with double piezoelectric defects, which is motivated by the splitting phenomenon of defect bands, the following two design issues should be addressed: (1) relative position between the double defects in the mechanical domain and (2) electrical circuit connection between double defects in the electrical domain. In the part of the effects of the relative position, the

distance and arranging direction between double defects are under consideration. While the location of one defect is fixed, the location of the other defect is changed along the propagating direction (distance effect) of incident waves or along the circumferential direction (direction effect) with the fixed defect as the origin. In the part of the effects of the electrical connection, five connection types (i.e., on Independent connection, two Series connections, and two Parallel connections) are under consideration. These studies thoroughly investigate how design parameters (i.e., the supercell size and defect location for the single piezoelectric defect and the relative position and electrical circuit connection for the double piezoelectric electric defects) affect several physical quantities that include defect band frequencies in defect band analysis, peak frequencies in frequency response functions (FRFs), the maximum displacement, output voltage and electric power, and optimal external electrical resistances.

Research Thrust 2: New Design Concepts of a Phononic Crystal with Piezoelectric Defects for Broadband Energy Harvesting

Research Thrust 2 proposes two new design concepts of a PnC with piezoelectric defects for broadband energy localization and harvesting under bending waves. One is a PnC with L-shape arranged triple defects. If a single defect and double defects are separated by a large distance within a PnC, they behave as an independent set of defects. Then, a PnC with a single defect and a PnC with double defects can be superimposed to one PnC-based PEH system. In the case of the single defect, high output electric power can be obtained at a certain defect band frequency with narrow

bandwidth. In the case of the double defects, relatively broad bandwidth can be obtained at two split defect band frequencies with low output electric power. Thus, superposing these two systems enables to achieve broadband PEH. The other is a graded PnC with decoupled double defects. A graded PnC refers to a PnC that is designed by varying one or more design variables of their lattices. If double defects are introduced to be sufficiently far from each other, any coupling effect between them can be eliminated. Since the defect band frequency is determined based on the mass and stiffness of the lattices surrounding the relevant defect, this allows the graded PnC to separately design defect band frequencies corresponding to each of the double defects in terms of their locations. It leads to localizing elastic waves in the vicinity of each defect at the designed different defect band frequencies. Therefore, the graded PnC can successfully realize broadband PEH.

Appendix: An Analytical Model for a Phononic Crystal with Piezoelectric Defects for Formation and Splitting of Defect Bands

In Appendix, the following two topics are presented under longitudinal waves. One is a lumped-parameter model (i.e., a multi-degree-of-freedom (M-DOF) mass-spring system) of a one-dimensional PnC with single or double defects to fundamentally elucidate the formation and splitting of defect bands. When asymptotic approaches are applied into defect band analysis, the limiting behaviors of defect bands and corresponding defect mode shapes provide important keys to what the physical meaning of defect-mode-enabled energy localization is. By performing the comparison before and after asymptotic analysis through the regression model, we

demonstrate why the band gap is a prerequisite of the formation and splitting of defect bands. The other is an electroelastically coupled analytical model of a one-dimensional PnC with a single defect to predict defect bands and output performance of PEH. Newton's 2nd law and Gauss's law are used to derive a mechanical equation of motions and electrical circuit equation, respectively. By solving these coupled equations with the help of Green's function, the electroelastically coupled transfer matrix is derived in an explicit manner. Finally, based on the transfer matrix method (TMM) and S-parameter method (SPM), an analytical model of a PnC with piezoelectric defect is proposed that has abilities to predict band structures and output performance of PEH. The proposed model's predictive capability is validated by comparing the calculated results of the analytical model with those of the finite element method (FEM).

1.3 Dissertation Layout

This doctoral dissertation is organized as follows. Chapter 2 presents a single defect mode of a PnC for energy localization and harvesting from the perspective of the supercell size and defect location (Research Thrust 1). Chapter 3 presents the incorporation of double defect modes of a PnC into PEH from the perspective of the relative position and electrical circuit connection between the double defects (Research Thrust 1). Chapters 4 and 5 propose new design concepts of a PnC with L-shape arranged triple defects and a graded PnC with decoupled double defects to realize broadband PEH, respectively (Research Thrust 2). Chapter 6 summarizes the doctoral dissertation with its contributions and suggests future research directions. In order to help better understanding of the underlying physics of the defect-mode-

enabled energy localization, Appendix A presents an lumped-parameter model for PnCs with single or double defects to fundamentally elucidate the formation and splitting of defect bands. Besides, by deriving an explicit form of an electroelastically coupled transfer matrix, Appendix B proposes an analytical model of a PnC with a piezoelectric defect to investigate how the electroelastic coupling affects the output performance of the system.

Sections of this chapter have been published or submitted as the following journal articles:

1) Tae-Gon Lee, **Soo-Ho Jo**, Hong Min Seung, Sun-Woo Kim, Eun-Ji Kim, Byeng D, Youn, Sahn Nahm, and Miso Kim, "Enhanced Energy Transfer and Conversion for High Performance Phononic Crystal-Assisted Elastic Wave Energy Harvesting," *Nano Energy*, Vol. 78, pp. 105226, 2020.
2) Choon-Su Park, Yong Chang Shin, **Soo-Ho Jo**, Heonjun Yoon, Wonjae Choi, Miso Kim, and Byeng D. Youn, "Two-dimensional Octagonal Phononic Crystals for High Dense Piezoelectric Energy Harvesting," *Nano Energy*, Vol. 57, pp. 327-337, 2019.

Chapter 2

Single Defect Mode of a Phononic Crystal for Energy Localization and Harvesting – From the Perspective of Supercell Size and Defect Location

Appendix A was devoted to fundamentally elucidating the formation (for a single defect) and splitting (for double defects) of defect bands by using M-DOF mass-spring systems of PnCs with single or double defects. Appendix B was dedicated to the derivation of the electroelastically-coupled analytical model of a one-dimensional PnC with a piezoelectric defect considering the inertia, stiffness and electroelastic coupling of PEH devices and to the prediction of its defect bands and PHE performance. When expanding a PnC design into the two-dimension, there are two primary advantages that include (1) localizing not only normal but also oblique incident waves into a defect and (2) having more rooms for designing the defect, as well as a unit cell, to improve PEH performance. With this motivation in mind, a few research efforts have been made to exploit energy localization and harvesting by leveraging a two-dimensional PnC with a single defect [50, 66, 67, 75, 77]. However,

it should be emphasized that prior works have not provided any rationale for the key design parameters (i.e., supercell size and defect location) that they used. They performed numerical analysis or experiments by introducing a defect into the center of a supercell having a certain size without any description. As a supercell size increases, band gap characteristics would be more strengthened since the formation of band gaps are under the assumption of infinite periodicity. Besides, the amplitude of evanescent waves at each defect location would be different. It can be thus inferred that the energy localization and harvesting performance would depend on the supercell size and defect location. Therefore, there is a great need to physically interpret the relationships between such key design parameters and energy localization and harvesting performances.

The objective of this chapter is thus to investigates the effects of the two key design parameters (i.e., supercell size and defect location) on the output performance of a PnC-based PEH system from the viewpoint of the periodicity and resonance formation. First, we examine whether several important issues discussed in Appendix B can be generally applied in a two-dimensional PnC with a piezoelectric defect, such as the shift of defect bands due to electroelastic coupling effects and the selection of defect mode shapes considering voltage cancellation. For instance, unlike acoustic waves, not only longitudinal (P) but only shear (i.e., shear-horizontal (SH) and shear-vertical (SV)) waves are observed due to the existence of shear stresses, shear strains, and Poisson's ratio. In particular, Rayleigh-Lamb (P and SV are coupled), and SH waves are observed in a thin plate case. Therefore, the defect mode shapes are much more complicated. Second, we investigate the mechanical and electrical responses of several two-dimensional PnCs with a piezoelectric defect

for two following cases: (1) various supercell sizes having a fixed defect location and (2) various defect locations having a fixed supercell size. Physical quantities of interest are peak frequencies in FRFs, the maximum displacement, output voltage and electric power, and optimal external electrical resistances. To the best of the authors' knowledge, the unique contributions of this study are two-fold. First, this is the first attempt to explore the effects of electroelastic coupling of a PEH device on defect bands for various defect mode shapes of a two-dimensional PnC. Second, we thoroughly examine the effects of supercell size and defect location on the output performance of a PnC-based PEH system with a defect from the perspective of the periodicity and resonance formation.

The remainder of Chapter 2 is organized as follows. Section 2.1 presents a system description of a two-dimensional PnC with a single defect. Section 2.2 describes the results of defect band frequencies and defect mode shapes under short-circuit and open-circuit conditions. Sections 2.3 and 2.4 present how both mechanical and electric responses of the PnC-based PEH system vary with different supercell sizes and defect locations, respectively. Section 2.5 presents how the optimal defect location depends on the supercell size with several examples. Finally, the conclusions of this work are outlined in Section 2.6.

2.1 System Description of a Phononic Crystal with a Single Defect

The PnC-based PEH system considered in this chapter, as shown in Figure 2-1 (a), consists of a host aluminum plate and a PnC with a single defect to which the circular,

disc-type PEH device (PZT-4D (lead zirconate titanate, $Pb(Zr_xTi_{1-x})O_3$)) is attached. The unit cell of the PnC is composed of a square lattice of a cylindrical aluminum stub deposited on the top surface of the plate, as shown in Figure 2-1 (b). For the unit cell, a and t denote the lattice constant and thickness of the host plate, respectively. d_s and h_s denote the diameter and height of the cylindrical stub, respectively. Figure 2-1 (c) shows the 5×7 supercell of the PnC-based PEH system. In this doctoral dissertation, S_A and S_B in a supercell size of $S_A \times S_B$ refer to the number of unit cells along the directions that are perpendicular and parallel to the normal incident waves, respectively. When envisaging a top view of Figure 2-1 (a) in which incident elastic waves enter from the left, S_A and S_B can be readily understood as the number of rows and columns, respectively, if the array of unit cells is thought of a matrix. A single defect is introduced to the 5×7 supercell by replacing one unit cell with the PEH device, thereby breaking the periodicity of the PnC. The defect is introduced at the 3rd layer along the x-direction (parallel to the incident wave direction) and in the middle layer along the y-direction (perpendicular to the incident wave direction), as colored in red. The PZT-4D disc (SMD10T2R11WL, STEMiNC) has two geometric parameters; one is the diameter d_p and the other is the height h_p. Table 2-1 summarizes the geometric information of the unit cell and PEH device. Mechanical properties of the aluminum are listed in Table 2-2. Table 2-3 summarizes the mechanical and electrical properties of PZT-4D. To consider the mechanical loss in the system, a loss factor η of 0.001 is introduced for the analysis of the PnC- based PEH systems by attributing a complex elastic modulus to the materials. For instance, the elastic constant of s_{11}^E is changed to $s_{11}^E(1+\eta i)$. In general, when analyzing the elastic wave behaviors, the loss factor does not have an important meaning. However, as described in 6.2Appendix A, since the defect mode is attributed to the mechanical

resonance, the loss factor is the important physical quantity in evaluating PEH performance.

In this doctoral dissertation, commercially available FEM software, COMSOL Multiphysics 5.4, was used in all analyses. In the field of PnC-based PEH [43, 78-81], as well as elastic wave propagation [82-86], COMSOL Multiphysics is widely

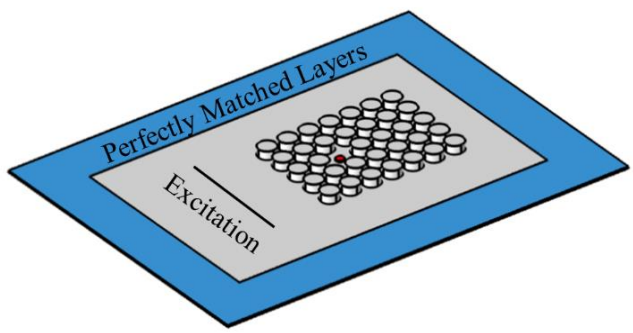

(a)

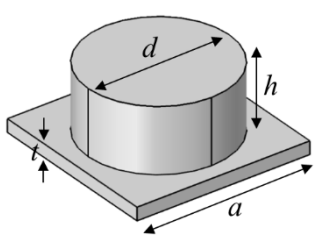

(b)

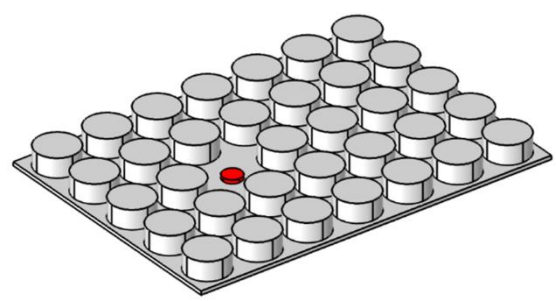

(c)

Figure 2-1 A schematic view of the two-dimensional PnC-based PEH system with a single defect: (a) the PEH system with excitation source and perfectly matched layers, (b) a cylindrical stub-type unit cell, and (c) the 5×7 supercell with the PEH device.

used due to its user-friendly interface and high predictive capability. As shown in Figure 2-1 (a), perfectly matched layers are set up at the boundaries of the host plate as an absorbing boundary condition to clearly observe the energy localization and harvesting performances upon the incident unidirectional plane waves. Other surfaces are in traction-free conditions. In addition, the A_0 Lamb wave is excited by harmonically loading the cross-section of the host plate in the transverse direction with a constant amplitude of 50 nm, marked in black in Figure 2-1 (a). In general, since the elastic wave propagates at an amplitude of several tens of nm in experiments, the amplitude of 20 nm is a reasonable value. To sufficiently excite the plane wave, the distance between the excitation source and the front row of the PnC was set to 100 mm, which is approximately six times the wavelength of the A_0 Lamb wave near 50 kHz.

Mesh elements of the whole structure are composed of hexahedrons. It should be noted that the maximum mesh size is considered to be one-tenth of the wavelength of the excited A_0 Lamb wave at the target defect band frequency. Referring to Tol *et al*. [79], for the mesh size of one-seventh of the wavelength of the excited A_0 Lamb wave, the numerical simulation were in good agreement with the experiments. Therefore, the mesh size used in this study would be enough to exhibit the high accuracy.

In terms of electroelastic coupling, three modules (i.e., solid mechanics, electrostatics, and electrical circuit modules) in COMSOL Multiphysics 5.4 are taken into account. The solid mechanics module has the ability to calculate the mechanical stress and strain of the PEH devices under given loading and boundary conditions. The electrostatics module has the ability to deal with linear

piezoelectricity. The electrical circuit module can calculate the output electric power across the external electrical resistance. Activating all modules provides proper modeling of the electroelastic coupling.

Table 2-1 Geometric dimensions of the unit cell and PEH device for a PnC with a single defect.

Unit cell (Aluminum)	Lattice constant	a	27 mm
	Thickness of plate	t	2 mm
	Diameter of stub	d_s	22 mm
	Height of stub	h_s	10 mm
PEH device (PZT-4D)	Diameter	d_p	10 mm
	Height	h_p	2 mm

Table 2-2 Mechanical properties of aluminum.

Unit cell (Aluminum)	Density	ρ_{al}	2700 kg/m^3
	Young's modulus	Y_{al}	70 GPa
	Poisson's ratio	d_{al}	0.33

Table 2-3 Mechanical and electrical properties of PZT-4D.

Mechanical properties	Density	ρ_{p}	7600 kg m^{-3}
	Compliances matrix	s_{11}^{E}	13.3 pm^2 N^{-1}
		s_{12}^{E}	-4.76 pm^2 N^{-1}
		s_{13}^{E}	-6.2 pm^2 N^{-1}
		s_{33}^{E}	16.8 pm^2 N^{-1}
		s_{55}^{E}	42 pm^2 N^{-1}
		s_{66}^{E}	36.1 pm^2 N^{-1}
Electrical properties	Piezoelectric strain coefficient	d_{31}	-135 pm V^{-1}
	Piezoelectric constant	e_{31}	-4.73 C m^{-2}
	Absolute permittivity	ε_0	8.85 pF m^{-1}
	Dielectric permittivity at constant stress	ε_{33}^{T}	12.83 nF m^{-1}
	Dielectric permittivity at constant strain	ε_{33}^{S}	6.75 nF m^{-1}
	Relative permittivity	ε_{r}	1450

2.2 Band Structure Analysis for a Phononic Crystal with a Single Defect

Defect band analysis was performed using a supercell calculation [51]. The supercell calculation has been widely used in defect band analysis [87-90]. However, it has a drawback that coupling between defects arranged in neighboring supercells can worsen the accuracy for calculating defect band frequencies when employing the Floquet-Bloch theorem into a supercell with a single defect [91, 92]. Therefore, to eliminate the coupling effects, it is required to make the distance between the defects be far enough. This implies that the size of the supercell with a defect should be sufficiently large [59, 93, 94]. It is assumed that the size of the supercell in Figure 2-1 (c) is enough large.

The governing equation for the elastic wave propagation in isotropic solids is considered as [61]:

$$\rho\frac{\partial^2\mathbf{u}}{\partial t^2}=\left(\lambda+2\mu\right)\nabla\nabla\cdot\mathbf{u}-\mu\nabla\times\nabla\times\mathbf{u}, \tag{2.1}$$

where ρ, λ and μ denote the density, the 1st and the 2nd Lame's constants of the solids, respectively. $\mathbf{u}$ denotes a vector of particle displacement fields. t is the time. and ∇ is a gradient operator. Note that Equation (2.1) is valid only for isotropic solids and can be decoupled into two equations representing the *xy*-mode (longitudinal and transverse waves) and the *z*-mode (transverse wave) when the supercell is periodically arranged in both *x*- and *y*-directions [95, 96]. For each of *xy*- and *z*-modes, the elastic wave propagation in isotropic solids can be expressed, respectively, as:

$$\rho\begin{bmatrix}\dfrac{\partial^2 u_x}{\partial t^2}\\ \dfrac{\partial^2 u_y}{\partial t^2}\end{bmatrix}=\left(\lambda+2\mu\right)\begin{bmatrix}\dfrac{\partial}{\partial x}\left(\nabla\cdot\mathbf{u}\right)\\ \dfrac{\partial}{\partial y}\left(\nabla\cdot\mathbf{u}\right)\end{bmatrix}-\mu\begin{bmatrix}\dfrac{\partial}{\partial y}\left(\dfrac{\partial u_y}{\partial x}-\dfrac{\partial u_x}{\partial y}\right)-\dfrac{\partial}{\partial z}\left(\dfrac{\partial u_x}{\partial z}-\dfrac{\partial u_z}{\partial y}\right)\\ \dfrac{\partial}{\partial z}\left(\dfrac{\partial u_z}{\partial y}-\dfrac{\partial u_y}{\partial z}\right)-\dfrac{\partial}{\partial x}\left(\dfrac{\partial u_y}{\partial x}-\dfrac{\partial u_x}{\partial y}\right)\end{bmatrix}, \quad (2.2)$$

$$\rho\frac{\partial^2 u_z}{\partial t^2}=\left(\lambda+2\mu\right)\frac{\partial}{\partial z}\left(\nabla\cdot\mathbf{u}\right)-\mu\left[\frac{\partial}{\partial x}\left(\frac{\partial u_x}{\partial z}-\frac{\partial u_z}{\partial x}\right)-\frac{\partial}{\partial y}\left(\frac{\partial u_z}{\partial y}-\frac{\partial u_y}{\partial z}\right)\right], \quad (2.3)$$

Floquet-Bloch theorem employs periodic boundary conditions into interfaces among adjacent supercells as follows [97, 98]:

$$\mathbf{u}\left(\mathbf{r}+\bar{\mathbf{r}}\right)=\mathbf{u}\left(\mathbf{r}\right)e^{i\mathbf{k}\cdot\bar{\mathbf{r}}}, \quad (2.4)$$

where $\mathbf{r}$ is a spatial vector, expressed as $x\mathbf{e}_x+y\mathbf{e}_y+z\mathbf{e}_z$; $\bar{\mathbf{r}}$ is a lattice vector, expressed $p\mathbf{a}_x+q\mathbf{a}_y$ ($p,\ q\in\mathbb{Z}$) where $\mathbf{a}_x$ and $\mathbf{a}_y$ are components of the lattice vector; $\mathbf{k}$ is a reciprocal wave vector, expressed as $m\mathbf{b}_x+n\mathbf{b}_y$ ($m,\ n\in\mathbb{R}$) where $\mathbf{b}_x$ and $\mathbf{b}_y$ are components of the reciprocal vector, defined by $\mathbf{a}_i\cdot\mathbf{b}_j=2\pi\delta_{ij}$ ($i,\ j=\{x,\ y\}$). δ_{ij} is Kronecker delta. Referring to the previous study [96], the lattice vector $\bar{\mathbf{r}}$ for the rectangular supercell having the size of $S_A\times S_B$ is expressed as $aS_A\mathbf{e}_x+aS_B\mathbf{e}_y$ where a is the lattice constant of the unit cell. Then, the reciprocal wave vector $\mathbf{k}$ is expressed as $2\pi m/aS_A\mathbf{e}_x+\ 2\pi n/aS_B\mathbf{e}_y$ ($m,\ n\in\mathbb{R}$). It is known that the reciprocal wave vector $\mathbf{k}$ belongs to the borderline of the 1st irreducible Brillouin zone (M→Γ→X→M→Y→Γ), as shown in Figure 2-2 (a) [99, 100]. Here, x- and y-directional components of the reciprocal wave vectors $\mathbf{k}$ range from 0 to π/aS_A and from 0 to π/aS_B, respectively. When assuming the harmonic motions of the supercell, an eigenvalue problem can be formulated by substituting Equation (2.4) into Equation (2.1) as:

$$\left(\left[\mathbf{K}\left(\mathbf{k}\right)\right]-\omega^2\left[\mathbf{M}\right]\right)\left\{\mathbf{q}\right\}=\mathbf{0}\,, \tag{2.5}$$

where [**K**(**k**)] is the stiffness matrix of the supercell as a function of the reciprocal wave vector **k**. [**M**] and {**q**} are the mass matrix and the displacement vector of the supercell, respectively. Finally, the band structures can be obatined numerically by calculating eigenfrequencies for the given reciprocal wave vectors **k** belonging to the 1st irreducible Brillouin zone (M→Γ→X→M→Y→Γ) [99, 100]. Here, it should be noted that the band gap analysis was performed at a unit cell level since the main concern of this chapter is defect bands. For the band gap analysis, because the unit cell has four-fold symmetry, it is well known that the 1st irreducible Brillouin zone for this kind of unit cells is Γ→X→M→Y. With the observations of the flatness of defect bands with respect to the wavenumbers in Appendix A and Appendix B, we perform the defect band analysis in Γ→X→M→Y, instead.

Figure 2-2 (b) presents the dispersion curves of the defected PnC with attaching PZT-4D, ranging from 50 kHz to 70 kHz. We confirmed that our unit cell under consideration has a full band gap, colored in the sky-blue box in the figure, ranging from 53.36 to 66.31 kHz. A full band gap is referred to as a band gap within which all polarized modes of elastic waves (longitudinal and transverse waves) are prohibited from being transmitted for all values of the wave vector. It can be obtained from an overlap between the band gaps for the longitudinal and transverse waves [95, 96]. Since a governing equation of elastic waves is a tensor form of the 4th order partial differential equations, the displacement fields in each direction are coupled to each other. This implies that defect modes for each polarized wave are coupled as well. Therefore, a full band gap characteristic is a prerequisite that a two-dimensional

PnC should possess for the formation of defect bands under elastic waves. For acoustic waves, however, a complete band gap is enough to realize formation of defect bands; complete band gaps are valid only for a certain polarized mode.

As demonstrated in Appendix B, the stiffness and mass of a surface-bonded PEH device attached to the structural layer could change the defect band frequency and corresponding defect mode shape. Likewise, after attaching the PEH device to the defect of the two-dimensional PnC, it is of great importance to consider the attachment of the PEH device in the supercell calculation.

In Figure 2-2 (b), six defect bands, which are flat passbands, are observed to be created within the full band gap. Here, only the mechanical coupling between the PEH device and host plate is considered under the external electrical resistance of 0 Ω. The frequencies of the defect bands, labeled from A to F, are as follows: 54.20 kHz (A), 55.62 kHz (B), 55.83 kHz (C), 58.62 kHz (D), 64.45 kHz (E), and 65.83 kHz (F). It should be noted that the number and value of defect bands, as well as the range of the band gap, depend on the geometric dimensions and material properties of the unit cell and PEH device [101-103]. In summary, the unit cell (aluminum) under consideration possesses the full band gap from 53.36 to 66.31 kHz; introducing the PEH device (PZT-4D) into the defect creates six defect bands within the full band gap.

Since all of the defect bands are flat, regardless of any reciprocal wave vectors **k**, the evanescent wave can be confined inside and in the vicinity of the defect at the defect band frequency with zero energy transport velocity. The slope of the tangent in the dispersion curves represents the energy transport velocity (or group velocity)

[104]. This interpretation is analogous to the results in Appendix A. Since several unit cells that surround the defect behave as the fixed boundary conditions, there is no preferred directionality. This implies that energy can be trapped into the defect no matter which direction the waves are incident. If the supercell size and defect location are determined, it can be inferred that the amount of mechanical energy transferred to the PEH device may vary depending on the incident direction of elastic waves since both the degree of the periodicity near the defect and displacement amplitudes of evanescent waves can be also dependent. However, investigating the effects of the incident directions are beyond the scope; this topic can be one of future works.

In a thin plate, three kinds of elastic waves are observed: the symmetric and antisymmetric modes (S mode and A mode) of Rayleigh-Lamb waves (in short, Lamb waves), and the SH wave [61]. These can be distinguished by the polarized direction of displacement fields in the structure. The main concern of this study is A_0 Lamb wave (zero-order antisymmetric mode of Lamb wave), which is polarized in the transverse direction. Figure 2-3 shows the defect mode shapes (*z*-directional displacement fields) at each of the six defect band frequencies that correspond to the results in Figure 2-2 (b).

When selecting a target defect band frequency, we need to recall the concept of voltage cancellation. Since the output voltage generated by a PEH device is proportional to the strains, tensile strains yield the positive voltage, and vice versa. Referring to the previous study by Erturk *et al*. [105, 106], the output voltage generated by the PEH device can dramatically decrease if the PEH device is subjected to both tensile and compressive strains. For the transversely polarized

waves, strain is proportional to geometric curvature. Hence, it is worth pointing out that the relationship between the geometric curvature and voltage phase should be taken into consideration to avoid voltage cancellation. The defect band frequency of 55.83 kHz (Case C in Figure 2-3) that corresponds to the monopole-like defect mode shape seems most desirable in terms of voltage cancellation. Except for the monopole-like defect mode shape in Figure 2-3 (c), the remaining defect mode shapes contain strain nodal lines (zero strain) in the PEH device, thus leading to the decrease in the output voltage. Therefore, the defect mode shape of Case C is selected as a target defect mode shape. Since the monopole-like defect mode shape in Figure 2-3 (c) is the transversely polarized displacement fields (i.e., out-of-plane mode shape), it can localize A_0 Lamb waves. If the selection rationale of defect mode shapes based on the voltage cancellation for one-dimensional PnCs, presented in Appendix B, can be expanded to two-dimensional PnCs, the monopole-like defect mode shape should represent the largest amount of the shift of the defect band frequency when switching the electrical boundary condition from the short-circuit to open-circuit conditions.

To investigate the electroelastic coupling effects of the PEH device on the defect band frequencies, Table 2-4 summarizes the results of defect band analysis we perform under the external electrical resistances of 0 Ω (short-circuit) and 100 MΩ (open-circuit) when the reciprocal wave vector **k** is equal to (0, 0). It is observed that all of the defect band frequencies except for Case E slightly increase, as the external electrical resistance is shifted from 0 Ω to100 MΩ. From this chapter, it is assumed that the external electrical resistance of 100 MΩ can make the electrical boundary condition close to the open-circuit condition. For instance, the defect band

frequency corresponding to the monopole-like defect mode shape (Case C) increases from 55.83 kHz to 55.96 kHz. The effective elastic stiffness of piezoelectric materials increases when the external electrical resistance is shifted from 0 Ω to 100 MΩ [105]. The amount of the frequency shift depends on the electroelastic coupling if the other conditions are fixed. In general, the bigger the electroelastic coupling, the larger the frequency shift. In Figure 2-3 (c), the electroelastic coupling is strong due to the absence of a strain nodal line; whereas, in Figure 2-3 (e) there is nearly zero electroelastic coupling due to the presence of the nodal line in the PEH device. Therefore, it can be concluded that the investigation of the defect-induced energy localization of a one-dimensional PnC, demonstrated in Appendix B, can be extended to the two-dimensional PnC case. To the best of the authors' knowledge, this is the first attempt to explore the effects of electroelastic coupling of a PEH device on the defect band for the various defect mode shapes of the two- dimensional PnC.

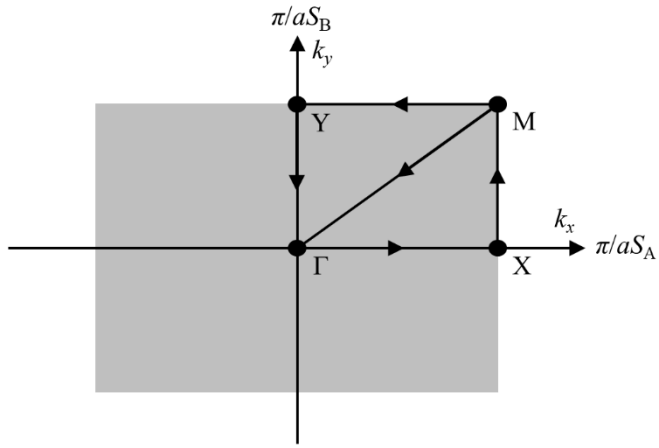

(a)

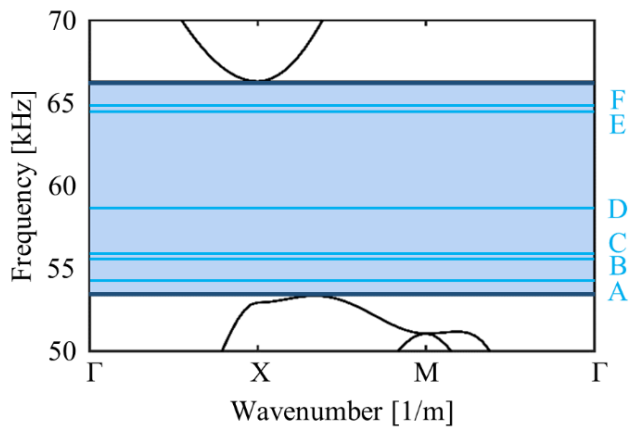

(b)

Figure 2-2 Band structure analysis for a 5×7 supercell with a single defect under the external electrical resistance 0 Ω (short-circuit): (a) the 1st irreducible Brillouin zone (M→Γ→X→M→Y→Γ) and (b) formation of six defect bands within the full band gap, ranging from 53.36 to 66.31 kHz (54.20 kHz (A), 55.62 kHz (B), 55.83 kHz (C), 58.62 kHz (D), 64.45 kHz (E), and 65.83 kHz (F)).

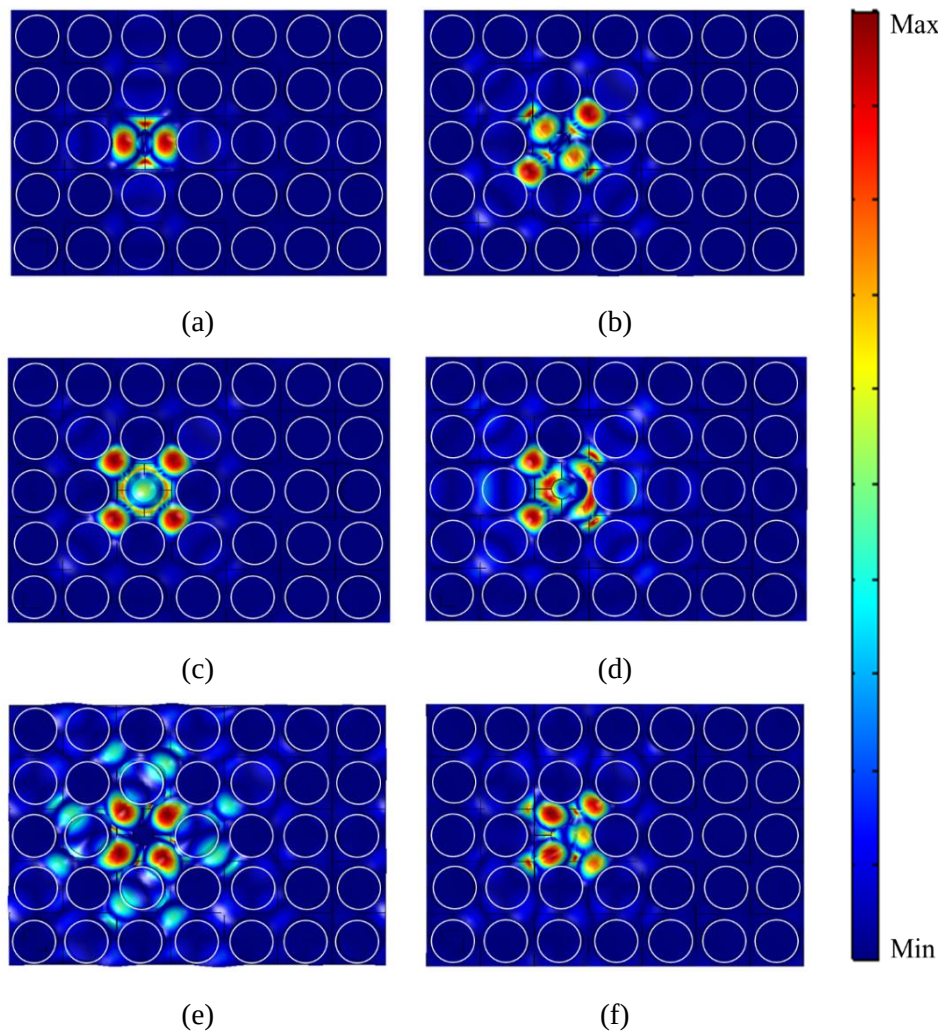

Figure 2-3 Various defect mode shapes (*z*-directional displacement fields) for a 5×7 supercell with a single defect under the external electrical resistance of 0 Ω (short-circuit): (a) 54.197 kHz (A), (b) 55.618 kHz (B), (c) 55.825 kHz (C), (d) 58.617 kHz (D), (e) 64.446 kHz (E), and (f) 65.834 kHz (F).

Table 2-4 Defect band frequencies under the external electrical resistances of 0 Ω (short-circuit) and 100 MΩ (open-circuit) when **k**=(0, 0).

Defect mode	Defect band frequency [kHz]		Difference [Hz]
	0 Ω (short-circuit)	100 MΩ (open-circuit)	
A	54.20	54.21	10
B	55.62	55.64	20
C	55.83	55.96	130
D	58.62	58.62	0
E	64.45	64.45	0
F	64.83	64.86	30

2.3 Effects of the Supercell Size on Energy Localization and Harvesting Performance

The research outlined in this section is devoted to investigating the effects of the supercell size on the output performances of the PnC-based PEH system with the defect. In this study, the supercell size increases only along the *x*-direction (i.e., direction of propagating waves) from 5×4 to 5×7. The supercell size of the five lattices along the *y*-direction (i.e., perpendicular direction of propagating waves) remains unchanged to keep the incident wave energy transferred to the PnC-based PEH system constant. Section 2.3.1 describes the mechanical output performance and Section 2.3.2 investigates the electrical output performance at various external electrical resistances with supercell sizes.

2.3.1 Mechanical Output Performance with Different Supercell Sizes

The mechanical output performance is analyzed by investigating the displacement of the PEH device attached to the center of the defect in the PnC. In Section 2.2, we identified the defect band that shows the monopole-like defect mode shape at 55.83 kHz and 55.96 kHz under the external electrical resistances of 0 Ω (short-circuit) and 100 MΩ (open-circuit), respectively. The displacement fields are investigated near the defect band frequencies under both circuit conditions. Figure 2-4 presents the operating deflection shapes (*z*-directional displacement fields) of the 5×4, 5×5, 5×6, and 5×7 supercells at each peak frequency under the external electrical resistance of 0 Ω (short-circuit), respectively. The white circles indicate the cylindrical stubs of unit cells, as described in Section 2.1. For all cases, the defect is introduced at the 3rd layer of the PnC along the *x*-axis direction. Here, the sinusoidal excitation (A_0

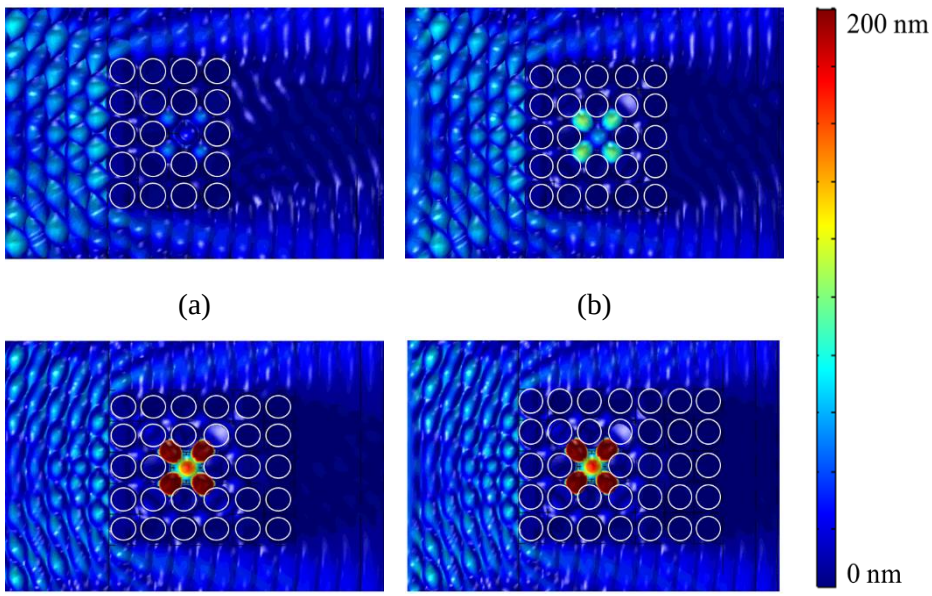

Figure 2-4 Operating deflection shapes (*z*-directional displacement fields) under the external electrical resistance of 0 Ω (short-circuit) at each peak frequency when the defect is introduced in: (a) 5×4 supercell, 55.73 kHz, (b) 5×5 supercell, 55.78 kHz, (c) 5×6 supercell, 55.81 kHz, and (d) 5×7 supercell, 55.82 kHz.

Lamb wave) of 50 nm is loaded at the left end of the host plate. At each peak frequency, the defect vibrates with the monopole-like defect mode shape, as shown in Figure 2-3 (c). These results are analogous to those for the one-dimensional PnC case in Figures 2-3 (c) and 2-5.

It is observed that the energy localization performance is drastically enhanced especially when the supercell size increases from 5×4 to 5×5. This is mainly attributed to the degree of the periodicity of the unit cells surrounding the defect. For

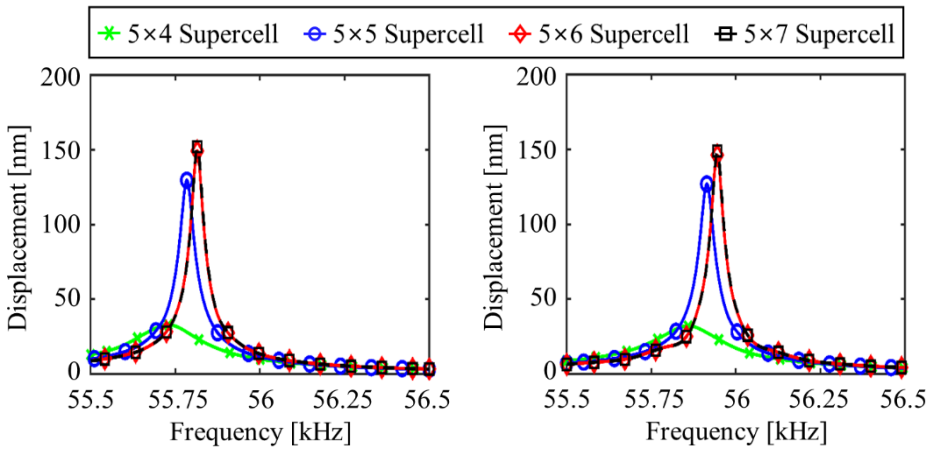

Figure 2-5 Mechanical displacement FRFs for different supercell sizes under the external electrical resistances of (a) 0 Ω (short-circuit) and (b) 100 MΩ (open-circuit).

the 5×4 supercell, there is only one layer to the right of the defect. This means that the number of unit cells surrounding the defect is insufficient to exhibit the band gap characteristics. The sufficient periodicity that arises by increasing the supercell size ensures the band gap characteristics. Then, the formation of mechanical resonance, induced by fixed-like boundary conditions, is more strengthened by generating more clear evanescent wave fields within the PnC. Thereby, the amount of the input energy transferred to the defect can be enhanced as the periodicity near the defect is sufficient.

Figures 2-5 (a) and 2-5 (b) show the FRFs for the *z*-directional displacement of the PEH device attached to the defect of the PnC, ranging from 55.5 kHz to 56.5

kHz, under the external electrical resistances of 0 Ω (short-circuit) and 100 MΩ (open-circuit), respectively. Here, the *z*-directional displacement is calculated at the center of the top surface of the PEH device for different supercell sizes. The maximum displacement results at peak frequencies under the external electrical resistance of 100 MΩ (open-circuit), shown in Figure 2-5 (b), are smaller than those observed at peak frequencies under the external electrical resistance of 0 Ω (short-circuit), shown in Figure 2-5 (a), due to the shunt resistive damping effect. It is observed that all peak frequencies slightly increase as the external electrical resistances is shifted from 0 Ω (short-circuit) to 100 MΩ (open-circuit). The shift results are analogous to those for the one-dimensional PnC case shown in Figure B-6 (a).

As shown in Figures 2-5 (a) and 2-5 (b), it is worth noticing that peak frequencies, as well as corresponding maximum displacements, increase under both circuit conditions as the supercell size increases until the supercell size reaches 5×6. Next, when a certain size of supercell is reached (5×6 supercell here), peak frequencies and corresponding maximum displacement converge toward each maximum value. Therefore, it can be demonstrated that a sufficient number of unit cells is required to exhibit the band gap characteristics or energy localization in the vicinity of the defect of the PnC systems in both electroelastically uncoupled and coupled systems.

In examining the theory of the band gap and formation of defect bands with infinitely arranged unit cells, it is notable that peak frequencies under the external electrical resistances of 0 Ω (short-circuit) and 100 MΩ (open-circuit) converge to the defect band frequencies of 55.83 kHz and 55.96 kHz, respectively. From the

viewpoint of the periodicity, this implies that peak frequencies will be consistent with defect band frequencies under each circuit condition, respectively, when much larger supercells would be analyzed. This idea is supported by the results of the 5×4 supercell, which has peak frequencies of 55.73 kHz (0 Ω, short-circuit) and 55.86 kHz (100 MΩ, open-circuit). These peak frequencies are far from the defect band frequencies. This is because there is only one unit cell on the right side of the defect in the 5×4 supercell from the top view. Hence, there is a lack of periodicity. Thus, when the excitation frequency is adjacent to the defect band frequency, it can be concluded from the results that the defect mode of the PnC leads to energy localization if a large enough supercell size is considered. An underestimation of those frequencies is attributed to the loss factor and is not considered in the defect mode analysis. Table 2-5 lists maximum displacement, shown in Figures 2-5 (a) and 2-5 (b), and corresponding peak frequencies for different supercell sizes. To investigate the amplification ratio of the mechanical response, the *z*-directional displacements at the center of the PEH device for a host plate in the absence of the PnC are calculated as 10.82 nm at 55.82 kHz and 10.72 nm at 55.95 kHz under the external electrical resistances of 0 Ω (short-circuit) and 100 MΩ (open-circuit), respectively.

Here, we need to recall the principles of the formation of defect bands and the assumption of supercell calculation. The observations in this section is consistent with the physical interpretation that some crystals far from the defect get near-zero displacements due to the attenuating properties of evanescent waves. Therefore, they behave as fixed-like boundary conditions. Moreover, it is still consistent with the previous studies' statement that the number of unit cells should be sufficiently large

to guarantee high accuracy of the supercell calculation [59, 93, 94].

2.3.2 Electrical Output Performance with Different Supercell Sizes

Effects of supercell size on the output voltage and electric power of the PnC-based PEH system are analyzed among various external electrical resistances. Figure 2-6 shows the output voltage FRFs, ranging from 55.5 kHz to 56.5 kHz under the external electrical resistance of 100 MΩ (open-circuit). The maximum output voltage at each peak frequency is calculated as 3.358 V, 13.69 V, 15.88 V, and 16.19 V in 5×4, 5×5, 5×6, and 5×7 supercells, respectively. Similar to the trends observed for maximum displacement, the maximum output voltage rises and becomes saturated to a certain maximum value as the supercell size increases until the supercell size reaches 5×7. To investigate the amplification ratio of the mechanical response, the output voltage generated by the PEH device for a host plate in the

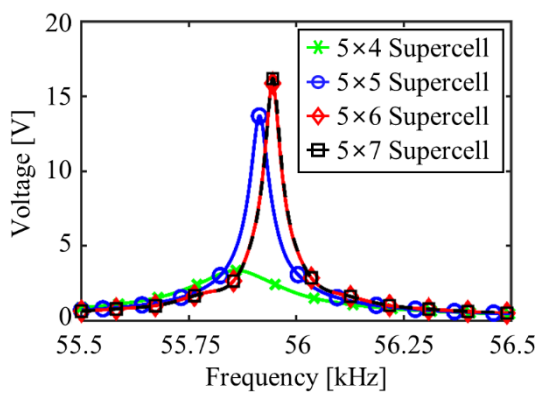

Figure 2-6 Output voltage FRFs for different supercell sizes under the external electrical resistance of 100 MΩ (open-circuit).

absence of the PnC was calculated as 1.034 V at 55.95 kHz. It should be noted that the voltage cancellation always occurs over time, since the diameter of the PEH device is larger than the half-wavelength near 55 kHz. Table 2-5 summarizes the maximum output voltage at each peak frequency, shown in Figure 2-6, for different supercell sizes.

Here and hereafter, the short-circuit and open-circuit resonance frequencies are defined as peak frequencies in mechanical displacement FRFs for the sake of simplicity, when the external electrical resistances are 0 Ω (short-circuit) and 100 MΩ (open-circuit), respectively [20, 29, 30]. Figure 2-7 (a) shows the output voltage as a function of external electrical resistance ranging from 0 Ω (short-circuit) to 100 MΩ (open-circuit) at each open-circuit resonance frequency (55.91 kHz, 55.94 kHz, and 55.95 kHz) for different supercell sizes, 5×5, 5×6, and 5×7, respectively. Due to the lack of periodicity for the 5×4 supercell, this case cannot be physically regarded as energy localization and harvesting that leverage a defect mode of a PnC. Therefore, it is not included in this analysis. For all supercell sizes, the output voltage asymptotically increases and converges toward the maximum values that are peak output voltage under the external electrical resistance of 100 MΩ (open-circuit). Observation suggests that the larger supercell size contributes to the higher output voltage generation due to satisfaction of sufficient periodicity and, thus, a larger energy localization effect.

Figures 2-7 (b) and 2-7 (c) depict the output electric power as a function of the external electrical resistance at each short-circuit resonance frequency (55.78 kHz, 55.81 kHz, and 55.82 kHz) and at each open-circuit resonance frequency (55.91 kHz, 55.94 kHz, and 55.95 kHz) for supercell sizes of 5×5, 5×6, and 5×7, respectively.

Since the behavior of the output electric power with changing the external electrical resistance is non-monotonic, there exists the optimal value of the external electrical resistance at which the maximum output electric power can be achieved. In Figure B-6, the maximum output electric power at the short-circuit resonance frequency is the same as that at the open-circuit resonance frequency. To obtain the maximum output electric power at the short-circuit and open-circuit resonance frequencies, therefore, the optimal values of the external electrical resistance were found by sweeping it. The optimal external electrical resistance for each supercell size of 5×5, 5×6, and 5×7 at corresponding short-circuit resonance frequency is found as 912 Ω, 759 Ω, and 759 Ω, respectively. That at corresponding open-circuit resonance frequency is calculated as 38,019 Ω, 45,709 Ω, and 45,709 Ω, respectively.

As the supercell size increases, the maximum output electric power increases and converges toward the maximum value. The output electric power for each supercell size of 5×5, 5×6, and 5×7 at corresponding short-circuit resonance frequency reaches up to 1.202 mW, 1.363 mW, and 1.392 mW, respectively, while at corresponding open-circuit resonance frequency reaches up to 1.213 mW, 1.368 mW, and 1.387 mW, respectively. Table 2-6 lists the calculated results of the maximum output electric power of the PnC-based PEH system at corresponding optimal external electrical resistances for different supercell sizes. Here, it should be noted that the maximum mechanical power of guided bending waves that transferred to the host medium by excitation is calculated as near 3.94 mW at the frequency of 55 kHz [107]. Even though the larger supercell size would provide higher PEH performance, it is usefully found that the supercell does not need to be larger than a certain size once it fulfills the periodicity of the unit cells near the defect.

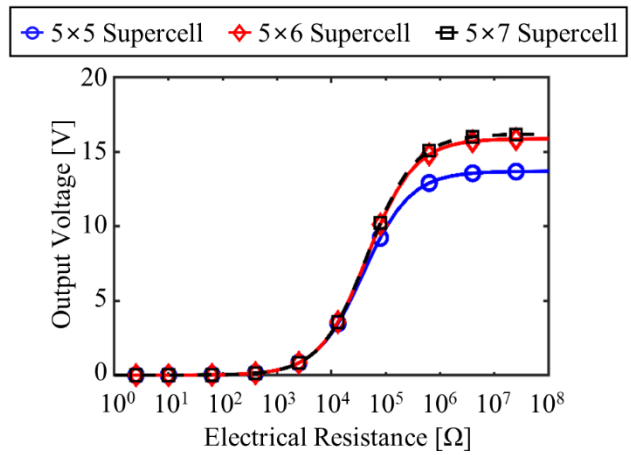

(a)

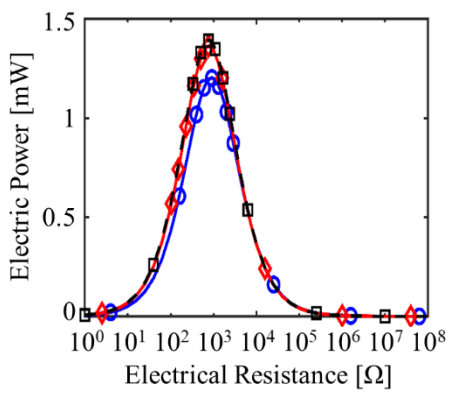

(b)

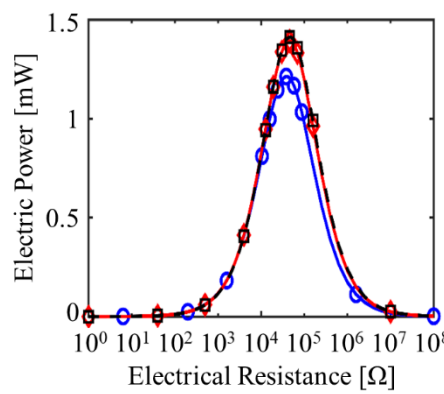

(c)

Figure 2-7 Electrical output performances with respect to the external electrical resistance for different supercell sizes: (a) output voltage at an open-circuit resonance frequency, (b) output electric power at a short-circuit resonance frequency, and (c) output electric power at an open-circuit resonance frequency.

Table 2-5 Output performances under external electrical resistances of 0 Ω (short-circuit) and 100 MΩ (open-circuit) for different supercell sizes.

External electrical resistance	Physical quantity	Supercell size			
		5×4	5×5	5×6	5×7
0 Ω (short-circuit)	Peak frequency [kHz]	55.73	55.78	55.81	55.82
	Displacement [nm]	33.88	129.6	149.3	152.0
100 MΩ (open-circuit)	Peak frequency [kHz]	55.86	55.91	55.94	55.95
	Displacement [nm]	32.00	126.9	146.2	148.9
	Output voltage [V]	3.358	13.69	15.88	16.19

Table 2-6 The maximum output electric power at the optimal external electrical resistance for different supercell sizes.

Frequency	Physical quantity	Supercell size		
		5×5	5×6	5×7
Short-circuit resonance frequency	Optimal external electrical resistance [Ω]	912	759	759
	Maximum output electric power [mW]	1.202	1.363	1.392
Open-circuit resonance frequency	Optimal external electrical resistance [Ω]	38,019	45,709	45,709
	Maximum output electric power [mW]	1.213	1.368	1.387

2.4 Effects of the Defect Location on Energy Localization and Harvesting Performance

In order to identify the optimal location of a defect in a given supercell size of a PnC for energy localization and harvesting, this section is dedicated to investigating the effects of the defect location on the output performance of a PnC-based PEH system with a defect. The supercell size is fixed to the 5×7 supercell. We sequentially change the defect location from the 1st layer to the last layer along the *x*-direction (i.e., direction of propagating waves) while the position along the *y*-direction is fixed at the center of the host structure. Section 2.4.1 describes the mechanical output performance, while Section 2.4.2 investigates the electrical output performance at various external electrical resistances when a single defect is introduced at different locations inside the PnC.

2.4.1 Mechanical Output Performance with Different Defect Locations

Figure 2-8 presents the operating deflection shapes (*z*-directional displacement fields) of the PnC-based PEH system at each peak frequency when the defect is positioned at five different locations inside the same 5×7 supercell under the external electrical resistance of 0 Ω (short-circuit). In Figures 2-8 (a) to 2-8 (e), the defect location is changed from the 2nd to the 5th layer along the *x*-axis. Here, the sinusoidal excitation (A_0 Lamb wave) of 50 nm is loaded at the left end of the host plate.

Observation of the results in Figure 2-8 suggests that there exists an apparent optimal location for a defect from the perspective of energy localization and harvesting. When we move the defect location from the 2nd layer to the 6th layer,

the highest displacement amplitude up to 152.0 nm is observed in Figure 2-8 (b), where the defect is located at the 3rd layer. This can be explained by the trade-off relationship between the sufficient periodicity of unit cells surrounding the defect and the attenuation of the evanescent waves. As presented in Appendix A, in order to more clearly form the fixed boundary conditions by the evanescent waves in the vicinity of the defect, the band gap characteristics need to be strengthened further. Thus, more number of unit cells are required to be arranged near the defect. However, from the perspective of the magnitudes of evanescent waves under the assumption of unidirectional waves, it would be more advantageous to locate the defect as close to the 1st layer as in order to lose less energy and thus gather more energy since the evanescent waves are exponentially attenuated through the PnC in the incident wave direction. Therefore, the trade-off relationship between the sufficient periodicity of unit cells surrounding the defect and the attenuation of the evanescent waves leads to making the optimal defect location for a certain supercell size. From the viewpoint of the periodicity of the unit cells surrounding the defect, the cases in which the defect is located at the 2nd or 6th layers (as seen in Figures 2-8 (a) and 2-8 (e)) are insufficient to create band gaps (and thus insufficient to create defect bands) due to a lack of periodicity on either side. As a result of this trade-off, the case where the defect is positioned at the 3rd layer exhibits the highest energy localization performance even though the 2nd layer is closer to the excitation source. Hence, it is essential to select an optimal defect location in PnCs for enhanced energy localization and harvesting by considering both (1) the sufficient periodicity of the unit cells surrounding the defect for band gap creation, and (2) the attenuation of evanescent waves for sufficient energy gathering. One thing we should note here is that the optimal defect location depends on the configurations of a unit cell and a

defect. Thereby, it is difficult to mention a generalized optimal defect location. It is required to perform a parametric study to find the optimal defect location for a system of interest.

Figures 2-9 (a) and 2-9 (b) depict the results of displacement FRFs, ranging from 55.5 kHz to 56.5 kHz, under the external electrical resistances of (a) 0 Ω (short-circuit) and (b) 100 MΩ (open-circuit), respectively, at different defect locations. When the defect is located at the 1st or 7th layers, it is worth noting that no peak appears around the defect band frequencies of 55.83 kHz (0 Ω, short-circuit) or 55.96 kHz (100 MΩ, open-circuit) in Figures 2-9 (a) and 2-9 (b), respectively. Due to the absence of periodicity, the defect band has a difficult time to be formed. The absence of unit cells surrounding the defect makes it difficult for the defect to vibrate with the monopole-like defect mode shape, shown in Figure 2-3 (c). Hence, it is hard to localize elastic waves.

It can be found that the peak frequencies under both circuit conditions in the cases of the 2nd and 6th layers are slightly smaller than those in the other cases. When the defect is introduced at the 2nd or 6th layer, the number of unit cells is insufficient to realize a defect-induced energy localization. When the number of unit cells surrounding the defect is not large enough, the fixed boundary conditions are unclear and the unit cells, as well as the defect, tend to vibrate more. Therefore, the stiffness of the defect can be lowered. This is why the peak frequency increases and converges to the defect band frequency as the number of unit cells surrounding the defect increases. The tendency of the defect band frequency with respect to the supercell size and defect location can be commonly elucidated in terms of the periodicity near the defect. To support this interpretation, when the defect is imposed

at the 4th layer, the peak frequency of 55.83 kHz is the closest to the defect band frequency of 55.83 kHz under the external electrical resistance of 0 Ω, as can be seen in Table 2-7. This fact also leads to the conclusion that defect band formation is strengthened the most when the defect is imposed at the 4th layer. Table 2-7 summarizes the results of the peak frequencies and corresponding maximum displacements for different defect locations.

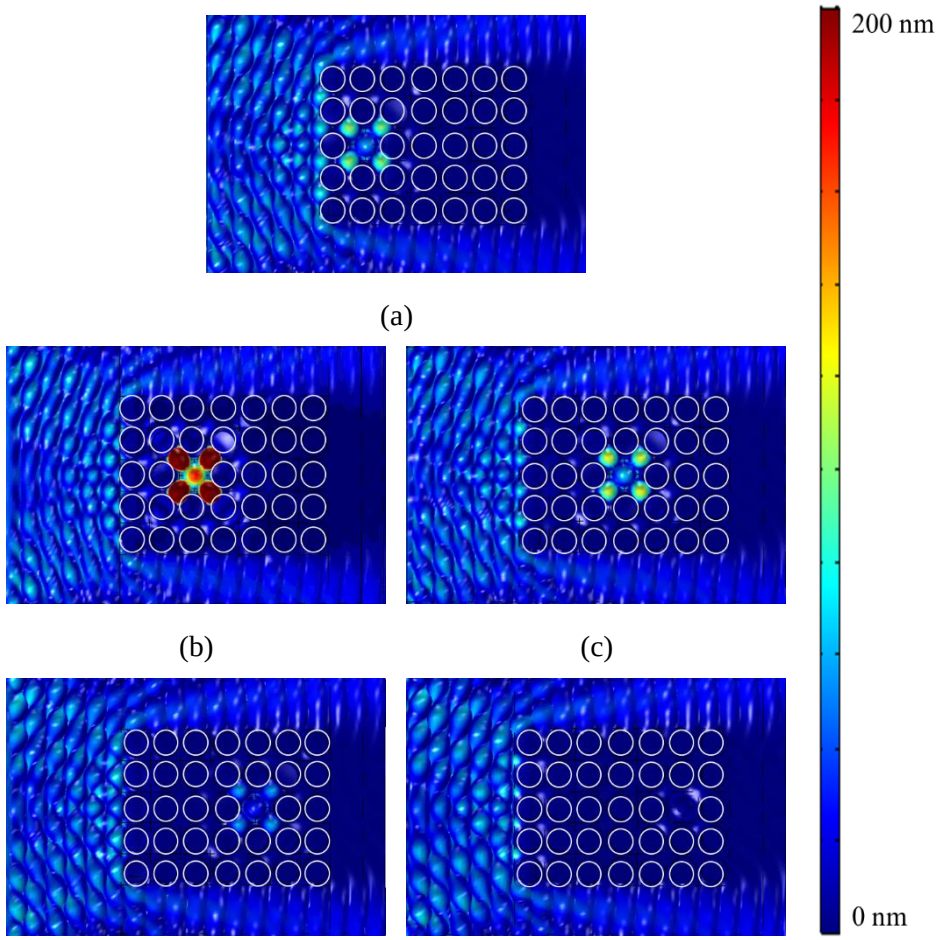

Figure 2-8 Operating deflection shapes (*z*-directional displacement fields) under the external electrical resistance of 0 Ω (short-circuit) at each peak frequency when the defect is introduced at: (a) 2nd layer, 55.74kHz, (b) 3rd layer, 55.82 kHz, (c) 4th layer, 55.83 kHz, (d) 5th layer, 55.81 kHz, and (e) 6th layer, 55.76 kHz.

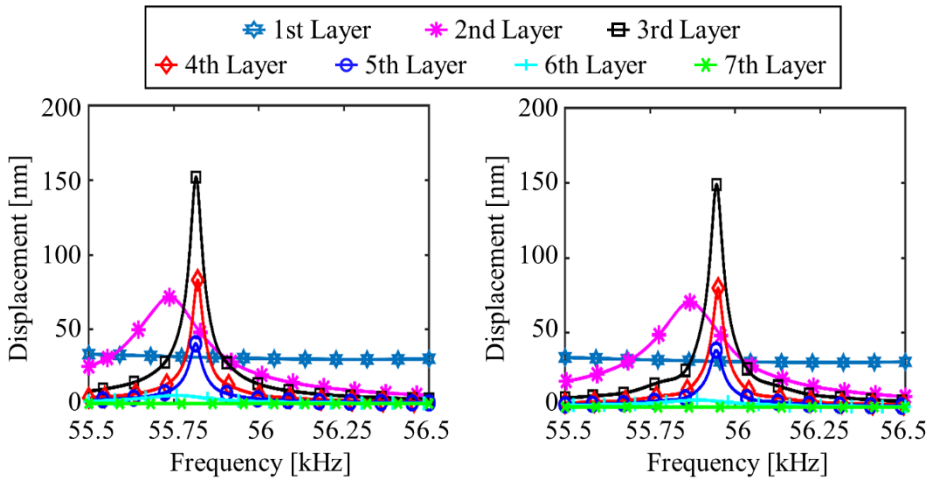

Figure 2-9 Mechanical displacement FRFs at different defect locations under the external electrical resistances of (a) 0 Ω (short-circuit) and (b) 100 MΩ (open-circuit).

2.4.2 Electrical Output Performance with Different Defect Locations

Figure 2-10 shows the output voltage FRFs, ranging from 55.5 kHz to 56.5 kHz, for different defect locations under the external electrical resistance of 100 MΩ (open-circuit). As consistent with the trends of the maximum displacement, no peak appears in the output voltage FRFs when the defect is located at the 1st and 7th layers. The maximum output voltage at each peak frequency is calculated as 7.350 V, 16.19 V, 8.750 V, 4.165 V, and 0.535 V at the defect locations moving from the 2nd to the 6th layers, respectively. As expected, the highest output performances can be achieved when the defect is imposed at the 3rd layer. The further the defect location is away from the excitation source, the lower the output voltage becomes after the 3rd layer. As a reference, it should be noted that the output voltage generated by the

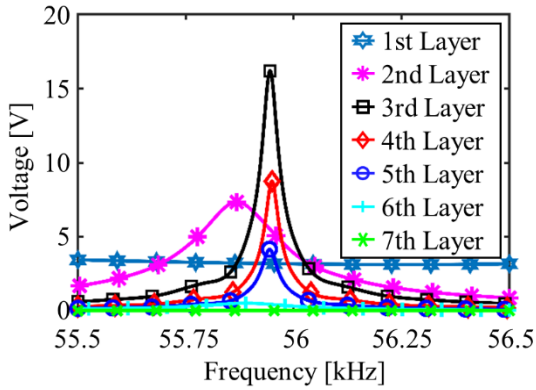

Figure 2-10 Output voltage FRFs at different defect locations under the external electrical resistance of 100 MΩ (open-circuit).

PEH device for a host plate in the absence of the PnC was calculated as 1.034 V at 55.95 kHz. Table 2-7 summarizes the maximum output voltage at each peak frequency, shown in Figure 2-10, at different defect locations.

Figure 2-11 (a) shows the effects of the defect location on the output voltage generated by the PnC-based PEH system at each open-circuit resonance frequency (55.82 kHz, 55.83 kHz, and 55.81 kHz); the external electrical resistance ranges from 0 Ω (short-circuit) to 100 MΩ (open-circuit). Here, the cases of the 3rd, 4th, and 5th layers are investigated. Due to the lack of periodicity near a defect located in the 2nd and 6th layers, these cases cannot be physically regarded as energy localization and harvesting that leverage a defect modes of a PnC. For all defect locations, as the external electrical resistance increases, the output voltage monotonically increases and converges to the maximum value, as listed in Table 2-7. Next, following a certain value of the external electrical resistance, the case in the 3rd layer-defect results in

the highest output voltage generation. Even though the periodicity is sufficient in cases where the defect is introduced at the 4th or 5th layers, evanescent waves gradually attenuated, thereby decreasing the amount of transferred energy, and thus less voltage generation.

Figures 2-11 (b) and 2-11 (c) depict the output electric power as a function of the external electrical resistance at each short-circuit resonance frequency (55.82 kHz, 55.83 kHz, and 55.81 kHz) and at each open-circuit resonance frequency (55.95 kHz, 55.96 kHz, and 55.94 kHz) at different defect locations of the 3rd, 4th, and 5th layers, respectively. The optimal external electrical resistance of the 3rd, 4th, and 5th layers at corresponding short-circuit resonance frequency is found as 759 Ω, 631 Ω, and 759 Ω, respectively. That at corresponding open-circuit resonance frequency is calculated as 45,709 Ω, 54,954 Ω, and 45,709 Ω, respectively. The output electric power for different defect locations of the 3rd, 4th, and 5th layers at corresponding short-circuit resonance frequency reaches up to 1.392 mW, 0.350 mW, and 0.098 mW, respectively, while at corresponding open-circuit resonance frequency reaches up to 1.387 mW, 0.348 mW, and 0.094 mW, respectively. Here, it should be noted that the maximum mechanical power of guided bending waves that transferred to the host medium by excitation is calculated as near 3.94 mW at the frequency of 55 kHz [107].

Here, it is worth pointing out that even though energy localization and harvesting performance is the largest in the 3rd layer, it is the 4th layer where the peak frequency is the closest to the defect band frequency under both circuit conditions. Besides, at the 4th layer, it is intriguing to note that the optimal external electrical resistance corresponding to the short-circuit resonance frequency is the

smallest, while that corresponding to the open-circuit resonance frequency is the largest. In the field of PVEH, the same trends of the optimal external electrical resistance are observed as the degree of the electroelastic coupling increases. Therefore, these observations imply that the defect-mode-enabled energy localization property itself is the strongest in the 4th layer because the periodicity is the most sufficient.

Table 2-8 lists the calculated results of output electric power across the power-optimal external electrical resistance at short-circuit and open-circuit resonance frequencies for these three different defect locations. The maximum output electric power can be achieved when the defect is positioned at the 3rd layer in the 5×7 supercell. Thus, the defect at the 3rd layer is confirmed to provide the optimal system for both mechanical energy localization and electrical harvesting power generation in the given 5×7 supercell PnCs, as a result of the trade-off between the degree of periodicity and the evanescent wave attenuation effect.

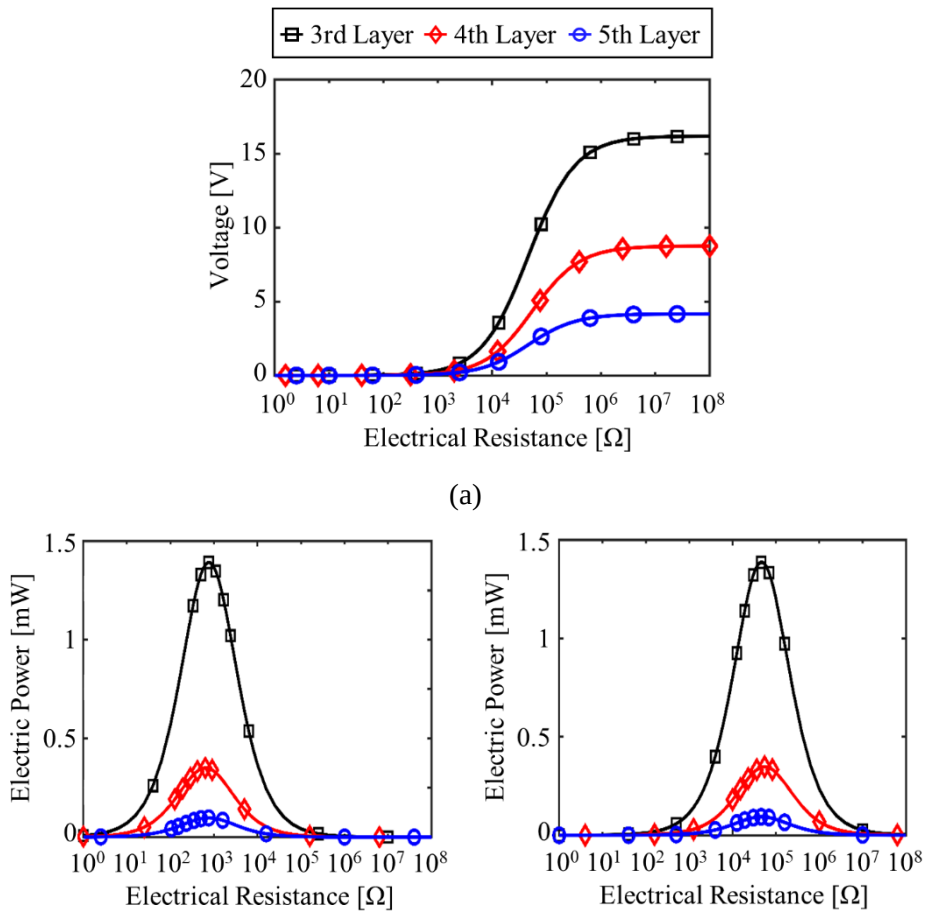

Figure 2-11 Electrical output performances with respect to the external electrical resistance at different defect locations: (a) output voltage at an open-circuit resonance frequency, (b) output electric power at a short-circuit resonance frequency, and (c) output electric power at an open-circuit resonance frequency.

Table 2-7 Output performances under external electrical resistances of 0 Ω (short-circuit) and 100 MΩ (open-circuit) at different defect locations.

External electrical resistance	Physical quantity	Defect location				
		2nd	3rd	4th	5th	6th
0 Ω (short-circuit)	Peak frequency [kHz]	55.738	55.816	55.820	55.814	55.758
	Displacement [nm]	71.582	152.02	82.095	40.386	5.817
100 MΩ (open-circuit)	Peak frequency [kHz]	55.868	55.946	55.950	55.944	55.888
	Displacement [nm]	70.298	148.86	79.750	38.256	5.086
	Peak output voltage [V]	7.350	16.185	8.750	4.165	0.535

Table 2-8 The maximum output electric power at the optimal external electrical resistances at different defect locations.

Frequency	Physical quantity	Defect location		
		3rd	4th	5th
Short-circuit resonance frequency	Optimal external electrical resistance [Ω]	759	631	759
	Maximum output electric power [mW]	1.392	0.350	0.098
Open-circuit resonance frequency	Optimal external electrical resistance [Ω]	45,709	54,954	45,709
	Maximum output electric power [mW]	1.387	0.348	0.094

2.5 Effects of the Supercell Size on the Optimal Defect Location

In Sections 2.4 and 2.5, the thorough investigation of how the supercell size and defect location affect the energy localization and harvesting performance, respectively. The main points of each section can be organized as follows: (1) in terms of the effects of supercell size with a given defect location, the PEH performance monotonically rises and converges as the supercell size increases, (2) with regard to the effects of defect location with enough large supercell size, there exists an optimal defect location where the maximum PEH performance can be achieved. Here, one may have an interesting question: how does the optimal defect location vary with the supercell size? When envisaging an engineered situation that a PnC with a single defect is going to be deployed on a top surface of a certain structure, the room or space can be limited to install a large supercell that ensures the sufficient periodicity requirement. It means that there is a need to investigate how the optimal defect location depends on the supercell size.

As demonstrated in this chapter, four supercell sizes are under consideration: 5×4, 5×5, 5×6, and 5×7 supercells. Referring to the results in Figures 2-6 and 2-10, the 2nd and 3rd layers are the admissible locations where the maximum energy harvesting performance can be obtained for a certain supercell size. Therefore, Figure 2-12 depicts the output voltage FRFs with different supercell sizes and defect locations under the external electrical resistance of 100 MΩ (open-circuit). Figures 2-12 (a) to 2-12 (b) are results for 5×4 to 5×7 supercells, respectively. Lines with star-pink and square-black indicate the results of the 2nd and 3rd layers, respectively.

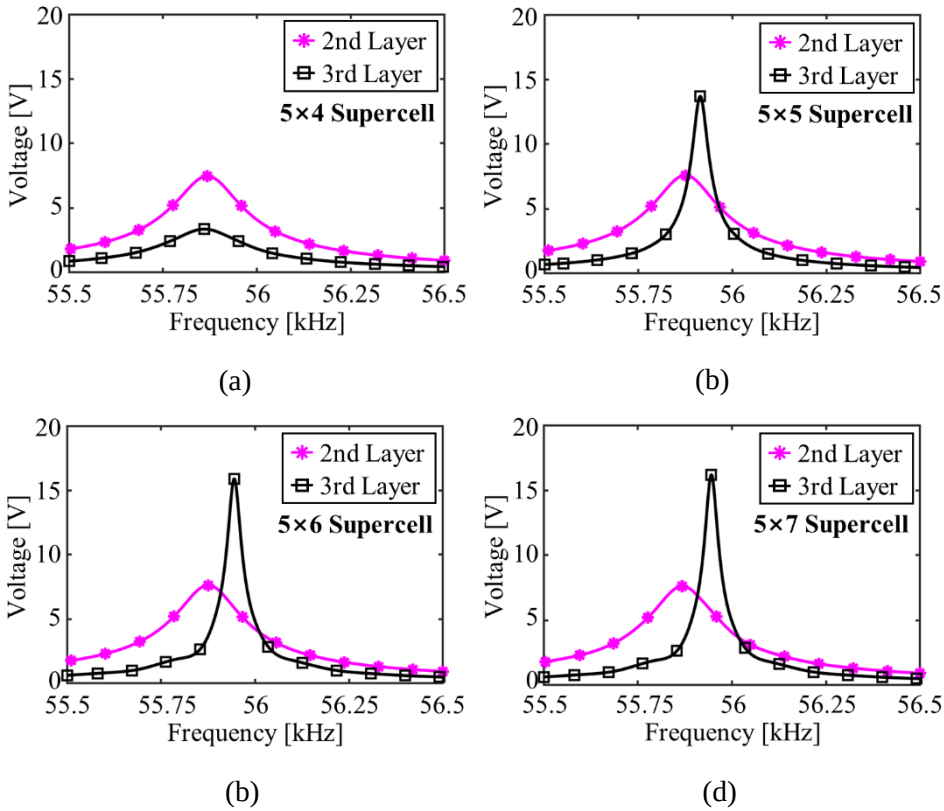

Figure 2-12 Output voltage FRFs for different supercell sizes and defect locations under the external electrical resistance of 100 MΩ (open-circuit): (a) 2nd and 3rd layers in 5×4 supercell, (b) 2nd and 3rd layers in 5×5 supercell, (c) 2nd and 3rd layers in 5×6 supercell, and 2nd and 3rd layers in 5×7 supercell.

It can be found that the maximum output voltage at the corresponding peak frequency, obtained in each case of 2nd and 3rd layers, becomes increasing as the supercell size increases. However, compared with the case of 3rd layer, the output voltage in the case of 2nd layer slowly increases. This implies that the periodicity near the 2nd layer is satisfied to some extent in terms of the defect for even the

smallest supercell size of 5×4. Surprisingly, for the 5×4 supercell, the energy localization and harvesting performance generated by the PEH device in 2nd layer is much greater than that in the 3rd layer. This result can be also demonstrated by the periodicity and evanescent waves. In the case of the 2nd layer, one and two unit cells are arranged on the left and right, respectively. In the case of the 3rd layer, two and one unit cells are arranged on the left and right, respectively. Therefore, it can be seen that the defect in the 2nd layer and that in the 3rd layer are aligned with the same state from the perspective of the periodicity. Therefore, the best PEH performance is obtained in the 2nd layer due to the larger displacement of evanescent waves. Through this, it is examined that the optimal defect location varies with the supercell size and this result can be explained from the viewpoint of the periodicity and evanescent waves.

2.6 Summary and Discussion

When expanding a PnC design into the two-dimension, there are two primary advantages that include (1) localizing not only normal but also oblique incident waves into a defect and (2) having more rooms for designing the defect, as well as a unit cell, to improve PEH performance. However, it should be emphasized that prior works have not provided any rationale for the key design parameters (i.e., supercell size and defect location) that they used. Due to the variation of the degree of the periodicity and band gap characteristics, energy localization and harvesting performances would depend on the supercell size and defect location. Therefore, there is a great need to physically interpret the relationships between such key design

parameters and energy localization and harvesting performance.

The objective of this chapter is thus to investigates the effects of the two key design parameters (i.e., supercell size and defect location) on the output performance of a PnC-based PEH system from the viewpoint of the periodicity and resonance formation. In terms of the effects of supercell size with a given defect location, the PEH performance monotonically raised and converged as the supercell size increases. With regard to the effects of defect location with a sufficiently large supercell size, there existed an optimal defect location where maximum PEH performance could be achieved. In terms of attenuation of the evanescent waves, it was better to locate a defect as close to the 1st layer as possible. From the viewpoint of the periodicity of the unit cells surrounding the defect, in cases where the defect was imposed at the 2nd or 6th layers, it was difficult to form defect bands due to a lack of periodicity. In addition, it was found that the optimal defect location depended on the supercell size. When the periodicity was not enough, the 2nd layer exhibited the best PEH performance. Therefore, the key findings of this study lied in that there was a trade-off between the fulfilment of resonance formation and the amplitude of the evanescent wave. This was governed by the periodicity of the PnC. Therefore, when designing a PnC-based PEH system with a defect, it was essential to identify a certain supercell size that exhibits sufficiently converged PEH performance and an optimal defect location that has the highest PEH performance. In this study, the highest output performances of energy localization and harvesting could be obtained when the defect is imposed at the 3rd layer for a 5×7 supercell.

The two-fold novel aspects of this study include (1) incorporating electroelastic coupling of a PEH device on defect bands for various defect mode shapes of a two-

dimensional PnC from the perspective of defect band shift and defect mode selection and (2) thoroughly examining the effects of supercell size and defect location on the PnC-based PEH system from the perspective of periodicity. We believe that this study provides design guidance and rationale for a PnC-based PEH system with a defect under elastic waves.

It should be noted that a PnC-based PEH with a single defect, as examined in the current work, might have limitations when operating under a random excitation environment due to the narrow bandwidth of mechanical resonance. Therefore, further investigation of the feasibility of the broadband PEH will be studied in next chapter by using a PnC with double defects.

Sections of this chapter have been published or submitted as the following journal articles:

1) **Soo-Ho Jo**, Heonjun Yoon, Yong Chang Shin, Wonjae Choi, Choon-Su Park, Miso Kim, and Byeng D. Youn, "Designing a Phononic Crystal with Defect for Energy Localization and Harvesting: Supercell Size and Defect Location," *International Journal of Mechanical Sciences*, Vol. 179, pp. 105670, 2020.

Chapter 3

Double Defect Modes of a Phononic Crystal for Energy Localization and Harvesting – From the Perspective of Relative Position and Electrical Circuit Connection

Chapter 2 was devoted to demonstrating design rationales of a two-dimensional PnC with a single defect from the perspective of the supercell size and defect location. Including the previous work in Chapter 2, most of the previous works have demonstrated successfully to utilize a defect mode for a two-dimensional PnC for energy localization and harvesting. However, they limited their examination to a single defect. As mentioned in Appendix A, since defect-mode-enabled energy localization results from mechanical resonance within a PnC where several unit cells that surround a single defect behave as fixed-liked boundary conditions, the frequency bandwidth for energy localization and harvesting is inherently low. In other words, it means that the Q-factor is very high. Therefore, there is a great need to widen the bandwidth for PEH, and we consider a design concept of a two-dimensional PnC with double defects.

In acoustic domains, some previous studies have explored a PnC with double defects via numerical simulations and experiments. Evanescent modes localized in the double defects interact with each other and generate a splitting of the frequencies of the defect modes when double defects are created sufficiently close to each other along the incident wave direction inside a two-dimensional PnC [57-60]. For elastic waves, only a few research has been reported due to complexity of tensor-form governing equations, attributed to the existence of shear stresses/strains, and Poisson's ratio [108]. Analogous to the phenomena in acoustics, the splitting of defect bands is still observed. Moreover, in-phase and out-of-phase defect mode shapes are presented. Underlying principles of the splitting of defect bands are presented in Appendix A. However, it should be emphasized that the incorporation of the splitting of defect bands into PEH has been untouched yet.

The research described in this chapter thus newly proposes a two-dimensional PnC-based PEH system with double defects arranged apart from each other. Here, two PEH devices are attached to the center of each defect. When designing a PnC-based PEH system with double defects, the following design issues should be addressed: (1) relative position between the double defects in the mechanical domain and (2) electrical connection between the double defects in the electrical domain. Therefore, this chapter aims at physically interpreting how the relative position and electrical circuit configuration affect output performances of energy localization and harvesting. With this motivation in mind, the distance and arranging direction between double defects are under consideration in the part of effects of the relative position. In addition, five connection types (i.e., Independent, Series Types A and B, and Parallel Types C and D) are under consideration in the part of effects of the

electrical connection. This study provides design and selection guidelines of the relative position and electrical circuit for the best use of double defects modes of a two-dimensional PnC to improve PEH performance under elastic waves. To the best of the authors' knowledge, the unique contributions of this study are two-fold. First, this is the first attempt to incorporate the splitting of defect bands into PEH and it enables enhancement of the output electric power at both frequencies of split defect bands. Second, we thoroughly investigate how the splitting of defect bands and output performance of PEH can vary with the relative position as well as the electrical connection between double defects.

The remainder of Chapter 3 is organized as follows. Section 3.1 presents a system description of a two-dimensional PnC with double defects. Sections 3.2 and 3.3 describe the results of defect band frequencies and defect mode shapes for a single defect case and double defects case under the open-circuit condition. Sections 3.4 and 3.5 present how both mechanical and electric responses of the PnC-based PEH system vary with the relative position (i.e., distance and arranging direction) and electrical circuit connection between the double defects, respectively . Finally, the conclusions of this work are outlined in Section 3.6.

3.1 System Description of a Phononic Crystal with Double Defects

The PnC-based PEH system considered in this chapter, as shown in Figure 3-1, consists of a host aluminum plate and a PnC with double defects to which the circular, disc-type PEH device (PZT-4D) is attached. The unit cell under consideration,

consists of a square lattice with a circular hole inside at the center in an aluminum plate. For the unit cell, a and t denote the lattice constant and thickness of the host plate, respectively. d_h denotes the diameter of the circular hole. In Chapter 2, it was found that the energy localization and harvesting performance increases and converges to the maximum value as the supercell size increases. Since one of the main issues in this chapter is to investigate the effects of the relative position between double defects, a large supercell size (17×17) of the PnC is taken into account. Here, the initial defect is introduced at the center of the 4th array by attaching a circular disc-type PZT-4D as a PEH device without puncturing one unit cell of the 17×17 array PnC. The PZT-4D disc has two geometric parameters, the diameter d_p and the height h_p. the thickness of the electrodes is negligible. Referring to Chapter 2, it was confirmed that the 4th layer along the x-direction (propagating direction of incident waves) showed the highest displacement amplification performance in the preliminary studies. Therefore, the 4th layer is selected as the location of the initial defect. In addition, an additional defect is introduced at the location that is three unit cells away from the initial defect along the x-direction. The configuration of the additional defect is the same with that of the initial defect. Both defects are arranged in the middle layer along the y-direction (perpendicular to the incident wave direction), as colored in dark-blue. In this chapter, the initial and secondary defects are called 'PEH Device 1' and 'PEH Device 2,' respectively. Table 3-1 summarizes the geometric information of the unit cell and PEH device. Mechanical properties of the aluminum are listed in Table 2-2. Table 2-3 summarizes the mechanical and electrical properties of PZT-4D. Here, the loss factor is set to be 0.0001 for the analysis of the PnC- based PEH systems.

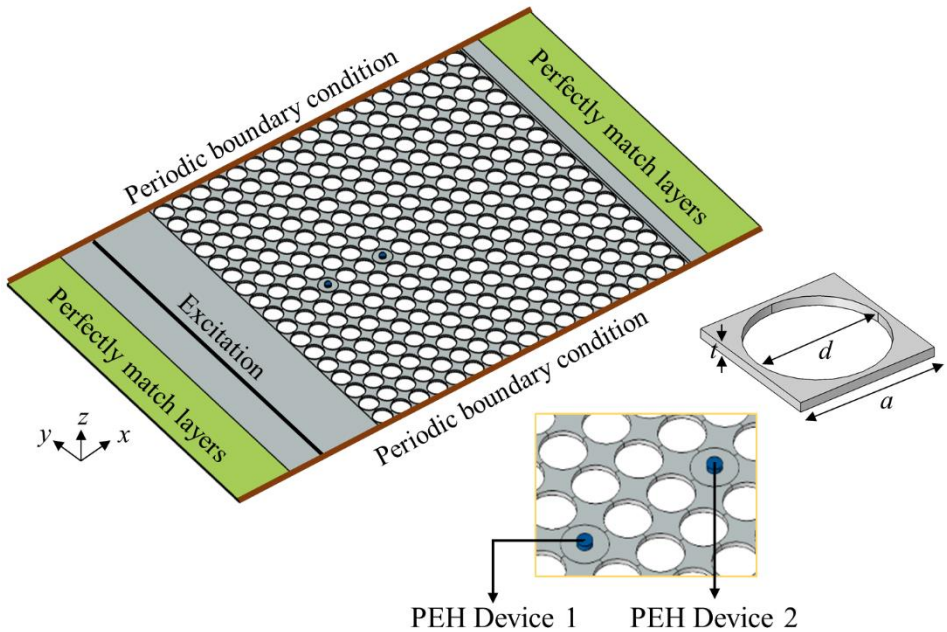

Figure 3-1 A schematic view of the two-dimensional PnC-based PEH system with double defects: periodic boundary condition and perfectly matched layers as the boundary conditions and transversely polarized A_0 Lamb wave as the excitation condition.

To investigate the PEH performance under unidirectional plane waves, we applied two boundary conditions at the boundaries of the host plate: (1) a perfectly matched layer as an absorbing boundary condition in the *x*-direction (propagating direction of incident waves) and (2) a periodic boundary condition guaranteeing the infinite domain in the *y*-direction (perpendicular direction to incident waves) [109-111]. The perfectly matched layer and periodic boundary condition are colored in green and sky-blue in Figure 5, respectively. In the *z*-direction, traction-free condition is employed. The incident flexural A_0 Lamb waves were excited by

transversely loading the cross-section of the host plate with a constant amplitude of 20 nm, regardless of the frequency [66]. To sufficiently excite the plane wave, the distance between the excitation source and the front row of the PnC was set to 100 mm, which is approximately six times the wavelength of the A_0 Lamb wave near 60 kHz.

It should be noted that the a meshing scheme of the PnC with decoupled double defects is that (1) the mesh elements of the whole structure are composed of hexahedrons and (2) the maximum mesh size is set to be one-tenth of the wavelength of the excited A_0 Lamb wave at 60 kHz. In terms of electroelastic coupling, three modules, including solid mechanics, electrostatics, and electrical circuit modules, are used. A detailed description is available in Chapter 2.

Table 3-1 Geometric dimensions of the unit cell and PEH device for a PnC with double defects.

Unit cell (Aluminum)	Lattice constant	a	33 mm
	Thickness of plate	t	2 mm
	Diameter of stub	d_h	30 mm
PEH device (PZT-4D)	Diameter	d_p	10 mm
	Height	h_p	2 mm

3.2 Defect Band Analysis for a Phononic Crystal with a Single Defect

To demonstrate the split of defect bands and corresponding defect mode shapes for the case of double defects, this section is devoted to performing the defect band analysis for a PnC with a single defect. Here, the single defect means the initial defect which is introduced in the 4th layer. The overall procedure for investigation is similar to that in Chapter 2. Defect band analysis was performed using the supercell calculation [112]. The supercell size of 17×17 is sufficiently large to neglect the coupling effects of the defects between adjacent supercells which are attributed to the Floquet-Bloch theorem. As emphasized in Appendix B, the attachment of the PEH device is taken into account. When solving the eigenvalue problem of the PnC with the single defect, the wavevector is swept in the 1st irreducible Brillouin zone (Γ→X→M→Y), shown in Figure 3-2 (a) with the observations of the flatness of defect bands with respect to the wavenumbers in Chapter 2.

Figure 3-2 (b) presents the dispersion curves of the defected PnC with attaching two PZT-4D, which are calculated along the border line of the 1st irreducible Brillouin zone for the given supercell, ranging from 55 kHz to 65 kHz. We confirmed that our unit cell under consideration has a full band gap, colored in the sky-blue box in the figure, ranging from 56.55 kHz to 62.51 kHz. In Figure 3-2 (b), six defect bands, which are flat passbands, are observed to be created within the full band gap, under the external electrical resistance of 0 Ω. The frequencies of the defect bands, labeled from A to F, are as follows: 57.04 kHz (A), 57.20 kHz (B), 57.55 kHz (C), 59.94 kHz (D), 61.62 kHz (E), and 62.39 kHz (F).

Figure 3-3 shows the defect mode shapes (*z*-directional displacement fields) at

each of the six defect band frequencies that correspond to the results in Figure 3-2. It should be noted that these defect mode shapes in Figure 3-3 are different from those for the circular stub-type unit cell, presented in Figure 2-3. These results support that both defect mode shapes and defect band frequencies highly depend on the design of unit cells. Here, when selecting a target defect band frequency, we need to recall the concept of voltage cancellation. The defect band frequency of 59.94 kHz (highlighted with black bold line in Figure 3-2, Case D in Figure 3-3 (d)) that corresponds to the monopole-like defect mode shape seems most desirable. Except for the monopole-like defect mode shape in Figure 3-3 (d), the remaining defect mode shapes contain strain nodal lines (zero strain) in the PEH device, thus leading to the decrease in the output voltage. Since the monopole-like defect mode shape represents the transversely polarized displacement fields, elastic waves can be localized when the flexural A_0 Lamb wave is excited near 59.94 kHz. It is worth pointing out the configurations of the unit cell and defect under consideration have advantages that the defect bands, labeled from A to C and from E to F in Figure 3-2, are far from the defect band (D) corresponding to the monopole-like defect mode shape. Therefore, the mechanical and electrical responses for the monopole-like defect mode shape can be readily observed without any interruption of other defect mode shapes.

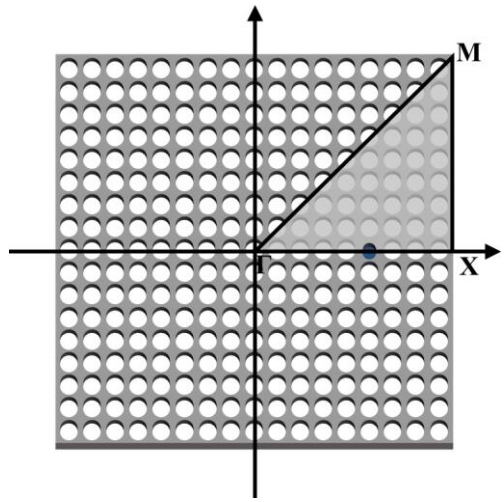

(a)

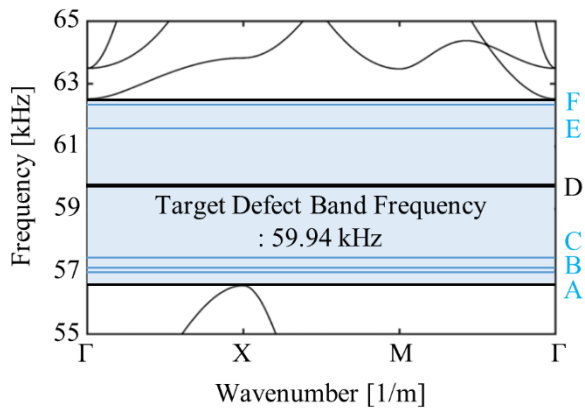

(b)

Figure 3-2 Defect band analysis for a 17×17 supercell with a single defect under the external electrical resistance 0 Ω (short-circuit): (a) the 1st irreducible Brillouin zone (Γ→X→M→Y) and (b) formation of six defect bands within the full band gap, ranging from 56.55 kHz to 62.51 kHz (57.04 kHz (A), 57.20 kHz (B), 57.55 kHz (C), 59.94 kHz (D), 61.62 kHz (E), and 62.39 kHz (F)).

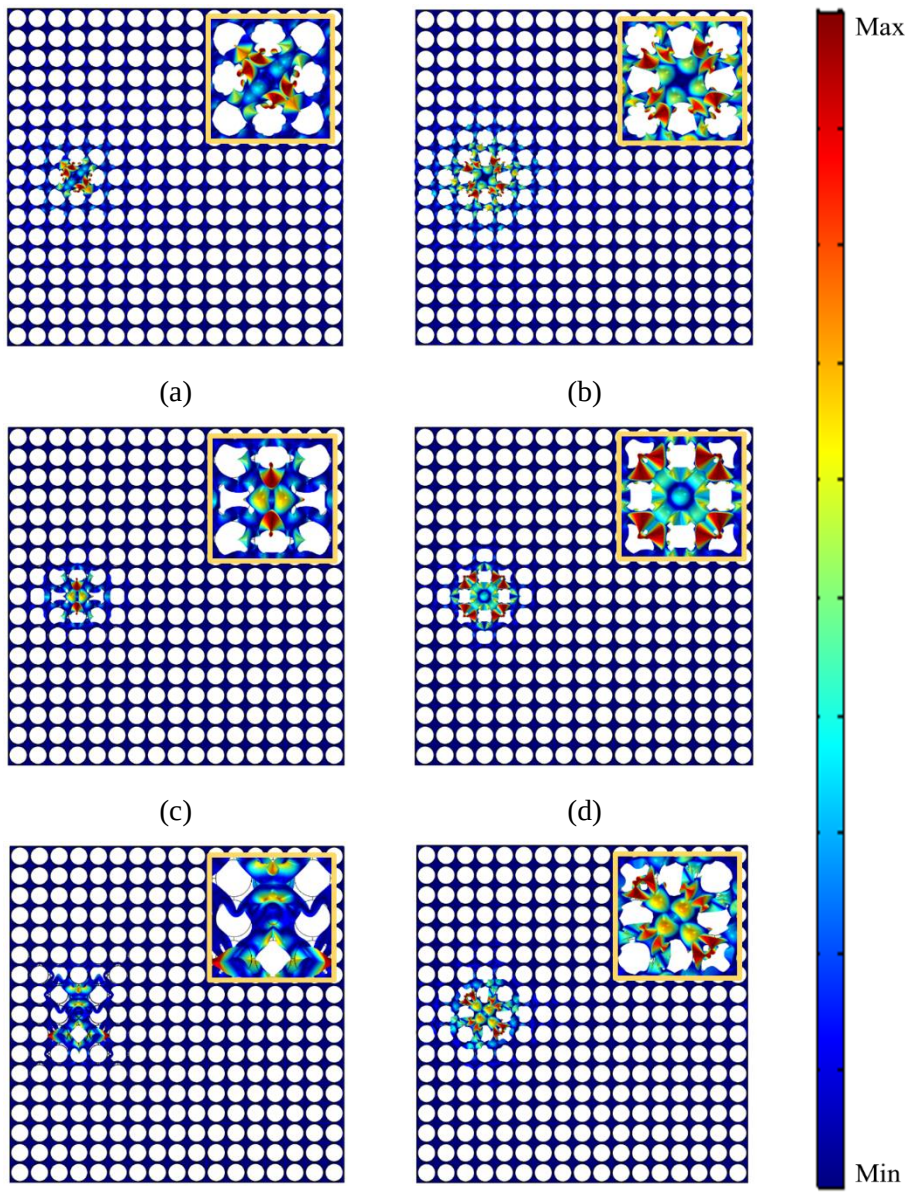

Figure 3-3 Various defect mode shapes (*z*-directional displacement fields) for a 17×17 supercell with a single defect under the external electrical resistance of 0 Ω (short-circuit): (a) 57.04 kHz (A), (b) 57.20 kHz (B), (c) 57.55 kHz (C), (d)

59.94 kHz (D), (e) 61.62 kHz (E), and (f) 62.39 kHz (F).

3.3 Defect Band Analysis for a Phononic Crystal with Double Defects

For the PnC with the double defects arranged in 4th and 7th layers, defect band analysis was also performed using the supercell calculation [57]. Similarly, when solving the eigenvalue problem of the PnC with the single defect, the wavevector is swept in the 1st irreducible Brillouin zone (Γ→X→M→Y), shown in Figure 3-4 (a).

Figure 3-4 (b) presents the dispersion curves of the defected PnC with attaching two PEH devices, ranging from 55 kHz to 65 kHz, under the external electrical resistance of 0 Ω. It can be confirmed the splitting of each of the six defect bands observed in Figure 3-2 takes place and results in twelve defect bands within the band gap [59, 113]. The frequencies of the defect bands, labeled from A to L, are as follows: 57.03 kHz (A), 57.05 kHz (B), 57.13 kHz (C), 59.28 kHz (D), 57.41 kHz (E), 57.70 kHz (F), 59.79 kHz (G), 60.11 kHz (H), 61.59 kHz (I), 61.65 kHz (J), 62.11 kHz (K), and 62.78 kHz (L). The defect band which frequency is 57.04 kHz (Figure 3-3 (a)) is split into two defect bands which frequencies are 57.03 kHz (Figure 3-5 (b)) and 57.05 kHz (Figure 3-5 (d)). The defect band which frequency is 57.20 kHz (Figure 3-3 (b)) is split into two defect bands which frequencies are 56.71 kHz (Figure 3-5 (a)) and 57.13 kHz (Figure 3-5 (c)). The defect band which frequency is 57.28 kHz (Figure 3-3 (c)) is split into two defect bands which frequencies are 57.41 kHz (Figure 3-5 (c)) and 57.70 kHz (Figure 3-5 (f)). The defect band which frequency is 59.94 kHz (Figure 3-3 (d)) is split into two defect bands

which frequencies are 59.79 kHz (Figure 3-5 (g)) and 60.11 kHz (Figure 3-5 (h)). The defect band which frequency is 61.62 kHz (Figure 3-3 (e)) is split into two defect bands which frequencies are 61.59 kHz (Figure 3-5 (i)) and 61.65 kHz (Figure 3-5 (j)). The defect band which frequency is 62.39 kHz (Figure 3-3 (f)) is split into two defect bands which frequencies are 62.11 kHz (Figure 3-5 (k)) and 62.78 kHz (Figure 3-5 (l)). Note that the degree of the splitting of each defect band in Figure 3-3 varies with the defect mode shape when locations of the double defects are fixed. It implies that the degree of the coupling between the double defects depends on the corresponding defect mode shape.

It is worth pointing out that all defect bands for the PnC with the double defects are flat, regardless of any reciprocal wave vectors **k**. This interpretation is analogous to the results in Appendix A. Since several unit cells that surround the double defects behave as the fixed boundary conditions, there is no preferred directionality. This implies that energy can be trapped into the double defects no matter which direction the waves are incident.

Figure 3-5 shows the defect mode shapes (*z*-directional displacement fields) at each of the twelve defect band frequencies that correspond to the results in Figure 3-5 (b). Comparison of Figures 3-3 and 3-5 confirms that the defect mode shape at each defect band frequency observed in the single defect case are all maintained as well after the splitting of defect bands occurs with double defects. Therefore, it can be found that the monopole-like defect mode shape is still observed in both Figures 3-5 (g) and (h). Although the same monopole-like mode shapes are maintained at two different split band frequencies, they behave differently. Double defects behave in-phase mode at the lower split frequency of 59.79 kHz while they behave in out-

of-phase mode behaviors at higher frequency of 60.11 kHz. Here, the meaning of the in-phase behavior is that the defect mode shape of each defect in Figure 3-5 is polarized in the same direction. On the other hand, the out-of-phase behaviors indicate that the defect mode shape of each defect in Figure 3-5 is polarized in the opposite direction.

In summary, under the external electrical resistance of 0 Ω (short-circuit), the defect band frequency that corresponds to the monopole-like defect mode shape is 59.94 kHz in the case of the single defect which is arranged at the 4th layer. When the additional defect is introduced at the 4th layer, the defect band for the single defect is split into two bands whose frequencies are 59.79 kHz and 60.01 kHz. At each frequency of split defect bands, in-phase and out-of-phase monopole-like defect mode shapes are observed, respectively. Furthermore, when switching the electrical boundary condition from the short-circuit to open-circuit, the defect band frequency of 59.94 kHz in the case of the single defect increases up to 60.01 kHz and defect band frequencies in the case of the double defects increase up to 59.87 kHz and 60.19 kHz, respectively.

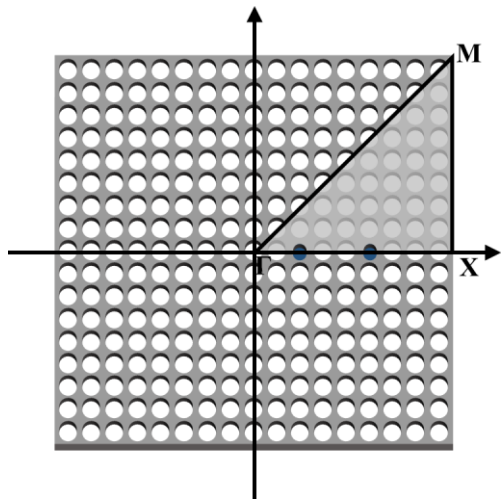

(a)

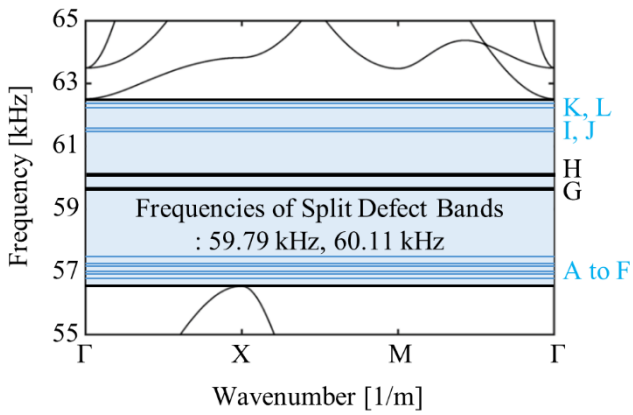

(b)

Figure 3-4 Defect band analysis for a 17×17 supercell with double defects under the external electrical resistance 0 Ω (short-circuit): (a) the 1st irreducible Brillouin zone (Γ→X→M→Y) and (b) formation of twelve defect bands within the full band gap (57.03 kHz (A), 57.05 kHz (B), 57.13 kHz (C), 59.28 kHz (D), 57.41 kHz (E), 57.70 kHz (F), 59.79 kHz (G), 60.11 kHz (H), 61.59 kHz (I), 61.65 kHz (J), 62.11 kHz (K), and 62.78 kHz (L)).

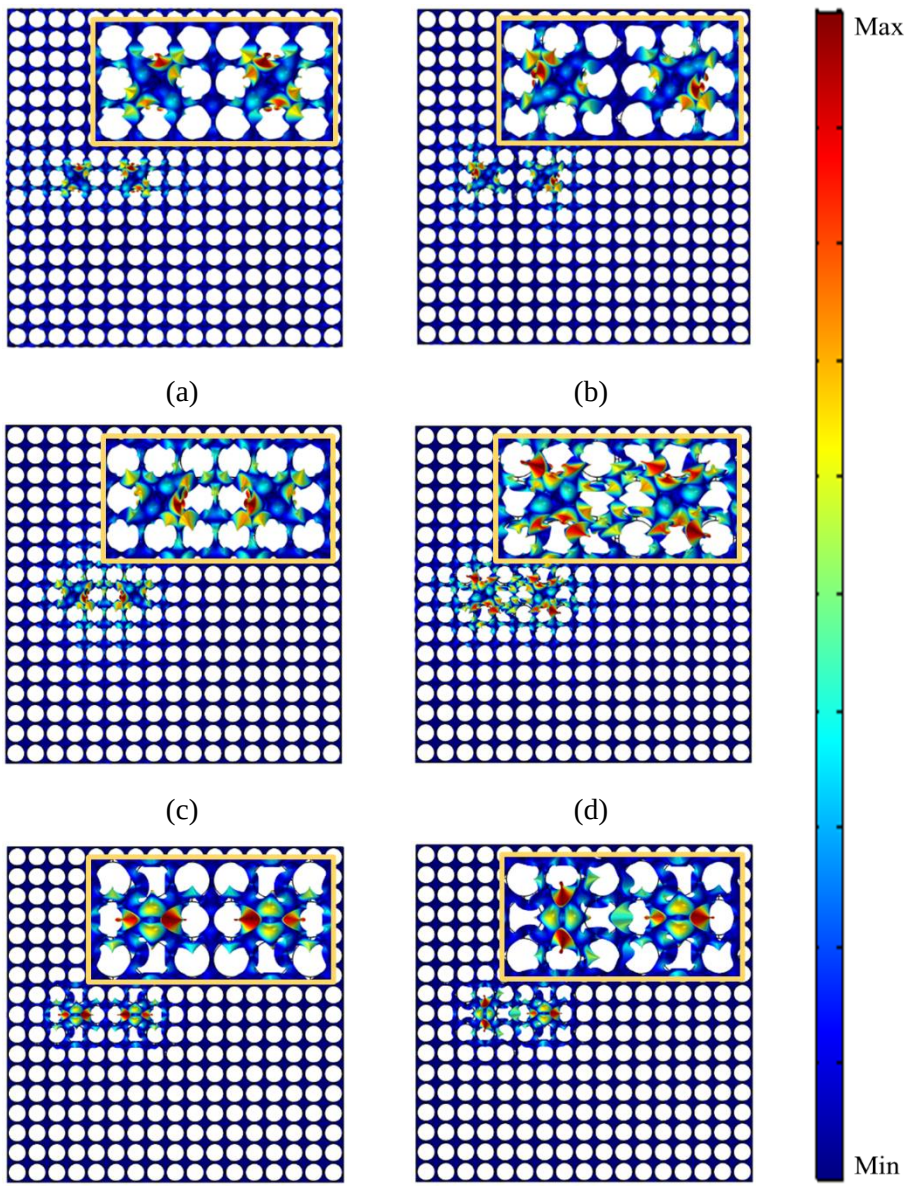

(a) (b)

(c) (d)

(e) (f)

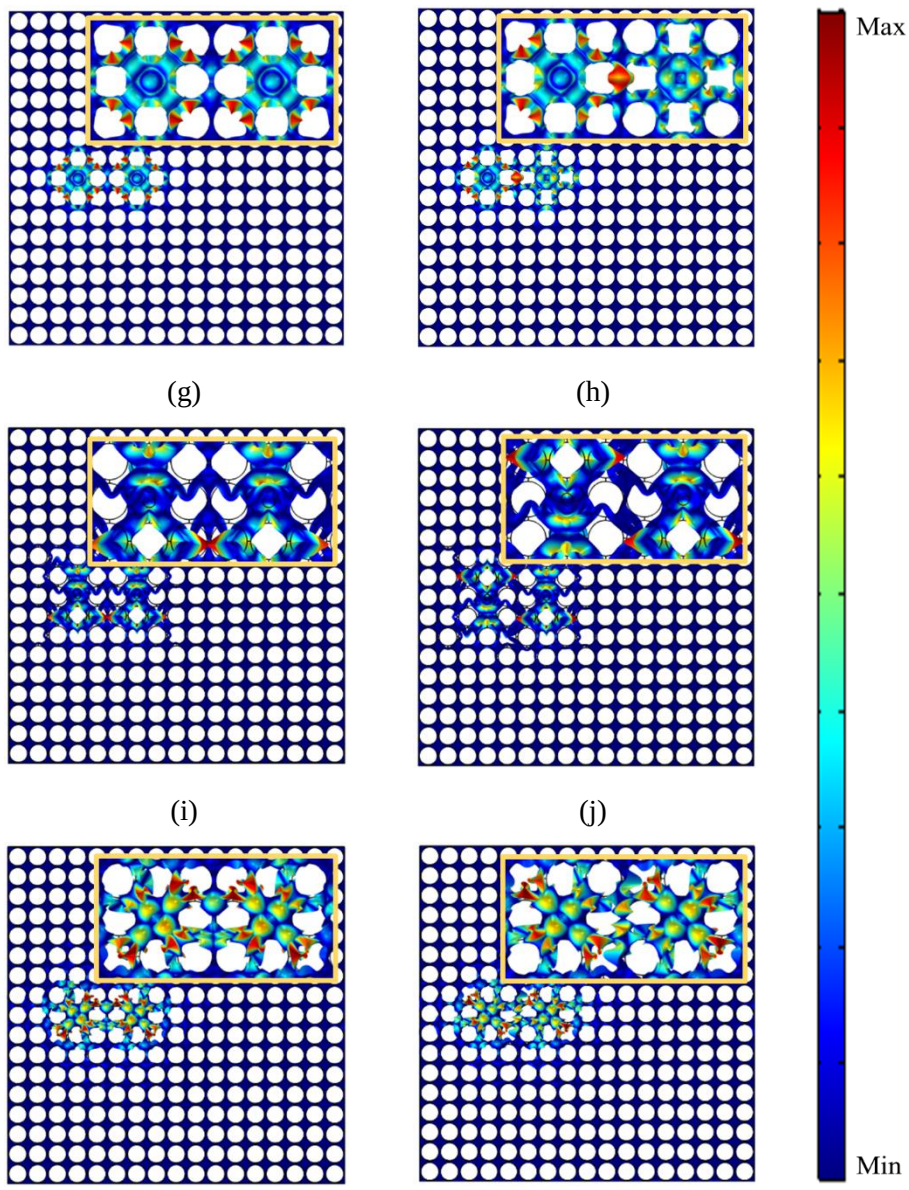

Figure 3-5 Various defect mode shapes (*z*-directional displacement fields) for a 17×17 supercell with double defects under the external electrical resistance of 0 Ω (short-circuit): (a) 57.03 kHz (A), (b) 57.05 kHz (B), (c) 57.13 kHz (C), (d)

57.28 kHz (D), (e) 57.41 kHz (E), (f) 57.70 kHz (F), (g) 59.79 kHz (G), (h) 60.11 kHz (H), (i) 61.59 kHz (I), (j) 61.65 kHz (J), (k) 62.11 kHz (K), and (l) 62.78 kHz (L).

3.4 Effects of the Relative Position between Double Defects on Energy Localization and Harvesting Performance

The research outlined in this section is devoted to investigating the effects of the relative position on the output performances of the PnC-based PEH system with the double defects. In this study, there can two aspects in terms of the relative position. They are (1) the distance and (2) arranging direction between double defects. In the part of the distance effects, the initially introduced defect is fixed at the 4th layer while the location of the additional defect is changed from 7th to 10th along the *x*-direction (i.e., the direction of propagating waves). Here, it should be noted that both defects are arranged in the center of the supercell along the *y*-direction (i.e., the perpendicular direction of propagating waves). In the part of the arranging direction effects, the location of the additional defect is changed along the circumferential direction (direction effect) with the initially introduced defect as the origin. Each of the distance and arranging direction effects are demonstrated in Sections 3.4.1 and 3.4.2, respectively. In addition, there is one more thing that should be emphasized. Even though the coupling of defect modes in a PnC with double or multiple defects has also drawn attention in acoustic regimes, efforts to experimentally validate the splitting phenomenon of defect bands can be rarely found in the elastic realm. Therefore, the experimental validation of the splitting of defect bands under elastic waves is provided in Section 3.4.3.

3.4.1 Mechanical and Electrical Output Performances with Different Distances under the Open-circuit Condition

The mechanical output performance is analyzed by investigating the displacement of the PEH device attached to the center of the defects in the PnC. In addition, the electrical output performance is analyzed by investigating the voltage generated by each PEH device in the PnC. Under the external electrical resistance of 100 MΩ (open-circuit), Figure 3-6 (a) presents the operating deflection shape (*z*-directional displacement field) in the case of the single defect at the peak frequency of 60.11 kHz and Figures 3-6 (b) and 3-6 (c) depicts the operating deflection shapes (*z*-directional displacement fields) in the case of the double defects which are arranged in the 4th and 7th layers at the 59.87 kHz and 60.19 kHz, respectively. Here, sinusoidal excitation (A_0 Lamb wave) of 20 nm is loaded at the left end of the host plate. It can be found that the defect vibrates with the monopole-like defect mode shape, as shown in Figure 3-3 (d). In addition, the double defects vibrates with in-phase and out-of-phase defect mode shapes, as shown in Figure 3-5 (g) and Figure 3-5 (h), respectively. It should be mentioned that the defect band frequencies under the external electrical resistance of 100 MΩ are equal to peak frequencies since the supercell size (17×17) considered in this chapter is enough large to assume the sufficient periodicity near the defect.

Here, it can be found that the magnitude of the displacement fields in the vicinity of each defect is similar. As demonstrated in Chapter 2, for a PnC-based PEH system with a single defect, the energy amplification performance decreases as the single defect location gets farther away from the excitation source in the unidirectional plane wave, due to the evanescent characteristics of the band gap. In contrast, when introducing double defects, even though the distances from the

excitation source to the defects are different, the maximum displacements of PEH Devices 1 and 2 are almost the same at each resonance frequency. It can be readily understood by the following physical phenomenon that this is not a system that transfers the mechanical energy to PEH Device 1 and then sequentially transfers it to PEH Device 2; rather, it is a system in which PEH Device 2 oscillates together with PEH Device 1 with the in- or out-of-phase defect mode shapes. These results are in the same context as the physical demonstration in Appendix A that the unit cells surrounding both double defects behave as fixed-like boundary conditions and defect modes can be thought of normal modes due to the mechanical resonance.

To investigate the distance effects, four scenarios are under consideration: (4, 7), (4, 8), (4, 9), and (4, 10) as shown in Figure 3-7. Here, the notation (*m*, *n*) stands for the double defects which are arranged in *m*-th layer and *n*-th layer along the *x*-direction (i.e., the direction of propagating waves) while both defects are arranged in the centerline along the *y*-direction (i.e., the perpendicular direction of propagating waves). This notation will be used in Sections 3.4.1 and 3.4.3. Figures 3-8 (a) to 3-8 (d) show the FRFs for the displacements at the center of PEH Devices 1 and 2 in the cases of (4, 7), (4, 8), (4, 9), and (4, 10), respectively, ranging from 59.8 kHz to 60.3 kHz, under the external electrical resistances of 100 MΩ (open-circuit). Lines with black indicate the mechanical and electrical output performances for the single defect. Lines with blue and red indicate those for PEH Devices 1 and 2 for the double defects.

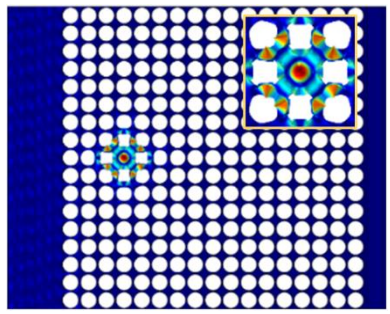

(a)

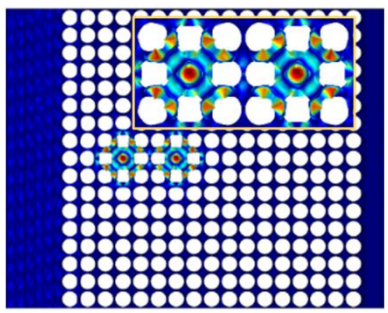

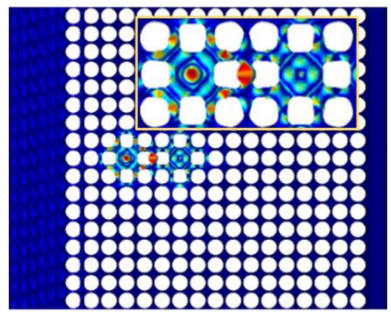

(b) (c)

Figure 3-6 Operating deflection shapes (*z*-directional displacement fields) under the external electrical resistance of 100 MΩ (open-circuit) at each peak frequency when the defect is introduced in: (a) the 4th layer in the case of the single defect, (b) the 4th layer and (c) the 7th layer in the case of the double defects.

The peak frequency of the single defect case is 60.01 kHz and corresponding maximum displacement is 296.2 nm. In Figure 3-8 (a), the peak displacements for PEH Devices 1 and 2 of the double defects (4, 7) are drastically amplified up to (1) 168.8 nm and 170.3 nm at 59.87 kHz (in-phase defect mode shape) and (2) 194.6 nm and 195.8 nm at 60.19 kHz (out-of-phase defect mode shape), respectively. The difference between the peak frequencies is 320 Hz. In Figure 3-8 (b), the peak

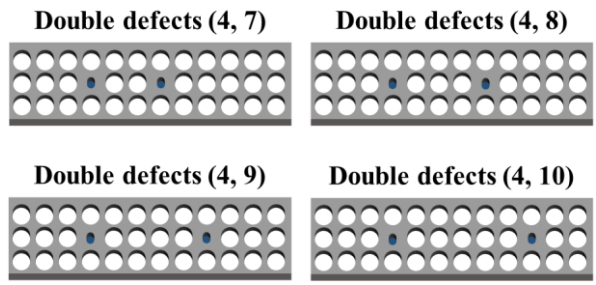

Figure 3-7 A schematic configuration of a PnC with double defects with four different distances.

displacements for PEH Devices 1 and 2 of the double defects (4, 9) are drastically amplified up to (1) 180.0 nm and 194.2 nm at 59.97 kHz (in-phase defect mode shape) and (2) 175.7 nm and 197.4 nm at 60.06 kHz (out-of-phase defect mode shape), respectively. The difference between the peak frequencies is 90 Hz. In Figure 3-8 (c), the peak displacements for PEH Devices 1 and 2 of the double defects (4, 9) are drastically amplified up to (1) 187.3 nm and 195.4 nm at 60.00 kHz (in-phase defect mode shape) and (2) 194.2 nm and 197.6 nm at 60.03 kHz (out-of-phase defect mode shape), respectively. The difference between the peak frequencies is 30 Hz. In Figure 3-8 (d), the peak frequencies of the double defects (4, 10) are 60.01 kHz and corresponding maximum displacements are 295.7 nm and 74.04 nm, respectively.

There are three following points that should be emphasized. First, as the distance between the double defects becomes further, the difference between the peak frequencies becomes smaller. From the underlying physics of the splitting of defect bands presented in Appendix A, the coupling consists of mass and stiffness between the double defects. When the double defects become further, there would

be more mass and stiffness. Therefore, the effective stiffness that connects the double defects becomes smaller. It was also revealed that the defect band frequencies are analogous to natural frequencies in vibrations. When the PnC with the double defects is regarded as the 2-DoF mass-spring system having fixed boundary conditions at the ends, it is well known that the splitting of natural frequencies becomes smaller when the stiffness between the double defects gets smaller. Second, as the distance between the double defects becomes further, the displacement at the peak frequency becomes larger. Assuming that (1) the input mechanical energy transferred to the PnC is all the same regardless of the distance between the double defects and (2) there is no energy loss, the displacement of each PEH device should be larger. It is because elastic energy stored in the effective stiffness between the double defects would become decreasing as the effective stiffness gets decreasing. To preserve energy conservation, the reduced elastic energy is compensated for increasing the kinetic energy of masses. Last, if the double defects are arranged significantly far, they are decoupled. It implies that they behave as an independent single defect. Therefore, it can be found that the peak frequency of each PEH device in the case of double defects is equal to that in the case of single defects. Furthermore, the displacement generated in PEH Device 1 is similar to that in the case of single while the displacement generated in PEH Device 2 is much less than that in the case of single due to evanescent wave effects as presented in Section 2.4.

Figure 3-9 (a) to 3-9 (d) show the FRFs for the output voltage generated in PEH Devices 1 and 2 in the cases of (4, 7), (4, 8), (4, 9), and (4, 10), respectively, ranging from 59.8 kHz to 60.3 kHz, under the external electrical resistances of 100 MΩ (open-circuit). Here, it should be mentioned that each PEH devices is independently

connected to an external electrical resistance. In the setting of the independent connection, the top and bottom electrodes of the two PEH devices are independently connected to the terminal and ground, respectively. For other electrical circuit connections, such as series and parallel connections, are deeply investigated in Section 3.5

The maximum output voltage of the single defect case is 32.88 V. In Figure 3-9 (a), the output voltages generated in PEH Devices 1 and 2 of the double defects (4, 7) are drastically amplified up to (1) 19.02 V (PEH Device 1) and 19.08 V (PEH Device 2) at 59.87 kHz (in-phase defect mode shape) and (2) 21.98 V (PEH Device 1) and 21.84 V (PEH Device 2) at 60.19 kHz (out-of-phase defect mode shape), respectively. In Figure 3-9 (b), the output voltages generated in PEH Devices 1 and 2 of the double defects (4, 8) are drastically amplified up to (1) 20.14 V (PEH Device 1) and 21.76 V (PEH Device 2) at 59.97 kHz (in-phase defect mode shape) and (2) 19.76 V (PEH Device 1) and 22.14 V (PEH Device 2) at 60.06 kHz (out-of-phase defect mode shape), respectively. In Figure 3-9 (c), the output voltages generated in PEH Devices 1 and 2 of the double defects (4, 8) are drastically amplified up to (1) 20.90 V (PEH Device 1) and 21.90 V (PEH Device 2) at 60 kHz (in-phase defect mode shape) and (2) 22.2 V (PEH Device 1) and 22.16 V (PEH Device 2) at 60.03 kHz (out-of-phase defect mode shape), respectively. In Figure 3-9 (d), the peak frequencies of the double defects (4, 10) are 60.01 kHz and corresponding output voltages are 32.88 V and 4.11 V, respectively.

Similar to the investigation of the displacement FRFs, as the distance between the double defects becomes further, the difference between the peak frequencies become smaller while the output voltage at the peak frequency becomes larger. In

addition, it can be found that they are decoupled if the double defects are arranged significantly far. As compared with a PnC-based PEH system with a single defect, it should be emphasized that the output voltage generated in each PEH device deployed in a PnC-based PEH system with double defects is smaller; however, the total bandwidth is almost doubled.

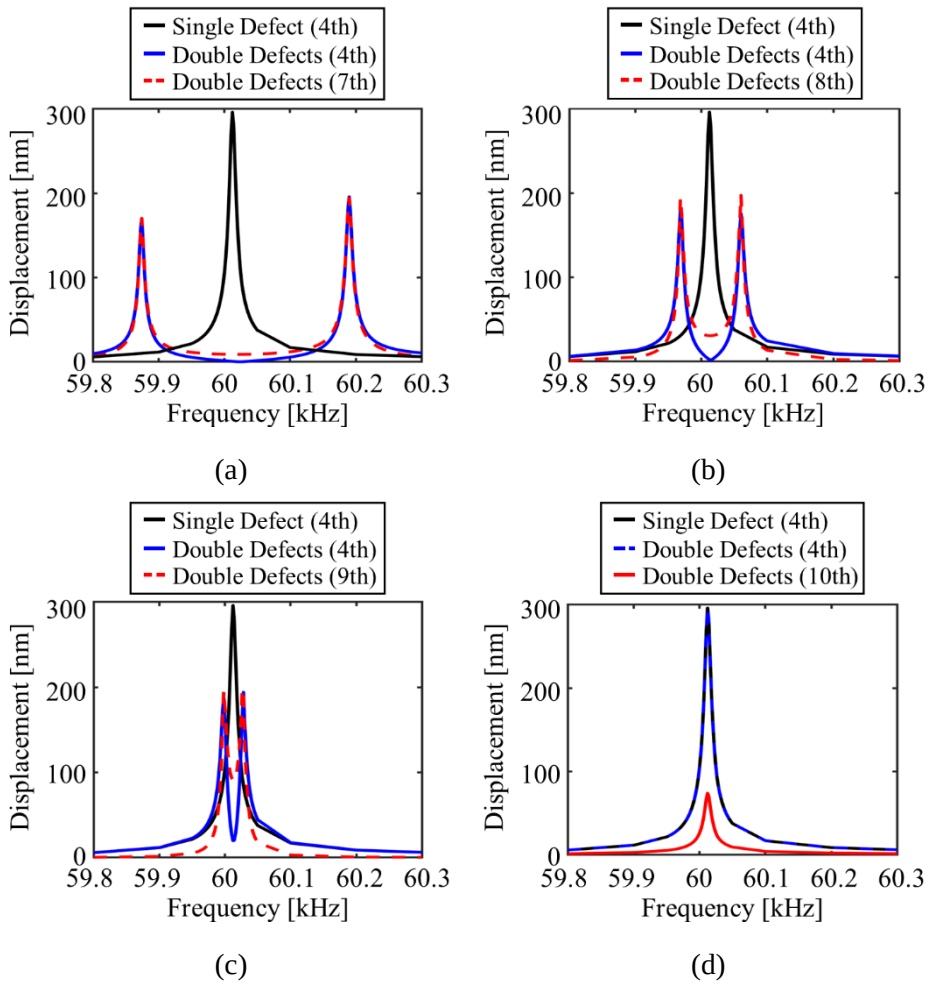

Figure 3-8 Mechanical displacement FRFs for four different distances of double defects under the external electrical resistances of 100 MΩ (open-circuit): (a) (4, 7), (b) (4, 8), (c) (4, 9), and (d) (4, 10).

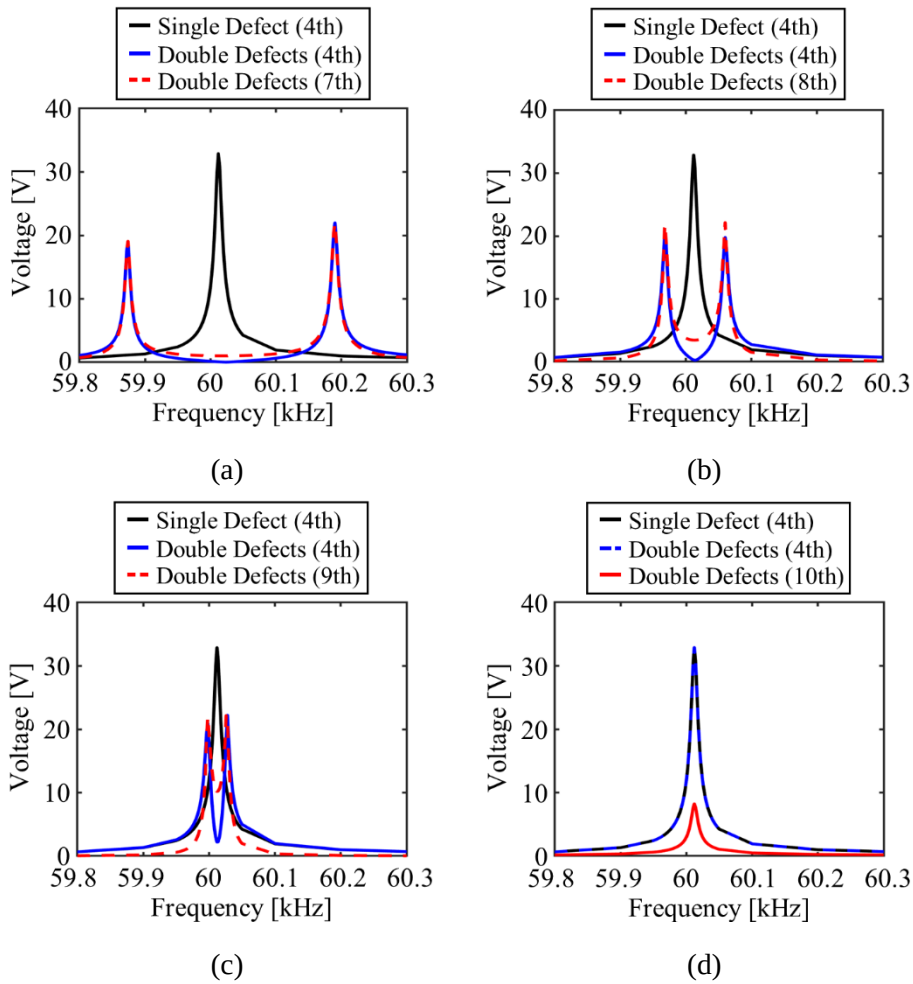

Figure 3-9 Output voltage FRFs for four different distances of double defects under the external electrical resistances of 100 MΩ (open-circuit): (a) (4, 7), (b) (4, 8), (c) (4, 9), and (d) (4, 10).

3.4.2 Mechanical and Electrical Output Performances with Different Arranging Directions under the Open-circuit Condition

To investigate the arranging direction effects, four scenarios are under consideration: (4, 7-⓪), (4, 6-①), (4, 5-②), and (4, 4-③) as shown in Figure 3-10. Here, the notation (*m*, *n*-ⓚ) stands for the double defects which are arranged in *m*-th layer and *n*-th layer along the *x*-direction (i.e., the direction of propagating waves) while the defect in the *m*-th layer is in the centerline along the *y*-direction (i.e., the perpendicular direction of propagating waves) and the defect in the *n*-th layer is offset by ⓚ unit cells from the center axis along the *y*-direction. Figures 3-11 (a) to 3-11 (d) show the FRFs for the displacements at the center of PEH Devices 1 and 2 in the cases of (4, 7-⓪), (4, 6-①), (4, 5-②), and (4, 4-③), respectively, ranging from 59.8 kHz to 60.3 kHz, under the external electrical resistances of 100 MΩ (open-circuit). Lines with black indicate the mechanical and electrical output performances for the single defect. Lines with blue and red indicate those for PEH Devices 1 and 2 for the double defects.

The peak frequency of the single defect case is 60.01 kHz and corresponding maximum displacement is 296.2 nm. In Figure 3-11 (a), the peak displacements for PEH Devices 1 and 2 of the double defects (4, 7-⓪) are drastically amplified up to (1) 168.8 nm and 170.3 nm at 59.87 kHz (in-phase defect mode shape) and (2) 194.6 nm and 195.8 nm at 60.19 kHz (out-of-phase defect mode shape), respectively. The difference between the peak frequencies is 320 Hz. In Figure 3-11 (b), the peak frequencies of the double defects (4, 6-①) are 60.01 kHz and corresponding maximum displacements are 295.7 nm and 41.17 nm, respectively. In Figure 3-11 (c), the peak frequencies of the double defects (4, 5-②) are 60.01 kHz and corresponding maximum displacements are 295.7 nm and 175.9 nm, respectively. In

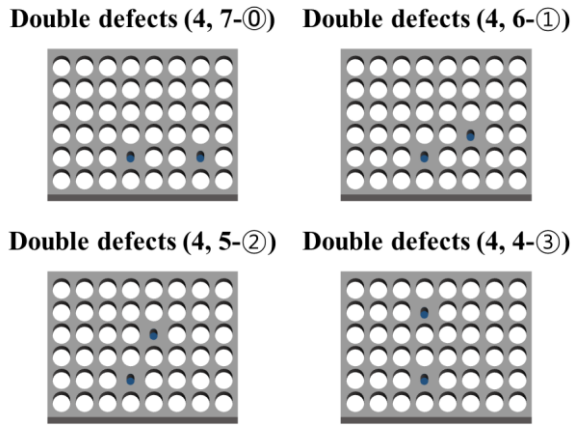

Figure 3-10 A schematic configuration of a PnC with double defects with four different arranging directions.

Figure 3-11 (d), the peak displacements for PEH Devices 1 and 2 of the double defects (4, 4-③) are drastically amplified up to 294.7 nm and 295.8 nm at 59.87 kHz (in-phase defect mode shape), respectively, while there are no peaks near 60.19 kHz (out-of-phase defect mode shape).

There are two following points that should be emphasized. First, even though the distance between the fixed defect in the 4th layer and the defect in (4, 6-①) or (4, 5-②) is less than the distance between the fixed defect in the 4th layer and the defect in (4, 7-⓪), the decoupling between the double defects occur. It implies that the coupling characteristics are weakened along the diagonal axis. In other words, the coupling characteristics are the most strengthened along the direction of propagating waves. Since the double defects are decoupling, each of the defects behaves as an independent single defect. That's why the defect in (4, 6-①) has much lower displacement than the defect (4, 5-②) from the perspective of the defect

location effects presented in Section 2.4. Second, when the additional defect is arranged in (4, 4-③), it can be found that the only peak frequency of the in-phase defect mode shape occur. It implies that vertically arranged double defects cannot oscillate with the out-of-phase defect mode shape. This interesting phenomenon is attributed to the in-phase normal incident waves. Since the in-phase normal incident waves are excited toward the PnC, the mechanical energy transferred to to the vertically arranged double defects is in-phase.

Figures 3-12 (a) to 3-12 (d) show the FRFs for the output voltage generated in PEH Devices 1 and 2 in the cases of (4, 7-⓪), (4, 6-①), (4, 5-②), and (4, 4-③), respectively, ranging from 59.8 kHz to 60.3 kHz, under the external electrical resistances of 100 MΩ (open-circuit. In Figure 3-12 (a), the output voltages generated in PEH Devices 1 and 2 of the double defects (4, 7) are drastically amplified up to (1) 19.02 V (PEH Device 1) and 19.08 V (PEH Device 2) at 59.87 kHz (in-phase defect mode shape) and (2) 21.98 V (PEH Device 1) and 21.84 V (PEH Device 2) at 60.19 kHz (out-of-phase defect mode shape), respectively. In Figure 3-12 (b), the peak frequencies of the double defects (4, 6-①) are 60.01 kHz and corresponding output voltages are 32.88 V and 5.16 V, respectively. In Figure 3-12 (c), the peak frequencies of the double defects (4, 5-②) are 60.01 kHz and corresponding maximum displacements are 33.64 V and 20.4 V, respectively. In Figure 3-11 (d), the peak displacements for PEH Devices 1 and 2 of the double defects (4, 4-③) are drastically amplified up to 34.20 V and 33.12 nm at 59.87 kHz (in-phase defect mode shape), respectively, while there are no peaks near 60.19 kHz (out-of-phase defect mode shape).

Similar to the investigation of the displacement FRFs, the decoupling between

the double defects occur when the defect is introduced in (4, 6-①) or (4, 5-②). Since the double defects are decoupling, the defect in (4, 6-①) has much lower displacement than the defect (4, 5-②) from the perspective of the defect location effects presented in Section 2.4. In addition, it can be found that the only peak frequency of the in-phase defect mode shape occur due to the in-phase normal incident waves.

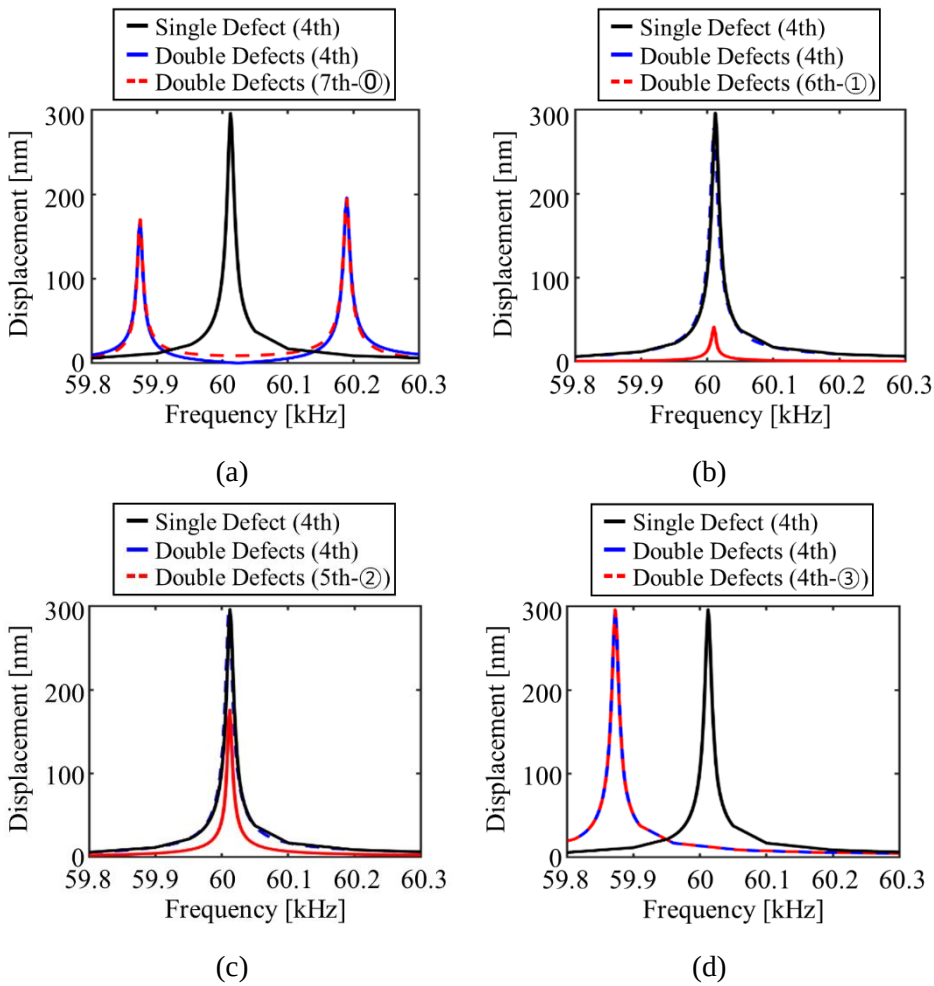

Figure 3-11 Mechanical displacement FRFs for four different arranging directions of double defects under the external electrical resistances of 100 MΩ (open-circuit): (a) (4, 7-⓪), (b) (4, 6-①), (c) (4, 5-②), and (d) (4, 4-③).

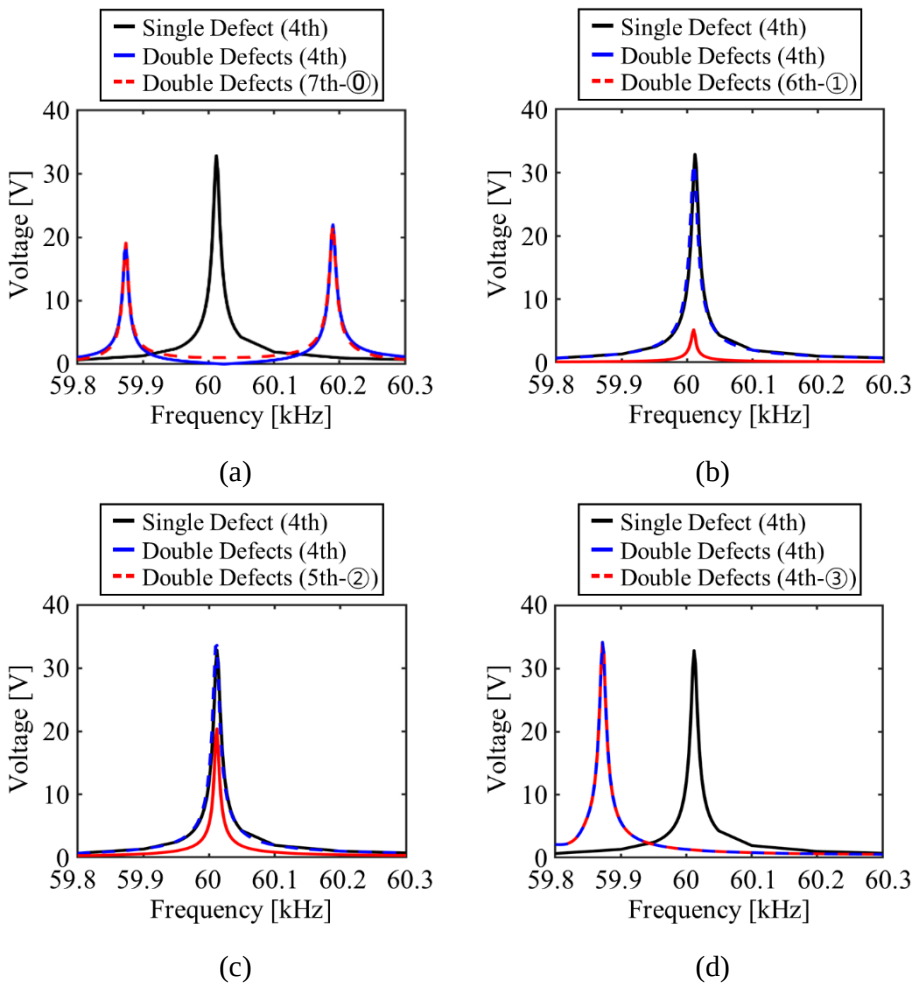

Figure 3-12 Output voltage FRFs for four different arranging directions of double defects under the external electrical resistances of 100 MΩ (open-circuit): (a) (4, 7-⓪), (b) (4, 6-①), (c) (4, 5-②), and (d) (4, 4-③).

3.4.3 Experimental Validation of the Splitting of Defect Bands under Elastic Waves

This chapter aims to demonstrate double defect modes-enabled energy localization and harvesting for a two-dimensional PnC under elastic waves. Furthermore, Section 3.4 provides numerical simulations of how the relative position between double defects affects the output performances of PEH. Here, there is a very important thing that should be emphasized. Even though the coupling of defect modes in a PnC with double or multiple defects has also drawn attention in acoustic regimes, efforts to experimentally validate the splitting phenomenon of defect bands can be rarely found in the elastic realm. To support the effectiveness of the output performance amplification of a PnC-based PEH system that leverages double defect modes, there is a great need to experimentally demonstrate the splitting phenomenon of defect bands. Therefore, in this section, various aspects of the splitting of defect bands in a two-dimensional PnC under A_0 Lamb waves are experimentally validated. Since the main concern of this section is the experimental measurement of (1) the splitting of defect band frequencies, effects of the distance between the double defects on (2) the degree of the splitting of defect bands, and (3) defect mode shapes, a circular hole-type PnC, shown in Figure 3-1, in the absence of PEH devices is under consideration.

Figure 3-13 depicts a schematic illustration of the PnC with double defects in a 2 mm-thick aluminum plate used in this work. The designed PnC structure consists of a 17×17 array of unit cells and each unit cell is composed of a square lattice with a circular hole at the center. Three cases of double defects depending on their relative inter-distances are taken into account. As illustrated in Figure 3-13, one defect is introduced by not creating the circular hole in the 4^{th} unit cell along the *x*-direction when the closest unit cell is considered as the 1^{st} unit cell in reference to the incident

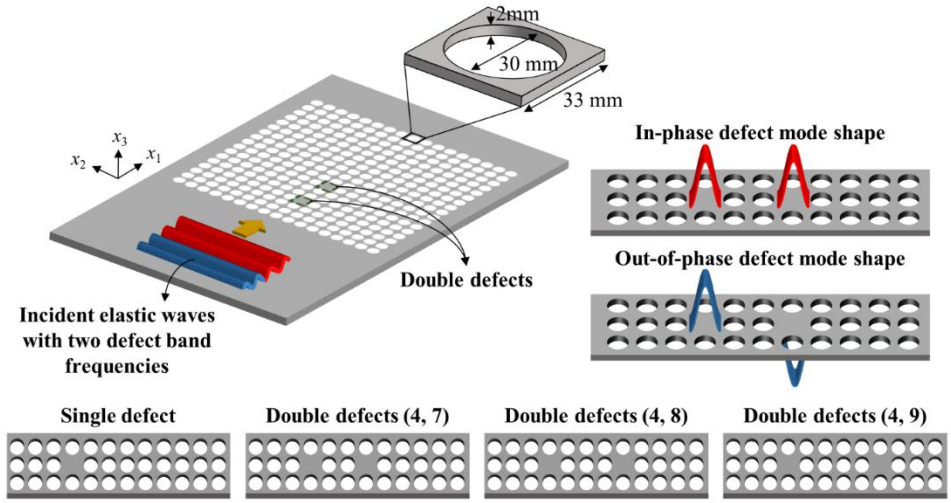

Figure 3-13 A schematic illustration of elastic wave localization using a two-dimensional PnC with double defects, relative incident waves.

waves. The other defects are then introduced in the same manner at the (1) 7th, (2) 8th, and (3) 9th unit cells along the *x*-direction to create three different cases of double defect. These three double defect cases are denoted by (4, 7), (4, 8), and (4, 9). Note that the same PnC with a single defect at the 4th unit cell location is used for comparison throughout this work.

Similar to Sections 3.2 and 3.3, band structure analysis is performed for the PnC without PEH devices. In the case of a single defect, five defect bands are observed within the band gap and a defect band frequency that corresponds to the monopole-like defect mode shape is 59.65 kHz. In the case of double defects (4, 7), the five defect bands for the single defect case are split into two bands. Two defect band frequencies that correspond to the in-phase and out-of-phase monopole-like

defect mode shapes are 59.51 kHz and 59.85 kHz, respectively. The degree of the splitting of defect bands are 340 Hz. In the case of double defects (4, 8), two defect band frequencies that correspond to the in-phase and out-of-phase monopole-like defect mode shapes are 59.60 kHz and 59.70 kHz, respectively. The degree of the splitting of defect bands are 100 Hz. In the case of double defects (4, 9), two defect band frequencies that correspond to the in-phase and out-of-phase monopole-like defect mode shapes are 59.63 kHz and 59.66 kHz, respectively. The degree of the splitting of defect bands are 30 Hz. Table 3-2 summarizes the defect band frequencies for cases with a single defect and three double defect combinations.

As presented in Figure 3-1, when performing harmonic analysis, the infinite domain of the structure is assumed in numerical simulations by applying periodic boundary conditions and perfectly matched layers. However, in the case of the experiments, since the aluminum plate has the finite domain, reflection waves at the boundaries of the plate have possibilities to affect the observations of the splitting phenomenon of defect bands. Therefore, it is necessary to examine whether the resonance frequencies (defect band frequencies) can be observed in the same manner under the finite domain condition.

Figure 3-14 presents a schematic illustration of the large aluminum plate with the PnC having double defects (4, 7) under the finite domain condition. The length and height of the aluminum plate are 2000 mm and 1000 mm, respectively. The distance between the left end of the plate and circular holes in the 1st layer of the PnC is 1000 mm. Traction-free conditions are applied to all boundaries of the plates. When incident elastic waves at a certain frequency enter the 1st layer of the PnC, they will be reflected at the interfaces of the aluminum plate and a set of circular

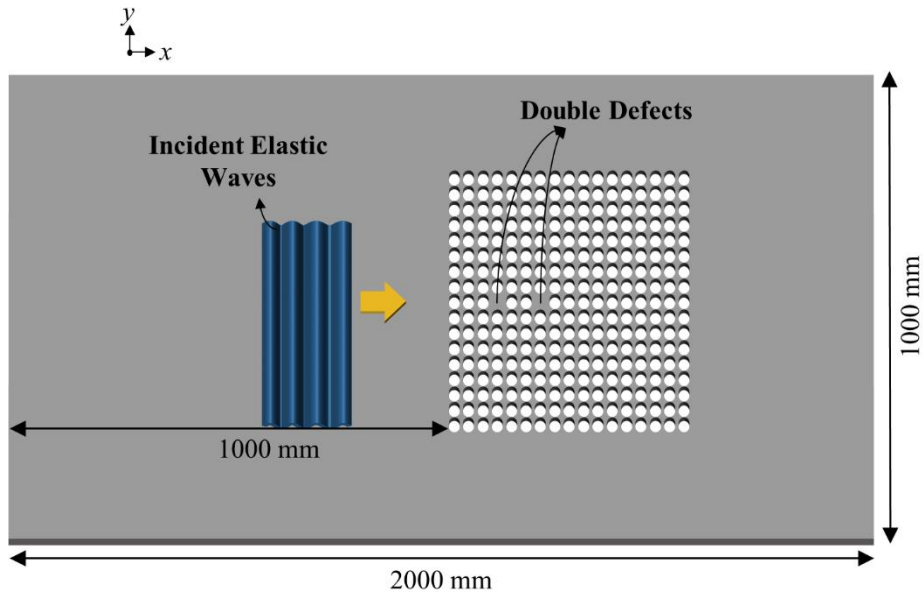

Figure 3-14 A schematic illustration of an aluminum plate with a PnC having double defects (4, 7) under the finite domain condition.

holes due to the impedance mismatch. Then, the reflected waves will propagate toward the edges of the plate and be reflected at the interfaces of the edges. After the repetitive reflections, the out-of-plane displacements are obtained at the center of each double defect.

Figures 3-15 (a) and 3-15 (b) depict the normalized out-of-plane displacement FRFs under the infinite and finite domain conditions, respectively. The overall trend of the displacement FRFs seems different due to the effects of the wave reflection at the edges of the plate. In Figure 3-15 (a), the peak frequencies are 59.51 kHz and 59.85 kHz. It is worth pointing out that the peak frequencies in Figure 3-15 (b) are

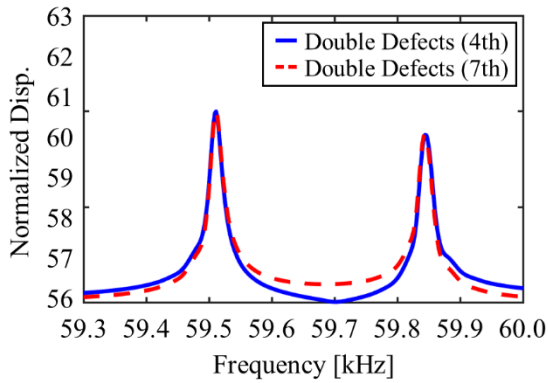

(a)

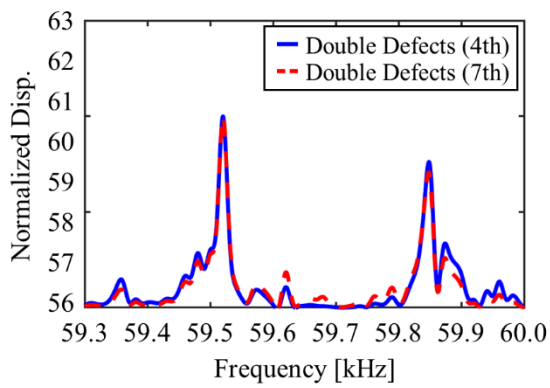

(b)

Figure 3-15 Normalized out-of-plane displacement FRF results under the (a) infinite and (b) finite domain conditions.

also obtained as 59.51 kHz and 59.85 kHz. From these results, it can be concluded that not only the splitting of defect bans but also the energy localization phenomenon can be observed regardless of whether the structure is under the infinite or finite domain conditions.

In order to experimentally validate the splitting phenomenon of defect bands, four 17×17 PnC supercell specimens with a single and three double defect combinations. First, four large aluminum plates (2000 mm×1000 mm×2 mm) are fabricated. To mimic the infinite domain condition in numerical simulations, the plates are made as large as possible while considering the available volume of the experiment room. Second, the computer-aided design (CAD) files of the PnCs with single or double defects are made by using the CAD software (i.e., Solidworks 2019). Next, one CAD file is inserted into a laser-cutting machine, and then the PnC is fabricated on the previously prepared aluminum plate. For all plates, a set of circular holes with the double defects is created to be biased to the center of the plate along the horizontal axis, while it is deployed in the center along the vertical axis. The distance between left ends of the plate and the circular hole in the 1st layer is 1000 mm. Note that no polishing is recommended to guarantee the high-intensity of the optical laser signal when measuring with scanning Laser Doppler Vibrometer (LDV).

Figure 3-16 (a) illustrates a schematic of the experimental setup along with the fabricated aluminum plate. Figure 3-16 (b) depicts a photo of the experimental setup. The experimental setup consists of (1) elastic wave generation system (i.e., disc-type lead zirconate titnanate (PZT) transducer (Cerocomp Co.) having a resonance frequency of 50 kHz, function generators (Keysight 33512B), and power amplifier (AE Techron 7224)) and (2) visualization system (i.e., LDV, data acquisition (DAQ), and controller (Polytec, PSV-400, OFV-5000)). To observe out-of-plane displacement FRFs measured at the center of the single or double defects, frequency-modulated continuous-waves are induced with ramp input signals in broadband frequencies ranging from 55 kHz to 60 kHz through the elastic wave generation

system. Moreover, to visualize mechanical behaviors of defects, we scan a square area (30 mm×30 mm) within the single or double defects while generating continuous-wave signals at certain peak frequencies in displacement FRFs; only one area is scanned at one frequency for the single defect case, while two areas are scanned at two frequencies for the double defects case.

For the cases of the single defect and double defects (4, 7), Figure 3-17 presents the measurement results of the out-of-plane displacements in the time domain, respectively. The sampling frequency is 5.12 MHz and the frequency sweeping time is 204.8 msec. The displacement is normalized with the maximum displacement in each case. It can be found that the single defect case would present a narrow peak in Figure 3-17 (a) while the double defects case would present a broader peak in Figures 3-17 (b) and 3-17 (c). Since the time contains frequency information that linearly increases from 55 kHz to 60 kHz, these experimental results of broadband characteristics are attributed to the splitting of defect bands. To investigate frequency responses of measured displacements, we perform fast Fourier transform into these data. With the given sampling frequency and time range, the frequency resolution is near 10 Hz. These kinds of data are also measured for the other specimens.

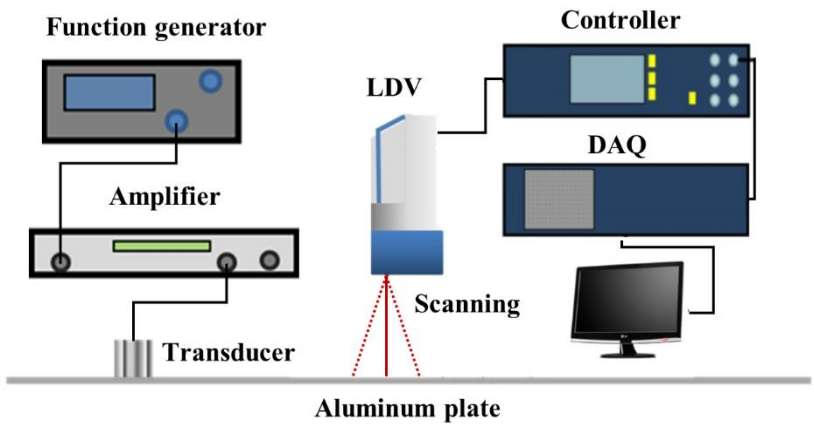

(a)

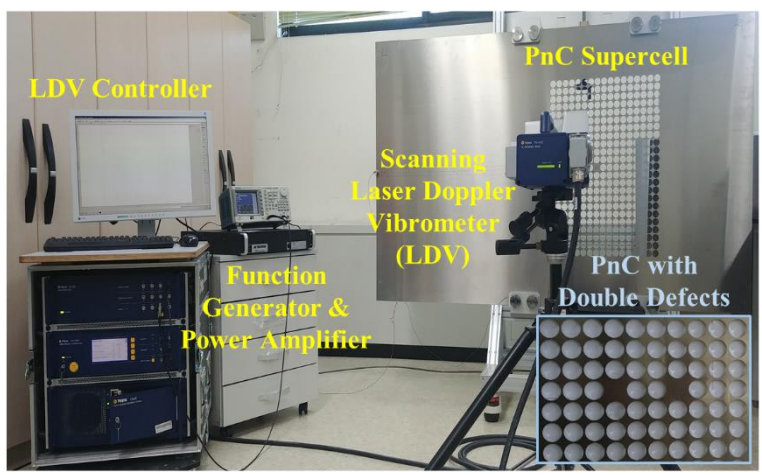

(b)

Figure 3-16 Experimental setup for elastic wave generation system and visualization system.

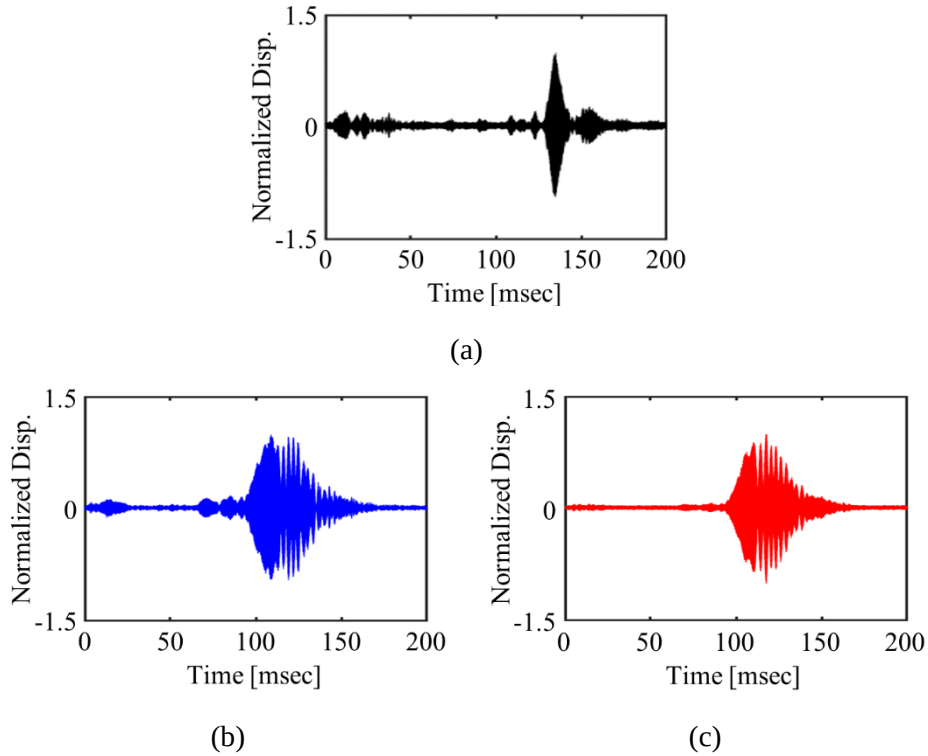

Figure 3-17 Measured out-of-plane displacements in the time domain for (a) the single defect and those for double defects in (b) 4th and (c) 7th layers.

Figure 3-18 contains both numerical simulation and experimental results of out-of-plane displacement FRFs at the center of each defect along with the experimentally visualized mode shapes over the defect area for all four cases: a single, (4, 7), (4, 8) and (4, 9). In Figures 3-18 (b) to 3-18 (d) and Figures 3-18 (f) to 3-18 (h), defect-band splitting with double defected PnCs are clearly confirmed not only numerically but also experimentally with two distinctive peaks having certain spacing in-between, particularly when compared with the single defected PnC in

Figures 3-18 (a) and 3-18 (e). Furthermore, the decreasing differences between the peak defect band frequencies with increasing spacing from (4, 7) to (4, 9) in Figures 3-18 (b) to 3-18 (d) are in excellent qualitative and quantitative agreement with their experimental counterparts in Figures 3-18 (f) to 3-18 (h). Calculated experimental peak frequencies are summarized in Table 3-2 for quantitative comparison.

It is quite challenging to precisely match the absolute values of peak frequencies obtained from numerical simulation with those from experiments due to the inherent physical uncertainties of material properties and manufacturing tolerance of geometric dimensions [114-117]. Based on the sensitivity analysis of the material and geometric properties of the PnC constituent (i.e., aluminum plate) which is described Figure 3-19, we could ensure that the differences between the two peak frequencies in experiments are in great agreement with those in numerical simulations within a reasonable fabrication-wise error range. By scanning displacement fields in the defected area, monopole-like defect mode shapes are experimentally visualized over the defect areas at each peak frequency, which are demonstrated in Figures 3-18 (i) to 3-18 (l). As predicted in the numerical analysis, in-phase behavior is observed at the lower split defect band frequencies whereas out-of-phase behavior is shown at the higher split defect band frequencies in PnCs with double defects experimentally.

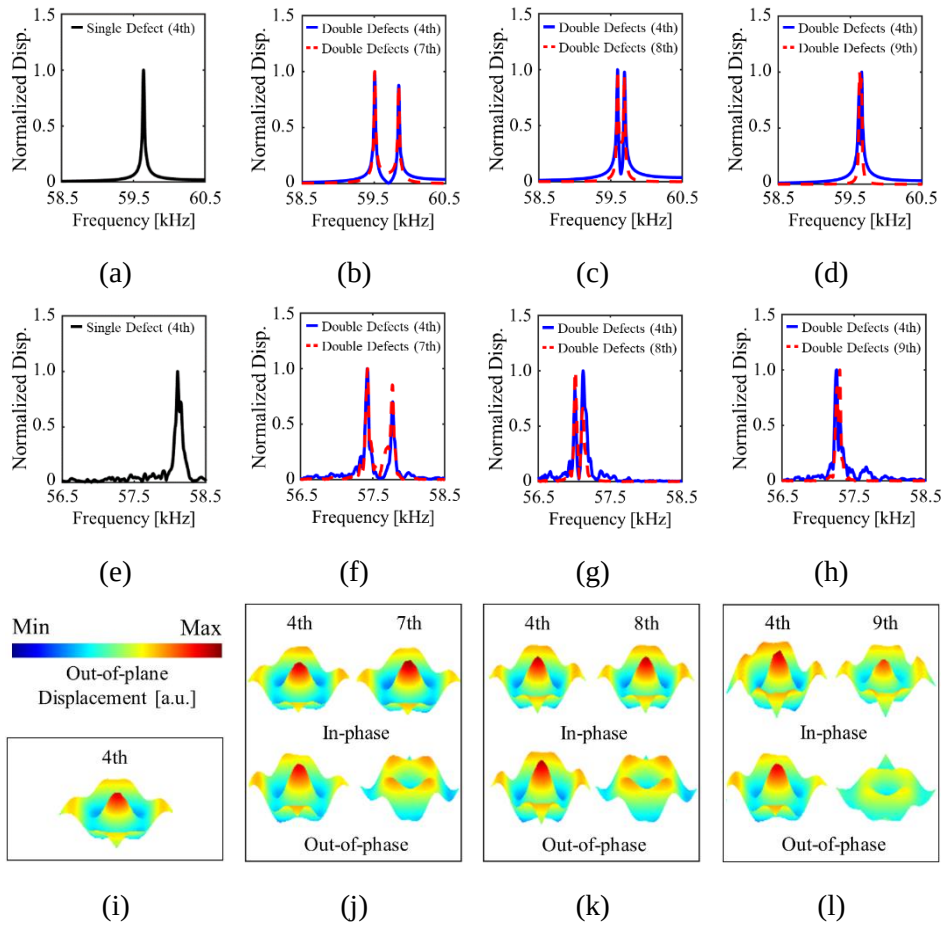

Figure 3-18 Comparison between numerical and experimental results for the single defect, double defects (4, 7), (4, 8), and (4, 9): numerically calculated out-of-plane displacement FRFs in (a) to (d); experimentally measured out-of-plane displacement FRFs in (e) to (h); and experimentally visualized mode shapes in (i) to (l).

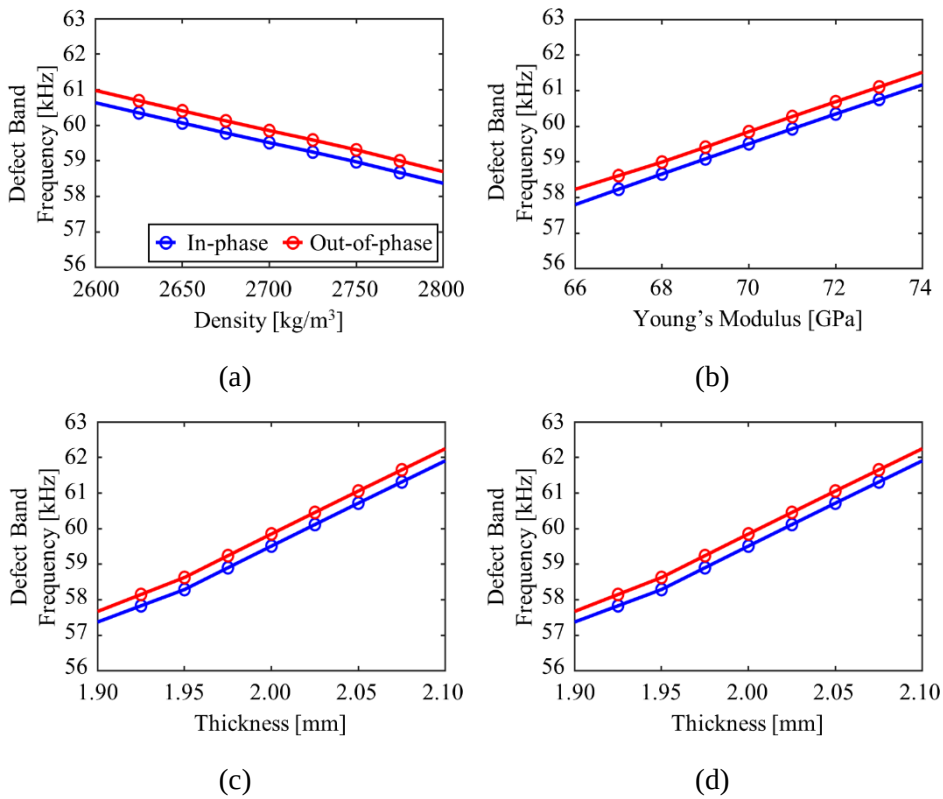

Figure 3-19 Effects of the (a) density, (b) Young's modulus, (c) diameter of the circular hole, and (d) thickness of the unit cell on the defect band frequencies that correspond to in and out-of-phase monopole-like defect mode shapes.

Table 3-2 Comparison between numerical and experimental results for the effects of the distance between double defects on the splitting of defect bands.

Number of defects	Defect location	Numerical simulations			Experiment		
		Defect band frequency [kHz]		Differences [Hz]	Defect band frequency [kHz]		Differences [Hz]
Single	4th	59.65		-	58.11		
Double	4th and 7th	59.51	59.85	340	57.43	57.78	350
	4th and 8th	59.60	59.70	100	57.02	57.12	100
	4th and 9th	59.63	59.66	30	57.26	57.30	40

3.5 Effects of the Electrical Circuit Connection between Double Defects on Energy Localization and Harvesting Performance

This section is dedicated to demonstrating the effects of the electrical connection between double defects on energy localization and harvesting performance. Five connection types (i.e., Independent, Series Types A and B, and Parallel Types C and D) are under consideration. Section 3.5.1 deals with the five electrical circuit configurations. When switching the electrical boundary condition from the short-circuit to the open-circuit conditions, Section 3.5.2 presents the shift patterns of split defect bands for the five scenarios. Under the open-circuit condition, Section 3.5.3 aims to analyze mechanical and electrical performances. Finally, the effects of the five electrical connection configurations on the maximum electric power and optimal external electrical resistance have been explained in Section 3.5.4.

3.5.1 Five Scenarios for Electrical Circuit Configuration

When the double defects are introduced in the 4th and 7th layers in the two-dimensional PnC as presented in Figure 3-1, we focus on the effects of the electrical circuit connections on the following physical quantities: (1) the shift patterns of the frequencies of the split defect bands when switching the electrical boundary condition from the short-circuit to the open-circuit conditions and (2) the maximum output voltage, electric power, and optimal external electrical resistances. Here, five electrical circuit connections are considered: (1) Independent, (2) Series-Type A, (3) Series-Type B, (4) Parallel-Type C, and (5) Parallel-Type D connections. Schematic illustration of each electrical circuit connection is provided in in Figure 3-20. Figure

3-20 (a) shows an enlarged side view of the PnC-based PEH system with double defects. In the first setting of an Independent connection (Figure 3-20 (b)), the top and bottom electrodes of the two PEH devices are independently connected to the terminal and ground, respectively. In a Series-Type A connection (Figure 3-20 (c)), the top electrodes of two PEH devices are directly connected to each other, while in a Series-Type B connection (Figure 3-20 (d)), the top electrode of one PEH device and the bottom electrode of the other PEH device are directly connected to each other. In both Series connections, the remaining electrodes are connected to the terminal and ground, respectively. In a Parallel-Type C connection (Figure 3-20 (e)), the top electrodes of both PEH devices are collectively connected to the terminal. In contrast, in a Parallel-Type D connection (Figure 3-20 (f)), the bottom electrode of one PEH device and the top electrode of the other PEH device are collectively connected to the terminal. In both Parallel connections, the remaining electrodes of the PEH devices are collectively connected to the ground.

In Section 3.4, it was found that electric currents generated by two PEH devices are synchronized with in-phase (0^o) or out-of-phase (180^o) while having the same magnitude at two frequencies of the split defect bands that correspond to monopole-like defect mode shapes. From this physical interpretation, the electric circuit connections presented in Figure 3-20 can be illustrated as several electrical circuit diagrams in Figure 3-21. Figure 3-21 (a) depicts the electrical circuit diagram that corresponds to each of PEH devices for the Independent connection (Figure 3-20 (b)). Figures 3-21 (b) and 3-21 (c) depict the cases of the Series connections (Figures 3-20 (c) and 3-20 (d)) when the electric current generated by each PEH device is under in-phase and out-of-phase, respectively. It should be noted that Figure 3-21 (b)

corresponds to the in-phase double defect modes for the Series-Type A (Figure 3-20 (c)) and out-of-phase double defect modes for the Series-Type B (Figure 3-20 (d)). On the other hand, Figure 3-21 (c) corresponds to out-of-phase double defect modes for the Series-Type A (Figure 3-20 (c)) and in-of-phase double defect modes for the Series-Type B (Figure 3-20 (d)). Figures 3-21 (d) and 3-21(e) depict the cases of the parallel connections (Figures 3-20 (e) and 3-20 (f)) when the electric current generated by each PEH device is under in-phase and out-of-phase, respectively. It should be noted that Figure 3-21 (d) corresponds to the in-phase double defect modes for the Parallel-Type C (Figure 3-20 (e)) and out-of-phase double defect modes for the Parallel-Type D (Figure 3-20 (f)). On the other hand, that Figure 3-21 (e) corresponds to out-of-phase double defect modes for the Parallel-Type C (Figure 3-20 (e)) and in-of-phase double defect modes for the Parallel-Type D (Figure 3-20 (f)).

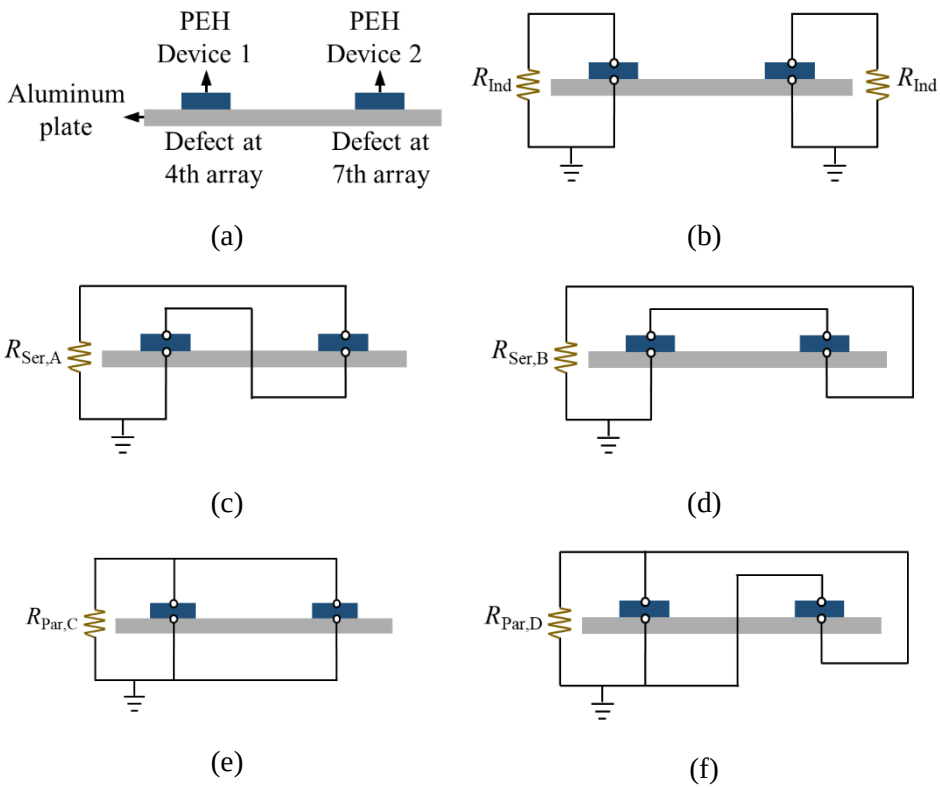

Figure 3-20 Electrical circuit configurations for two PEH devices, colored in dark-blue: (a) an enlarged side view of the PnC-based PEH system with double defects; (b) Independent, (c) Series-Type A, (d) Series-Type B, (e) Parallel-Type C, and (f) Parallel-Type D connections.

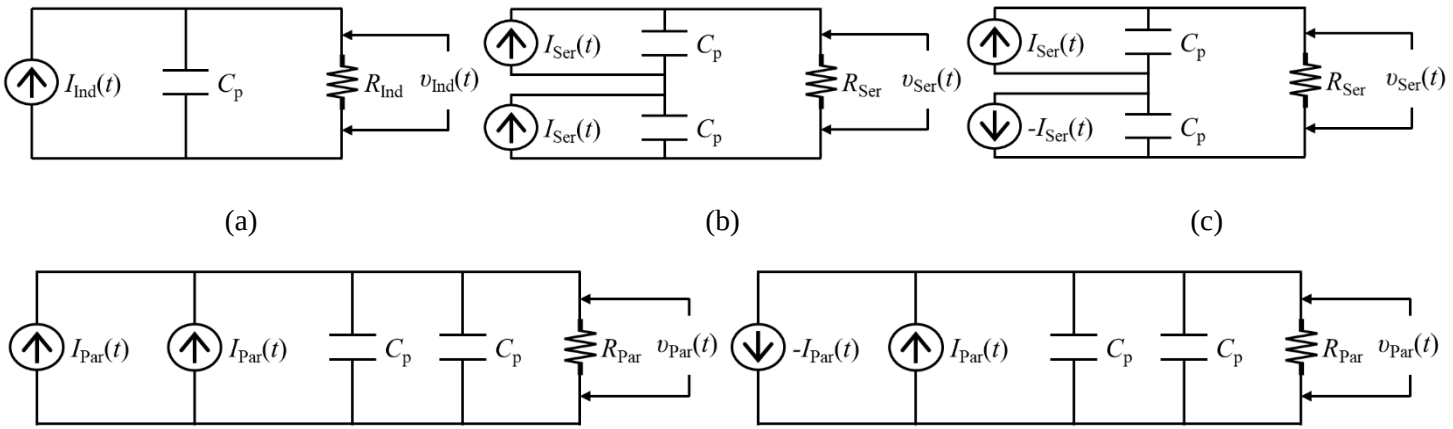

Figure 3-21 Electrical circuit diagrams between two PEH devices: (a) Independent connection, (b) in-phase and (c) out-of-phase electric current generation in the Series-Types A and B connections, (d) in-phase and (e) out-of-phase electric current generation in the Parallel-Types C and D connections.

3.5.2 Effects on Shift Patterns of the Split Defect Bands

When the electrical boundary condition is changed from the external electrical resistance of 0 Ω (short-circuit) to 100 MΩ (open-circuit), Table 3-3 summarizes the results of the frequencies of the split defect bands for different electrical circuit connections. It is observed that the shift patterns of the frequencies of the split defect bands in the Series-Type A and B connections coincide with those in the Independent connection. The frequencies of the split defect bands slightly increase from 59.79 kHz (in-phase) and 60.11 kHz (out-of-phase defect mode shape) to 59.87 kHz (in-phase defect mode shape) and 60.19 kHz (out-of-phase defect mode shape), respectively, in both Independent and Series connections. On the other hand, in the Parallel-Type C connection, the lower defect band frequency of 59.79 kHz (in-phase defect mode shape) under the external electrical resistance of 0 Ω (short-circuit) is shifted to that found in the Independent connection (59.87 kHz) under the external electrical resistance of 100 MΩ (open-circuit), while the higher defect band frequency of 60.11 kHz (out-of-phase defect mode shape) stays constant. In contrast, in the Parallel-Type D connection, the lower defect band frequency of 59.79 kHz (in-phase defect mode shape) stays steady, while the higher defect frequency of 60.11 kHz (out-of-phase defect mode shape) under the external electrical resistance of 0 Ω (short-circuit) is shifted to that found in the Independent connection (60.19 kHz) under the external electrical resistance of 100 MΩ (open-circuit).

The different shift patterns of the defect band frequencies in the Parallel connections can be explained in terms of the electroelastic coupling of the PEH devices, as shown in Figure 3-22. For the in-phase monopole-like defect mode shape (Figure 3-22 (b)), since two PEH devices are stretched or compressed together, they

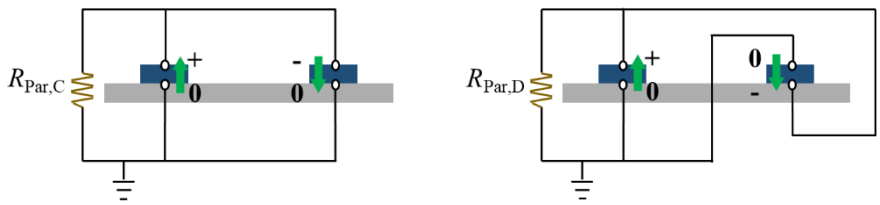

(a) (b)

Figure 3-22 Cancellation of electric current (or voltage) generated by two PEH devices for the out-of-phase defect mode shape in the Parallel-Type C connection and in-phase defect mode shape in the Parallel-Type D connection.

have the same sign of strain at the top and bottom electrodes, respectively. On the other hand, for the out-of-phase monopole-like defect mode shape (Figure 3-22 (a)), since one PEH device is stretched and the other PEH device is compressed, they have different signs of strain at top and bottom electrodes, respectively. The surface area of each PEH device, connected to the terminal, exhibits the opposite sign of the strain for the out-of-phase defect mode shape in the case of the Parallel-Type C connection (Figure 3-22 (a)) and in -phase defect mode shape in the case of the Parallel-Type D connection (Figure 3-22 (b)); this induces nearly zero electroelastic coupling. In a field of PEH, as the electrical boundary condition is switched from the short-circuit to open-circuit conditions, the degree of the resonance frequency shift depends on the electroelastic coupling; thereby, the different shift patterns of the defect band frequencies are observed in the Parallel-Type C and D connections.

The effects of the electric circuit configuration on the shift patterns of the split defect bands can be also explicitly demonstrated with the help of the mathematical

approach demonstrated presented in Appendix B. Here, it should be noted that the proposed electroelastical coupled analytical model in Appendix B was developed for a one-dimensional PnC with a piezoelectric defect under longitudinal waves. The engineered situation under consideration in this chapter is a two-dimensional PnC with double defects which is exposed to A_0 Lamb waves (close to bending waves). The engineering problems look different. However, since the piezoelectric materials in both cases are polarized in 31-mode, a concept of the electrical circuit equation in Section B.2.2 can be still utilized. In both cases of the Parallel-Types C and D where the defect bands do not shifted, the electrical circuit diagram is shown in Figure 3-21 (e). Using Gauss's law and Kirchhoff's law, the electric circuit equation can be expressed as

$$2C_{\mathrm{p}}\frac{d\upsilon_{\mathrm{Par}}(t)}{dt}+\frac{\upsilon_{\mathrm{Par}}(t)}{R_{\mathrm{Par}}}=\frac{\partial}{\partial t}\left(\int_{S_{\mathrm{p}}}\left(\varepsilon_{11}^{\mathrm{Par}}+\varepsilon_{11}^{\mathrm{Par}}\right)dS+\int_{S_{\mathrm{p}}}-\left(\varepsilon_{11}^{\mathrm{Par}}+\varepsilon_{11}^{\mathrm{Par}}\right)dS\right). \qquad (3.1)$$
$$=0.$$

As found in the right-hand of Equation (5.1), electric current generated by each PEH device has the opposite signs and should be cancelled. It indicates that both forward and backward electroelastic coupling do not occur at two frequencies of the split defect bands. Furthermore, it is expected that the output voltage generated by the PEH devices would be nearly zero at these frequencies for the out-of-phase defect mode shape in the case of the Parallel-Type C connection (Figure 3-22 (a)) and in -phase defect mode shape in the case of the Parallel-Type D connection (Figure 3-22 (b)).

Table 3-3 Shift patterns of the frequencies of the split defect bands that correspond to the monopole-like defect mode shape for five electrical circuit connections.

Number of defects	Electrical circuit connection	Phase of defect mode shape	Defect band frequency [kHz]		Degree of shift
			0 Ω (short-circuit)	100 MΩ (open-circuit)	
Single	-	-	59.94	60.01	Shift
Double	Independent	In-phase	59.79	59.87	Shift
		Out-of-phase	60.11	60.16	Shift
	Series-Types A and B	In-phase	59.79	59.87	Shift
		Out-of-phase	60.11	60.19	Shift
	Parallel-Type C	In-phase	59.79	59.87	Shift
		Out-of-phase	60.11	60.11	No shift
	Parallel-Type D	In-phase	59.79	59.79	No shift
		Out-of-phase	60.11	60.19	Shift

3.5.3 Effects on Mechanical and Electrical Performances under the Open-circuit Condition

This section aims to investigate how the mechanical and electrical performances vary with five electrical circuit connections. The mechanical output performance of interest is the *z*-directional displacement of the PEH devices attached to the center of the defects in the PnC. The electrical output performances of interest are output voltage. Since this section focuses more on output voltage than on electric current, the analysis was performed under the external electrical resistance of 100 MΩ (open-circuit).

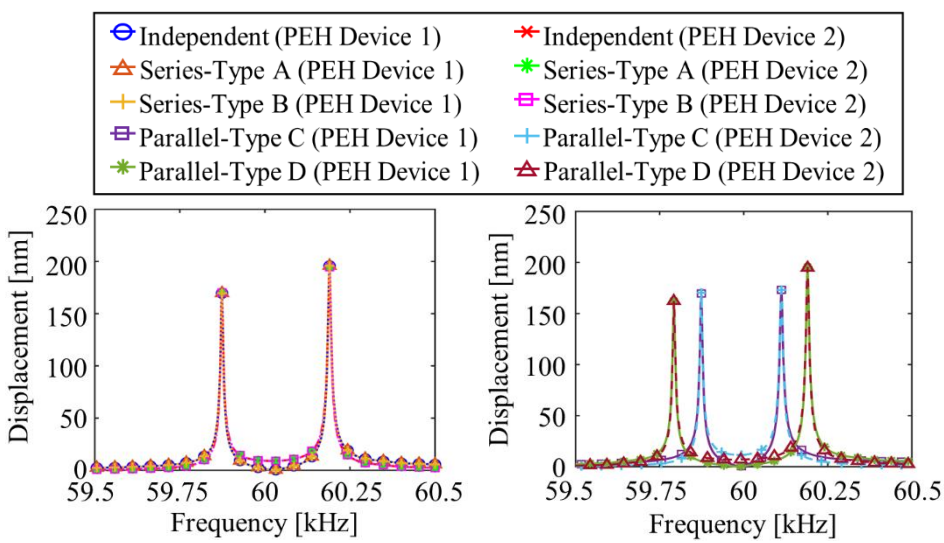

(a) (b)

Figure 3-23 Mechanical displacement FRFs for five electrical circuit connections under the external electrical resistances of 100 MΩ (open-circuit): (a) Independent, Series-Types A and B, (b) Parallel-Types C and D connections.

Figure 3-23 shows the FRFs for the displacement, ranging from 59.50 kHz to 60.50 kHz, for each electrical circuit connection under the external electrical resistance of 100 MΩ (open-circuit). In the Independent connection, the peak displacements for PEH Devices 1 and 2 are drastically amplified up to (1) 168.8 nm and 170.3 nm at 59.87 kHz (in-phase defect mode shape) and (2) 194.6 nm and 195.8 nm at 60.19 kHz (out-of-phase defect mode shape), respectively, as shown in Figure 3-23 (a).

Table 3-4 summarizes peak frequencies and corresponding peak displacements of the PnC-based PEH system with double defects under the external electrical resistance of 100 MΩ (open-circuit) for five different electrical circuit connection scenarios. For all connections, peak frequencies are equal to the calculated defect band frequencies under the external electrical resistance of 100 MΩ (open-circuit) which are listed in Table 3-3. It is found that the peak frequencies of 59.87 kHz (in-phase defect mode shape) and 60.19 kHz (out-of-phase defect mode shape) in the Series-Types A and B connections (Figure 3-23 (a)) coincide with those in the Independent connection (Figure 3-23 (a)). On the other hand, the higher peak frequency of 60.11 kHz (out-of-phase defect mode shape) in the Parallel-Type C connection (Figure 3-23 (b)) and the lower peak frequency of 59.79 kHz (in-phase defect mode shape) in the Parallel-Type D connection (Figure 3-23 (b)) are equal to the corresponding defect band frequencies in the Independent connection the external electrical resistance of 0 Ω (short-circuit), respectively. In addition, it can be found that the peak displacement is almost the same if the peak frequencies are the same among the types of electrical circuit connections; on the other hand, the amplified displacement is also different if the peak frequency is different. In

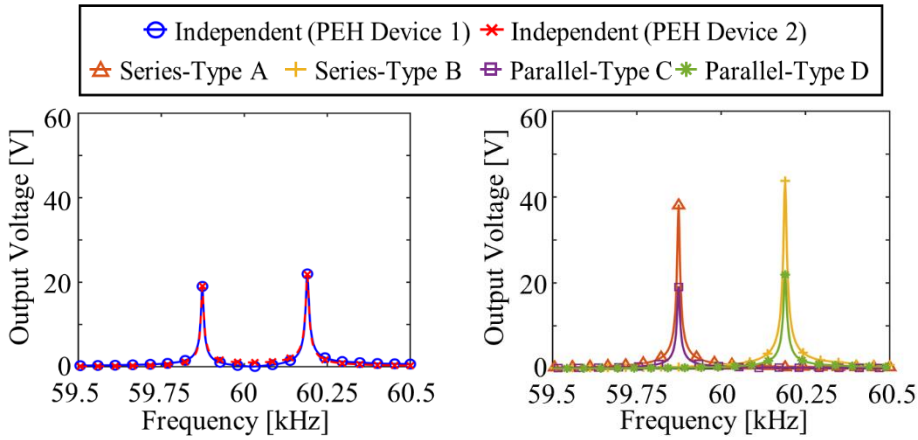

(a) (b)

Figure 3-24 Output voltage FRFs for five electrical circuit connections under the external electrical resistances of 100 MΩ (open-circuit): (a) Independent, (b) Series-Types A and B, Parallel-Type C and D connections.

Appendix A, if the frequency is different, the imaginary part in the band gap changes so that the degree of exponentially decaying properties would be different. Therefore, the change of locations where fixed-like boundary conditions are generated makes the amount of the displacement amplification depend on the frequency.

It seems that the different shift patterns of peak frequencies come from voltage cancellation in the PEH devices, as described in Section 3.5.2. To strengthen this physical interpretation, as well as estimate PEH performance, the output voltage FRFs are shown in Figure 3-24, ranging from 59.50 kHz to 60.50 kHz, under the external electrical resistance of 100 MΩ (open-circuit) for different electrical circuit connection scenarios. Solid lines with blue-circles and dashed lines with red-crosses

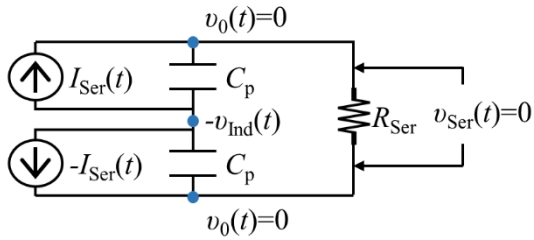

Figure 3-25 Zero electric potential difference between the external electrical resistance for the out-of-phase defect mode shape in the Series-Type A connection and in-phase defect mode shape in the Series-Type B connection.

indicate the electrical performance of PEH Devices 1 and 2 in the Independent connection, respectively. In addition, solid lines with orange-triangles, yellow-pluses, purple-squares, green-stars, and magenta-circles indicate the output voltage FRFs in Series-Type A, Series-Type B, Parallel-Type C, and Parallel-Type C connections, respectively.

In Figure 3-24 (a), the peak output voltages for DEH devices 1 and 2 are up to (1) 19.02 V (PEH Device 1) and 19.08 V (PEH Device 2) at 59.87 kHz (in-phase defect mode shape) and (2) 21.98 V (PEH Device 1) and 21.84 V (PEH Device 2) at 60.19 kHz (out-of-phase defect mode shape), respectively, in the Independent connection. Similar to the displacement FRFs, the output voltage magnitudes of PEH Devices 1 and 2 are almost the same at each peak frequency.

As shown in Figure 3-24 (b), the output voltage is enhanced only at 59.87 kHz (in-phase defect mode shape) in the Series-Type A and Parallel-C connections, and only at 60.19 kHz (out-of-phase defect mode shape) in the Series-Type B and

Parallel-Type D connections. As compared with the Independent connection, the peak output voltages of 38.04 V at 59.87 kHz (in-phase defect mode shape) in the Series-Type A connection and 43.76 V at 60.19 kHz (out-of-phase defect mode shape) in the Series-Type B connection are almost doubled, respectively. In addition, the peak output voltages of 19.06 V at 59.87 kHz (in-phase defect mode shape) in the Parallel-Type C connection and 21.92 V at 60.19 kHz (out-of-phase defect mode shape) in the Parallel-Type D connection are almost the same as those in the Independent connection, respectively. Effects of the electric circuit configuration on the maximum output voltage can be also demonstrated by the mathematical approach as presented in Appendix B. In the cases of Series and Parallel connections at the peak frequency of output voltage FRFs, the electrical circuit diagrams for each case are shown in Figures 3-21 (b) and 3-21 (d), respectively. Under the external electrical resistance of 100 MΩ (open-circuit), the electric circuit equations for Independent, Series, and Parallel connections that generate the in-phase electric currents, can be derived from Gauss's law and Kirchhoff's law, respectively, as

$$C_{\mathrm{p}}\frac{d\upsilon_{\mathrm{Ind}}(t)}{dt}=e_{31}\frac{\partial}{\partial t}\left(\int_{0}^{S_{\mathrm{p}}}\left(\varepsilon_{11}^{\mathrm{Ind}}+\varepsilon_{22}^{\mathrm{Ind}}\right)dS\right), \tag{3.2}$$

$$\frac{C_{\mathrm{p}}}{2}\frac{d\upsilon_{\mathrm{Ser}}(t)}{dt}=e_{31}\frac{\partial}{\partial t}\left(\int_{0}^{S_{\mathrm{p}}}\left(\varepsilon_{11}^{\mathrm{Ser}}+\varepsilon_{22}^{\mathrm{Ser}}\right)dS\right), \tag{3.3}$$

$$2C_{\mathrm{p}}\frac{d\upsilon_{\mathrm{Par}}(t)}{dt}=2e_{31}\frac{\partial}{\partial t}\left(\int_{0}^{S_{\mathrm{p}}}\left(\varepsilon_{11}^{\mathrm{Par}}+\varepsilon_{11}^{\mathrm{Par}}\right)dS\right). \tag{3.4}$$

Therefore, as compared with the generated output voltage in the Independent

connection, it can be found that output voltage is doubled in Series connections, while it is the same in Parallel connections when the electric current generated by each PEH device is synchronized with in-phase. The peak output voltage at the peak frequencies is summarized in Table 3-4.

On the other hand, no peak output voltage occurs at 60.19 kHz (out-of-phase defect mode shape) in the Series-Type A, at 59.87 kHz (in-phase defect mode shape) in the Series-Type B, at 60.11 kHz (out-of-phase defect mode shape) in the Parallel-Type C, and at 59.79 kHz (in-phase defect mode shape) in the Parallel-Type D connections despite the high amplification of the displacement at these peak frequencies. In the Parallel connections, as we expected, it can be distinctly seen that voltage cancellation takes place when the double defects oscillate with the out-of-phase mode shape behavior of the PEH devices in the Parallel-Type C connection and in-phase defect mode shape behavior of the PEH devices in the Parallel-Type D connection. In the case of the Series connections, the effects of the electric circuit configuration on the output voltage can be readily demonstrated by the mathematical approach as presented in Appendix B. The PEH devices with the in-phase defect mode shape have current sources of the same direction, while PEH devices with the out-of-phase defect mode shape have opposite direction sources. In both cases of Series-Types A and B where the nearly zero output voltage is obtained at the shifted defect band frequencies, the electrical circuit diagram is shown in Figure 3-25. Using Gauss's law and Kirchhoff's law, the electric circuit equation can be expressed as

$$\frac{C_{\mathrm{p}}}{2}\frac{d\upsilon_{\mathrm{Ser}}(t)}{dt}=0\,. \tag{3.5}$$

As shown in the right-hand of Equation (3.5), the electric potential difference between the external electric resistance becomes zero due to the opposite directions of current sources of the PEH devices. However, it should be noted that only electric potential difference is zero and electric current is still generated by each PEH device due to piezoelectric effects. That's why the shift of defect bands is observed in Table 3-3.

Table 3-4 Mechanical and electrical output performances at peak frequencies under the external electrical resistance of 100 MΩ (open-circuit) for five electrical circuit connections.

Electrical circuit connection	Phase of defect mode shape	Peak frequency [kHz]	Peak displacement [nm]		Peak voltage [V]	
			PEH Device 1	PEH Device 2	PEH Device 1	PEH Device 2
Independent	In-phase	59.87	168.8	170.3	19.02	19.08
	Out-of-phase	60.19	194.6	195.8	21.98	21.84
Series-Type A	In-phase	59.87	169.4	170.1	38.04	
	Out-of-phase	60.19	195.6	194.5	0.401	
Series-Type B	In-phase	59.87	169.4	170.1	0.322	
	Out-of-phase	60.19	195.6	194.5	43.76	
Parallel-Type C	In-phase	59.87	169.6	170.4	19.06	
	Out-of-phase	60.11	173.2	173.2	0.205	
Parallel-Type D	In-phase	59.79	162.3	162.3	0.162	
	Out-of-phase	60.19	195.7	194.8	21.92	

3.5.4 Effects on the Maximum Output Electric Power and Optimal External Electrical Resistance

As demonstrated in Chapter 2, since the behavior of the output electric power with changing the external electrical resistance is non-monotonic, there exists the optimal value of the external electrical resistance at which the maximum output electric power can be achieved. For five electrical circuit connection scenarios under the open-circuit condition, the optimal external electrical resistance can be found by sweeping it at the peak frequency listed in Table 3-4. Figure 3-26 shows the output voltage and output electric power at 59.87 kHz (in-phase defect mode shape) for the Independent, Series-Type A, and Parallel-Type C connections and at 60.19 kHz (out-of-phase defect mode shape for the Independent, Series-Type B, and Parallel-Type D connections with respect to the external electrical resistance, ranging from 0 Ω to 100 MΩ.

In Figures 3-26 (a) and 3-26 (b), as increasing the external electrical resistance, it can be observed that the output voltage for all electrical circuit connections monotonically increases and converges up to the peak value presented in Table 3-4. It should be noted that the trends of the output voltage for the Series and Parallel connections deviate from those for the Independent connection. This discrepancy can be described from the perspective of the electroelastic coupling and equivalent capacitance of the PEH devices. In the field of PVEH, it is well known that the electroelastic coupling in Series connections is the same, while the electroelastic coupling in Parallel connection becomes doubled; and the equivalent capacitance in the Series connections is halved, while the equivalent capacitance in the Parallel connections is doubled, as compared with that observed for an Independent connection [29].

In Figures 3-26 (c) and 3-26 (d), the optimal external electrical resistance is investigated for each electrical circuit connection. In the Independent connection, the optimal external electrical resistances of two PEH devices are the same as each other at each peak frequency; they were obtained as 120.2 kΩ at 59.87 kHz (in-phase defect mode shape) and 95.50 kΩ at 60.19 kHz (out-of-phase defect mode shape), respectively. It should be noted that the optimal external electrical resistance at each resonance frequency is doubled in the Series connections, while the optimal external electrical resistance is nearly halved in the Parallel connections, as compared with that found in the Independent connection. Since the optimal external electrical resistance is inversely proportional to an effective capacitance under an assumption of a very low loss factor [11, 115], this can describe variations of the optimal external electrical resistance. Table 3-5 summarizes the optimal external electrical resistances at peak frequencies for five electrical circuit connections. Here, it should be noted that the maximum mechanical power of guided bending waves that transferred to the host medium by excitation is calculated as near 5.78 mW at the frequency of 60 kHz

At the calculated optimal external electrical resistances, the output electric power FRFs are presented in Figure 3-27. Figures 3-27 (a) and 3-27 (b) depict the output electric power FRFs under the external electrical resistances of 120.2 kΩ and 95.50 kΩ, respectively, for the Independent connection. Under the optimal external electrical resistance of 95.50 kΩ, the peak electric power for PEH Devices 1 and 2 are up to (1) 0.727 mW (PEH Device 1) and 0.734 mW (PEH Device 2) at 59.87 kHz (in-phase defect mode shape) and (2) 1.255 mW and 1.235 mW at 60.19 kHz (out-of-phase defect mode shape), respectively. Under the optimal external electrical resistance of 120.2 kΩ, the peak electric power for PEH Devices 1 and 2 are up to

(1) 0.739 mW (PEH Device 1) and 0.745 mW (PEH Device 2) at 59.87 kHz (in-phase defect mode shape) and (2) 1.240 mW (PEH Device 1) and 1.222 mW (PEH Device 2) at 60.19 kHz (out-of-phase defect mode shape), respectively.

Compared with the Independent connection, the output electric power is nearly doubled in both connections, specifically: 1.484 mW at 59.87 kHz (in-phase defect mode shape) and 2.489 mW at 60.19 kHz (out-of-phase defect mode shape) in the Series-Type A and B connections (Figure 3-27 (c)), and 1.483 mW at 59.87 kHz (in-phase defect mode shape) and 2.488 mW at 60.19 kHz (out-of-phase defect mode shape) in the Parallel-Type C and D connections (Figure 3-27 (d)), respectively. This implies that the Series and Parallel connections can add up the individual output electric power generated by PEH Devices 1 and 2 in an Independent connection. Table 3-5 summarizes the maximum electric power across power-optimal external electrical resistance at peak frequencies for five electrical circuit connections.

Effects of the electric circuit configuration on the maximum electric power and corresponding optimal external electrical resistance can be also demonstrated by the mathematical approach as presented in Appendix B. Under an assumption that the backward coupling is neglected, the electric circuit equations across an arbitrarily external electrical resistance for the Independent, Series, and Parallel connections that generate the in-phase electric currents, can be derived from Gauss's law and Kirchhoff's law, respectively, as

$$C_{\mathrm{p}} \frac{d\upsilon_{\mathrm{Ind}}(t)}{dt} + \frac{\upsilon_{\mathrm{Ind}}(t)}{R_{\mathrm{Ind}}} = e_{31} \frac{\partial}{\partial t} \left(\int_0^{S_{\mathrm{p}}} \left(\varepsilon_{11}^{\mathrm{Ind}} + \varepsilon_{22}^{\mathrm{Ind}} \right) dS \right) = |\boldsymbol{A}| e^{j\omega t}, \tag{3.6}$$

$$\frac{C_{\mathrm{p}}}{2}\frac{d\upsilon_{\mathrm{Ser}}(t)}{dt}+\frac{\upsilon_{\mathrm{Ser}}(t)}{R_{\mathrm{Ser}}}=e_{31}\frac{\partial}{\partial t}\left(\int_{0}^{S_{\mathrm{p}}}\left(\varepsilon_{11}^{\mathrm{Ser}}+\varepsilon_{22}^{\mathrm{Ser}}\right)dS\right)=\left|\boldsymbol{A}\right|e^{j\omega t}, \tag{3.7}$$

$$2C_{\mathrm{p}}\frac{d\upsilon_{\mathrm{Par}}(t)}{dt}+\frac{\upsilon_{\mathrm{Par}}(t)}{R_{\mathrm{Par}}}=2e_{31}\frac{\partial}{\partial t}\left(\int_{0}^{S_{\mathrm{p}}}\left(\varepsilon_{11}^{\mathrm{Par}}+\varepsilon_{22}^{\mathrm{Par}}\right)dS\right)=2\left|\boldsymbol{A}\right|e^{j\omega t}. \tag{3.8}$$

With simple mathematical techniques, the maximum electric power and corresponding optimal external electric resistances are derived for each electrical circuit connection as

$$\left|\boldsymbol{P}\right|_{\mathrm{Ind,max}}\simeq\frac{\left|\boldsymbol{A}\right|^{2}}{2\omega C_{\mathrm{p}}}\left(R_{\mathrm{Ind,opti}}\simeq\frac{1}{\omega C_{\mathrm{p}}}\right), \tag{3.9}$$

$$\left|\boldsymbol{P}\right|_{\mathrm{Ser,max}}\simeq\frac{\left|\boldsymbol{A}\right|^{2}}{\omega C_{\mathrm{p}}}\left(R_{\mathrm{Ser,opti}}\simeq\frac{2}{\omega C_{\mathrm{p}}}\right), \tag{3.10}$$

$$\left|\boldsymbol{P}\right|_{\mathrm{Par,max}}\simeq\frac{\left|\boldsymbol{A}\right|^{2}}{\omega C_{\mathrm{p}}}\left(R_{\mathrm{Par,opti}}\simeq\frac{1}{2\omega C_{\mathrm{p}}}\right) \tag{3.11}$$

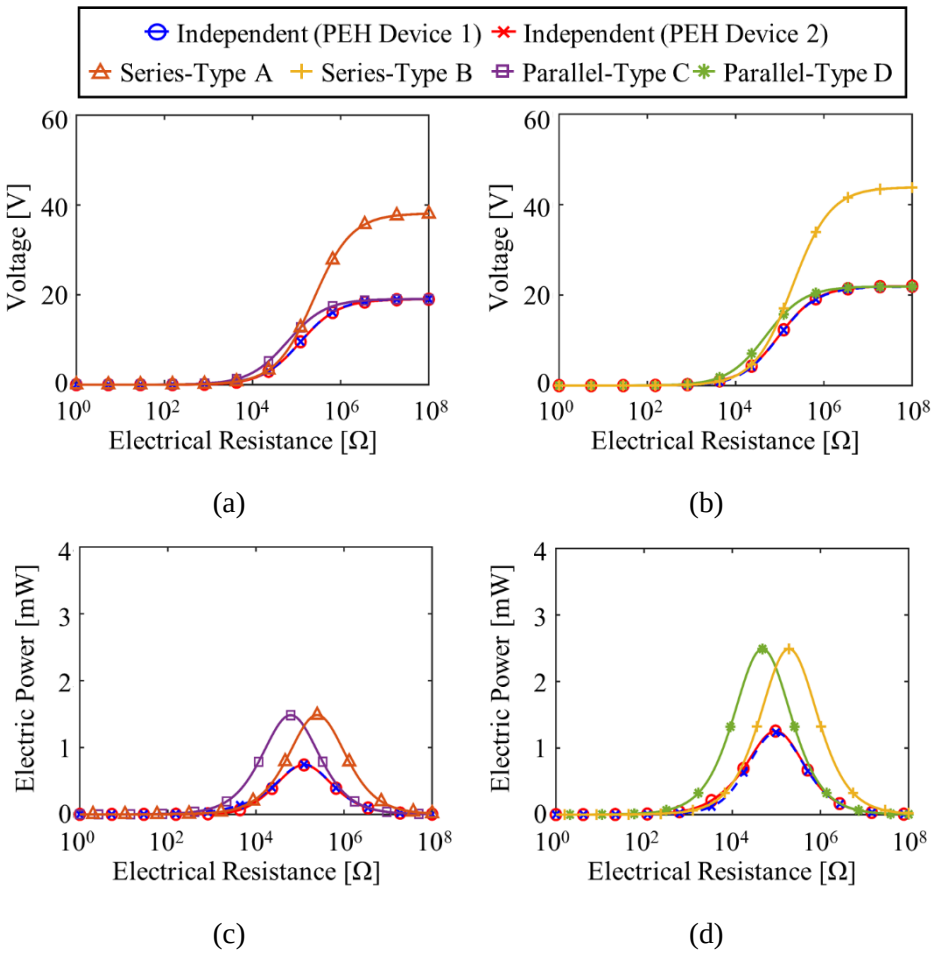

Figure 3-26 Output voltage and electric power across the external electrical resistance at peak frequencies for five electrical circuit connections: (a) output voltage and (c) output electric power at 59.87 kHz for the Independent, Series-Type A, and Parallel-Type C connections, (b) output voltage and (d) output electric power at 60.19 kHz for the Independent, Series-Type B, and Parallel-Type D connections.

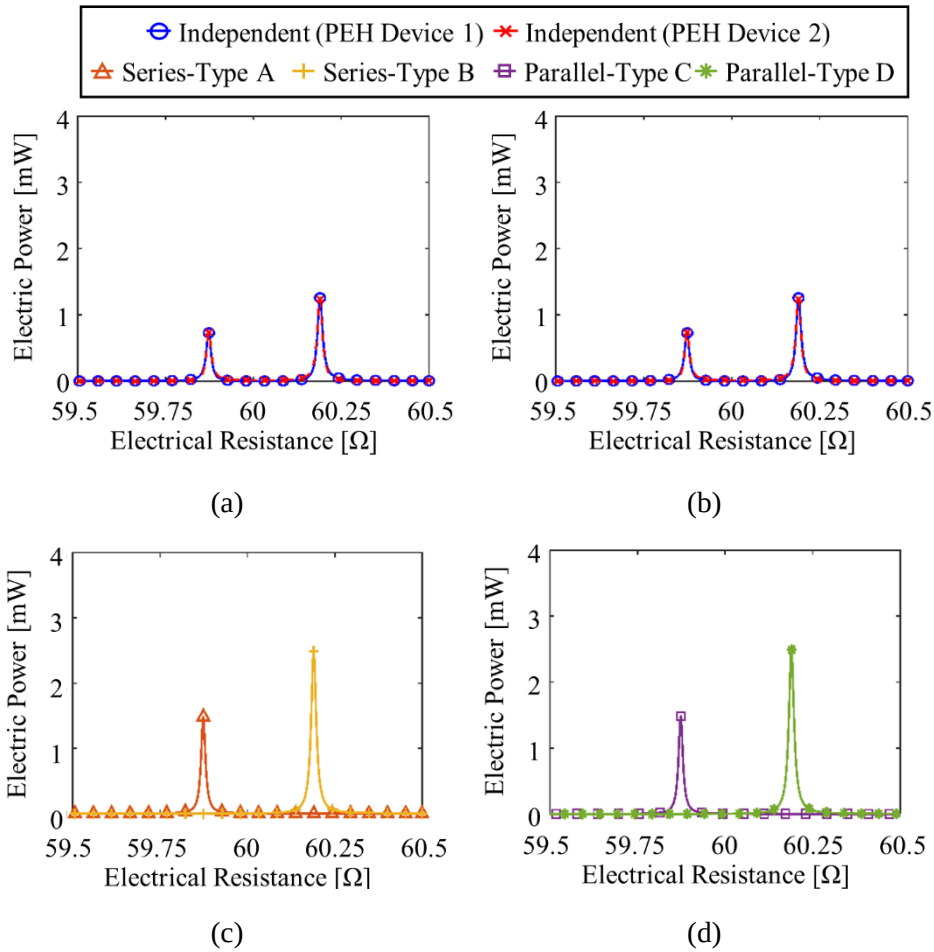

Figure 3-27 Output electric power FRFs across the optimal external electrical resistance for five electrical circuit connections: (a) Independent (120.2 kΩ), (b) Independent (95.50 kΩ), (c) Series-Types A (239.9 kΩ) and B (190.6 kΩ), and (d) Parallel-Types C (60.26 kΩ) and D (47.86 kΩ) connections.

Table 3-5 The maximum output electric power across the optimal external electrical resistance for five electrical circuit connections.

Electrical circuit connection	Optimal external electrical resistance [kΩ]	Peak frequency [kHz]	Peak output electric power [mW]	
			PEH Device 1	PEH Device 2
Independent	95.50	59.87	0.727	0.734
		60.19	1.255	1.235
	120.2	59.87	0.739	0.745
		60.19	1.240	1.222
Series-Type A	239.9	59.87	1.484	
Series-Type B	190.6	60.19	2.489	
Parallel-Type C	60.26	59.87	1.483	
Parallel-Type D	47.86	60.19	2.488	

3.6 Summary and Discussion

Since defect-mode-enabled energy localization results from mechanical resonance within a PnC where several unit cells that surround a single defect behave as fixed-liked boundary conditions, the frequency bandwidth for energy localization and harvesting is inherently low. Therefore, there is a great need to widen the bandwidth for PEH and a design concept of a two-dimensional PnC with double defects is taken into account. In acoustic domains, some previous studies have explored a PnC with double defects via numerical simulations and experiments. When double defects are created sufficiently close to each other, the interaction between the double defects generates a splitting of the frequencies of the defect modes For elastic waves, only a few research has been reported due to complexity of tensor-form governing equations. Analogous to the phenomena in acoustics, the splitting of defect bands is still observed. Moreover, in-phase and out-of-phase defect mode shapes are presented. However, it should be emphasized that the incorporation of the splitting of defect bands into PEH has been untouched yet.

The objective of this chapter is thus to newly propose a two-dimensional PnC-based PEH system with double defects arranged apart from each other. When designing a PnC-based PEH system with double defects, the following design issues should be addressed: (1) relative position between the double defects in the mechanical domain and (2) electrical connection between the double defects in the electrical domain. Therefore, this chapter aims at physically interpreting how the relative distance and electrical circuit configuration affect output performances of energy localization and harvesting.

In the part of effects of the electrical circuit connection, the distance and arranging direction between double defects are considered. In terms of the effects of the distance with a given arranging direction and electrical circuit connection, the initially introduced defect is fixed at the 4th layer while the location of the additional defect is changed from 7th to 10th along the *x*-direction (i.e., the direction of propagating waves). As the distance between the double defects becomes further, the difference between the peak frequencies becomes smaller while the mechanical and electrical output performances at the peak frequencies are slightly increased. In addition, if the double defects are arranged significantly far, they are decoupled and behave as an independent single defect. In terms of the effects of the arranging direction with a given electrical circuit connection, the location of the additional defect is changed along the circumferential direction (direction effect) with the initially introduced defect as the origin. Four scenarios are organized as (4, 7-⓪), (4, 6-①), (4, 5-②), and (4, 4-③). Even though the distance between the fixed defect in the 4th layer and the defect in (4, 6-①) or (4, 5-②) is less than the distance between the fixed defect in the 4th layer and the defect in (4, 7-⓪), the decoupling between the double defects occur due to weakened coupling characteristics along the diagonal axis. When the additional defect is arranged in (4, 4-③) which is perpendicular to the direction of incident waves, it can be found that vertically arranged double defects cannot oscillate with the out-of-phase defect mode shape due to in-phase normal incident waves.

In the part of effects of the electrical circuit connection with a given distance and arranging direction, five connection types (i.e., Independent, Series Types A and B, and Parallel Types C and D) are under consideration. It is found that the

frequencies of the split defect bands are slightly increased in both Independent and Series connections due to piezoelectric effects, while only one frequency of the split defect bands is slightly increased in the Parallel connection, due to voltage cancellation. Furthermore, performance analysis under an open-circuit condition shows no peak for the output voltage occurs at some resonance frequencies due to the direction of the current sources (for the Series connection) and due to voltage cancellation (for the Parallel connections), even though displacement amplification at those frequencies is observed. The maximum output electric power density in the Series and Parallel connections is found to be simply the sum of the individual maximum output electric power density generated by PEH Devices 1 and 2 in the Independent connection at power-optimal external electrical resistances. Here, compared with an Independent connection, the power-optimal external electrical resistance is doubled at each resonance frequency in Series connections, while it is halved in Parallel connections.

The two-fold novel aspects of this study include (1) incorporating the splitting of defect bands into PEH which enables the enhancement of the output electric power at both frequencies of split defect bands; and (2) thoroughly examining the effects of the relative position and electric circuit connection on the PnC-based PEH system. We believe that this study provides design and selection guidelines of the relative position and electrical circuit for the best use of double defects modes of a two-dimensional PnC to improve PEH performance under elastic waves.

It should be noted that a PnC-based PEH with double defects, as examined in the current work, might have limitations when operating under a random excitation environment from the following two viewpoints: (1) a degree of the defect band split

can be adjusted only in a discrete manner and (2) the output performance of the PEH devices attached to the defects rapidly decreases between two resonance frequencies. Therefore, to address these issues, further investigation of PnC designs to achieve broadband energy localization and harvesting will be studied in next chapter.

Sections of this chapter have been published or submitted as the following journal articles:

1) **Soo-Ho Jo**, Heonjun Yoon, Yong Chang Shin, Miso Kim, and Byeng D. Youn, "Elastic Wave Localization and Harvesting Using Double Defect Modes of a Phononic Crystal," *Journal of Applied Physics*, Vol. 127, pp. 164901, 2020.
2) **Soo-Ho Jo**, Yong Chang Shin, Wonjae Choi, Heonjun Yoon, Miso Kim, and Byeng D. Youn, "Experimentally Validated Defect-band Splitting in a Phononic Crystal with Double Defects under Elastic Wave," *Advanced Science*, Submitted, 2021.

Chapter 4

L-Shape Arranged Triple Defects for Broadband Piezoelectric Energy Harvesting – Superposition of Phononic Crystals with Single and Double Defects

Chapter 3 was dedicated to exploring the two-dimensional PnC-based PEH system that leverages double defect modes from the viewpoint of the relative position electrical circuit configuration between the double defects. It is needed to summarize the advantages and disadvantages of the PnC-based PEH systems with a single defect and with double defects. Here, the main concern of the PnC-based PEH system with double defects is the case when the double defects are arranged along the direction of propagating waves. In the case of the single defect, the PEH system enables high output electric power at a certain defect band frequencies; however, the harvestable bandwidth is narrow. On the other hand, in the case of the double defects, the PEH system achieves relatively wider (almost doubled) harvestable bandwidth with the help of the splitting of defect bands while the output electric power itself is lowered at both split defect band frequencies. Furthermore, it is worth pointing out that the

output performance of the PEH devices attached to the defects rapidly decreases between two resonance frequencies, which is an analogy to anti-resonance in a dynamic vibration absorber system. Here, one can pose the following question of interest: how can we combine both systems to make use of the advantages of each system?

With this motivation, the objective of this chapter is to newly propose a new design concept of superposing PnC-based PEH systems with a single defect and with double defects for broadband energy localization and harvesting purposes. The proposed idea is a PnC with L-shape arranged triple defects. In Chapter 3, it was confirmed that defects are decoupled when the distance between defects is considerably far. If a single defect and double defects are separated by a large distance within a PnC, they behave as an independent set of defects. It implies that a PnC with a single defect and a PnC with double defects are superimposed to one PnC-based system. Recalling the results of arranging direction effects presented in Chapter 3, it is the most suitable to introduce double defects along the direction of propagating waves from the perspective of the bandwidth. Referring to the results of defect location effects presented in Chapter 2, it is the most desirable to introduce the single defect and one of the double defects close to excitation sources along the perpendicular direction of propagating waves from the perspective of enhancing output electric power. Therefore, a PnC with L-shape arranged triple defect can achieve broadband energy localization and harvesting with the maximum output electric power. To the best of the authors' knowledge, the unique contributions of this study are two-fold. First, this is the first attempt to propose a new design concept of a PnC with L-shape arranged triple defects under elastic waves. Second, the PnC

with L-shape arranged triple defects enables to broaden the bandwidth for elastic wave localization and harvesting by complementing disadvantages of each of single and double defects.

The remainder of Chapter 4 is organized as follows. Section 4.1 presents a system description of a two-dimensional PnC with L-shape arranged triple defects. Energy localization and harvesting analyses are performed in Section 4.2. Finally, the conclusions of this work are outlined in Section 4.3.

4.1 System Description of a Phononic Crystal with L-Shape Arranged Triple Defects

The PnC-based PEH system considered in this chapter, as shown in Figure 6-1 (a), consists of a host aluminum plate and a PnC with L-shape arranged triple defects to which the circular, disc-type PEH device (PZT-4D) is attached. Material properties and geometric dimensions of the unit cell and PEH devices are the same with those presented in Chapter 3. To avoid the unwanted effects induced by a lack of the periodicity near the defects, a large supercell size (17×17) of the PnC is taken into account.

In Figure 4-1, triple defects are introduced by attaching a circular disc-type PZT-4D as a PEH device without puncturing three unit cells of the 17×17 array PnC. In this chapter, (i, j) denotes a certain location of a defect introduced in the i-th supercell along the x-direction and in the j-th unit cell along the y-direction. Each of triple defects are introduced in (4, 13), (4, 5), and (9, 5). Each defect is called as

“Defect (4, 13)”, “Defect (4, 5)”, and “Defect (9, 5)”, respectively. Each PEH device attached to “Defect (4, 13)”, “Defect (4, 5)”, and “Defect (9, 5)” is called as “PEH Device (4, 13)”, “PEH Device (4, 5)”, and “PEH Device (9, 5), respectively. Table 3-1 summarizes the geometric information of the unit cell and PEH device. Mechanical properties of the aluminum are listed in Table 2-2. Table 2-3 summarizes the mechanical and electrical properties of PZT-4D. Here, the loss factor is set to be 0.0001 for the analysis of the PnC- based PEH systems.

In Chapter 3, when the double defects were arranged along the direction of propagating waves, it was confirmed that coupling occurred until there were four unit cells between double defects and decoupling took place thereafter. Even though the trends were quite different in the case of vertically arranged double defects, it can be inferred that decoupling can also occur if more than four unit cells are deployed between double defects which are arranged along the direction perpendicular to incident waves. Since there are seven unit cells between Defect (4, 5) and Defect (4, 13), these defects will be decoupled and the Defect (4, 5) will be exhibit a single peak frequency in output response FRFs as an independent single defect. On the other hand, since there are four unit cells between Defect (4, 5) and Defect (9, 5), these defects will be coupled and it can be inferred that both defects will exhibit two peak frequencies in output response FRFs. Referring to Chapter 2, it was confirmed that the 4th layer along the x-direction (propagating direction of incident waves) showed the highest displacement amplification performance in the preliminary studies. Therefore, Defect (4, 5) and Defect (4, 13) are introduced in the 4th layer along the x-direction to maximize the harvestable electric power. Therefore, with this physical interpretation, the proposed PnC with L-shape arranged triple

defects is a superposition of a PnC-based PEH system with a single defect and that with double defects while it can realize high dense PEH from the perspective of the defect location effects.

To investigate the PEH performance under unidirectional plane waves, we applied two boundary conditions at the boundaries of the host plate: (1) a perfectly matched layer as an absorbing boundary condition in the *x*-direction (propagating direction of incident waves) and (2) a periodic boundary condition guaranteeing the infinite domain in the *y*-direction (perpendicular direction to incident waves). The perfectly matched layer and periodic boundary condition are colored in green and sky-blue in Figure 4-1, respectively. In the *z*-direction, traction-free condition is employed. The incident flexural A_0 Lamb waves were excited by transversely loading the cross-section of the host plate with a constant amplitude of 20 nm, regardless of the frequency. In general, since the elastic wave propagates at an amplitude of several tens of nm in experiments, the amplitude of 20 nm is a reasonable value [66]. To sufficiently excite the plane wave, the distance between the excitation source and the front row of the PnC was set to 100 mm, which is approximately six times the wavelength of the A_0 Lamb wave near 60 kHz.

It should be noted that the a meshing scheme of the PnC with decoupled double defects is that (1) the mesh elements of the whole structure are composed of hexahedrons and (2) the maximum mesh size is set to be one-tenth of the wavelength of the excited A_0 Lamb wave at 60 kHz. In terms of electroelastic coupling, three modules, including solid mechanics, electrostatics, and electrical circuit modules, are used. A detailed description is available in Chapter 2

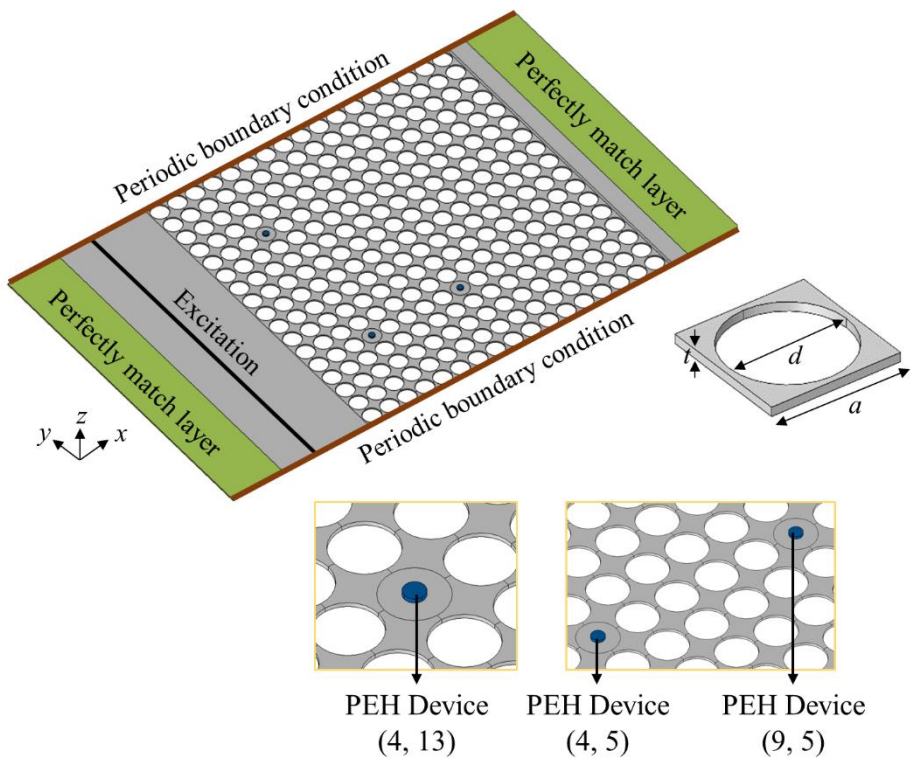

Figure 4-1 A schematic view of the two-dimensional PnC-based PEH system with L-shape arranged triple defects: periodic boundary condition and perfectly matched layers as the boundary conditions and transversely polarized A_0 Lamb wave as the excitation condition.

4.2 Energy Localization and Harvesting Analyses for the Phononic Crystal with L-shape Arranged Triple Defects

This section aims to perform energy localization and harvesting analyses for the PnC with L-shape arranged triple defects. To emphasize the superposition characteristics of the proposed L-shape arranged triple defects, output performances of PnCs with a single defect and with double defects are also investigated. Section 4.2.1 presents the maximum output voltage generated by each PEH device under the external electrical resistance of 100 MΩ (open-circuit). Section 4.2.2 deals with the maximum output electric power that corresponds to optimal external electrical resistance.

4.2.1 The Maximum Output Voltage under the Open-circuit Condition

Under the external electrical resistance of 100 MΩ (open-circuit), Figure 4-2 (a) presents the operating deflection shape (*z*-directional displacement field) at the peak frequency (i.e., 60.12 kHz) of PEH Device (4, 13). Figure 4-2 (b) and Figure 4-2 (c) depict the operating deflection shapes (z-directional displacement fields) at the peak frequencies (i.e., 60 kHz and 60.03 kHz) of PEH Device (4, 5) an PEH Device (4, 9), respectively. Here, sinusoidal excitation (A_0 Lamb wave) of 20 nm is loaded at the left end of the host plate. In each figure, the enlarged views in the vicinity of Defect (4, 13) (expressed as (1) in each figure) and Defect (4, 5) and Defect (9, 5) (expressed as (2) in each figure) are shown.

Here, it can be found that only Defect (4, 13) oscillate with the monopole-like defect mode at 60.12 kHz (Figure 4-2 (a)). On the other hand, Defect (4, 5) and Defect (9, 5) oscillate with in-phase and out-of-phase monopole-like defect mode

shapes at 60 kHz (Figure 4-2 (b)) and 60.03 kHz (Figure 4-2 (c)), respectively.

Figure 4-3 shows the output voltage FRFs, ranging from 59.9 kHz to 60.1 kHz under the external electrical resistance of 100 MΩ (open-circuit). For the PnC with L-shape arranged triple defects, lines with solid-black, solid-blue, and dashed-red indicate the output performances of PEH obtained from PEH Device (4, 13), PEH Device (4, 5), and PEH Device (9, 5), respectively. Dots with black-squares indicate the output performances of PEH obtained for the PnC with the single defect. Dots with blue-crosses and red-triangles indicate the output performances of PEH obtained for the PnC with the double defects.

There are two points of importance that should be emphasized. First, the output responses obtained from the PnC-based PEH system with the single defect are almost similar to those obtained from the PEH Device (4, 13). In addition, the output responses obtained from the PnC-based PEH system with the double defects are almost similar to those obtained from the PEH Device (4, 5) and PEH Device (9, 5). Second, even though there are triple defects in the proposed PEH system, it can be confirmed that only one peak exists in the output voltage FRFs obtained from PEH Device (4, 13). Moreover, only one peaks exist in the output voltage FRFs obtained from PEH Device (4, 5) and PEH Device (9, 5). Each peak is the same as the peak obtained in the PEH system with single or double defects. As expected, these results demonstrate the validity that the proposed PnC with L-shape arranged triple defects is a superposition of a PnC-based PEH system with a single defect and that with double defects.

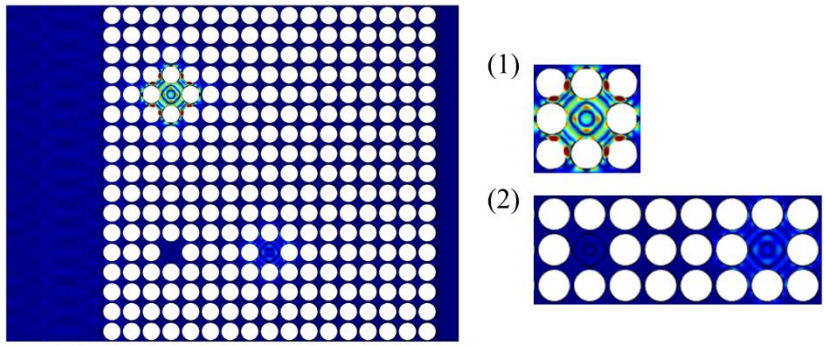

`(a)

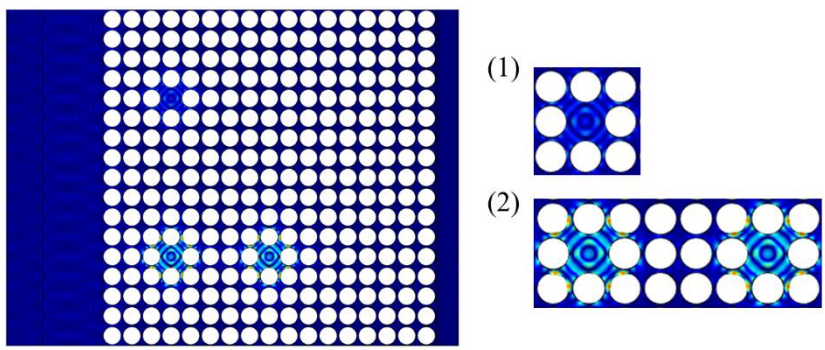

(b)

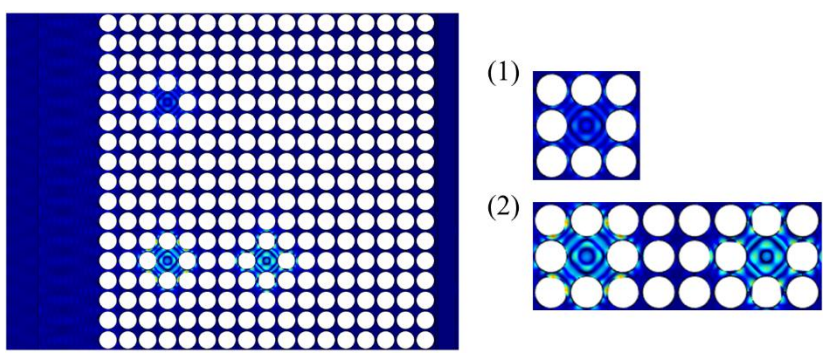

(c)

Figure 4-2 Operating deflection shapes (*z*-directional displacement fields) under the external electrical resistance of 100 MΩ (open-circuit) at (a) 60.01 kHz, (b) 60 kHz, and (c) 60.03 kHz.

Under an assumption that AC-DC converters (alternating current-to-direct current converters) are connected to each PEH device, a bridge rectifier with a capacitor [22, 31] in AC-DC converters can change the sinusoidal AC voltage signal into DC voltage signals. Then, the output voltage generated by each PEH device in the case of triple defects can be summed, which is indicated by the lines with green in Figure 4-3.

It was mentioned that -in the case of the single defect- the PEH system enables high output electric power at a certain defect band frequencies; however, the harvestable bandwidth is narrow. On the other hand, in the case of the double defects, the PEH system achieves relatively wider (almost doubled) harvestable bandwidth with the help of the splitting of defect bands while the output electric power itself is

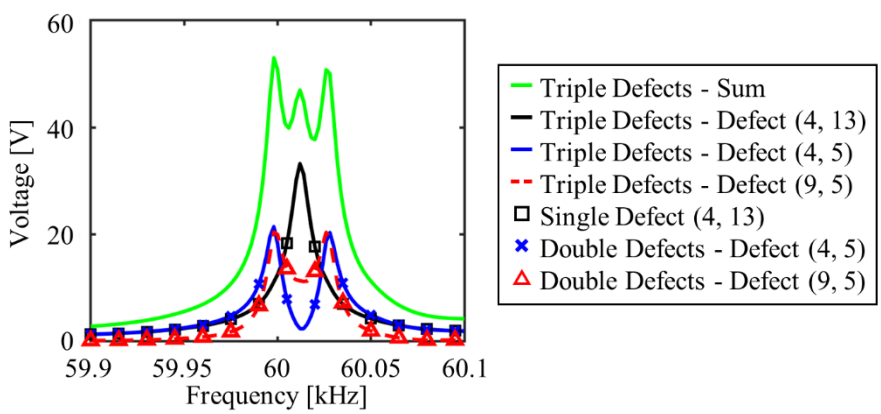

Figure 4-3 Output voltage FRFs for a PnC with L-shape arranged triple defects, a PnC with a single defect, and a PnC with double defects under the external electrical resistance of 100 MΩ (open-circuit).

lowered at both split defect band frequencies. In Figure 4-3, since the single peak of PEH Device (4, 13) is located between two peaks of PEH Device (4, 5) and PEH Device (9, 5), the existence of PEH Device (4, 13) compensates for the weakness of the PnC-based PEH system with double defects that the output performance of PEH dramatically decreases between the two peaks. In addition, the existence of PEH Device (4, 5) and PEH Device (9, 5) compensates for the weakness of the PnC-based PEH system with the single defect that the output performance of PEH is harvested in narrowband near a certain frequency. Therefore, broadband PEH can be realized with the concept of superposing two systems.

4.2.2 The Maximum Output Electric Power under the Optimal External Electrical Resistance

As demonstrated in Chapter 2, since the behavior of the output electric power with changing the external electrical resistance is non-monotonic, there exists the optimal value of the external electrical resistance at which the maximum output electric power can be achieved. At the peak frequency under the open-circuit condition, the optimal external electrical resistance can be found by sweeping it. As demonstrated in Section 4.2.1, since the proposed design is a superposition of two PnCs, the optimal external electrical resistance of each defect is independently found. In detail, for Defect (4, 13), the external electrical resistance is swept at the peak frequency of 60.01 kHz and the optimal external electrical resistance to maximize the output electric power is found as 91.2 kΩ. For Defect (4, 5) and Defect (9, 5), the external electrical resistances of each defect are swept at peak frequencies of 60 kHz and 60.03 kHz. The optimal external electrical resistances are found as 75.9 kΩ and 120.2

kΩ for Defect (4, 5) and Defect (9, 5), respectively, at the first peak frequency of 60 kHz; those are found as 45.7 kΩ and 125.9 kΩ for Defect (4, 5) and Defect (9, 5), respectively, at the second peak frequency of 60.03 kHz. The former one is denoted Case I and the latter one is denoted as Case II. Here, it should be noted that the maximum mechanical power of guided bending waves that transferred to the host medium by excitation is calculated as near 5.78 mW at the frequency of 60 kHz.

Figure 4-4 depicts the calculated output voltage and electric power FRFs for the PnC with L-shape arranged triple defects. Figure 4-4 (a) and Figure 4-4 (b) present the results of Case I. Figure 4-4 (c) and Figure 4-4 (d) present the results of Case II. Since the external electrical resistances are slightly different, the effective stiffness of the PEH devices is also different. It leads to the difference between electrical responses for Case I and Case II. However, it seems that the effects of the external electrical resistances on the bandwidth, the maximum electric power, and corresponding voltage are less sensitive. Therefore, any set of external electrical resistances can be selected. Compared with the cases of single or double defects, it should be emphasized that the proposed L-shape arranged triple defects for both cases enable to successfully harvest much more output performances of PEH.

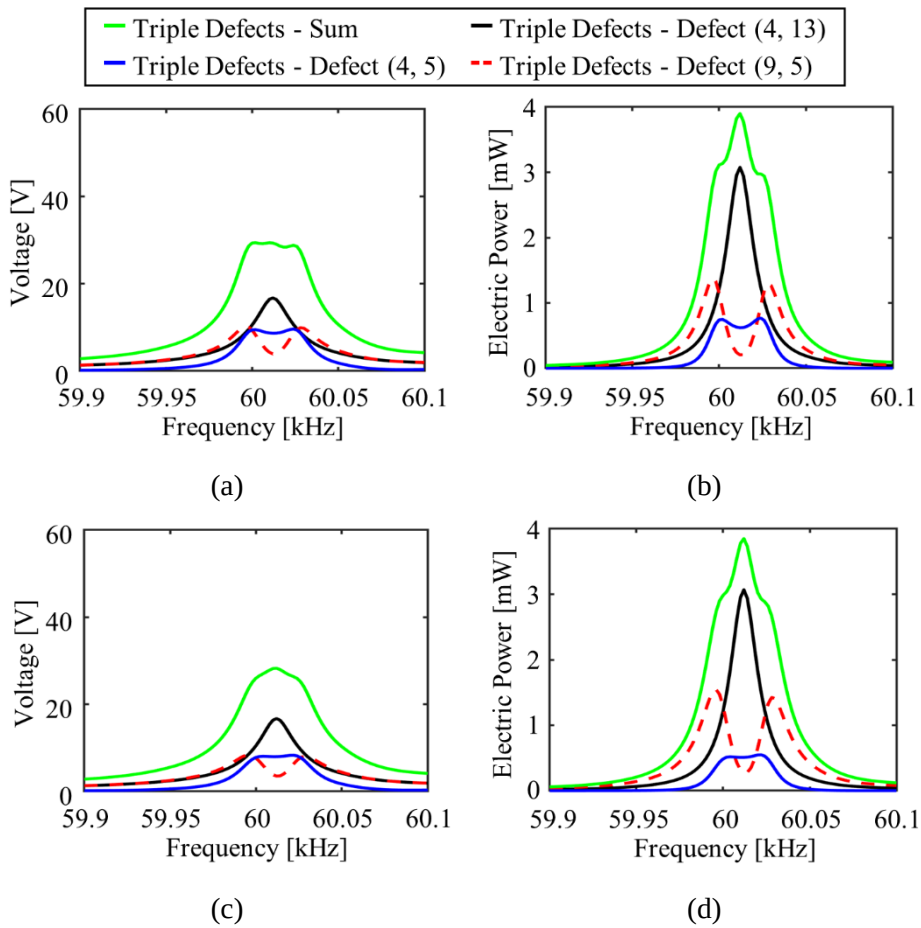

Figure 4-4 Output voltage and electric power FRFs for the PnC with L-shape arranged triple defects across optimal external electrical resistances: (a) output voltage and (b) electric power in Case I, and (c) output voltage and (d) electric power in Case II.

4.3 Summary and Discussion

In the case of the single defect, the PEH system enables high output electric power at a certain defect band frequencies; however, the harvestable bandwidth is narrow. On the other hand, in the case of the double defects, the PEH system achieves relatively wider (almost doubled) harvestable bandwidth with the help of the splitting of defect bands while the output electric power itself is lowered at both split defect band frequencies. Furthermore, it is worth pointing out that the output performance of the PEH devices attached to the defects rapidly decreases between two resonance frequencies, which is an analogy to anti-resonance in a dynamic vibration absorber system.

By combining both systems to make use of the advantages of each system, the objective of this chapter is to newly propose a new design concept of superposing PnC-based PEH systems with a single defect and with double defects for broadband energy localization and harvesting purposes. For the proposed design that consists of a circular hole-type PnC, since there were seven unit cells between Defect (4, 5) and Defect (4, 13), these defects were decoupled and the Defect (4, 5) could exhibit a single peak frequency in output response FRFs as an independent single defect. On the other hand, since there were four unit cells between Defect (4, 5) and Defect (9, 5), these defects were coupled and both defects exhibited two peak frequencies in output response FRFs. Therefore, a PnC with a single defect and a PnC with double defects was superimposed to one PnC-based system with L-shape arranged triple defects. By complementing disadvantages of each of single and double defects, a PnC with L-shape arranged triple defect can achieve broadband energy localization and harvesting with the maximum output electric power.

The unique contributions of this study are two-fold. First, this is the first attempt to propose a new design concept of a PnC with L-shape arranged triple defects under elastic waves. Second, the PnC with L-shape arranged triple defects enables to broaden the bandwidth for elastic wave localization and harvesting by complementing disadvantages of each of single and double defects.

Sections of this chapter have been published or submitted as the following journal articles:

1) **Soo-Ho Jo**, Yong Chang Shin, Wonjae Choi, Heonjun Yoon, Byeng D. Youn, and Miso Kim, "Superposition of Phononic Crystals with Single and Double Defects for Broadband Piezoelectric Energy Harvesting," *Nano Energy*, Submitted, 2021.

Chapter 5

A Graded Phononic Crystal with Decoupled Double Defects for Broadband Piezoelectric Energy Harvesting

Chapter 3 was dedicated to exploring the two-dimensional PnC-based PEH system that leverages double defect modes from the viewpoint of the relative position electrical circuit configuration between the double defects. Here, it is worth pointing out that since the distance between double defects can be changed just as much as an integer multiple of the lattice, a degree of the defect band split can be adjusted only in a discrete manner. This implies that it is restrictive to design the defect band frequencies, as well as bandwidth, for energy localization. If double defects are too closely arranged to each other, the coupling between them gets strong, and then the degree of the defect band split increases. In this case, the output performance of the PEH devices attached to the defects rapidly decreases between two resonance frequencies, which is an analogy to anti-resonance in a dynamic vibration absorber system. On the other hand, if double defects are arranged far away from each other, the defect band split does not occur because the coupling between them is weakened

or nearly zero. In this study, only one defect band exhibits, which corresponds to the single defect. This is traced to the fact that all unit cells of a PnC are uniform in terms of material properties and geometry.

With this motivation, the objective of this chapter is to newly propose a new design concept of a graded PnC with decoupled double defects for broadband energy localization and harvesting purposes. A graded PnC refers to a PnC that is designed by varying one or more design variables of their lattices [118, 119]. In this chapter, a circular stub type unit cell is under consideration and a graded PnC is built by varying the height of the circular stub along a certain direction. If the double defects are introduced to be sufficiently far from each other, any coupling effect between them can be eliminated; each of the defects behaves as an independent single defect. Then, the defect band frequency is determined based on the mass and stiffness of the lattices surrounding the relevant defect. This allows the graded PnC to separately design defect band frequencies corresponding to each of the double defects in terms of their locations. It leads to localizing elastic waves in the vicinity of each defect at the designed different defect band frequencies. Therefore, the graded PnC can successfully achieve the broadband energy localization. To the best of the authors' knowledge, the unique contributions of this study are two-fold. First, this is the first attempt to propose a new design concept of a graded PnC with decoupled double defects under elastic waves. Second, the graded PnC with the decoupled double defects enables to broaden the bandwidth for elastic wave localization and harvesting by separately designing defect band frequencies of each defect.

The remainder of Chapter 5 is organized as follows. Section 5.1 presents a configuration and band gap results of a graded PnC without defects. Section 5.2

shows the formation of defect bands within the band gap and covers the selection of defect mod shapes in terms of electroelastic coupling for a graded PnC with a single defect. In addition, to highlight the graded characteristics, a variation of defect band frequencies with respect to the defect location is presented. For a graded PnC with decoupled double defects, Section 5.3 aims to explain the results of defect bands, as well as defect mode shapes, and investigate the merits of the graded characteristics for PEH purposes from perspective of decoupling and graded characteristics. For the graded PnC-based PEH system with the decoupled double defects, energy localization and harvesting analyses are performed in Section 5.4. Finally, the conclusions of this work are outlined in Section 5.5.

5.1 Band Gap Analysis of a Graded Phononic Crystal without Defects

Figure 5-1 (a) and 5-1 (b) depict schematic and side views of a unit cell and a supercell of a graded PnC under consideration, respectively. The supercell is composed of a 14×1 array of unit cells; the unit cell consists of a square lattice with an aluminum circular stub that is deposited on a top surface of a thin aluminum plate. The unit cell has four geometric variables including the lattice constant a and thickness t of the plate; and the diameter d and height h of the circular stub. The graded PnC is built by varying only the height of the circular stubs. h_N stands for the height of the circular stub in the N-th unit cell along the y-direction. N ranges from zero to 14. The lowest circular stub (h_1) is 13.00 mm and the height gradually increases in the y-direction with a uniform difference of 0.15 mm; that is, the highest circular stub (h_{14}) is 14.95 mm. In this chapter, a unit cell having the lowest height

of the stub is regarded as the first unit cell. Similarly, a unit cell having the highest height of the stub is called the last unit cell. The height h_N can be expressed as:

$$h_N = 13.00\,\text{mm} + (N-1) \times 0.15\,\text{mm}. \tag{5.1}$$

Since this chapter is a kind of a follow-up to the work presented in Chapter 2, the remaining geometric dimensions are equal to the values in Table 2-1. The lattice constant (*a*) and thickness (*t*) of the square aluminum plate, and diameter (*d*) of the circular stub are equal to 27 mm, 2 mm, and 22 mm, respectively. The material properties of the aluminum are presented in Table 2-2.

To calculate bands structures of the supercell, the supercell calculation method was used. It should be noted that the supercell itself is a rectangle rather than a square. It is known that the reciprocal wave vector **k** belongs to the borderline of the 1st irreducible rectangular Brillouin zone (M→Γ→X→M→Y→Γ), as shown in Figure 2-2 [99, 100]. Here, the *x*- and *y*-directional components of the reciprocal wave vectors **k** range from 0 to π/a and from 0 to $\pi/14a$, respectively.

The calculated band structures of the supercell are shown in Figure 5-2, ranging from 40 kHz to 80 kHz. It can be thus confirmed that the supercell under consideration possesses the full band gap ranging from 50.79 kHz to 68.94 kHz. Please note that the full band gap range depends on the geometric dimensions and material properties of the unit cell [120, 121]; the geometric dimensions of the supercell make the calculated full band gap open around 55 kHz.

Previous studies using a concept of graded PnCs can be classified into the following two categories. The first topic is a gradient-index PnC, in which the wave

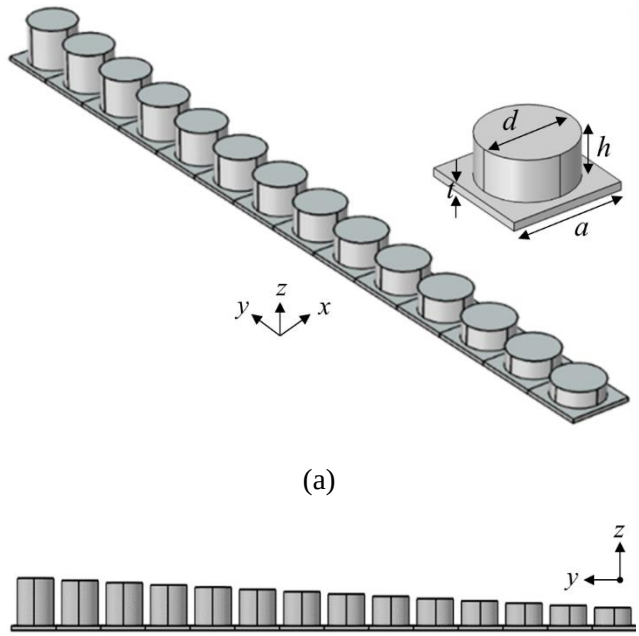

(a)

(b)

Figure 5-1 Configuration of the supercell of the graded PnC consisting of 14 unit cells: (a) a schematic view and (b) a side view.

propagation velocity (group velocity) differs in each unit cell. The main concern of this topic is to focus the normal incident waves toward the desired point via extraordinary refraction. The other topic aims to widen the range of band gaps. A graded PnC can be thought of as overlapping structures in which each unit cell is periodically and uniformly arranged. Since each structure would have a different range of band gaps, a union of these band gaps can be a band gap of the graded PnC. This study is in a similar context to the latter topic, and the explanation of a graded PnC with single or double defects is presented in the following sections.

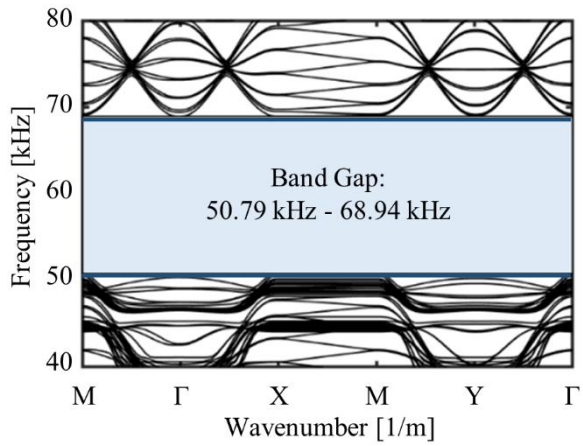

Figure 5-2 Calculated dispersion curves for the graded PnC without defects in the 1st irreducible Brillouin zone (M→Γ→X→M→Y→ Γ).

5.2 Defect Band Analysis of a Graded Phononic Crystal with a Single Defect

As presented in previous section, defect bands can be calculated from the supercell calculation. To neglect the coupling effects of defects between adjacent supercells, which are attributed to the periodic repetition of supercells with defects, as determined by Floquet-Bloch theorem [69, 70, 75, 122], the size of the graded PnC needs to be large. As mentioned in Chapter 2, a peak frequency in harmonic analysis converges to a defect band frequency when a supercell size increases. Therefore, we performed the preliminary studies while gradually increasing the supercell size from three layers to eight layers along the *x*-direction, it was confirmed that the peak frequency and the defect band frequency are almost the same when seven supercells were arranged. In addition, energy localization and harvesting performance highly

depends on the defect location for the fixed supercell size. Here, the effects of the defect location have two perspectives. First, for the unit cells at a given location along the *y*-direction, the defect location can be changed along the *x*-direction. Second, for the unit cells at a given location along the *x*-direction, the defect location can be changed along the *y*-direction. The former issue is related to the work in Chapter 3 and the latter issue is traced to the graded characteristics. In preliminary studies, it was confirmed that the 3rd layer along the *x*-direction showed the highest displacement amplification performance, regardless of the defect location along the *y*-direction. Thereby, the 3rd layer is selected as the target defect location along the *x*-direction. For the defect location along the *y*-direction, it was found that the energy localization performance is less sensitive.

Finally, a graded PnC with a single defect is built by arranging seven supercells the *x*-direction, while eliminating the 4th circular stub along the *y*-direction in the 3rd supercell. Here and hereafter, (*i*, *j*) denotes a certain location of a defect introduced in the *i*-th supercell along the *x*-direction and in the *j*-th unit cell along the *y*-direction. Then, a circular PEH device (PZT-5H) is attached to the defect, as shown in Figure 5-3 (a). A top (bottom) electrode of whose thickness is negligible is assumed to be connected to terminal (ground) on the top (bottom) surface of the piezoelectric patch. The poling direction of the piezoelectric patch is the thickness direction. The diameter and thickness of the PEH device are equal to 10 mm and 0.2667 mm, respectively. Mechanical and electrical properties of PZT-5H are summarized in Table B-2. It can be found that the thickness of the PEH device is much thinner than that in Chapter 2. Since this is the first attempt to incorporate a design of a graded PnC with decoupled double defects into PEH, it is needed to more

focus on the mechanical characteristics of the graded PnC, rather than the electroelastically coupled domain. Therefore, to less consider backward coupling effects in equation of motions presented in Equations (3.13) and (3.14), the thickness is set to be thinner.

Figure 5-3 shows that five defect bands are created within the full band gap, which correspond to the frequencies of 53.63 kHz (A), 55.17 kHz (B), 63.24 kHz (C), 66.62 kHz (D), and 67.47 kHz (E), respectively, under the external electrical resistance of 0 Ω (short-circuit). In Chapters 2 and 3, the defect mode shapes that correspond to several defect bands in the band gap have been investigated in the case of the two-dimensional uniform PnCs. These phenomena or considerations are expected to appear the same for the proposed graded PnC; however, it is still necessary to thoroughly examine both defect mode shapes and electroelastic coupling effects on the defect bands in order to insisting the validity of the effectiveness of the graded PnC.

Figure 5-4 shows the defect mode shapes (*z*-directional displacement fields) at each of the five defect band frequencies that correspond to the results in Figure 5-3. An enlarged view near the defect is also presented in each figure. The white circles indicate the top surfaces of the circular stubs. The main concern of this study is A_0 Lamb wave, which is polarized in the transverse direction. When selecting a target defect band frequency, we need to recall the concept of voltage cancellation. Since the other defect mode shapes, except for Figure 5-4 (b), possess strain nodal lines within the piezoelectric patch attached to the defect, the defect band frequency of 55.17 kHz (highlighted with sky-blue in Figure 5-3 (b)) that corresponds to the monopole-like defect mode shape would be the most desirable. When the graded

PnC with the single defect, presented in Figure 5-3 (a), is exposed to A_0 Lamb waves excited near 55.17 kHz, the elastic waves can be localized inside and in the vicinity of the defect while showing the monopole-like defect mode shape.

When switching the electrical boundary condition from external electrical resistances of 0 Ω (short-circuit) to 100 MΩ (open-circuit), Table 5-1 summarizes the results of calculated defect band frequencies when the reciprocal wave vector **k** is equal to (0, 0). Except for the monopole-like defect mode shape (B), the shift of defect band frequencies is negligible due to the effects of voltage cancellation. The defect band frequency corresponding to the monopole-like defect mode shape increases from 55.17 kHz to 55.74 kHz, as the external electrical resistance changes from of 0 Ω (short-circuit) to 100 MΩ (open-circuit). Through this work, it can be confirmed that the investigation of defect mode behaviors and electroelastic coupling effects on the defect bands is still valid for the graded PnC.

For a uniform PnC, if its defect configuration (i.e., geometric dimensions and material properties) and supercell size are fixed, the defect band frequencies in supercell calculation would be independent of the defect location, because the mass and stiffness of the lattices surrounding the defect remain unchanged. This interpretation can be explained by the viewpoint of the formation of defect bands, demonstrated in Appendix A. Due to the evanescent wave properties in a band gap, the defect behaves as a mechanical resonator while unit cells far from the defect act as fixed-like boundary conditions. The further away from the defect, the stronger the fixed-like boundary conditions. In this case, the mass and stiffness of unit cells should be involved in the values of defect band frequencies. To justify this physical interpretation, Figures 5-5 (a) and 5-5 (b) shows the trends of the defect band

frequency that corresponds to the monopole-like defect mode shape for a uniform PnC which height of circular stubs is 13.45mm with respect to the defect location under external electrical resistances of 0 Ω (short-circuit) and 100 MΩ (open-circuit), respectively. It can be observed that the defect band frequency are constant regardless of the defect location at 55.17 kHz and 55.74 kHz regardless of the defect location.

For the proposed graded PnC, however, since the heights of circular stubs deployed in one unit cell are gradually varied in the *y*-direction, the defect band frequencies can be changed with the defect location, while keeping a degree of the height variation. Alternatively, the defect band frequencies can also be designed by changing a degree of the height variation, while maintaining the location of the defect.

Figures 5-5 (a) and 5-5 (b) depict the effects of the defect location on the defect band frequency corresponding to the monopole-like defect mode under external electrical resistances of 0 Ω (short-circuit) and 100 MΩ (open-circuit), respectively. In Figure 5-5, the *x*-axis represents the *y*-directional defect location in the graded PnC shown in Figure 5-3 (a). It can be found that the defect band frequency of the graded PnC varies with the defect location. The defect band frequency tends to decrease as the height of circular stubs becomes increasing. In addition, even though the height linearly increases in terms of the defect location, nonlinear trends somewhat exhibit near minimum and maximum heights under both external electrical resistances of 0 Ω (short-circuit) and 100 MΩ (open-circuit). These nonlinear trends would be attributed to the sudden change of the height under periodic boundary conditions in supercell calculation. If the height of circular stubs

varies smoothly, defect band frequencies for the graded PnC might vary smoothly in terms of the defect location. To demonstrate this physical interpretation, another example of a graded PnC with a single defect is provided in Figure 5-6.

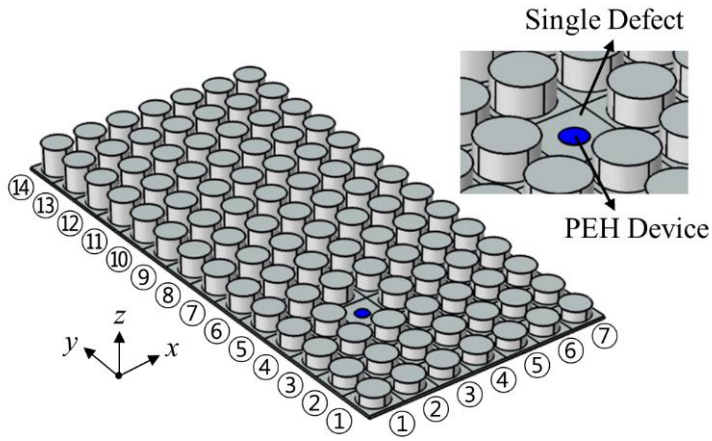

(a)

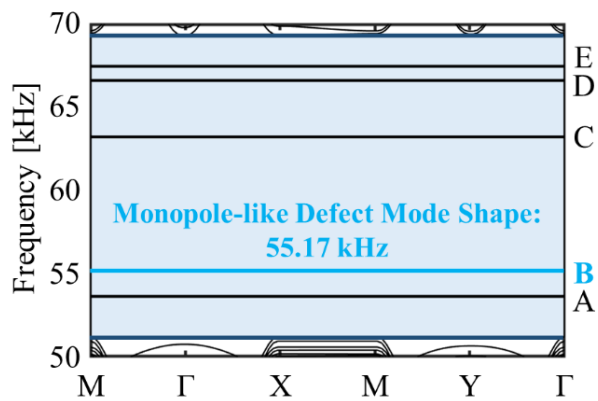

(b)

Figure 5-3 Defect band analysis for a graded PnC with a single defect imposed in (3, 4) under the external electrical resistance 0 Ω (short-circuit): (a) configuration of the graded PnC and (b) formation of five defect bands, labeled from A to E, within the full band gap ranging from 50.79 to 68.94 kHz.

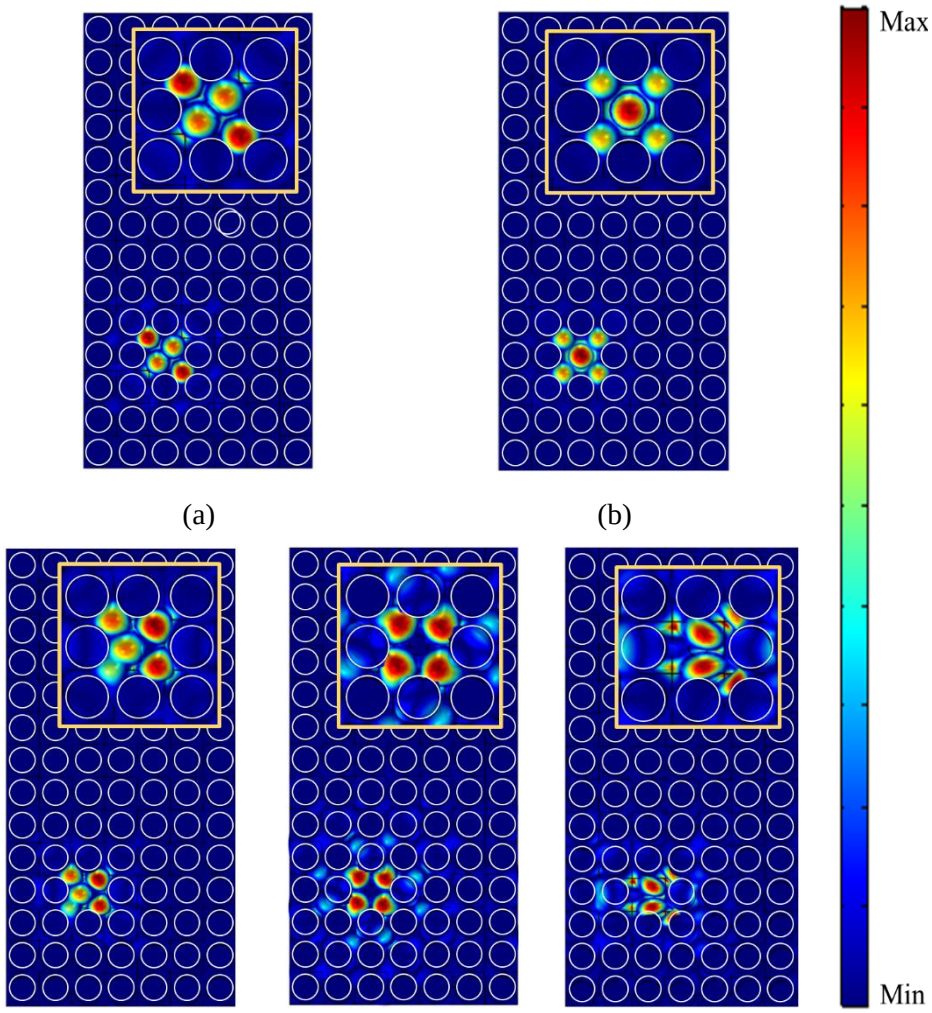

Figure 5-4 Various defect mode shapes (*z*-directional displacement fields) of a graded PnC with a single defect under the external electrical resistance of 0 Ω (short-circuit): (a) 53.63 kHz (A), (b) 55.17 kHz (B), (c) 63.24 kHz (C), (d) 66.62 kHz (D), and (e) 67.47 kHz (E).

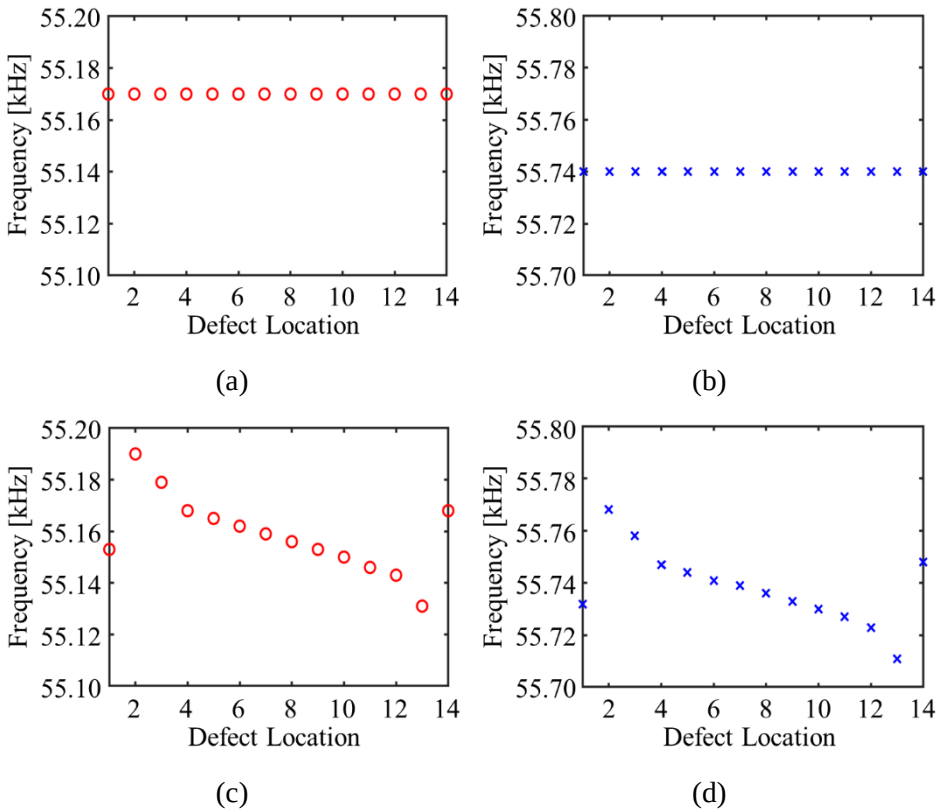

Figure 5-5 Trends of the defect band frequency that correspond to the monopole-like defect mode shape with respect to the defect location along the *y*-direction for the uniform PnC ((a) and (b)) and graded PnC ((c) and (d)) under external electrical resistances of 0 Ω (short-circuit, (a) and (c)) and 100 MΩ (open-circuit, (b) and (d)).

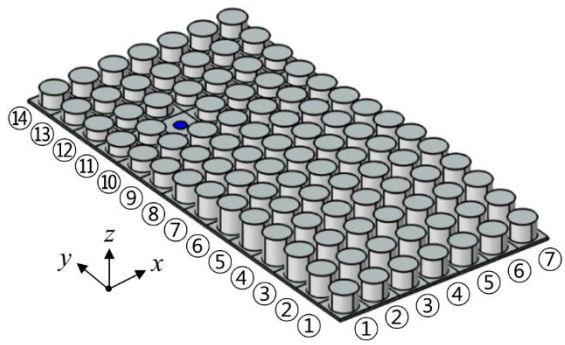

(a)

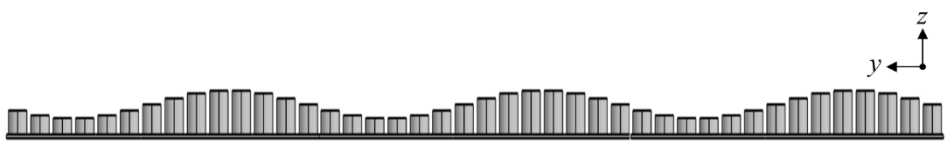

(b)

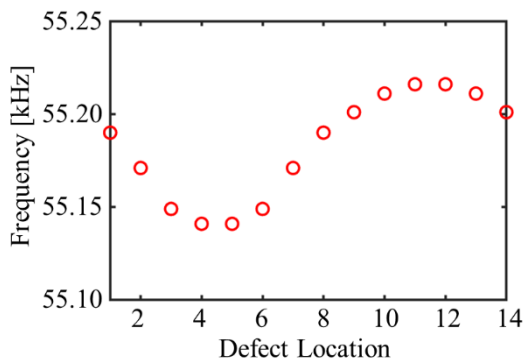

(c)

Figure 5-6 Results of a different graded PnC with a single defect where the height of circular stubs h_N is expressed as 13.00 mm+2.00 mm×sin{2π(N-1)/14}: (a) a schematic of the graded PnC, (b) a side view of the graded PnC under periodic boundary conditions, and (c) trends of the defect band frequency with respect to the defect location under the external electrical resistance of 0 Ω (short-circuit).

Table 5-1 Defect band frequencies for the graded PnC with the single defect under the external electrical resistances of 0 Ω (short-circuit) and 100 MΩ (open-circuit) when **k**=(0, 0).

Defect mode	Defect band frequency [kHz]		Difference [Hz]
	0 Ω (short-circuit)	100 MΩ (open-circuit)	
A	53.63	53.63	10
B	55.17	55.74	570
C	63.24	63.25	10
D	66.62	66.62	0
E	67.47	67.49	20

5.3 Defect Band Analysis of a Graded Phononic Crystal with Decoupled Double Defects

Figure 5-7 (a) shows the graded PnC with double defects (Case I). In Chapter 3, the effects between double defects on the splitting of defect bands were investigated. It was found that the degree of the splitting of defect bands becomes decreasing with

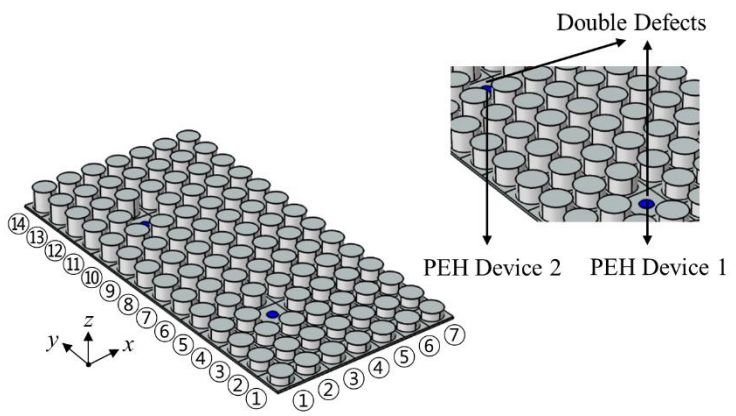

(a)

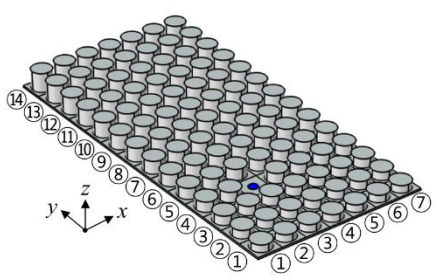

(b)

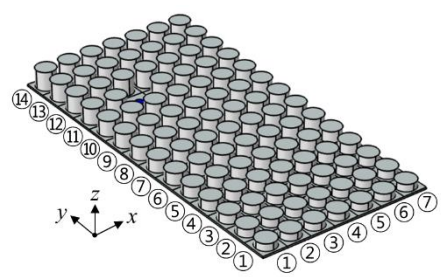

(c)

Figure 5-7 Configuration of graded PnCs with: (a) the double defects imposed at (3, 4) and (3, 11) (Case I); (b) the single defect imposed at (3, 4) (Case II); and (c) the single defect imposed at (3, 11) (Case III).

increasing distance between the double defects. It is expected that if the distance between the double defects is considerably far, the double defects do not recognize each other and can be decoupled. With our preliminary study that the location of the secondary defect is sequentially changed along the *y*-direction, it was confirmed that the primary and secondary defects are decoupled when six unit cell are arranged between the double defects. In other word, the double defects are introduced at (3, 4) and (3, 11), respectively, to eliminate any coupling effect. This decoupling characteristic allows each of the double defects to behave as an independent single defect. One PEH device attached to the primary defect is denoted as PEH Device 1 and the other attached to the secondary defect is denoted as PEH Device 2. The heights of the *x*-directional circular stubs corresponding to PEH Devices 1 and 2 are 13.45 mm and 14.50 mm, respectively. To emphasize the advantages of the characteristics of the decoupled double defects in the graded PnC, Figures 5-7 (b) and 5-7 (c) illustrate two graded PnC with a single defect imposed at (3, 4) (Case II) and at (3, 11) (Case III) for comparison, respectively.

Table 5-2 summarizes the defect band frequencies of Cases I, II, and III, respectively, under external electrical resistances of 0 Ω (short-circuit) and 100 MΩ (open-circuit) when $\mathbf{k}$=(0, 0). For both electrical boundary conditions, the defect band frequencies in Cases II and III coincide with those corresponding to each defect in Case I, respectively. This observation ascertains the fact that the graded PnC with the decoupled double defects (Case I) can be regarded as a superposition of the two graded PnCs with the single defect (Cases II and III). To be more generalized, multiple uniform PnCs with a single defect can be superimposed into one system called a graded PnC with decoupled multiple defects.

Figures 5-8 (a) and 5-8 (b) present the defect bands that correspond to the monopole-like defect mode shapes for the graded PnC with decoupled double defects (Case I) under the external electrical resistances of 0 Ω (short-circuit) and 100 MΩ (open-circuit), respectively. Figures 5-8 (c) and 5-8 (d) depict the monopole-like defect mode shapes at defect band frequencies of 55.15 kHz and 55.17 kHz, respectively. Note that the defect mode shapes at defect band frequencies of 55.72 kHz and 55.74 kHz do not exhibit significant differences, as compared with that at 55.15 kHz and 55.17 kHz; thus, these results are not shown in Figure 5-8. Since the graded PnC is built by varying the height of the circular stubs, the mass and stiffness of the lattices surrounding the defect are different for each location. That is why the defect band frequencies corresponding to each of the decoupled double defects are different from each other. It can be thus found that the elastic waves are localized inside of PEH Devices 1 and 2 at the defect band frequencies of 55.17 kHz and 55.15 kHz, respectively. This phenomenon can be also observed at the external electrical resistance of 100 MΩ (open-circuit).

To insist the merits of the graded PnC with decoupled double defects, a uniform PnC with decoupled double defects is presented in Figure 5-9 (a). For the uniform PnC, the height of all circular stubs is set to 13.45 mm, which is the same with the height of the 4th circular stub along the *y*-direction. As shown in Figure 5-9 (a), the double defects for the uniform PnC are introduced at the same location of those for the graded PnC in Figure 5-7 (a). Figure 5-9 (b) presents that the only five defect bands are created within the band gap for the uniform PnC. Besides, it can be found that both defects exhibit the monopole-like defect mode shapes at the same frequency of 55.17 kHz, as shown in Figure 5-9 (c). These results demonstrate the

superiority of the graded PnC over the uniform PnC that the defect band frequencies corresponding to each of the decoupled double defects can be designed separately; this enables to broaden the bandwidth of energy localization. Note that the difference between the defect band frequencies for each defect becomes bigger when a degree of the height variation gets larger since mass and stiffness of circular stubs that surround the defects would change more remarkably.

Table 5-2 Defect band frequencies for Cases I, II, and III under external electrical resistances of 0 Ω (short-circuit) and 100 MΩ (open-circuit) when **k**=(0, 0).

Electrical boundary condition	Graded PnC	Defect band frequency [kHz]				
0 Ω (short-circuit)	Case I	53.50	53.63	55.15	55.17	63.06
	Case II	−	53.63	−	55.17	−
	Case III	53.50	−	55.15	−	63.06
	Case I	63.24	66.62	66.89	67.26	67.47
	Case II	63.24	66.62	−	−	67.47
	Case III	−	−	66.89	67.26	−
100 MΩ (open-circuit)	Case I	53.50	55.63	55.72	55.74	63.07
	Case II	−	55.63	−	55.74	−
	Case III	53.50	−	55.72	−	63.07
	Case I	63.25	66.62	66.89	67.28	67.49
	Case II	63.25	66.62	−	−	67.49
	Case III	−	−	66.89	67.28	−

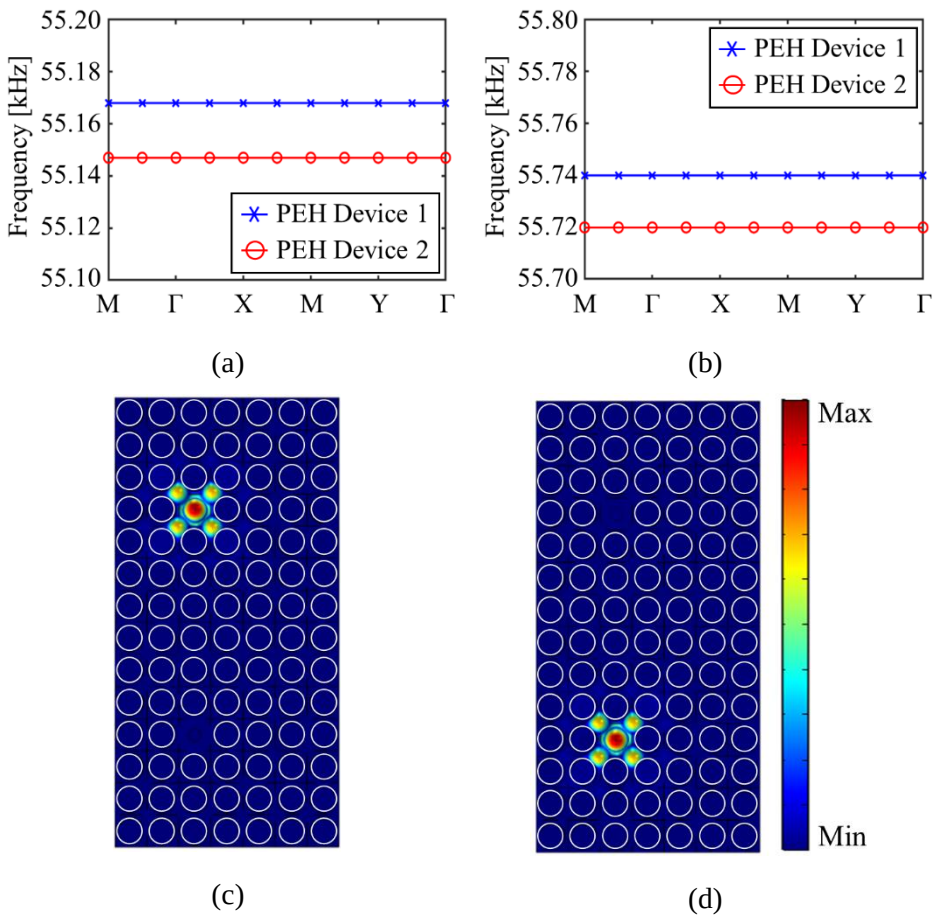

Figure 5-8 Defect band analysis for a graded PnC with decoupled double defects (Case I): (a) defect bands of 55.15 kHz and 55.17 kHz under the external electrical resistance of 0 Ω (short-circuit), (b) defect bands of 55.72 kHz and 55.74 kHz under the external electrical resistance of 100 MΩ (open-circuit), monopole-like defect mode shapes at (c) 55.15 kHz (PEH Device 2) and (d) 55.17 kHz (PEH Device 1).

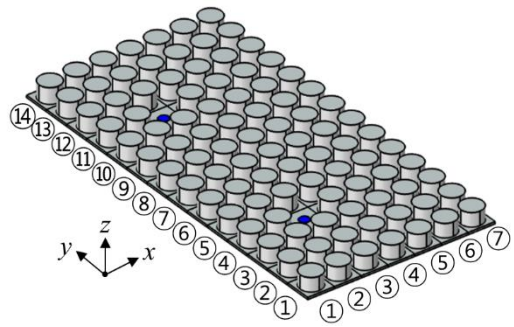

(a)

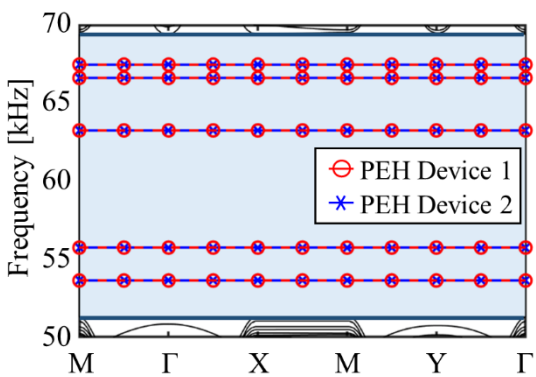

(b)

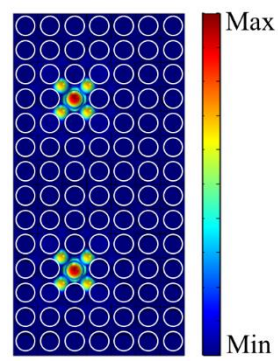

(c)

Figure 5-9 Defect band analysis for a uniform PnC with double defects of which the height of circular stubs is 13.45 mm under the external electrical resistance of 0 Ω (short-circuit): (a) configuration of the uniform PnC, (b) five defect bands within the band gap, and (c) monopole-like defect mode shape at 55.17 kHz.

5.4 Energy Localization and Harvesting Analyses for the Graded Phononic Crystal with the Decoupled Double Defects

This section aims to perform energy localization and harvesting analyses for the graded PnC with the decoupled double defects. To emphasize the merits of the proposed graded PnC (Case I), two cases of a graded PnC with a single defect (Cases II and III) are also investigated. Section 5.4.1 presents the numerical setting for harmonic analysis. Under the open-circuit condition, the maximum output voltage generated by each PEH device is demonstrated in Section 5.4.2. Finally, by exploring the output responses of electric power in terms of the external electrical resistance, Section 5.4.3 deals with the maximum output power.

5.4.1 Setting for Harmonic Analysis

Figure 5-10 shows the settings for harmonic analysis of the graded PnC with the decoupled double defects (Case I); PEH Devices 1 and 2 attached to the defects are colored in blue. For comparison, two graded PnCs with a single defect imposed at (3, 4) (Case II) and at (3, 11) (Case III), which were illustrated in Figures 5-7 (b) and 5-7 (c), respectively, are under consideration. The loss factor was set to be 0.0001.

The incident A_0 Lamb wave with a prescribed displacement of 30 nm is induced by exciting the cross-section of the plate in the *z*-direction (i.e., transverse direction). The distance between the loading section and the first array of the graded PnC is 100 mm, which is near five times the wavelength of A_0 Lamb wave at 55 kHz for an aluminum plate of 2 mm thickness [104]. To ensure unidirectional elastic plane waves, perfectly matched layers and periodic boundary conditions, colored in green

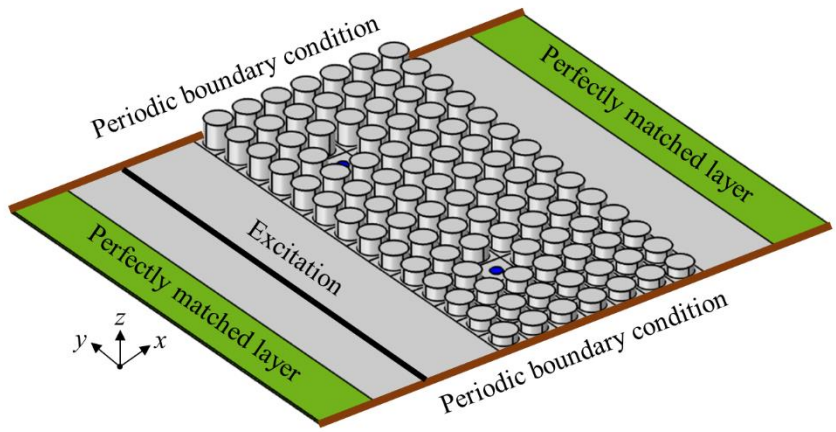

Figure 5-10 System configuration of the graded PnC-based PEH system with the decoupled double defects.

and brown, are applied in the *x*- and *y*-directions, respectively. In the *z*-direction, traction-free condition is employed.

A meshing scheme of the graded PnC with decoupled double defects (Case I) is that (1) the mesh elements of the whole structure are composed of hexahedrons and (2) the maximum mesh size is set to be one-tenth of the wavelength of the excited A_0 Lamb wave at 55 kHz. In terms of electroelastic coupling, three modules, including solid mechanics, electrostatics, and electrical circuit modules, are used. A detailed description is available in Chapter 2. This mesh scheme, loading and boundary conditions are equally applied to other cases (Cases II and III).

5.4.2 The Maximum Output Voltage under the Open-circuit Condition

Figure 5-11 shows output voltage FRFs for Cases I, II, and III under the external electrical resistance of 100 MΩ (open-circuit). Here and hereafter, the solid lines with red-circles and blue-squares correspond to PEH Devices 1 and 2 in Case I, respectively. The dashed line with sky blue-crosses corresponds to PEH Device 1 in Case II, while the dashed line with magenta-stars corresponds to PEH Device 2 in Case III. It is worth pointing out that the peak frequencies in the output voltage FRFs in Cases II (55.74 kHz) and III (55.72 kHz) are different to each other, since the graded characteristics allows to differently design defect band frequencies corresponding to each of the defects by changing the height of the circular stubs. Besides, in Case I, only one peak frequency appears in the output voltage FRFs for PEH Devices 1 (55.74 kHz) and 2 (55.72 kHz), respectively. This implies that the double defects are well decoupled. As found in previous studies [76, 108], if the double defects are coupled, double peaks should exhibit in FRFs of output responses (e.g., displacement and output voltage). Under an assumption that AC-DC converters (alternating current-to-direct current converters) are connected to each PEH device, a bridge rectifier with a capacitor [22, 31] in AC-DC converters can change the sinusoidal AC voltage signal into DC voltage signals. Then, the output voltage generated by PEH Devices 1 and 2 in Case I can be summed, which is indicated by the solid line with black-triangles in Figure 5-11.

Table 5-3 summarizes the maximum output voltage for Cases I, II, and III at each peak frequency under the external electrical resistance of 100 MΩ (open-circuit). For reference, the output voltage for an aluminum plate without the graded PnC was calculated as 0.45 V at both 55.72 kHz and 55.74 kHz. The graded PnC

with the decoupled double defects in a series connection can generate the maximum output voltage of 21.70 V at 55.72 kHz and 22.21 V at 55.74 kHz. Even though peak frequencies in Cases II and III coincide with those corresponding to each defect in Case I, respectively, small differences in the maximum output voltage are observed. This difference would result from multiple scattering. Scattering refers to a phenomenon that describes the reflection of waves due to the presence of discontinuities in space [123]. When elastic waves propagating through the thin plate are fed into a graded PnC, they would undergo multiple scattering (repetitive reflection and transmission) at interfaces of PEH devices and circular stubs due to the mechanical impedance mismatch [124]. For the graded PnCs with the single defect (Cases II and III), since the material properties and geometry of the piezoelectric patch and those of the circular stub are different, the amount of scattering would be different for each case. Therefore, the amount of mechanical energy transferred to each piezoelectric patch would be slightly different.

Figures 5-12 (a) and 5-12 (b) present operating deflection shapes (*z*-directional displacement fields) in Case I at peak frequencies of 55.72 kHz and 55.74 kHz, respectively, under the external electrical resistance of 100 MΩ (open-circuit). If the double defects are coupled, they oscillate with in-phase and out-of-phase monopole-like defect mode shapes [76, 108]. However, it can be found that each of the double defects oscillates with the monopole-like defect mode shape as an independent single defect at each defect band frequency, since they are decoupled.

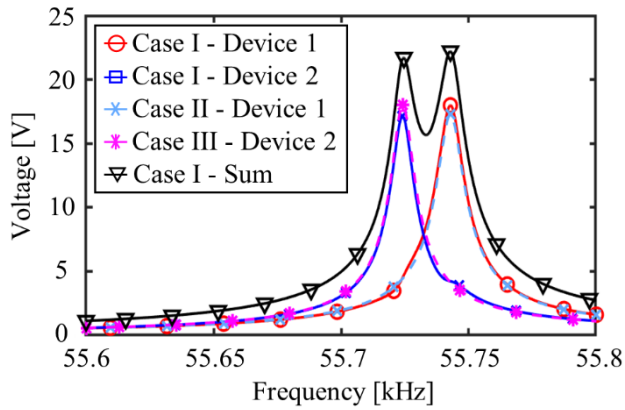

Figure 5-11 Output voltage FRFs for Cases I, II, and II under the external electrical resistance of 100 MΩ (open-circuit).

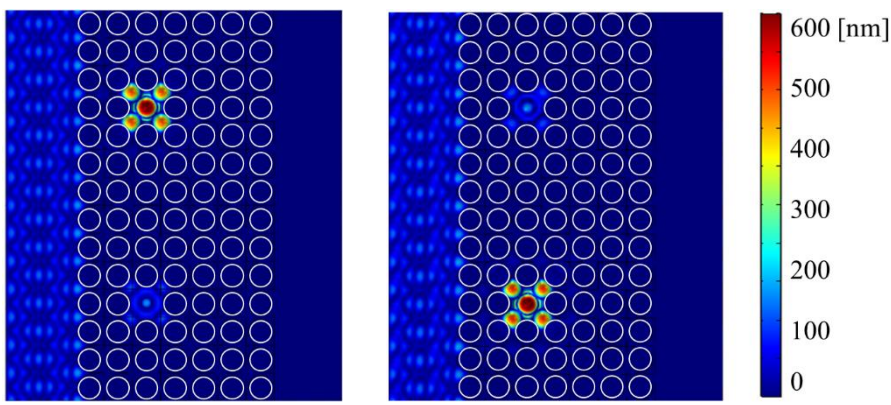

(a) (b)

Figure 5-12 Operating deflection shapes (*z*-directional displacement fields) in Case I under the external electrical resistance of 100 MΩ (open-circuit) at: (a) 55.72 kHz and (b) 55.74 kHz.

5.4.3 The Maximum Output Electric Power under the Optimal External Electrical Resistance

As demonstrated in Chapter 2, since the behavior of the output electric power with changing the external electrical resistance is non-monotonic, there exists the optimal value of the external electrical resistance at which the maximum output electric power can be achieved. At the peak frequency under the open-circuit condition, the optimal external electrical resistance can be found by sweeping it. Figure 5-13 depicts the output electric power with respect to the external electrical resistance at each peak frequency: 1) 55.74 kHz (solid lines with red-circles) and 55.72 kHz (solid lines with blue-squares) in Case I; 2) 55.74 kHz (dashed lines with sky blue-crosses) in Case II; and 3) 55.72 kHz (dashed lines with magenta-stars) in Case III. For Case I, the optimal external electrical resistances are calculated as 54.95 kΩ and 66.07 kΩ for PEH Device 1 at 55.74 kHz and PEH Device 2 at 55.72 kHz, respectively.

In the field of PVEH, it is well known that the optimal external electrical resistance $R_{load}^{opti,\,open}$ close to the open-circuit condition depends on the natural frequency ω_n, damping ratio ζ, effective capacitance C_p, and electroelastic coupling θ of a PEH device [115, 125] as

$$R_{load}^{opti,open} = \frac{1}{\omega_n C_p \sqrt{\dfrac{1-\zeta^2+\left(\dfrac{\theta^2}{2\omega_n C_p \zeta}\right)^2}{\left(1+\dfrac{\theta^2}{\omega_n^2 C_p}-\zeta^2\right)\left(1+\dfrac{\theta^2}{\omega_n^2 C_p}-2\zeta^2\right)}}} \tag{5.2}$$

Equation (7.2) was derived when mechanical vibrations are applied to a finite structure having explicit boundary conditions. The system under consideration is

exposed to not vibrations but waves. However, as discussed in Appendix A, a defect-induced PnC can be thought of as a vibration problem with fixed-like boundary conditions at a certain defect band frequency. Therefore, even though Equation (5.2) does not perfectly accord with the engineered situations we are looking at, the trends of the optimal external electrical resistance in terms of input variables would be similar. In Equation (5.2), the natural frequency ω_n would be the defect band frequency under a short-circuit condition. Since the configurations of PEH Devices 1 and 2 in Case I are the same as those in Cases II and III, respectively, the electroelastic coupling should be the same at each defect band frequency. That is why the power-optimal external electrical resistances in Cases II and III coincide with those corresponding to PEH Devices 1 and 2 in Case I, respectively.

Figure 5-14 presents the output electric power FRFs for Cases I, II, and III across the power-optimal external electrical resistance. The solid line with black-triangles clearly indicates that the proposed graded PnC with decoupled double defects can achieve the higher output electric power even between two peak frequencies, compared to the other cases. Table 5-4 summarizes the maximum electric power across the power-optimal external electrical resistance at each peak frequency. The maximum output electric power for PEH Device 1 at 55.74 kHz in Case I is slightly higher than that observed for Case II; whereas, the opposite results are found at 55.72 kHz. This can be readily demonstrated by multiple scattering, as mentioned in previous section. The graded PnC with the decoupled double defects in a series connection can generate the maximum output electric power of 1.46 mW at 55.72 kHz and 1.68 mW at 55.74 kHz. It can be thus concluded that the proposed graded PnC with decoupled double defects can be used for broadband energy

localization under realistic environments. Here, it should be noted that the maximum mechanical power of guided bending waves that transferred to the host medium by excitation is calculated as near 3.78 mW at the frequency of 55 kHz.

Finally, if one wants to achieve broadband energy localization and harvesting near a target operating frequency, it is needed to optimize a graded PnC with decoupled double defects following the design optimization flowchart presented in Appendix B. Here, the design variables can be a lattice constant of a unit cell, a diameter of the circular stub, initial height and the degree of the height variation. Since the decoupled double defects' location is a discrete variable, their locations are fixed while guaranteeing the decoupling characteristics. Note the function of height variation can also be one of the design spaces. Geometric dimensions of the PEH devices can also be the design variables; but, if a commercially available element is used as it is, the geometry should be fixed.

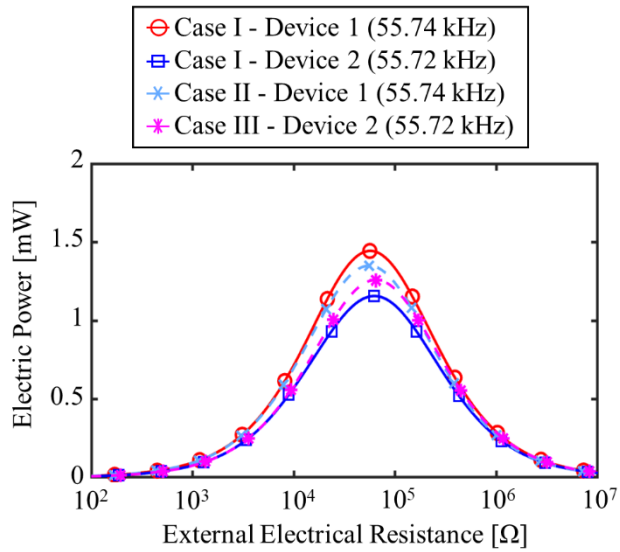

Figure 5-13 Output electric power for Cases I, II, and III with respect to external electrical resistances at each peak frequency.

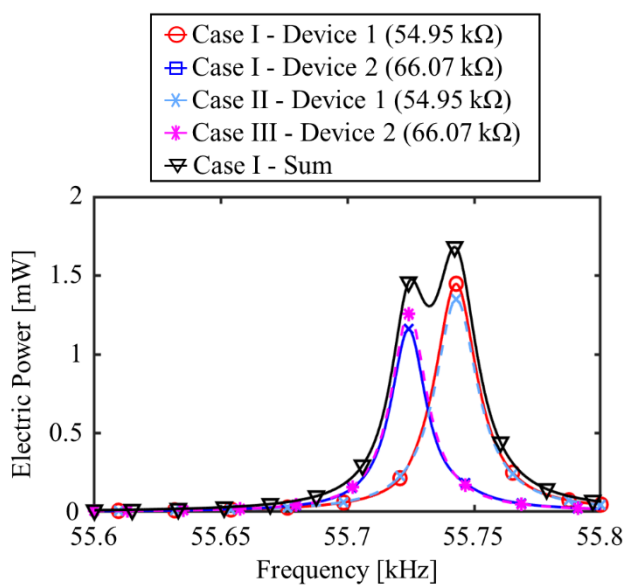

Figure 5-14 Output electric power FRFs for Cases I, II, and III across the optimal external electrical resistance.

Table 5-3 The maximum output voltage at each peak frequency for Cases I, II, and III under the external electrical resistance of 100 MΩ.

Peak frequency	Physical quantities	Case I		Case II	Case III
		PEH Device 1	PEH Device 2	PEH Device 1	PEH Device 2
55.72 kHz	Output voltage	4.58 V	17.12 V	4.51 V	18.00 V
	Voltage sum	21.70 V		-	-
55.74 kHz	Output voltage	17.99 V	4.22 V	17.28 V	4.11 V
	Voltage sum	22.21 V		-	-

Table 5-4 The maximum output electric power at each peak frequency for Cases I, II, and III across the optimal external electrical resistance.

Peak frequency	Physical quantities	Case I		Case II	Case III
		PEH Device 1	PEH Device 2	PEH Device 1	PEH Device 2
55.72 kHz	Optimal external electric resistance	-	66.07 kΩ	-	66.07 kΩ
	Output electric power	0.30 mW	1.16 mW	0.30 mW	1.26 mW
	Power sum	1.46 mW		-	-
55.74 kHz	Optimal external electric resistance	54.95 kΩ	-	54.95 kΩ	-
	Output electric power	1.45 mW	0.23 mW	1.35 mW	0.22 mW
	Power sum	1.68 mW		-	-

5.5 Summary and Discussion

A PnC-based PEH system with double defects have the following challenges for broadband harvesting performance. Since the distance between double defects can be changed just as much as an integer multiple of the lattice, a degree of the defect band split can be adjusted only in a discrete manner. This implies that it is restrictive to design the defect band frequencies, as well as bandwidth, for energy localization. If double defects are too closely arranged to each other, the coupling between them gets strong, and then the degree of the defect band split increases. In this case, the output performance of the PEH devices attached to the defects rapidly decreases between two resonance frequencies, which is an analogy to anti-resonance in a dynamic vibration absorber system. On the other hand, if double defects are arranged far away from each other, the defect band split does not occur because the coupling between them is weakened or nearly zero. In this study, only one defect band exhibits, which corresponds to the single defect. This is traced to the fact that all unit cells of a PnC are uniform in terms of material properties and geometry.

With this motivation, the objective of this chapter is to newly propose a graded PnC with decoupled double defects for broadband energy localization and harvesting. The graded PnC was composed of a 14×7 array of square lattices with aluminum circular stubs that are deposited on a top surface of a thin aluminum plate, while the height of the circular stub varies in the *y*-direction (i.e., perpendicular direction of propagating waves). The double defects were introduced in (3, 4) and (3, 11), respectively, which are sufficiently far from each other to eliminate any coupling effect between them. This decoupling characteristic allows each of the double defects to behave as an independent single defect. Once the defect location is fixed,

the defect band frequency is determined based on the mass and stiffness of the lattices surrounding the relevant defect. Unlike a conventional uniform PnC, therefore, the graded PnC allows to separately design defect band frequencies corresponding to each of the defects by changing a degree of the variation in the height of the circular stub. The peak frequencies in the FRFs for the output voltage and electric power in the two graded PnCs with a single defect (Cases II and III) coincide with those corresponding to each defect in the graded PnC with decoupled double defects (Case I), respectively. This observation ascertains the fact that Case I can be regarded as a superposition of Cases II and III. The graded PnC with decoupled double defects in a series connection can generate the maximum output voltage of 21.70 V at 55.72 kHz and 22.21 V at 55.74 kHz, and the maximum output electric power of 1.46 mW at 55.72 kHz and 1.68 mW at 55.74 kHz. In addition, it can be seen that the bandwidth of the graded PnC with decoupled double defects (Case I) is much larger, compared to the others (Cases II and III). The proposed graded PnC with decoupled double defects can broaden the bandwidth for elastic wave localization, thereby enhancing PEH under realistic environments.

The unique contributions of this study are two-fold. First, this is the first attempt to propose a new design concept of a graded PnC with decoupled double defects under elastic waves. Second, the graded PnC with the decoupled double defects enables to broaden the bandwidth for elastic wave localization and harvesting by separately designing defect band frequencies of each defect.

It should be noted that there are two ways to manipulate the defect band frequencies of a graded PnC with decoupled double defects. First, the defect band frequencies can be changed with the defect location, while keeping a degree of the

height variation. Second, the defect band frequencies can also be designed by changing a degree of the height variation, while maintaining the location of the defect. However, in both cases, there are limitations in that the fabricated prototype cannot be changed or modified anymore after designing the system for a target frequency range. Unlike this work, when a unit cell is designed with smart materials (e.g., piezoelectric materials), the connected electrical loads, such as inductance, capacitance, and resistance, can be varied instead of the geometric dimensions of unit cells. Therefore, incorporating smart materials into a graded PnC with decoupled double defect makes more actively design defect band frequencies. This topic can be future work.

Sections of this chapter have been published or submitted as the following journal articles:

1) **Soo-Ho Jo**, Heonjun Yoon, Yong Chang Shin, and Byeng D. Youn, "A Graded Phononic Crystal with Decoupled Double Defects for Broadband Energy Localization," *International Journal of Mechanical Sciences*, Vol. 183, pp. 105833, 2020.

Chapter 6

Conclusion

6.1 Contributions and Significance

The proposed research in this doctoral dissertation aims at bridging the domains of defect-mode-enabled energy localization of a PnC and PEH. This doctoral dissertation is composed of two research thrusts and one co-related study: (1) parametric studies on structural and electrical circuit designs of a PnC with piezoelectric defects; (2) new design concepts of a PnC with piezoelectric defects for broadband PEH; and (3) an analytical model for a PnC with piezoelectric defects for the formation and splitting of defect bands. It is expected that the proposed research offers the following potential contributions and broader impacts in PnC-based PEH fields.

Contribution 1: Guidelines of How to Select a Target Defect Mode Shape for High Dense Piezoelectric Energy Harvesting

This doctoral dissertation explores the electroelastic coupling effects of a PEH device on defect bands for various defect mode shapes of a two-dimensional PnC

with piezoelectric defects when switching electric boundary conditions from the short-circuit to open-circuit conditions. Even though the main concerns of waves are both space and time, the spatial positions of strain nodal lines are determined for each defect mode shape since it was revealed that the defect mode shape is similar to normal modes of vibrations. Therefore, avoiding strain nodal lines within a PEH device is the most important issue from the perspective of amplifying PEH performance. In terms of the degree of the frequency shift of defect bands, it was found that the monopole-like defect mode shape is the best target one.

Contribution 2: Demonstration of Guidelines and Rationales for Design Parameters of a Phononic Crystal with Single or Double Piezoelectric Defects

This doctoral dissertation aims to provide guidelines and rationales for key design parameters for the purpose of maximizing the harvestable electric power. Here, design parameters include: the supercell size, defect location, and relative position between double defects in the mechanical domain and the electrical circuit connection between double defects in the electrical domain. The effects of those design parameters on defect bands and PEH performance are thoroughly investigated with physical interpretation that is revealed by the proposed lumped-parameter model and electroelastically coupled analytical model. These parametric studies provide a deeper insight into the defect mode-enabled PEH.

Contribution 3: Realization of Broadband Energy Localization and Harvesting

This doctoral dissertation proposes an electroelastically coupled analytical model of a PnC with a piezoelectric defect to predict defect bands and output performances of PEH while considering the inertia, stiffness, and electroelastic coupling effects of PEH devices. To the best of the authors' knowledge, the unique contributions of this study are two-fold. First, it is a pioneer work to propose an electroelastically coupled analytical model of a PnC with a piezoelectric defect for energy harvesting. Second, an electroelastically coupled transfer matrix is parameterized in an explicit manner for a structure to which PEH devices are attached while considering both forward and backward electroelastic coupling. Compared with FEM, the proposed analytical model requires much less computation time to execute both defect band analysis and PEH performance analysis.

Contribution 4: Elucidation of How Defect Bands Can Be Formed or Split by Using Asymptotic Analysis

This doctoral dissertation fundamentally elucidates the underlying principles of the formation and splitting of defect bands by incorporating asymptotic analysis into defect band analysis of a lumped-parameter model of one-dimensional PnCs with single or double defects. The key findings of this study are two-fold. First, exponentially attenuating properties of evanescent waves in the band gap generate fixed-like boundary conditions in unit cells surrounding single or double defects. Seconds, mechanical resonance, induced by fixed-like boundary conditions, leads to

the formation and splitting of defect bands.

Contribution 5: An Electroelastically Coupled Analytical Model of a Phononic Crystal with a Piezoelectric Defect

This doctoral dissertation proposes an electroelastically coupled analytical model of a PnC with a piezoelectric defect to predict defect bands and output performances of PEH while considering the inertia, stiffness, and electroelastic coupling effects of PEH devices. The unique contributions of this study are two-fold. First, it is a pioneer work to propose an electroelastically coupled analytical model of a PnC with a piezoelectric defect for energy harvesting. Second, an electroelastically coupled transfer matrix is parameterized in an explicit manner for a structure to which PEH devices are attached while considering both forward and backward electroelastic coupling. Compared with FEM, the proposed analytical model requires much less computation time to execute both defect band analysis and PEH performance analysis.

6.2 Suggestions for Future Research

Although the technical advances proposed in this doctoral dissertation successfully address some issues in the field of defect-mode-enabled energy localization and harvesting, there are still several research topics that further investigations and developments are required to bring PnC-based PEH into an alternative solution for

powering wireless sensor networks or low-power electronics. Specific suggestions for future research are listed as follows.

Suggestion 1: Uncertainty Propagation Analysis under Variabilities in Material Properties and Geometry

To realized self-powered wireless sensors in the field, the output power generated by PEH devices has to be larger than the threshold at which it is set to activate the operation of wireless sensors [21]. To meet this requirement, it is essential to develop accurate analytical or develop models of a PnC-based PEH system with single or multiple defects to predict the output power under the expected operating conditions. However, one of the great challenges is to systematically characterize variability in its material properties and geometry. Unless various physical uncertainties in the material properties and geometry are properly addressed, the output power generated by the piezoelectric energy harvester will vary, which ultimately lead to unreliable prediction for the performance [114, 126] . Therefore, there is a great need to characterize how the physical uncertainties of material properties and geometry affect defect band frequencies, defect mode shapes, and output electrical power through uncertainty propagation analysis. It should be emphasized that little attention has been paid to uncertainty propagation analysis in the field of PnC-based PEH.

Suggestion 2: Reliability-based Design Optimization under Physical

Uncertainties

An important issue for maximizing the output performance of defect mode-enabled PEH is to match the defect band frequency at the optimal external electrical resistance with a target excitation frequency via design optimization. However, a variety of uncertainties results in a stochastic nature of the defect band frequency and makes it hard to guarantee reliable and satisfactory performance. Therefore, reliability-based design optimization can be a potential solution that the optimized design with the consideration of the parametric uncertainties will be more robust in terms of the worst-case power compared to the deterministically optimized designs [11, 127]. It should be emphasized that the study or reliability-based design optimization of a PnC-based with defects has not been touched yet.

Suggestion 3: Designing a Uniform Phononic Crystal Having Piezoelectric Defects with Different Configurations for Broadband Proposes

In this doctoral dissertation, energy localization and harvesting based on double and triple defects were presented. However, it should be mentioned that the design space for the defects themselves was not taken into account when designing the PnC-based PEH system. Via the physical interpretation of the defect-mode-enabled energy localization, more focus has been placed on coupling and decoupling between the double defects at the system level. If the geometric dimensions of defects can be considered as design variables, it is expected that broadband PEH will be possible in a different way from the afore-mentioned L-shape arranged tripled defects or a

graded PnC with decoupled double defects. In previous studies, analysis of a PnC with multiple defects with different geometry has not been touched yet. For a simple example, a uniform PnC with decoupled double defects with different configurations may enable broadband PEH.

Suggestion 4: Investigation of Effects of Partial Debonding between a Host Medium and Piezoelectric Materials on Output Electric Power

Interface between the host medium and the piezoelectric material plays a significant role in the stress and strain transfer mechanisms [124]. If the thickness of the adhesive layer increases, in-plane normal strains might be decreased, thereby reducing the output voltage. Furthermore, one prerequisite in previous studies is that the piezoelectric materials are perfectly bonded to the host medium. However, the piezoelectric materials can be debonded from the host medium due to impact loading, bonding defects, environmental effects, fatigue loading, or high free-edge stresses [125, 126]. The larger the surface of the piezoelectric material, the greater the likelihood that imperfect bonding is present. Here, the defective piezoelectric materials can make the developed electroelastically coupled analytical model or FEM mispredict output electric power of a PnC-based PEH system with single or double defects. As debonding increases, the effective area of the surface-bonded piezoelectric layer could be decreased, resulting in a reduction in the output voltage [127]. Therefore, this issue highlights one research need of performance degradation assessment of a PnC-based PEH system in the presence of partial debonding.

Suggestion 5: Enhancement of the Electroelastically Coupled Analytical Model by Considering Thermal Effects

It should be stated that lots of mechanical systems (e.g., railway [121]) that a PnC-based PEH system may be equipped with are exposed to dynamic thermal loading. The temperature of the systems can be determined by two factors. One is the external temperature environment and the other is the Joule heating during operation. Since the strain and stress of both host medium and piezoelectric materials can change due to the temperature effects, the characteristics of the system can be partially change; thus, the output electric power in a PnC-based PEH system should depend on the thermal loading [122]. With this motivation in mind, several studies have been reported to analyze the temperature effects on defect band frequencies and PEH performances using numerical models [71, 73, 123]. However, there are few attempts to develop an electroelastically coupled analytical model that considers thermal effects.

Suggestion 6: Improvement of the Electroelastically Coupled Analytical Model by Considering Lateral Deformations and Shear Effects under Longitudinal Waves

The background of the proposed analytical model is based on the classical rod theory under longitudinal waves. The basic premise of the classical rod theory is that the length of the rod is much longer than both the height and width of it. If the length of the rod becomes shorter, the lateral deformations, which is induced by Poisson's ratio, become important in the PnC-

based PEH system. Compared with the classical rod theory, the lateral deformations makes additional kinetic energy in the given system. Besides, if the excitation frequency is much higher, the effects of shear strains and stresses should be taken into account. These shear effects leads to modifying both kinetic and potential energy. The former and the latter are called Rayleigh-Love rod theory [128] and Rayleigh-Bishop rod theory [129], respectively. With the consideration of lateral deformations and/or shear effects, the analytical model can be further improved; thus, it can be expected that the enhanced analytical model has capabilities to predict the output performance of PEH with high accuracy under given excitation conditions.

Suggestion 7: Derivation of an Electroelastically Coupled Transfer Matrix under Flexural Waves and Its Application to Analytical Modeling for a Phononic Crystal with Piezoelectric Defects

In the doctoral dissertation, an analytical model to predict the output electric power, as well as the defect bands, was developed under longitudinal waves. However, when measuring the ultrasonic waves in industrial applications, flexural waves usually appear. Therefore, there is a need to develop an electroelastically coupled analytical model of a PnC with a defect under flexural waves. The overall procedure would be similar. Due to bending moments or shear forces, transverse motions occur in a beam and the equation of motions is 4th order partial differential equation. For a thin beam, Euler-Bernoulli beam theory will provide a key role in deriving the electroelastically coupled transfer matrix [130]. Since the evanescent waves, as well as propagating waves, exist throughout the beam, the transfer matrix will lie in the form of 4×4 matrix. When the rotary inertia, shear stresses, and shear strains are taken into

account for a thick beam, Timoshenko beam theory can enhance the analytical model under flexural waves [131].

Suggestion 8: Incorporation of Defect Modes into Actuators

The reverse piezoelectric effect, as opposed to the piezoelectric effect, is a phenomenon in which mechanical strain is generated in piezoelectric materials in response to an applied electric field. Therefore, the developed analytical model or PnC designs can be used as actuators that can excite elastic waves. Based on the narrowband characteristics of defect bands, a PnC with piezoelectric defects can play a key role as resonant-type actuators. Furthermore, incorporating other smart materials into PnC designs, it can be feasible to tune adaptively defect band frequencies of propagating elastic waves.

Appendix A

A Lumped-parameter Model of Phononic Crystals with Single and Double Defects for Formation and Splitting of Defect Bands under Longitudinal Waves

Several prior research efforts have been dedicated to comprehensively exploring energy localization that leverages a defect mode of a PnC with single or double defects from phenomenon observation to potential applications (e.g., PEH) under elastic waves [73, 89, 108, 132-135] . Here, it should be emphasized that the previous studies have not provided any answer to the following question: why can elastic wave be localized in PnCs with defects? In the case of Bragg-type band gap, it is physically and intuitively reasonable that the locally broken periodicity of unit cells leads to forming several bands within the band gap since the underlying mechanism of the formation of the Bragg-type band gap is destructive interference induced by the periodicity of unit cells at the order of the wavelengths [136, 137]. However, no further in-depth consideration has been made on demonstrating (1) why such defect

bands are observed at only specific frequencies and (2) how the band gap physically plays a role in defect-mode-enabled energy localization. Moreover, when double defects are created sufficiently close to each other along the incident wave direction inside a PnC, it has been presented that one of the double defects is coupled to the other defect and this coupling generates splitting of defect bands for the single defect case [108]. However, there is no further investigation of what the physical meaning of the coupling is and how the coupling leads to the splitting of defect bands. Since the ultimate goal of the PnC-based PEH system with defects is to enhance the PEH performance by matching the defect band frequencies with the operating frequencies, it is of great importance to fully understand the underlying physics of the formation and splitting of defect bands. In the future, it is expected that this understanding will provide intuitive design guidelines for a PnC with a defect for high dense PEH.

Therefore, the objective of this appendix is to fundamentally elucidate the formation (for a single defect) and splitting (for double defects) of defect bands. We consider a lumped-parameter model (i.e., M-DOF mass-spring system) of a one-dimensional PnC with single or double defects under longitudinal elastic waves. Even though lumped models are weak with respect to the accuracy of physical quantity calculation, they have strong advantages of providing intuitive insights when analyzing physical behaviors at a macroscopic level. The primary interest herein is to thoroughly investigate how defect bands and corresponding defect mode shapes asymptotically behave when asymptotic approaches are applied into defect band analysis. The limiting behaviors provide important keys to what the physical meaning of defect-mode-enabled energy localization is. Next, by using regression models for comparison before and after asymptotic analysis, this appendix provides

new information about why the band gap is essential for defect-mode-enabled energy localization. To the best of the authors' knowledge, the key findings of this study are two-fold. First, exponentially attenuating properties of evanescent waves in the band gap generate fixed-like boundary conditions in unit cells which surround single or double defects. Seconds, mechanical resonance, induced by the fixed-like boundary conditions, leads to the formation and splitting of defect bands.

The remainder of Appendix A is organized as follows. Section A.1 describes system configurations of one-dimensional PnCs with single or double defects under consideration and model assumptions for M-DOF mass-spring systems. Based on the lumped-parameter models, Section A.2 deals with eigenvalue problems of PnCs (1) without defects, (2) with single, and (3) with double defects for dispersion analysis. Section A.3 presents band gap analysis for a PnC without defects. Section A.4 and Section A.5 elucidate the fundamental principles of the formation (for a single defect) and splitting (for double defects) of the defect bands, using asymptotic analysis, respectively. Finally, the conclusions of this work are summarized in Section A.6.

A.1 System Configuration and Modeling Assumption for a Lumped-parameter Model

In Figures A-1 (a) and A-1 (b), a unit cell under consideration is shown as a one-dimensional, bi-layered stack composed of the host (colored in gray) and embedded (colored in blue) mediums. In this appendix, subscripts 'a' and 'b' stand for the host

and embedded stacks, respectively. The unit cell has six geometric variables, including the length l_a, the height h_a, and the width w_a of the host medium and those (l_b, w_b, and h_b) of the embedded medium. A lattice constant l_{unit} of the unit cell is calculated as l_a+l_b. A PnC is built by arranging N unit cells. In Figure A-1 (a), a single defect is introduced by replacing the embedded medium in the K-th unit cell with the host medium with a length of l_{defect}. In Figure A-1 (b), an additional defect is introduced at the location, T unit cells away from the initial defect. the defect configuration (i.e., geometric dimensions and material properties) is the same as that in the single-defect case. In other word, the secondary defect is introduced by replacing the embedded medium in the ($K+T$)-th unit cell with the host medium with a length of l_{defect}.

The PnCs with defects can be modeled as 2N-DOF mass-spring systems, as shown in Figures A-1 (c) and A-1 (d), when the length of each medium is smaller than the wavelength of the longitudinal waves [138-146]. The unit cell can be a diatomic crystal with lumped masses (m_a and m_b) and linear springs (s_a and s_b). Note that the two springs s_a and s_b, connected in series, can be replaced with one equivalent spring s_{eq}^{unit}. The lumped mass and linear spring of the defect are denoted as m_{defect} and s_{defect}, respectively. Likewise, the two springs s_a and s_{defect} are substituted for one equivalent spring s_{eq}^{defect}.

When the PnCs vibrate only in the longitudinal direction, the x-directional displacements for the host and embedded mediums in the n-th unit cell are denoted as $u_{a,n}(t)$ and $u_{b,n}(t)$, respectively. In Figure A-1 (c), the displacement for the single defect is denoted as $u_{sd}(t)$. In Figure A-1 (d), the displacements for the double defects are denoted as $u_{dd1}(t)$ and $u_{dd2}(t)$, respectively. Here and hereafter, the subscripts 'sd'

and ‘dd’ denote ‘single defect’ and ‘double defects’, respectively. Assuming harmonic motions in time, the displacements $u_{a,n}(t)$, $u_{b,n}(t)$, $u_{sd}(t)$, $u_{dd1}(t)$, and $u_{dd2}(t)$ can be expressed as $U_{a,n}e^{-i\omega t}$, $U_{b,n}e^{-i\omega t}$, $U_{sd}e^{-i\omega t}$, $U_{dd1}e^{-i\omega t}$, and $U_{dd2}e^{-i\omega t}$, respectively.

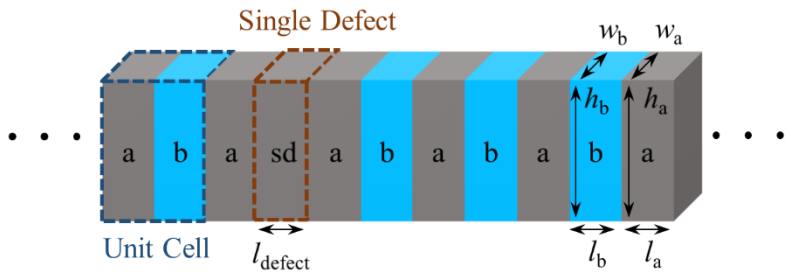

(a)

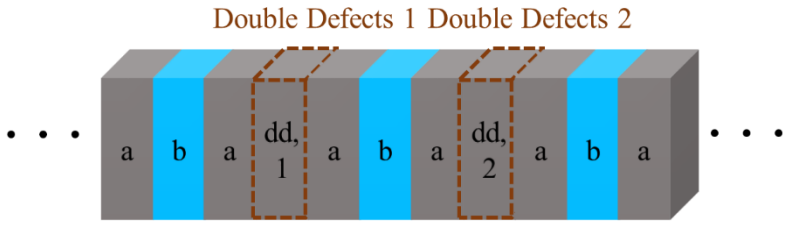

(b)

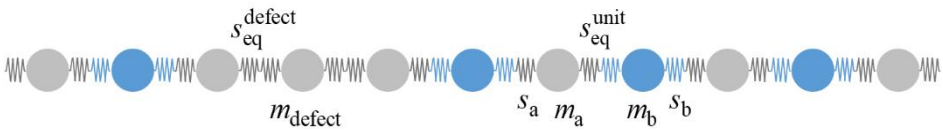

(c)

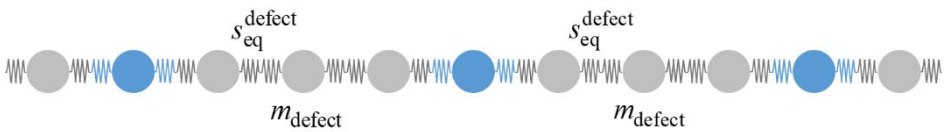

(d)

Figure A-1 Configuration of PnCs with defects: a PnC with (a) a single defect and (b) double defects, a M-DOF mass-spring system for a PnC with (c) a single defect and (d) double defects.

A.2 Eigenvalue Problems of Phononic Crystals for Dispersion Analysis

This section is devoted to demonstrating eigenvalue problems of PnCs (1) without defects, (2) with single, and (3) with double defects for dispersion analysis. Section A.2.1 presents a case of a PnC without defects for band gap analysis. Sections A.2.2 and A.2.3 present two cases of PnCs with single and double defects for defect band analysis, respectively. Finally, planning for analyzing band structures is described in Section A.2.4.

A.2.1 A Phononic Crystal without Defects

Analogous to photonic crystals [147, 148], dispersion analysis can be performed using supercell calculation [88, 112, 149] for a PnC without defects. Here, a supercell refers to a bunch of unit cells that may include defects (called an 'imperfect supercell') or not (called a 'perfect supercell'). There are 2N equations of motions for 2N crystals and 2N harmonic displacement fields. Periodic boundary conditions, according to Floquet-Bloch theorem, is applied as $U_{\mathrm{a},N+1}=U_{\mathrm{a},1}e^{ik_{\mathrm{wd}}Nl_{\mathrm{unit}}}$ and $U_{\mathrm{b},N+1}=U_{\mathrm{b},1}e^{ik_{\mathrm{wd}}Nl_{\mathrm{unit}}}$, where k_{wd} is a reciprocal wavenumber [96]. The subscript 'wd' stands for 'without defects'. By inserting the harmonic displacement fields and periodic boundary conditions into the equations of motions, an eigenvalue problem for the PnC without defects can be formulated as [150, 151]:

$$\left(\left[\mathbf{K}_{\mathrm{wd}}\left(k_{\mathrm{wd}}\right)\right]-\omega_{\mathrm{wd}}{}^{2}\left[\mathbf{M}_{\mathrm{wd}}\right]\right)\left\{\mathbf{U}_{\mathrm{wd}}\right\}=\left\{\mathbf{0}\right\}, \tag{A.1}$$

where $[\mathbf{K}_{\mathrm{wd}}(k_{\mathrm{wd}})]$ and $[\mathbf{M}_{\mathrm{wd}}]$ are 2N×2N matrices of stiffness and mass, respectively.

$\{\mathbf{U}_{\mathrm{wd}}\}$ and ω_{wd} are calculated $2N\times1$ eigenvectors of displacement fields and eigenfrequencies, respectively. $\{\mathbf{0}\}$ is a $2N\times1$ zero vector. Details of Equation (A.1) are available in below.

$$\left[\mathbf{M}_{\mathrm{wd}}\right]_{ij}=\begin{cases} m_{\mathrm{a}} & i=j=\text{odd number} \\ m_{\mathrm{b}} & i=j=\text{even number} \\ 0 & \text{otherwise} \end{cases}, \tag{A.2}$$

$$\left[\mathbf{K}_{\mathrm{wd}}\right]_{ij}=\begin{cases} 2s_{\mathrm{eq}}^{\mathrm{unit}} & i=j \\ -s_{\mathrm{eq}}^{\mathrm{unit}} & i=j\pm1 \\ -s_{\mathrm{eq}}^{\mathrm{unit}}e^{ik_{\mathrm{wd}}Nl_{\mathrm{unit}}} & (i,j)=(1,2N),(2N,1) \\ 0 & \text{otherwise} \end{cases}, \tag{A.3}$$

where $[\cdot]_{ij}$ stands for an element in i-th column and j-th row of a $2N\times2N$ matrix $[\cdot]$; i and j are integers ranging from one to $2N$. Dispersion curves can be obtained by calculating a set of complex normalized wavenumbers $k_{\mathrm{wd}}Nl_{\mathrm{unit}}$ for a given range of frequencies. The real parts of the wavenumbers belong to the 1st irreducible Brillouin zone, ranging from zero to π [152, 153].

A.2.2 A Phononic Crystal with a Single Defect

When a single defect is introduced into a perfect supercell, as shown in Figure A-1 (c), it leads to the change of some elements, to which the single defect and neighboring crystals are related, in both stiffness and mass matrices ($[\mathbf{K}_{\mathrm{wd}}(k_{\mathrm{wd}})]$ and $[\mathbf{M}_{\mathrm{wd}}]$). $[\mathbf{K}_{\mathrm{sd}}(k_{\mathrm{sd}})]$ and $[\mathbf{M}_{\mathrm{sd}}]$ are modified stiffness and mass matrices, respectively. Consequently, by replacing $[\mathbf{K}_{\mathrm{wd}}(k_{\mathrm{wd}})]$ and $[\mathbf{M}_{\mathrm{wd}}]$ in equation (A.1) with $[\mathbf{K}_{\mathrm{sd}}(k_{\mathrm{sd}})]$ and $[\mathbf{M}_{\mathrm{sd}}]$, respectively, an eigenvalue problem for the PnC with the single defect

can be expressed as

$$\left(\left[\mathbf{K}_{\mathrm{sd}}\left(k_{\mathrm{sd}}\right)\right]-\omega_{\mathrm{sd}}{}^{2}\left[\mathbf{M}_{\mathrm{sd}}\right]\right)\left\{\mathbf{U}_{\mathrm{sd}}\right\}=\left\{\mathbf{0}\right\}. \tag{A.4}$$

Details of Equation (A.4) are available in below:

$$\left[\mathbf{M}_{\mathrm{sd}}\right]_{ij}=\begin{cases} m_{\mathrm{a}} & i=j=\text{odd number} \\ m_{\mathrm{b}} & i=j=\text{even number}\neq 2K \\ m_{\mathrm{defect}} & i=j=2K \\ 0 & \text{otherwise} \end{cases}, \tag{A.5}$$

$$\left[\mathbf{K}_{\mathrm{sd}}\right]_{ij}=\begin{cases} 2s_{\mathrm{eq}}^{\mathrm{unit}} & i=j\neq 2K,2K\pm 1 \\ -s_{\mathrm{eq}}^{\mathrm{unit}} & i=j\pm 1 \text{but } (i,j)\neq(2K,2K\pm 1),(2K\pm 1,2K) \\ -s_{\mathrm{eq}}^{\mathrm{unit}}e^{ik_{\mathrm{sd}}Nl_{\mathrm{unit}}} & (i,j)=(1,2N),(2N,1) \\ 2s_{\mathrm{eq}}^{\mathrm{defect}} & i=j=2K \\ s_{\mathrm{eq}}^{\mathrm{defect}}+s_{\mathrm{eq}}^{\mathrm{unit}} & i=j=2K\pm 1 \\ -s_{\mathrm{eq}}^{\mathrm{defect}} & (i,j)=(2K,2K\pm 1),(2K\pm 1,2K) \\ 0 & \text{otherwise} \end{cases}. \tag{A.6}$$

Defect bands can be obtained by calculating a set of complex normalized wavenumbers $k_{\mathrm{sd}}Nl_{\mathrm{unit}}$ for frequencies within the band gap.

A.2.3 A Phononic Crystal with Double Defects

Imposing a secondary defect into a PnC with a single defect, as shown in Figure A-1 (d), leads to the change of some elements in both stiffness and mass matrices ($[\mathbf{K}_{\mathrm{sd}}(k_{\mathrm{sd}})]$ and $[\mathbf{M}_{\mathrm{sd}}]$) in the same manner as that of the single-defect case. $[\mathbf{K}_{\mathrm{dd}}(k_{\mathrm{dd}})]$ and $[\mathbf{M}_{\mathrm{dd}}]$ are the modified stiffness and mass matrices, respectively. Consequently, for the PnC with double defects, the eigenvalue problem in Equation (A.4) can be

modified as

$$\left(\left[\mathbf{K}_{\mathrm{dd}}\left(k_{\mathrm{sd}}\right)\right]-\omega_{\mathrm{dd}}{}^{2}\left[\mathbf{M}_{\mathrm{dd}}\right]\right)\left\{\mathbf{U}_{\mathrm{dd}}\right\}=\left\{\mathbf{0}\right\}. \tag{A.7}$$

Details of Equation (A.7) are available in below:

$$\left[\mathbf{M}_{\mathrm{dd}}\right]_{ij}=\begin{cases} m_{\mathrm{a}} & i=j=\text{odd number} \\ m_{\mathrm{b}} & i=j=\text{even number}\neq 2K,2K+2T \\ m_{\mathrm{defect}} & i=j=2K,2K+2T \\ 0 & \text{otherwise} \end{cases}, \tag{A.8}$$

$$\left[\mathbf{K}_{\mathrm{dd}}\right]_{ij}=\begin{cases} 2s_{\mathrm{eq}}^{\mathrm{unit}} & i=j\neq 2K,2K\pm 1,2K+2T,2K+2T\pm 1 \\ -s_{\mathrm{eq}}^{\mathrm{unit}} & i=j\pm 1\text{but }(i,j)\neq(2K,2K\pm 1),(2K\pm 1,2K), \\ & (2K+2T,2K+2T\pm 1),(2K+2T\pm 1,2K+2T) \\ -s_{\mathrm{eq}}^{\mathrm{unit}}e^{ik_{\mathrm{dd}}Nl_{\mathrm{unit}}} & (i,j)=(1,2N),(2N,1) \\ 2s_{\mathrm{eq}}^{\mathrm{defect}} & i=j=2K,2K+2T \\ s_{\mathrm{eq}}^{\mathrm{defect}}+s_{\mathrm{eq}}^{\mathrm{unit}} & i=j=2K\pm 1,2K+2T\pm 1 \\ -s_{\mathrm{eq}}^{\mathrm{defect}} & (i,j)=(2K,2K\pm 1),(2K\pm 1,2K), \\ & (2K+2T,2K+2T\pm 1),(2K+2T\pm 1,2K+2T) \\ 0 & \text{otherwise} \end{cases}. \tag{A.9}$$

Likewise, defect bands can be obtained by calculating a set of complex normalized wavenumbers $k_{\mathrm{dd}}Nl_{\mathrm{unit}}$ for frequencies within the band gap.

A.2.4 Planning for Band Structure Analysis

In the research outlined in this appendix, we considered a situation where the host and embedded mediums consist of aluminum and steel, respectively. Since both

density and Young's modulus of the steel are larger than those of the aluminum, the mechanical impedance of the steel, which is calculated by (density×Young's modulus)$^{1/2}$ is larger than that of the aluminum. Tables A-1 and A-2 summarize the geometric dimensions and material properties of each medium, respectively. The lattice constant (l_u) and length of the defect (l_d) are 10 cm and 5 cm, respectively. It is known that several previous studies present that the number of unit cells should be sufficiently large to guarantee the high accuracy of the supercell calculation [49-51]. Therefore, we considered twenty unit cells (N=20) are arranged in the incident wave direction. In the meantime, the steel stacks in the 9th and 11th unit cells (K=9 and T=2) are replaced with aluminum stacks as the initial and the secondary defects, respectively.

Table A-1 Geometric dimensions of aluminum and steel stacks.

Unit cell	Aluminum stack	Length, l_a	50 mm
		Height, h_a	10 mm
		Width, w_a	10 mm
	Steel stack	Length, l_b	50 mm
		Height, h_b	10 mm
		Width, w_b	10 mm

Table A-2 Material properties of aluminum and steel stacks.

Unit cell	Aluminum stack	Density, ρ_a	2,700 kg/m^3
		Young's modulus, Y_a	70 GPa
		Poisson's ration, v_a	0.33
	Steel stack	Density, ρ_b	7,850 kg/m^3
		Young's modulus, Y_b	200 GPa
		Poisson's ration, v_b	0.30

A.3 Band Gap Analysis for a Phononic Crystal without Defects

Band structures for a PnC without defects, shown in Figure A-2, are calculated using Equations (A.1) - (A.3). Lines with solid-blue and solid-red in Figure A-2, correspond to real and imaginary parts of the calculated complex normalized wavenumbers ($k_{wd}Nl_{unit}$), respectively. It is confirmed that two band gaps, colored in sky-blue boxes, are created in the band structures. In band gaps, a PnC oscillates in evanescent waves with non-real complex normalized wavenumbers [154, 155]. The real and imaginary parts of one non-real complex normalized wavenumber in a band gap govern the phase difference (sign) of the displacement fields and the exponentially attenuating rate of the evanescent waves, respectively [156]. The frequencies ($f_{bg,1}^{lower}$, $f_{bg,1}^{upper}$, and $f_{bg,1}^{lower}$) that correspond to the bounds of the band gaps can be calculated at the bounds (i.e., zero and π) of the Brillouin zone. With simple mathematical techniques, the frequencies $f_{bg,1}^{lower}$, $f_{bg,1}^{upper}$, and $f_{bg,1}^{lower}$ can be explicitly derived as:

$$
\begin{aligned}
f_{bg,1}^{lower} &= \frac{1}{2\pi}\sqrt{\frac{2s_{eq}^{unit}}{m_b}} \\
f_{bg,1}^{upper} &= \frac{1}{2\pi}\sqrt{\frac{2s_{eq}^{unit}}{m_a}} \\
f_{bg,2}^{lower} &= \frac{1}{2\pi}\sqrt{\frac{2s_{eq}^{unit}}{m_a}+\frac{2s_{eq}^{unit}}{m_b}}
\end{aligned}
\qquad \text{(A.10)}
$$

where $f_{bg,1}^{lower}$, $f_{bg,1}^{upper}$, and $f_{bg,1}^{lower}$ denote the lower and upper edges for the first band gap, and the lower edge of the second band gap, respectively. The first band gap

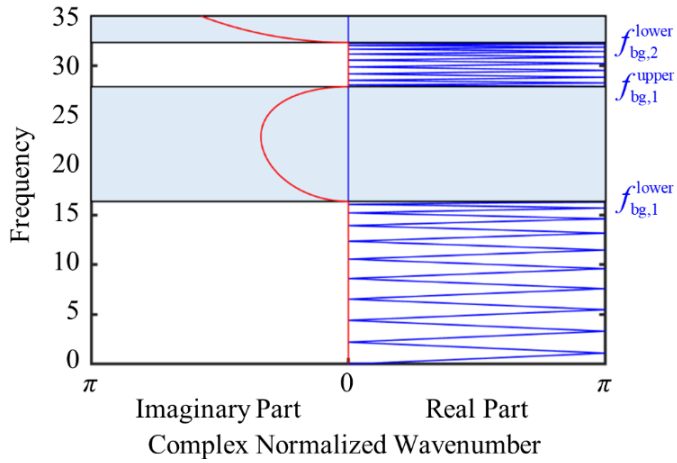

Figure A-2 Formation of band gaps with complex dispersion curves that are obtained from a lumped-parameter model of a one-dimensional PnC without defects under longitudinal elastic waves.

ranges from 16.36 kHz to 27.90 kHz. The second band gap's lower edge is at 32.34 kHz. Note that the band gap ranges, obtained by supercell calculation, are exactly equal to those obtained at a unit cell level. The only difference is that the passbands are folded N times when supercell calculation is applied into a set of N unit cell [157].

A.4 Principles of Formation of Defect Bands for a Phononic Crystal with a Single Defect

This section is dedicated to fundamentally elucidating principles of the formation of defect bands for a PnC with a single defect. With given values of system parameters,

Section A.4.1 shows the results of the formation of defect bands within the band gap and corresponding normalized displacement fields (so-called defect mode shapes) of the PnC. When applying the asymptotic analysis to defect band analysis, Section A.4.2 presents the limiting behaviors of the defect bands and defect mode shapes. Lastly, the comparison before and after asymptotic analysis is performed via an exponential regression model in Section A.4.3.

A.4.1 Formation of Defect Bands within Band Gaps and Corresponding Defect Mode Shapes

Defect bands for the PnC with the single defect, shown in Figure A-3, are calculated by Equations (A.4) - (A.6). Figure A-3 (a) shows that two defect bands are formed within the first band gap. Defect band frequencies of 18.29 kHz and 26.70 kHz are labeled as $f_{sd,1}$ and $f_{sd,2}$, respectively. Normalized displacement fields of crystals at the two defect band frequencies are illustrated in Figures A-3 (b) and A-3 (c), respectively. Here, the normalized displacement fields indicate the eigenvectors that are obtained from Equation (A.4) at the defect band frequencies. These calculations confirm that displacements of the defect or neighboring crystals are dramatically amplified. The defect has the maximum displacement in Figure A-3 (b). The two crystals adjacent to the defect have the maximum displacements, while the defect exhibits a near-zero displacement, as shown in Figure A-3 (c). It should be noted that the PnC with the single defect would behave as one of the defect mode shapes when longitudinal elastic waves enter the PnC at the corresponding defect band frequency.

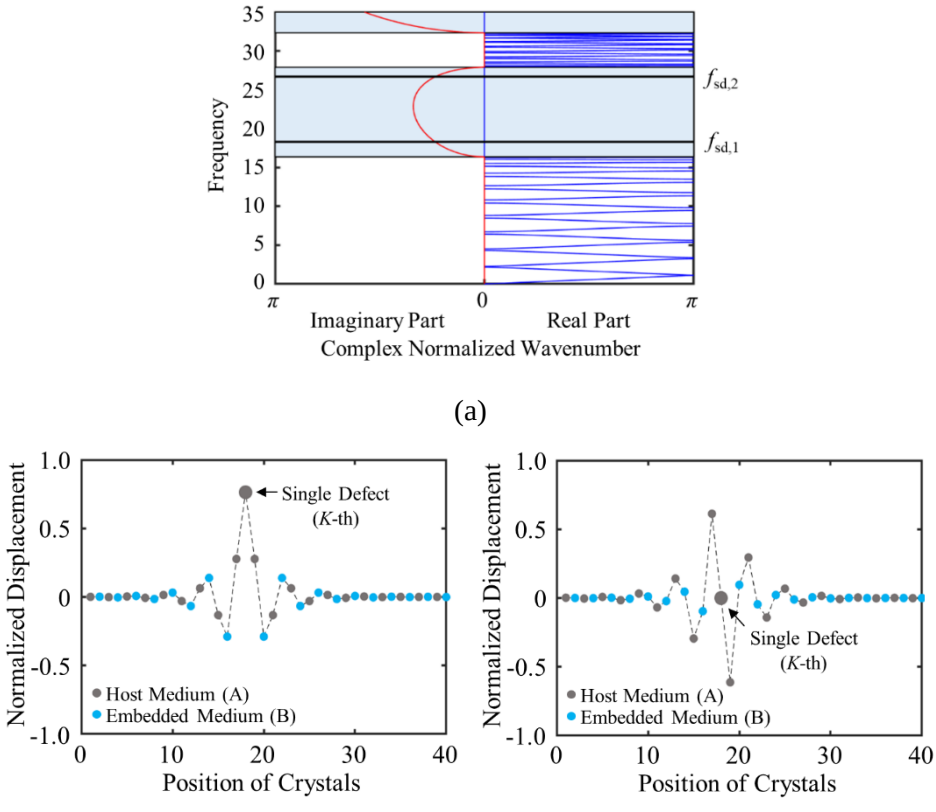

Figure A-3 Defect band analysis for a PnC with a single defect: (a) the formation of two defect bands within the first band gap; corresponding defect mode shapes at frequencies of (b) $f_{sd,1}$ and (c) $f_{sd,2}$.

A.4.2 Asymptotic Analysis of the Formation of Defect Bands

In Figure A-1 (c), the two embedded mediums, arranged in the (K-1)-th and (K+1)-th unit cells, surround the defect and the two adjacent crystals. When envisaging that the mass m_b of the embedded mediums becomes very large, the limiting behaviors of defect bands and corresponding defect mode shapes can be investigated.

Asymptotically equivalent behaviors of a PnC with a single defect may provide important keys to elucidating the fundamental principles of the formation of defect bands. Figure A-4 (a) depicts the asymptotic results of band structures with respect to the real parts of wavenumbers. Five flat bands are observed. Three of them ($f_{\mathrm{pb},1}^{\mathrm{lim(sd)}}$, $f_{\mathrm{pb},2}^{\mathrm{lim(sd)}}$, and $f_{\mathrm{pb},3}^{\mathrm{lim(sd)}}$) and the remaining bands ($f_{\mathrm{sd},1}^{\mathrm{lim}}$ and $f_{\mathrm{sd},2}^{\mathrm{lim}}$) are related to limiting behaviors of passbands and defect bands that are presented in Figure A-3 (a), respectively. The superscript 'lim' and the subscript 'pb' denote 'limiting behavior' and 'passband', respectively. Frequencies of $f_{\mathrm{pb},1}^{\mathrm{lim(sd)}}$, $f_{\mathrm{pb},2}^{\mathrm{lim(sd)}}$, and $f_{\mathrm{pb},3}^{\mathrm{lim(sd)}}$ are 0 kHz, 27.90 kHz, and 31.07 kHz, respectively. Those of $f_{\mathrm{sd},1}^{\mathrm{lim}}$ and $f_{\mathrm{sd},2}^{\mathrm{lim}}$ are 14.55 kHz, and 25.53 kHz, respectively.

The physical meanings of passbands $f_{\mathrm{pb},1}^{\mathrm{lim(sd)}}$ and $f_{\mathrm{pb},2}^{\mathrm{lim(sd)}}$ can be demonstrated using Equation (A.10). As the mass m_{b} of the embedded medium approaches infinity, it can be found that the lower edges $f_{\mathrm{bg},1}^{\mathrm{lower}}$ and $f_{\mathrm{bg},2}^{\mathrm{lower}}$ of the first and the second band gap converge to zero ($f_{\mathrm{pb},1}^{\mathrm{lim(sd)}}$) and to the upper edge $f_{\mathrm{bg},1}^{\mathrm{upper}}$($=f_{\mathrm{pb},2}^{\mathrm{lim(sd)}}$) of the first band gap, respectively. Thus, in asymptotic analysis, the whole frequency range – except for $f_{\mathrm{bg},1}^{\mathrm{upper}}$($=f_{\mathrm{pb},2}^{\mathrm{lim(sd)}}$) – can be thought of a band gap. This means that $f_{\mathrm{pb},1}^{\mathrm{lim(sd)}}$ and $f_{\mathrm{pb},2}^{\mathrm{lim(sd)}}$ are the limiting behaviors of the frequencies that encompass the band gap edges.

The frequencies $f_{\mathrm{sd},1}$ and $f_{\mathrm{sd},2}$ of the two defect bands in Figure A-3 (a) asymptotically converge to $f_{\mathrm{sd},1}^{\mathrm{lim}}$ and $f_{\mathrm{sd},2}^{\mathrm{lim}}$ in Figure A-4 (a), respectively. Figures A-4 (b) and A-4 (c) illustrate the normalized displacement fields at the converged defect band frequencies. In Section A.4, the set that includes the defect and the two adjacent crystals is called the 'inner crystals.' It can be found that all crystals – except for the inner crystals – have zero displacements. Further, mechanical behaviors of

both the defect and the two adjacent crystals in Figures A-4 (b) and A-4 (c) are considerably similar to those in Figures A-3 (b) and A-3 (c), respectively. This indicates that the formation of defect bands is closely associated with the limiting behaviors of crystals that surround both the defect and the adjacent crystals. The infinite mass condition means that the crystals have zero displacement, in spite of the external forces. They thus behave as fixed boundary conditions. On the other hand, a finite domain having boundary conditions can be defined even though the periodic unit cells are infinitely arranged. Then, mechanical resonance occurs at natural frequencies of the finite structure with 3-DOFs. The calculated natural frequencies are $f_{\mathrm{sd},1}^{\mathrm{lim}}$, $f_{\mathrm{sd},2}^{\mathrm{lim}}$ and $f_{\mathrm{pb},3}^{\mathrm{lim(sd)}}$. The asymptotic analysis shows that some crystals surrounding both the defect and the adjacent crystals behave as fixed-like boundary conditions. Further, mechanical resonance leads to the formation of defect bands. Therefore, defect mode shapes are associated with normal modes in vibrations, rather than propagating wave modes.

It is important to note here that the number of natural frequencies in asymptotic analysis is one more than the number of defect band frequencies in defect band analysis. A normalized displacement field of crystals at the natural frequency $f_{\mathrm{pb},3}^{\mathrm{lim(sd)}}$, illustrated in Figure A-4 (d), shows t that the displacement amplitudes near the defect are highly amplified due to mechanical resonance. However, a defect band corresponding to this frequency does not appear in the band gaps in Figure A-3 (a), since this frequency is involved in the passbands. This investigation provides an important clue related to the following question: how can some crystals behave as fixed-like boundary conditions? It can be inferred that the formation of fixed-like boundary conditions in a PnC with a defect would not be a result of simply breaking

the periodicity of unit cells by introducing a defect. Rather, this formation stems from some of the physical properties of the band gaps. In the following section, an in-depth analysis of the principles of the formation of fixed-like boundary conditions is presented.

A.4.3 Formation of Fixed-like Boundary Conditions by Band Gaps

When examining the displacement fields of crystals of the same medium except for the defect, Figures A-3 (b) and A-3 (c) show that the displacement signs sequentially change from positive to negative, or vice-versa. These results coincide with the trends of the displacement signs induced in the real parts (π in the first band gap) of the complex normalized wavenumbers in band gap analysis. This implies that band gaps play a role in defect modes.

To neglect the effects sign changes, absolute normalized displacement fields of the PnC at defect band frequencies $f_{sd,1}$ and $f_{sd,2}$ are shown in Figures A-5 (a) and A-5 (b), respectively. The solid red lines represent exponential regression models ($y=Ae^{-Bx}$; y is the normalized displacement; A is the initial displacement; B is the exponent; and x is the order of crystals) that are obtained from host mediums, arranged to the right of the defect. The exponents B are estimated as 0.738 and 0.732 in Figures A-5 (a) and A-5 (b), respectively. It is of great importance to emphasize that these exponents are almost equal to the values of the imaginary parts of the complex normalized wavenumbers at $f_{sd,1}$ and $f_{sd,2}$ in Figure A-3 (a). This supports that evanescent waves in band gaps exist throughout the defect mode shapes. Note that the exponential regression model can be also developed from the host mediums

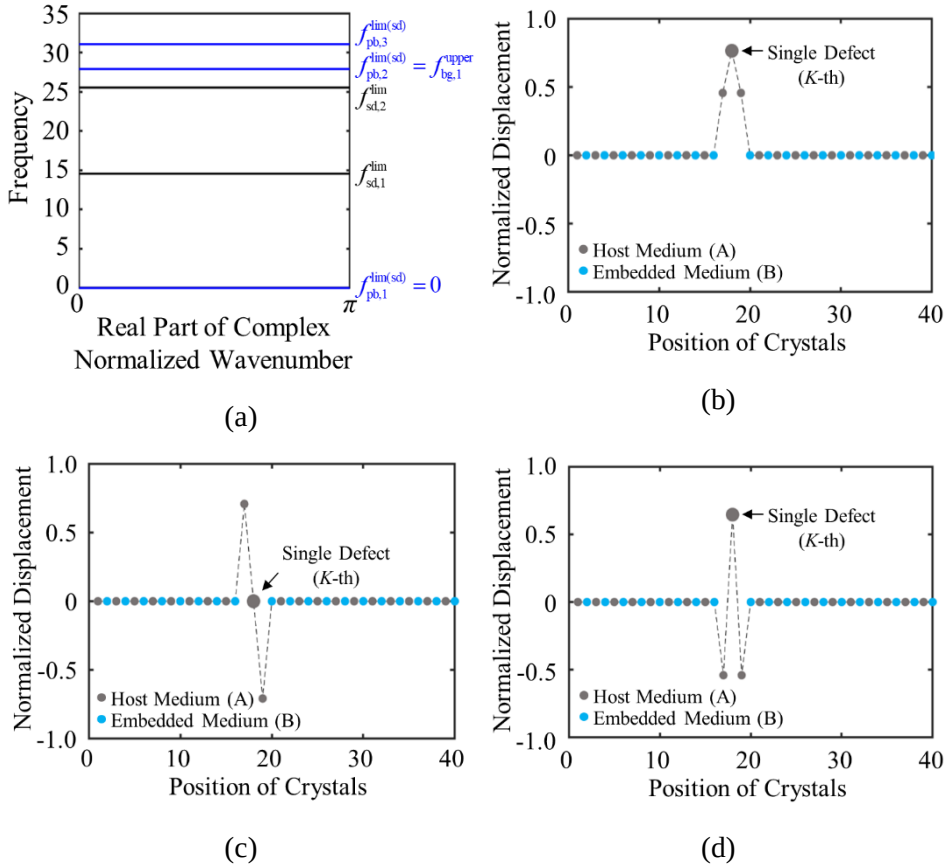

Figure A-4 Asymptotic analysis for a PnC with a single defect: (a) the limiting behaviors of passbands and two defect bands; normalized displacement fields at frequencies of (b) $f_{\mathrm{sd},1}^{\mathrm{lim}}$, (c) $f_{\mathrm{sd},2}^{\mathrm{lim}}$, and (d) $f_{\mathrm{pb},3}^{\mathrm{lim(sd)}}$.

arranged at two unit-cell intervals, which have the same displacement signs, for the defect mode shapes shown in Figure A-3.

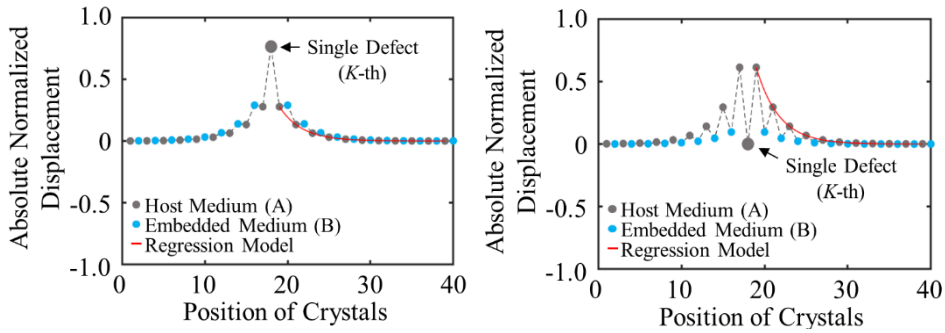

Figure A-5 Absolute normalized displacement fields a PnC with a single defect at frequencies of (a) $f_{sd,1}$ and (b) $f_{sd,2}$.

There are two underlying characteristics of evanescent waves. First, the displacement amplitude exponentially decays and converges to zero in a particular direction. Second, compared with the propagating waves, evanescent waves do not travel along with structures, like standing waves and vibrations. Due to the evanescent waves' attenuating properties, some crystals away from the single defect get near-zero displacements; thus, they behave as fixed-like boundary conditions. When applying asymptotic analysis to crystals significantly away from the defect, to ensure enough attenuation, defect band frequencies in the defect band analysis will be close to natural frequencies in the asymptotic analysis. This interpretation is consistent with the previous studies' statement that the number of unit cells should be sufficiently large to guarantee high accuracy of the supercell calculation [93, 94]. Further, mechanical resonance observed in vibrations is analogous to the second characteristic of evanescent waves. Therefore, the band gap is a prerequisite for

defect-mode-induced energy localization because the fixed-like boundary conditions, created by evanescent waves in the band gap, lead to mechanical resonance at natural frequencies and, furthermore, to the formation of defect bands within the band gap.

A.5 Principles of Splitting of Defect Bands for a Phononic Crystal with Double Defects

This section is dedicated to fundamentally elucidating principles of the splitting of defect bands for a PnC with double defects. With given values of system parameters, Section A.5.1 shows the results of the splitting of defect bands for the case of the single defect and defect mode shapes of the PnC. Similar to Section A.4.2, Section A.5.2 presents the limiting behaviors of the defect bands and defect mode shapes. Lastly, similar to Section A.4.3, an exponential regression model is used for comparison before and after asymptotic analysis in Section A.5.3.

A.5.1 Splitting of Defect Bands within Band Gaps and Corresponding Defect Mode Shapes

Defect bands for the PnC with the single defect, shown in Figure A-6, are calculated by Equations (A.7) - (A.10). Figure A-6 (a) depicts that the two defect bands, shown in Figure A-3 (a), are split into four bands; the corresponding frequencies, labeled from $f_{dd,1}$ to $f_{dd,4}$, are 16.90 kHz, 19.02 kHz, 26.19 kHz, and 27.60 kHz, respectively. Figures A-6 (b) to A-6 (e) illustrate the corresponding defect mode shape at each defect band frequency, respectively. Comparison of Figures A-3 and A-6 confirms

that the defect mode shape at each defect band frequency observed in a single defect case is all maintained after the splitting of defect bands occurs with double defects. Although the defect mode shapes are maintained at two frequencies of the split defect bands, they behave differently. The double defects present out-of-phase and in-phase behaviors at the lower and upper frequencies of the split-defect bands, respectively, as [59, 94].

A.5.2 Asymptotic Analysis of the Splitting of Defect Bands

In Figure A-1 (d), the two embedded mediums, arranged in the (K-1)-th and (K+3)-th unit cells, enclose the double defects, the two neighboring crystals outward from the defects, and the three crystals between the defects. Here and hereafter, we call the set of these seven crystals (including the double defects) 'inner crystals'. We consider a situation where the mass m_b of the remaining embedded mediums, except for one arranged between the double defects, approaches infinity. Figure A-7 (a) depicts the asymptotic results of band structures with respect to the real parts of wavenumbers. Nine flat bands are observed. Five of them ($f_{\mathrm{pb},1}^{\mathrm{lim(dd)}}$, $f_{\mathrm{pb},2}^{\mathrm{lim(dd)}}$, $f_{\mathrm{pb},3}^{\mathrm{lim(dd)}}$, $f_{\mathrm{pb},4}^{\mathrm{lim(dd)}}$, and $f_{\mathrm{pb},5}^{\mathrm{lim(dd)}}$) and the remaining bands ($f_{\mathrm{dd},1}^{\mathrm{lim}}$, $f_{\mathrm{dd},2}^{\mathrm{lim}}$, $f_{\mathrm{dd},3}^{\mathrm{lim}}$, and $f_{\mathrm{dd},4}^{\mathrm{lim}}$) are associated with the limiting behaviors of passbands and defect bands, respectively. Frequencies from $f_{\mathrm{pb},1}^{\mathrm{lim(dd)}}$ to $f_{\mathrm{pb},5}^{\mathrm{lim(dd)}}$ are 0 kHz, 5.59 kHz, 27.90 kHz, 31.07 kHz, and 31.90 kHz, respectively. Those from $f_{\mathrm{dd},1}^{\mathrm{lim}}$ to $f_{\mathrm{dd},4}^{\mathrm{lim}}$ are 14.65 kHz, 17.46 kHz, 25.53 kHz, and 27.76 kHz, respectively.

Similar to the single-defect case, $f_{\mathrm{pb},1}^{\mathrm{lim(dd)}}$ and $f_{\mathrm{pb},3}^{\mathrm{lim(dd)}}$ are the asymptotic results of the passbands, involved in band gap edges. The whole frequency range –

except for $f_{pb,3}^{lim(dd)}$ ($=f_{bg,1}^{up}$) – becomes a band gap. The frequencies from $f_{dd,1}$ to $f_{dd,4}$ in Figure A-6 (a) asymptotically converge to those from $f_{dd,1}^{lim}$ to $f_{dd,4}^{lim}$ in Figure A-7 (a), respectively. Figures A-7 (b) to A-7 (h) depict the normalized displacement fields at these frequencies, except for $f_{pb,1}^{lim(dd)}$ and $f_{pb,3}^{lim(dd)}$. Mechanical behaviors of inner crystals in Figures A-7 (c) to A-7 (f) are in agreement with those in Figures A-6 (b) to A-6 (e), respectively. This result provides the following implication. First, the double defects are mechanically coupled with each other in terms of the masses and springs of the crystals (or unit cells) between them. Second, some crystals surrounding the inner crystals (including both defects) behave as fixed-like boundary conditions, resulting in mechanical resonance. A PnC with double defects would be a system in which the double defects vibrate with synchronous motions as normal modes in vibrations. This interpretation is analogous to that of the single-defect case. The splitting of defect bands is thus traced to both the mechanical coupling and the formation of fixed-like boundary conditions. The asymptotic analysis provides a critical message that the fixed-like boundary conditions, aided by the mechanical coupling, contributes to the splitting of defect bands.

Since the finite structure of inner crystals has 7-DOFs, it is important to point out that the number of natural frequencies in asymptotic analysis is three more than defect band frequencies in defect band analysis. Despite the high amplification of displacement amplitudes of double defects at natural frequencies $f_{pb,2}^{lim(dd)}$, $f_{pb,4}^{lim(dd)}$, and $f_{pb,5}^{lim(dd)}$, as illustrated in Figures A-7 (b), A-7 (g), and A-7 (h), defect bands corresponding to these frequencies do not appear in band gaps, shown in Figure A-6 (a), since these frequencies are involved in the passband ranges. Therefore, the formation of fixed-like boundary conditions in a PnC with double defects would also

stem from the exponentially attenuating properties of evanescent waves in the band gaps. In the following section, to support this interpretation, evanescent wave fields in a PnC with double defects are compared with the exponential regression models.

A.5.3 Formation of Fixed-like Boundary Conditions by Band Gaps

Similar to the single-defect case, displacement fields of the same mediums outward from the double defects in Figures A-6 (b) to A-6 (e) show that the displacement signs sequentially change from positive to negative, or vice-versa. Absolute normalized displacement fields of the PnC at defect band frequencies from $f_{dd,1}$ and $f_{dd,4}$ are shown in Figures A-8 (a) to A-8 (d), respectively. Exponents of the exponential regression model ($y=Ae^{-Bx}$) that are obtained from host mediums, arranged to the right of the defect, are calculated as 0.396, 0.840, 0.837, and 0.409 for each defect mode shape, respectively. As expected, these exponents are almost equal to the values of the imaginary parts of the complex normalized wavenumbers at frequencies from $f_{dd,1}$ to $f_{dd,4}$ in Figure A-6 (a). This observation supports that the exponentially attenuating properties of evanescent waves make some crystals, away from both double defects, behave as fixed-like boundary conditions. This leads to mechanical resonance at natural frequencies and, furthermore, to the splitting of defect bands that is aided by mechanical coupling.

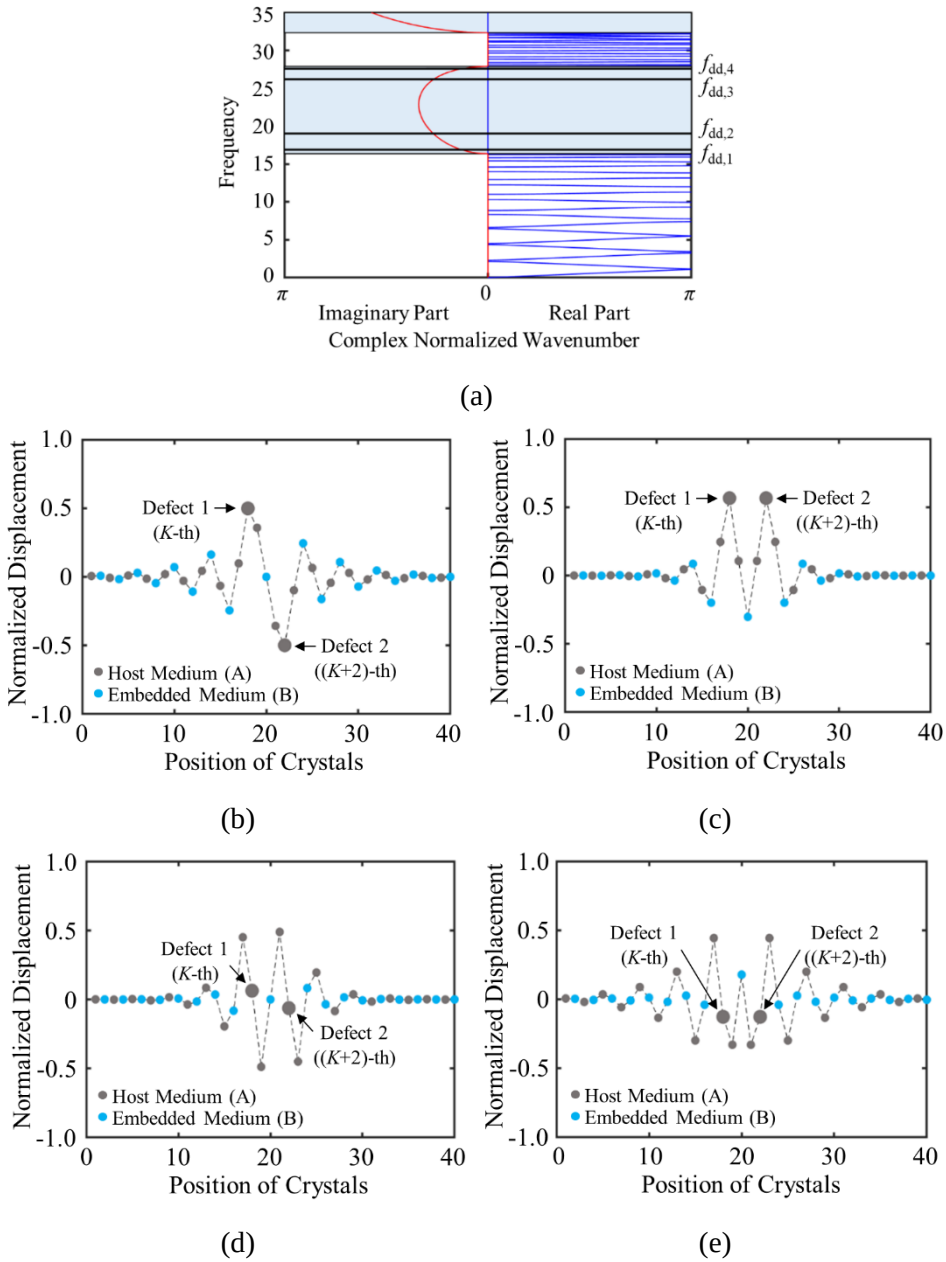

Figure A-6 Defect band analysis for a PnC with double defects: (a) the splitting of two defect bands into four defect bands; corresponding defect mode shapes at frequencies of (b) $f_{dd,1}$, (c) $f_{dd,2}$, (d) $f_{dd,3}$, and (e) $f_{dd,4}$.

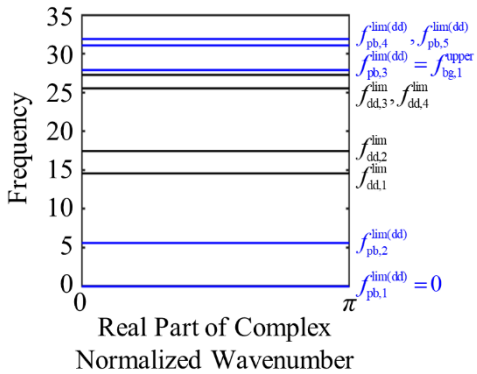
Frequency
Real Part of Complex
Normalized Wavenumber

(a)

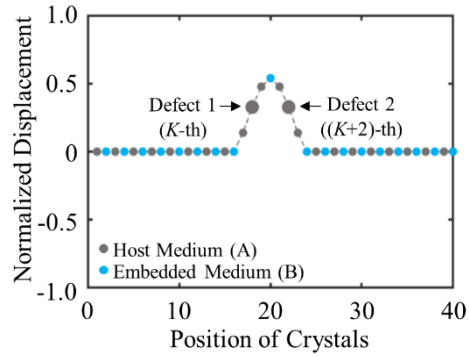
Normalized Displacement
Defect 1
(K-th)
Defect 2
((K+2)-th)
Host Medium (A)
Embedded Medium (B)
Position of Crystals

(b)

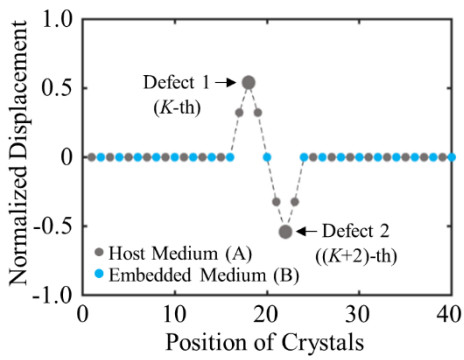
Normalized Displacement
Defect 1
(K-th)
Defect 2
((K+2)-th)
Host Medium (A)
Embedded Medium (B)
Position of Crystals

(c)

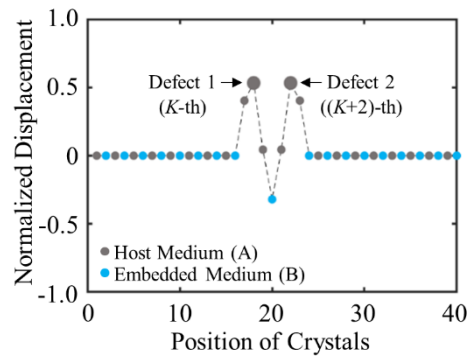
Normalized Displacement
Defect 1
(K-th)
Defect 2
((K+2)-th)
Host Medium (A)
Embedded Medium (B)
Position of Crystals

(d)

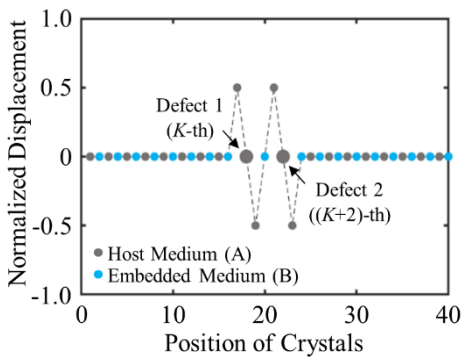
Normalized Displacement
Defect 1
(K-th)
Defect 2
((K+2)-th)
Host Medium (A)
Embedded Medium (B)
Position of Crystals

(e)

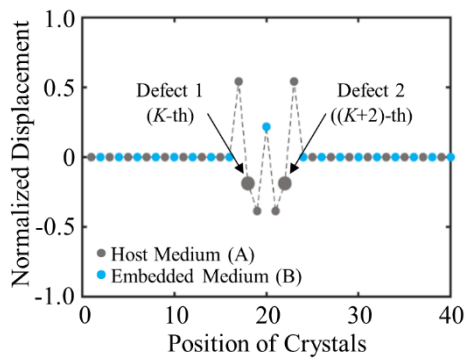
Normalized Displacement
Defect 1
(K-th)
Defect 2
((K+2)-th)
Host Medium (A)
Embedded Medium (B)
Position of Crystals

(f)

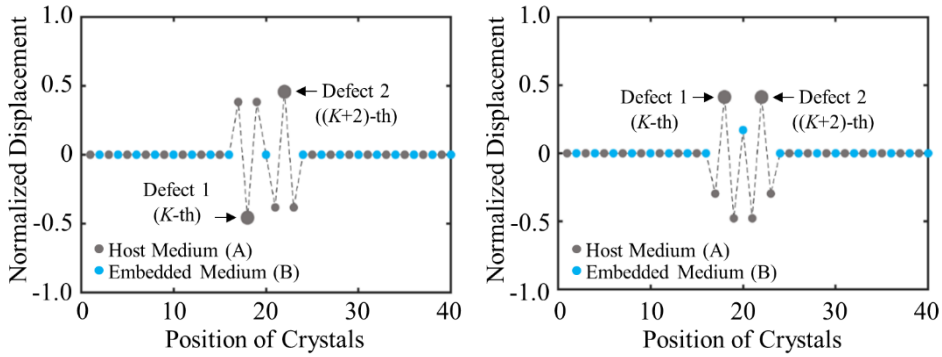

(g) (h)

Figure A-7 Asymptotic analysis for a PnC with double defects: (a) limiting behaviors of passbands and four defect bands; normalized displacement fields at frequencies of (b) $f_{\mathrm{pb},2}^{\mathrm{lim(dd)}}$, (c) $f_{\mathrm{dd},1}^{\mathrm{lim}}$, (d) $f_{\mathrm{dd},2}^{\mathrm{lim}}$, (e) $f_{\mathrm{dd},3}^{\mathrm{lim}}$, (f) $f_{\mathrm{dd},4}^{\mathrm{lim}}$, (g) $f_{\mathrm{pb},4}^{\mathrm{lim(dd)}}$, and (h) $f_{\mathrm{pb},5}^{\mathrm{lim(dd)}}$.

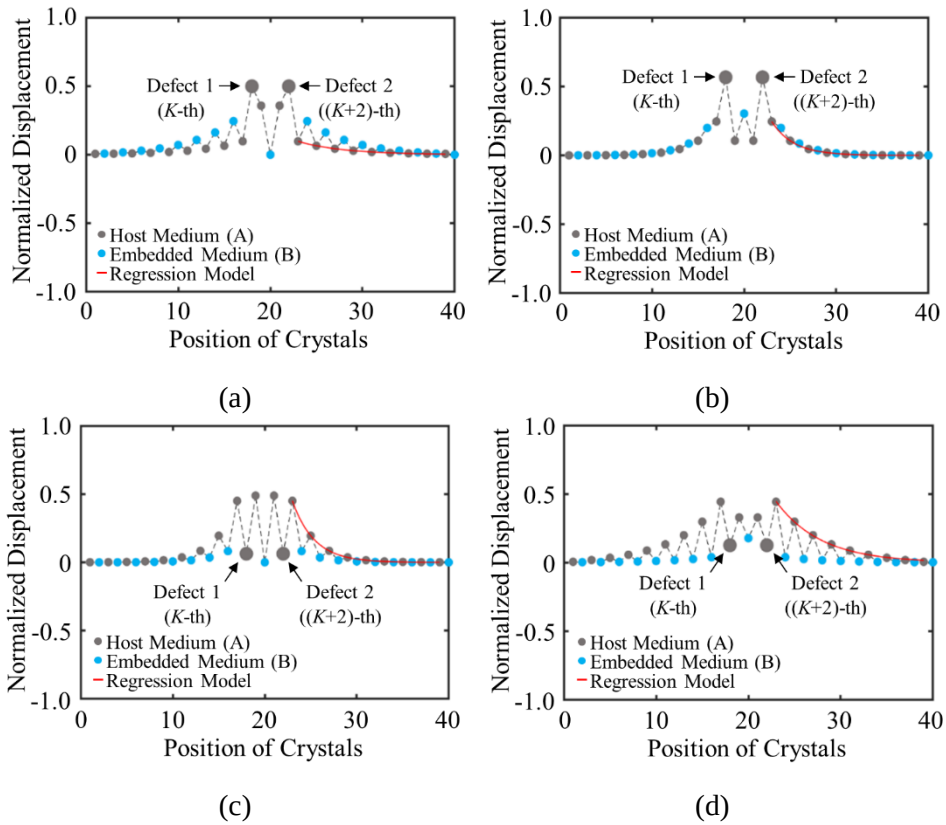

Figure A-8 Absolute normalized displacement fields at frequencies of (a) $f_{dd,1}$, (b) $f_{dd,2}$, (c) $f_{dd,3}$, and (d) $f_{dd,4}$.

A.6 Summary and Discussion

Several prior research efforts have been dedicated to comprehensively exploring energy localization that leverages a defect mode of a PnC with single defect from phenomenon observation to potential applications (e.g., PEH) under elastic waves. However, no further in-depth consideration has been made on demonstrating the fundamental principles of the formation of defect bands at certain frequencies.

Moreover, there are several attempts to investigate double defect modes of a PnC. When double defects are created sufficiently close to each other along the incident wave direction inside a PnC, it has been presented that one of the double defects is coupled to the other defect and this coupling generates splitting of defect bands for the single defect case. However, there is no further investigation of what the physical meaning of the coupling is and how the coupling leads to the splitting of defect bands. Since the ultimate goal of the PnC-based PEH system with defects is to enhance the PEH performance by matching the defect band frequencies with the operating frequencies, it is of great importance to fully understand the underlying physics of the formation and splitting of defect bands.

This appendix elucidated the fundamental principles of the formation and splitting of defect bands for PnCs with single and double defects, respectively, by applying asymptotic analysis into defect band analysis. A M-DOF mass-spring system of a one-dimensional PnC with single or double defects was studied When the masses of some crystals that surrounded the defects and the neighboring crystals approached infinity, the asymptotically equivalent behaviors of defect-band frequencies and corresponding defect-mode shapes represented the formation of fixed-like boundary conditions. Mechanical resonance, induced by the fixed-like boundary conditions, resulted in the formation and splitting of defect bands. Thus, defect mode shapes are associated with normal modes in vibrations, rather than propagating wave modes. Moreover, by comparing the exponentially attenuating rate of displacement fields with the imaginary part of the complex normalized wavenumber in band gaps, we found that evanescent wave fields, the main characteristics of band gaps, attributed to the formation of fixed-like boundary

conditions. This study suggested that the band gap was the premise of defect-mode-enabled energy localization from the viewpoint of mechanical resonance formation, not merely from the perspective of periodicity breaking.

As a potential application of this study, the presented approach can reduce the amount of time required for defect band calculation when designing a PnC with defects to have a desired defect mode shape near a target excitation frequency. Using the proposed approach, we can achieve a good approximation of both defect bands and defect mode shapes in much less time by performing modal analysis on a reduced regime of unit cells that includes defects with fixed boundary conditions.

Sections of this appendix have been published or submitted as the following journal articles:

1) **Soo-Ho Jo**, Heonjun Yoon, Yong Chang Shin, and Byeng D. Youn, "Why Can Elastic Waves Be Localized in Phononic Crystals with Defects?," *International Journal of Mechanical Sciences*, Submitted, 2021.

Appendix B

An Electroelastically Coupled Analytical Model for a Phononic Crystal with a Piezoelectric Defect for Energy Harvesting under Longitudinal Waves

Appendix A was devoted to fundamentally elucidating the formation (for a single defect) and splitting (for double defects) of defect bands by using M-DOF mass-spring systems of PnCs with single or double defects. The lumped-parameter model is useful for intuitively analyzing physical phenomena, but it is well-known that the model accuracy of predicting physical quantities is considerably lower than continuum-mechanics-based distributed models. Moreover, compared with a case in the absence of PEH devices, a new physical phenomenon, called electroelastic coupling, is newly incorporated into the PnC domain.

To predict mechanical and electrical responses of a PnC-based PEH system that leverages a defect mode of a PnC, most of previous studies have focused on numerical models, such as finite element method (FEM) [66-68, 73-75]. However,

little research effort has been made to date to develop an electroelastically coupled analytical model of a PnC with a piezoelectric defect for PEH. Compared with numerical methods, it is well known that an analytical model has primary advantages that include (1) calculating output responses in a cost-effective manner and (2) representing the explicit relationships between the physical behaviors of the target system and input variables, via physical parameterization [125]. When developing the analytical model for our engineering problem, the following two issues can arise. First, the inertia and stiffness of the PEH device should be considered. This is important, because when attaching a PEH device to a defect, defect band frequencies are changed due to the inertia and stiffness effects, as outlined in [73, 75]. Second, the electroelastically coupling of a PEH device should be taken into account when calculating output performance of PEH. Since the effective stiffness of a piezoceramic material depends on a given electrical boundary condition [19-21], defect band frequencies can be shifted accordingly, as presented in [158]. If an excitation frequency does not align with the shifted defect band frequency, the output electric power will be significantly decreased. To match the defect band frequencies with the operating frequencies in future, these issues should be addressed.

This appendix thus proposes an electroelastically coupled analytical model of a one-dimensional PnC with a piezoelectric defect under longitudinal elastic waves. The proposed analytical model enables prediction of the output electric power and the defect bands while considering the inertia, stiffness, and electroelastic coupling effects of a PEH device. First, an electroelastically coupled transfer matrix is developed for a structure where PEH devices are fully attached. In this work, a transfer matrix relates vectors of the velocity and force at both ends of the structure.

Newton's 2nd law and constitutive equations of linear piezoelectricity are used to derive a mechanical equation of motions. Gauss's law and Kirchhoff's law are used to derive an electrical circuit equation. By solving these coupled equations with the help of Green's function, the electroelastically coupled transfer matrix is derived in an explicit manner. Using the derived electroelastically coupled transfer matrix, band structures (i.e., defect band frequency and defect mode shape) and output performance of PEH (i.e., output voltage, current, and electric power) are calculated based on TMM and SPM, respectively. To evaluate the model's predictive capability, the results of the proposed electroelastically coupled analytical model are compared with those of FEM. To the best of the authors' knowledge, the unique contributions of this study are two-fold. First, this work is the first attempt to propose an electroelastically coupled analytical model of a PnC with a piezoelectric defect for energy harvesting. Second, an electroelastically coupled transfer matrix is parameterized in an explicit manner for a structure to which PEH devices are attached while considering both forward and backward electroelastic coupling.

The remainder of Appendix B is organized as follows. Section B.1 describes system configuration under consideration and modeling assumption. Section B.2 demonstrates the derivation of an electroelastically coupled transfer matrix for a structure to which piezoelectric materials are attached. By using the proposed electroelastically coupled transfer matrix, Section B.3 presents the proposed methods for predicting defect bands and PEH performance based on TMM and SPM, respectively. Section B.4 outlines the predictive capability evaluation of the proposed electroelastically-coupled analytical model of a PnC with a piezoelectric defect, as compared with FEM. Section B.5 presents the application of the proposed

analytical model into design optimization for the purpose of matching the defect band frequency with an operating frequency while maximizing the output electric power across an optimal external electrical resistance. Finally, the conclusions of this work are provided in Section B.6.

B.1 System Configuration and Modeling Assumption for an Electroelastic Coupled Analytical Model

The unit cell under consideration is a one-dimensional, bi-layered stack consisting of a host medium (colored in gray and dark gray) and an embedded medium (colored in sky-blue), as shown in Figure B-1 (a). In this appendix, subscripts m and M stand for the host stack and embedded stack, respectively. In the unit cell, there are six geometric variables, including the length l_m, height h_m, and width w_m of the host stack, as well as those of the embedded stack. The height and width of the embedded stack (h_M and w_M) are the same as those of the host stack (h_m and w_m), respectively. The lattice constant of the unit cell is denoted as l_{unit}, calculated by l_m+l_M.

A PnC is built by arranging N unit cells in the x-direction. In this study, the unit cells' periodicity is locally broken by substituting the embedded material in the K-th unit cell with the host material while the length l_M of the embedded stack is maintained. Since the replaced beam and two adjacent stacks consist of the same material, a set of these three stacks is called a defect in this study. The length l_{defect} of the defect is obtained from $2l_m+l_M$. Bimorph PEH devices, colored in dark-yellow, are attached at the center of the top and bottom surfaces of the defect. In the PEH

device, there are three geometric variables, including the length l_p, height h_p, and width w_p. In this study, the width of the PEH device (w_p) is the same as that of the host stack (w_m). To satisfy the classical rod theory's assumptions, we assume that the heights (h_m, h_M, and h_p) of the stacks and PEH devices are much smaller than the other geometric dimensions of them.

Figure B-1 (b) shows an enlarged view of a piezoelectric defect with an electrical circuit configuration. Here, a series connection between the PEH devices is under consideration. The top electrode of the upper PEH device and the bottom electrode of the lower PEH device are connected with the external electrical resistance R_{load}. The thickness of the electrodes, colored in blue, is assumed to be negligible. The PEH devices are assumed to be transversely isotropic piezoceramic (e.g., PZT-5A and PZT-5H) and poled only in the *z*-direction.

Assuming that the PEH devices are perfectly bonded to the host medium, the structure in Figure B-1 (b) is regarded as an effective medium [125, 159]. The effective medium vibrates only in the longitudinal direction (i.e., *x*-direction) due to axial forces. Then, the mass and stiffness of the effective medium per unit length can be denoted as m_{eff} and s_{eff}, respectively, which are calculated by

$$m_{\text{eff}} = \rho_{\text{m}} h_{\text{m}} w_{\text{m}} + 2\rho_{\text{p}} h_{\text{p}} w_{\text{p}}, \tag{B.1}$$

$$s_{\text{eff}} = Y_{\text{m}} h_{\text{m}} w_{\text{m}} + 2c_{11}^{E} h_{\text{p}} w_{\text{p}}, \tag{B.2}$$

where notations ρ and Y are the density and Young's modulus of the stacks; and c_{11}^{E} is the elastic constant of the PEH devices at a constant electric field E, which is calculated by an inverse of the compliance s_{11}^{E} of them in accordance with the

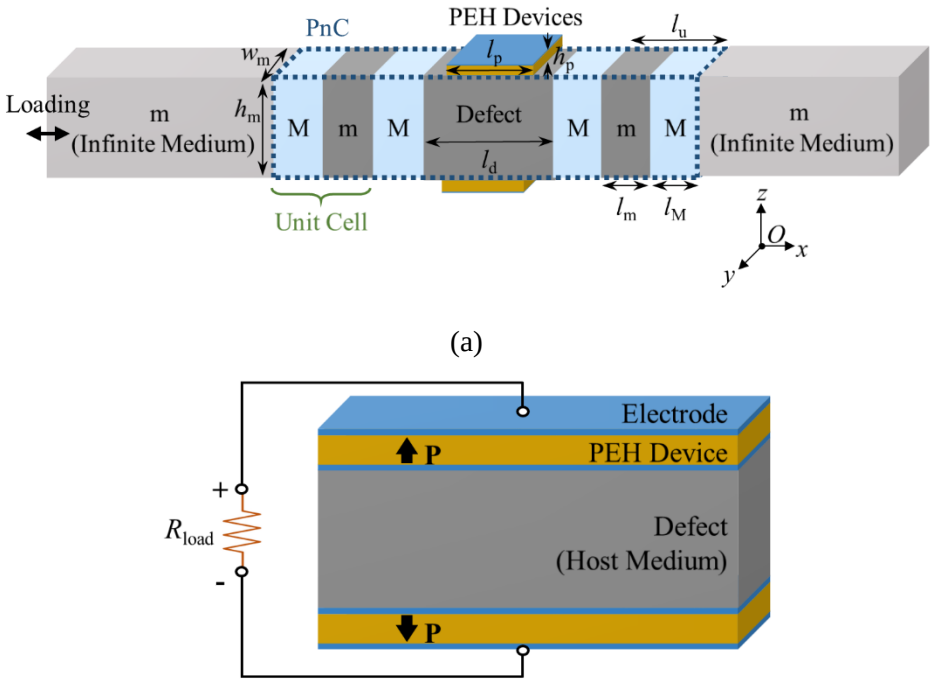

Figure B-1 A PnC-based PEH system with a defect: (a) a schematic view and (b) an enlarged view of a piezoelectric defect, with an electrical circuit configuration.

classical rod theory. The inertia and stiffness effects of PEH devices are considered in the second terms of right-hand sides of Equations (B.1) and (B.2), respectively.

B.2 Derivation of an Electroelastically Coupled Transfer Matrix

This section explains the derivation of a transfer matrix when bimorph PEH devices

are attached to a host structure and they are electroelastically coupled. Sections B.2.1 and Section B.2.2 demonstrate the derivation of mechanical equation of motions and electrical circuit equation, respectively. From the solutions of two governing equations, the derivation of the electroelastically coupled transfer matrix is presented in Section B.2.3.

B.2.1 Mechanical Equation of Motions

The *x*-directional displacement and axial force at an arbitrary space *x* and time *t* are denoted as $u(x, t)$ and $f(x, t)$, respectively. The axial force $f(x, t)$ applied to the effective medium in Figure B-1 (b) is a sum of the forces applied to each cross-section of the host medium and PEH devices. For an infinitesimal element *dx*, Newton's 2nd law provides the partial differential equation that governs the longitudinal motions in the effective medium as

$$m_{\text{eff}} \frac{\partial^2 u}{\partial t^2} = h_{\text{m}} w_{\text{m}} \frac{\partial \sigma_{\text{m}}}{\partial x} + 2 h_{\text{p}} w_{\text{p}} \frac{\partial \sigma_{\text{p}}}{\partial x} . \tag{B.3}$$

The notations σ_{m} and σ_{p} denote stresses that are loaded in the normal direction of each cross-section of the host medium and one PEH device, respectively.

If the magnitude of the normal strain $|\partial u/\partial x|$ is small, the normal stress σ_{m} is proportional to the normal strain $\partial u/\partial x$ with a coefficient of Young's modulus Y_{m}; this is called Hooke's law. Under plane stress conditions in the *y*-direction, a stress-charge form of the constitutive relations of linear piezoelectricity can be reduced [20] as

$$\begin{bmatrix} \sigma_{\mathrm{p}} \\ D \end{bmatrix} = \begin{bmatrix} c_{11}^{E} & -e_{31} \\ e_{31} & \varepsilon_{33}^{S} \end{bmatrix} \begin{bmatrix} \dfrac{\partial u}{\partial x} \\ E \end{bmatrix}, \tag{B.4}$$

where D is an electric displacement; e_{31} is a piezoelectric constant; and ε_{33}^{S} is the dielectric permittivity at a constant strain. Note that the normal stress σ_{p} and electric displacement D of the PEH device are electroelastically coupled due to the piezoelectric constant e_{31}. Substituting Hooke's law and Equation (B.4) into Equation (B.3) leads to

$$m_{\mathrm{eff}} \frac{\partial^2 u}{\partial t^2} = s_{\mathrm{eff}} \frac{\partial^2 u}{\partial x^2} - 2h_{\mathrm{p}} w_{\mathrm{p}} e_{31} \frac{\partial}{\partial x} \left\{ E\left[H\left(x\right) - H\left(x - l_{\mathrm{p}}\right) \right] \right\}, \tag{B.5}$$

where $H(*)$ is the Heaviside unit step function representing an area covered by the PEH devices [125]. It is of great importance to note that the electric field E is a function of only time t. Thus, the piezoelectric coupling term will vanish when we differentiate it with respect to x to derive the mechanical equation of longitudinal motions. Motivated by this, the electrical term should be multiplied by $H(x)$-$H(x$-$l_{\mathrm{p}})$, that enables to ensure the survival of the backward coupling term when differentiating it with respect to the space x. Even though this mathematical technique has been used in the field of vibration energy harvesting [29, 30, 125], it is a pioneering work to derive the electroelastically coupled transfer matrix of a PnC with a piezoelectric defect for elastic wave energy harvesting where the use of the Heaviside unit step function sets our study apart from previous research for wave energy harvesting [160, 161].

The output voltage $\upsilon(t)$ generated by the PEH devices is assumed to be spatially

uniform over the attachment area. For the series connection, the top and the bottom piezoelectric patches have different sign of the piezoelectric constant e_{31} since the poling direction is opposite. Therefore, the electric fields E in the top and the bottom piezoelectric patches are poled in the same direction, which are expressed as [29, 162]

$$E = -\frac{\upsilon(t)}{2h_{\mathrm{p}}}. \tag{B.6}$$

Finally, the mechanical equation of motion under longitudinal elastic waves can be expressed as

$$m_{\mathrm{eff}}\frac{\partial^2 u}{\partial t^2} - s_{\mathrm{eff}}\frac{\partial^2 u}{\partial x^2} = e_{31}w_{\mathrm{p}}\upsilon(t)\left[\delta(x) - \delta\left(x - l_{\mathrm{p}}\right)\right], \tag{B.7}$$

which takes the inertia, stiffness, and the piezoelectric coupling of the PEH devices into account. Here, $\delta(x)$ and $\delta(x\text{-}l_{\mathrm{p}})$ are the Dirac delta functions, the derivatives of the Heaviside unit step functions $H(x)$ and $H(x\text{-}l_{\mathrm{p}})$ with respect to x, respectively. It can be shown that the derived mechanical equation of motion is a form of an inhomogeneous 2nd order partial differential equation.

B.2.2 Electrical Circuit Equation

An electrical circuit equation plays an important role in quantifying the output voltage $\upsilon(t)$ (or electric current $i(t)$) generated by the PEH devices in response to their mechanical strain. Followed by Gauss's law, the electric current $i(t)$ can be calculated in terms of the electric displacement D as

$$i(t) = \frac{d}{dt}\left(\int_{S_p} D dS \right), \tag{B.8}$$

where S_p is the top surface area of the PEH devices, and dS is an infinitesimal surface area. By substituting Equation (B.6) into Equation (B.4), the electric displacement D can be rewritten as

$$D = e_{31} \frac{\partial u}{\partial x} - \varepsilon_{33}^{S} \frac{\upsilon(t)}{2h_p}. \tag{B.9}$$

By substituting Equation (B.9) into Equation (B.8), the electric current $i(t)$ generated by the PEH devices can be obtained as

$$i(t) = e_{31} w_p \frac{\partial}{\partial t}\left(\int_0^{l_p} \frac{\partial u}{\partial x} dx \right) - \frac{C_p}{2} \frac{d\upsilon(t)}{dt}, \tag{B.10}$$

where C_p denotes the capacitance of one PEH device, which is defined as

$$C_p = \frac{\varepsilon_{33}^{S} w_p l_p}{h_p}. \tag{B.11}$$

Note that the electric current $i(t)$ across the external electrical resistance R_{load} is expressed as $\upsilon(t)/R_{load}$. From Kirchhoff's law, the electric current $i(t)$ generated by the piezoelectric patches should be equal to $\upsilon(t)/R_{load}$. Note that the definite integral in the right-hand side of Equation (B.10) has the finite range from the left end (x=0) to the right end (x=l_p) of the effective medium. The differentiation with respect to time t – and the definite integral with respect to position x – indicate the variation of slope difference between the left and right ends of the effective medium over time

t. By rearranging Equation (B.10), therefore, the electric circuit equation is derived as

$$\frac{C_{\mathrm{p}}}{2}\frac{d\upsilon(t)}{dt}+\frac{\upsilon(t)}{R_{\mathrm{load}}}=e_{31}w_{\mathrm{p}}\left(\left.\frac{\partial u}{\partial t}\right|_{x=l_{\mathrm{p}}}-\left.\frac{\partial u}{\partial t}\right|_{x=0}\right). \tag{B.12}$$

Unlike the previous works [163-166], this study considers the non-uniform strain field along the x-direction in deriving an electroelastically coupled transfer matrix while accounting for the backward as well as forward electroelastic coupling.

B.2.3 Electroelastically Coupled Transfer Matrix

Assuming that the effective medium vibrates in harmonic motions over time, the displacement $u(x, t)$, axial force $f(x, t)$, and output voltage $\upsilon(t)$, are expressed as $\boldsymbol{U}(x)e^{i\omega t}$, $\boldsymbol{F}(x)e^{i\omega t}$, and $\boldsymbol{V}(\omega)e^{i\omega t}$, respectively. These forms leads to modifying the mechanical equation of transverse motions (Equations (B.7)) and electrical circuit equation (Equation (B.12)), respectively, as

$$\frac{d^2U(x)}{dx^2}+k_{\mathrm{eff}}^2\boldsymbol{U}(x)=-\frac{e_{31}w_{\mathrm{p}}}{s_{\mathrm{eff}}}\boldsymbol{V}(\omega)\left[\delta(x)-\delta\left(x-l_{\mathrm{p}}\right)\right], \tag{B.13}$$

$$\left(\frac{i\omega C_{\mathrm{p}}}{2}+\frac{1}{R_{\mathrm{load}}}\right)\boldsymbol{V}(\omega)=i\omega e_{31}w_{\mathrm{p}}\left[\boldsymbol{U}\left(l_{\mathrm{p}}\right)-\boldsymbol{U}(0)\right], \tag{B.14}$$

where an effective wavenumber k_{eff} can be calculated by $\omega(m_{\mathrm{eff}}/s_{\mathrm{eff}})^{1/2}$. This implies that the characteristics of elastic wave propagation depend on the mass and stiffness of both the host medium and the PEH devices.

It can be found that the right-hand sides in Equations (B.13) and (B.14) make the mechanical equation of motions and electrical circuit equation be coupled with each other. Each right-hand side is called backward and forward coupling, respectively. Electroelastic coupling terms in Equations (B.13) and (B.14) work as the external force and current source, respectively. Equation (B.13) is a form of the 2nd linear inhomogeneous ordinary differential equation. The homogenous solution to Equation (B.13) can be readily obtained as $\boldsymbol{A}e^{-ik_{\text{eff}}x}+\boldsymbol{B}e^{ik_{\text{eff}}x}$. For this particular solution, it should be noted that the electroelastic coupling term in Equation (B.13) is expressed in a form of a Dirac delta function; it plays a role as two impulsive forces applied to the left and right ends (x=0 and l_{p}) of the effective medium in opposite directions. Here, it is worth pointing out that the particular solution to the nonhomogeneous wave equation under an impulsive force is known as Green's function [123]. Therefore, the particular solution to Equation (B.13) is a sum of two Green's functions with an amplitude of $e_{31}w_{\text{p}}/s_{\text{eff}}$ that correspond to each impulsive force. Finally, the general solution to Equation (B.13), which is the sum of the homogenous and particular solutions, can be written as

$$\boldsymbol{U}\left(x\right)=\boldsymbol{A}e^{-ik_{\text{eff}}x}+\boldsymbol{B}e^{ik_{\text{eff}}x}+\frac{e_{31}w_{\text{p}}}{2ik_{\text{eff}}s_{\text{eff}}}\boldsymbol{V}\left(\omega\right)\left[e^{-ik_{\text{eff}}x}-e^{ik_{\text{eff}}\left(x-l_{\text{p}}\right)}\right]. \tag{B.15}$$

By inserting Equation (B.15) into Equation (B.14), the output voltage amplitude $\boldsymbol{V}(\omega)$ can obtained by

$$\boldsymbol{V}\left(\omega\right)=\frac{iw_{\text{p}}e_{31}\omega\left[\boldsymbol{A}\left(e^{-ik_{\text{eff}}l_{\text{p}}}-1\right)+\boldsymbol{B}\left(e^{ik_{\text{eff}}l_{\text{p}}}-1\right)\right]}{\frac{1}{R_{\text{load}}}+\frac{i\omega C_{\text{p}}}{2}-\frac{\left(w_{\text{p}}e_{31}\right)^{2}}{\sqrt{s_{\text{eff}}m_{\text{eff}}}}\left(e^{-ik_{\text{eff}}l_{\text{p}}}-1\right)}. \tag{B.16}$$

Finally, inserting Equation (B.16) into Equation (B.15) provides the displacement amplitude $\boldsymbol{U}(x)$ as

$$\boldsymbol{U}(x) = \boldsymbol{A}e^{-ik_{\text{eff}}x} + \boldsymbol{B}e^{ik_{\text{eff}}x} + \frac{\frac{\left(w_{\text{p}}e_{31}\right)^2}{2\sqrt{s_{\text{eff}}m_{\text{eff}}}}\left[\boldsymbol{A}\left(e^{-ik_{\text{eff}}l_{\text{p}}}-1\right)+\boldsymbol{B}\left(e^{ik_{\text{eff}}l_{\text{p}}}-1\right)\right]}{\frac{1}{R_{\text{load}}}+\frac{i\omega C_{\text{p}}}{2}-\frac{\left(w_{\text{p}}e_{31}\right)^2}{\sqrt{s_{\text{eff}}m_{\text{eff}}}}\left(e^{-ik_{\text{eff}}l_{\text{p}}}-1\right)}\left[e^{-ik_{\text{eff}}x}-e^{ik_{\text{eff}}\left(x-l_{\text{p}}\right)}\right]. \tag{B.17}$$

In can be shown that the electroelastic coupling term (inhomogeneous term) makes the particular solution depend on the homogenous solution.

The velocity can be readily expressed as $i\omega\boldsymbol{U}(x)$. From Hooke's law and Equation (B.4), the axial force $F(x)$ applied to the effective medium can be expressed as

$$\boldsymbol{F}(x) = s_{\text{eff}}\frac{d\boldsymbol{U}(x)}{dx} + w_{\text{m}}e_{31}\boldsymbol{V}(\omega). \tag{B.18}$$

By inserting Equations (B.16) and (B.17) into Equation (3.18), the axial force $F(x)$ can be rewritten as

$$\boldsymbol{F}\left(x\right)=ik_{\mathrm{eff}}s_{\mathrm{eff}}\left\{\begin{array}{l}-\boldsymbol{A}e^{-ik_{\mathrm{eff}}x}+\boldsymbol{B}e^{ik_{\mathrm{eff}}x}\\ -\dfrac{\dfrac{\left(w_{\mathrm{p}}e_{31}\right)^{2}}{2\sqrt{s_{\mathrm{eff}}m_{\mathrm{eff}}}}\left[\boldsymbol{A}\left(e^{-ik_{\mathrm{eff}}l_{\mathrm{p}}}-1\right)+\boldsymbol{B}\left(e^{ik_{\mathrm{eff}}l_{\mathrm{p}}}-1\right)\right]}{\dfrac{1}{R_{\mathrm{load}}}+\dfrac{i\omega C_{\mathrm{p}}}{2}-\dfrac{\left(w_{\mathrm{p}}e_{31}\right)^{2}}{\sqrt{s_{\mathrm{eff}}m_{\mathrm{eff}}}}\left(e^{-ik_{\mathrm{eff}}l_{\mathrm{p}}}-1\right)}\\ \quad\times\left[e^{-ik_{\mathrm{eff}}x}+e^{ik_{\mathrm{eff}}\left(x-l_{\mathrm{p}}\right)}-2\right]\end{array}\right\}. \tag{B.19}$$

From these equations, the velocity and force at the left and right ends (x=0 and l_{p}) of the effective medium can be obtained as functions of $\boldsymbol{A}$ and $\boldsymbol{B}$. This implies that the vector of the velocity and force at each end can be expressed as the product of a 2×2 matrix ($\mathbf{P}_{\mathrm{l}}$ for the left end and $\mathbf{P}_{\mathrm{r}}$ for the right end) and a vector of $\boldsymbol{A}$ and $\boldsymbol{B}$ as

$$\begin{aligned}\begin{bmatrix}i\omega\boldsymbol{U}\\ \boldsymbol{F}\end{bmatrix}_{x=0}&=i\omega\begin{bmatrix}1+\theta e^{-ik_{\mathrm{eff}}l_{\mathrm{p}}} & 1-\theta\\ -Z_{\mathrm{eff}}\left(1-\theta e^{-ik_{\mathrm{eff}}l_{\mathrm{p}}}\right) & Z_{\mathrm{eff}}\left(1-\theta\right)\end{bmatrix}\begin{bmatrix}\boldsymbol{A}\\ \boldsymbol{B}\end{bmatrix}_{x=0}\\ &=\mathbf{P}_{\mathrm{l}}\begin{bmatrix}\boldsymbol{A}\\ \boldsymbol{B}\end{bmatrix}_{x=0}\end{aligned}, \tag{B.20}$$

$$\begin{aligned}\begin{bmatrix}i\omega\boldsymbol{U}\\ \boldsymbol{F}\end{bmatrix}_{x=l_{\mathrm{p}}}&=i\omega e^{-ik_{\mathrm{eff}}l_{\mathrm{p}}}\begin{bmatrix}1-\theta & 1+\theta e^{ik_{\mathrm{eff}}l_{\mathrm{p}}}\\ -Z_{\mathrm{eff}}\left(1+\theta\right) & Z_{\mathrm{eff}}\left(1+\theta e^{ik_{\mathrm{eff}}l_{\mathrm{p}}}\right)\end{bmatrix}\begin{bmatrix}\boldsymbol{A}\\ \boldsymbol{B}\end{bmatrix}_{x=l_{\mathrm{p}}}\\ &=i\omega e^{-ik_{\mathrm{eff}}l_{\mathrm{p}}}\begin{bmatrix}1-\theta & 1+\theta e^{ik_{\mathrm{eff}}l_{\mathrm{p}}}\\ -Z_{\mathrm{eff}}\left(1+\theta\right) & Z_{\mathrm{eff}}\left(1+\theta e^{ik_{\mathrm{eff}}l_{\mathrm{p}}}\right)\end{bmatrix}\begin{bmatrix}e^{-ik_{\mathrm{eff}}l_{\mathrm{p}}} & 0\\ 0 & e^{ik_{\mathrm{eff}}l_{\mathrm{p}}}\end{bmatrix}\begin{bmatrix}\boldsymbol{A}\\ \boldsymbol{B}\end{bmatrix}_{x=0}\\ &=\mathbf{P}_{\mathrm{r}}\begin{bmatrix}\boldsymbol{A}\\ \boldsymbol{B}\end{bmatrix}_{x=0}\end{aligned}, \tag{B.21}$$

where Z_{eff} is the effective mechanical impedance, which is calculated by $(m_{\mathrm{eff}}s_{\mathrm{eff}})^{1/2}$

and θ is defined as electroelastic coupling coefficient, calculated by

$$\theta = \frac{\dfrac{\left(w_{\mathrm{p}} e_{31}\right)^2}{\sqrt{s_{\mathrm{eff}} m_{\mathrm{eff}}}}\left[1-\cos\left(k_{\mathrm{eff}} l_{\mathrm{p}}\right)\right]}{\dfrac{1}{R_{\mathrm{load}}} + \dfrac{i\omega C_{\mathrm{p}}}{2} - \dfrac{\left(w_{\mathrm{p}} e_{31}\right)^2}{\sqrt{s_{\mathrm{eff}} m_{\mathrm{eff}}}}\left(e^{-ik_{\mathrm{eff}} l_{\mathrm{p}}} - 1\right)}. \tag{B.22}$$

The electroelastically coupled transfer matrix $\mathbf{T}_{\mathrm{eff}}$ can be thus obtained by $\mathbf{P}_{\mathrm{r}}\mathbf{P}_{\mathrm{l}}^{-1}$ as

$$\begin{bmatrix} i\omega \boldsymbol{U} \\ \boldsymbol{F} \end{bmatrix}_{x=l_{\mathrm{p}}} = \mathbf{P}_{\mathrm{r}}\mathbf{P}_{\mathrm{l}}^{-1}\begin{bmatrix} i\omega \boldsymbol{U} \\ \boldsymbol{F} \end{bmatrix}_{x=0} = \mathbf{T}_{\mathrm{eff}}\begin{bmatrix} i\omega \boldsymbol{U} \\ \boldsymbol{F} \end{bmatrix}_{x=0}. \tag{B.23}$$

Finally, $\mathbf{T}_{\mathrm{eff}}$ can be expressed as

$$\begin{aligned} \mathbf{T}_{\mathrm{eff}} = {} & \frac{1}{1-\theta}\begin{bmatrix} \cos\left(k_{\mathrm{eff}} l_{\mathrm{p}}\right) & \dfrac{i\sin\left(k_{\mathrm{eff}} l_{\mathrm{p}}\right)}{Z_{\mathrm{eff}}} \\ iZ_{\mathrm{eff}}\sin\left(k_{\mathrm{eff}} l_{\mathrm{p}}\right) & \cos\left(k_{\mathrm{eff}} l_{\mathrm{p}}\right) \end{bmatrix} \\ & + \frac{\theta}{1-\theta}\begin{bmatrix} -e^{-ik_{\mathrm{eff}} l_{\mathrm{p}}} & \dfrac{\left(1+e^{-ik_{\mathrm{eff}} l_{\mathrm{p}}}\right)}{Z_{\mathrm{eff}}} \\ Z_{\mathrm{eff}}\left(e^{-ik_{\mathrm{eff}} l_{\mathrm{p}}} - 1\right) & -e^{-ik_{\mathrm{eff}} l_{\mathrm{p}}} \end{bmatrix}. \end{aligned} \tag{B.24}$$

Since the system is linear and reciprocal, the determinant of the transfer matrix $\mathbf{T}_{\mathrm{eff}}$ is one [167]. It should be emphasized that a transfer matrix for an electroelastically coupled structure is physically parameterized with an effective wavenumber k_{eff}, an effective mechanical impedance Z_{eff}, an electroelastic coupling coefficient θ, and a structure length l_{m}.

It should be noted that there are two cases where the electroelastic coupling coefficient θ becomes zero. The first case is when the external electric resistance does not exist (i.e., R_{load}=0). The second case is when the length l_p is equal to the wavelength (=$2\pi/k_{eff}$). This is the result of the sign change of the strain phase within the effective medium. Referring to the previous work by Erturk *et al.* [105], the output voltage generated by a PEH device can significantly decrease when the PEH device is subjected to both tensile and compressive strains. This phenomenon is called voltage cancellation. In both cases, the host medium and the PEH device are only mechanically coupled (i.e., θ=0) and the output voltage amplitude $\boldsymbol{V}(\omega)$ becomes zero. In this condition, a form of the proposed electroelastically coupled transfer matrix $\mathbf{T}_{eff}$ is equivalent to the transfer matrix for a homogeneous solid m having a length l_m [136] as

$$\mathbf{T}_m = \begin{bmatrix} \cos(k_m l_m) & \dfrac{i}{Z_m}\sin(k_m l_m) \\ iZ_m \sin(k_m l_m) & \cos(k_m l_m) \end{bmatrix}. \tag{B.25}$$

B.3 Methods for Output Performance Prediction

This section is dedicated to demonstrating how the output performances (i.e., defect bands and PEH performance) can be predicted by using the electroelastically coupled transfer matrix $\mathbf{T}_{eff}$. In general, TMM and SPM have been widely used in band structure analysis and harmonic analysis, respectively. With this fact in mind, Sections B.3.1 and B.3.2 explain band structure calculation and output voltage calculation, respectively.

B.3.1 Band Structure Calculation Based on Transfer Matrix Method

To predict band structures that include defect bands, the supercell calculation is adopted, which is based on the TMM [57, 168]. A 2×2 transfer matrix $\mathbf{T}_{\mathrm{PEH}}$ that relates the physical quantities at the left end with those at the right end of a PnC can be obtained from the continuity conditions of the longitudinal displacement $\boldsymbol{U}$ and axial force $\boldsymbol{F}$ at the interfaces among all adjacent stacks in the PnC. Under an assumption that the unit cells are infinitely periodic along the x-direction, Floquet-Bloch theorem results in applying periodic boundary conditions to the left and right ends of the PnC [96, 151]. From the transfer matrix $\mathbf{T}_{\mathrm{PEH}}$ and periodic boundary conditions, an eigenvalue problem to obtain the band structures can be formulated as:

$$\begin{aligned}&\left[\left(\mathbf{T}_{\mathrm{m}}\mathbf{T}_{\mathrm{M}}\right)^{N-K}\mathbf{T}_{\mathrm{rem}}\mathbf{T}_{\mathrm{eff}}\mathbf{T}_{\mathrm{rem}}\mathbf{T}_{\mathrm{M}}\left(\mathbf{T}_{\mathrm{m}}\mathbf{T}_{\mathrm{M}}\right)^{K-2}-e^{-ikNl_{\mathrm{u}}}\mathbf{I}\right]\begin{bmatrix}i\omega\boldsymbol{U}\\ \boldsymbol{F}\end{bmatrix}\\ &=\left[\mathbf{T}_{\mathrm{PEH}}-e^{-ikNl_{\mathrm{u}}}\mathbf{I}\right]\begin{bmatrix}i\omega\boldsymbol{U}\\ \boldsymbol{F}\end{bmatrix}=\{\mathbf{0}\}\end{aligned}, \tag{B.26}$$

where $\mathbf{T}_{\mathrm{m}}$ and $\mathbf{T}_{\mathrm{M}}$ are transfer matrices of the host and embedded stacks, respectively; and $\mathbf{T}_{\mathrm{rem}}$ is a transfer matrix of the two stacks, to which PEH devices are not attached within the defect. Each remaining stack is a host stack with a length of $(l_{\mathrm{defect}}\text{-}l_{\mathrm{p}})/2$. If the length of the PEH devices (l_{p}) is equal to that of the defect (l_{defect}), $\mathbf{T}_{\mathrm{rem}}$ becomes an identity matrix $\mathbf{I}$. In addition, if no PEH device is attached ($l_{\mathrm{p}}=0$), $\mathbf{T}_{\mathrm{eff}}$ in Equation (B.26) becomes an identity matrix $\mathbf{I}$ as well. Band structures can be numerically obtained by calculating eigenfrequencies for a reciprocal wavenumber k belonging to the border line of the 1st irreducible Brillouin zone (Γ→X) [153, 169].

B.3.2 Output Voltage Calculation Based on S-Parameter Method

To explore the output performance of the PnC-based PEH system with the defect in harmonic analysis, while avoiding unwanted reflection that can be generated outside the PnC domain, it is assumed that two infinite bars that consist of the host medium are attached to the left and right ends of the PnC, respectively, as shown in Figure B-1 (a). The height and width of these bars are equal to those of the host stack (h_m and w_m), respectively. Then, longitudinal elastic waves enter from one end and go out the other end. Displacement fields at each end of the bars can be written as $\boldsymbol{u}_{in}= \boldsymbol{A}_{in}e^{i(\omega t-k_m x)}+\boldsymbol{B}_{in}e^{i(\omega t+k_m x)}$ and $\boldsymbol{u}_{out}= \boldsymbol{A}_{out}e^{i(\omega t-k_m x)}+\boldsymbol{B}_{out}e^{i(\omega t+k_m x)}$, respectively. In this study, the concept of SPM is used to observe wave reflection and transmission induced by the PnC. A scattering matrix $\mathbf{S}_{PEH}$ extracts the relationship between vectors of displacement amplitudes at the attached infinite host mediums as [170, 171]

$$\begin{aligned}\begin{bmatrix}\boldsymbol{A}_{out}\\ \boldsymbol{B}_{out}\end{bmatrix} &= \mathbf{P}_m^{-1}\mathbf{T}_M\left(\mathbf{T}_m\mathbf{T}_M\right)^{N-K-1}\mathbf{T}_d\mathbf{T}_{eff}\mathbf{T}_d\mathbf{T}_M\left(\mathbf{T}_m\mathbf{T}_M\right)^{K-2}\mathbf{P}_m\begin{bmatrix}\boldsymbol{A}_{in}\\ \boldsymbol{B}_{in}\end{bmatrix}\\ &= \mathbf{S}_{PEH}\begin{bmatrix}\boldsymbol{A}_{in}\\ \boldsymbol{B}_{in}\end{bmatrix}\end{aligned}, \tag{B.27}$$

where the transfer matrix of the PnC in Equation (B.26) is multiplied by $\mathbf{P}_m^{-1}$ and $\mathbf{P}_m$, which represent the relationship between the vector of the displacement amplitudes and the vector of velocity and force for the attached mediums. For a homogenous solid, this relationship is knowns as

$$\mathbf{P}_m = i\omega\begin{bmatrix}1 & 1\\ -Z_m & Z_m\end{bmatrix}. \tag{B.28}$$

Here, since this engineered situation is a sort of radiation problems, the assumption

of an infinite domain outside the PnC results in a zero value for $\boldsymbol{B}_{\text{out}}$. Then, the reflection coefficient $\boldsymbol{B}_{\text{in}}/\boldsymbol{A}_{\text{in}}$ and the transmission coefficient $\boldsymbol{A}_{\text{out}}/\boldsymbol{A}_{\text{in}}$ can be calculated, respectively, by

$$\frac{\boldsymbol{B}_{\text{in}}}{\boldsymbol{A}_{\text{in}}} = -\frac{\mathbf{S}_{\text{PEH}}(2,1)}{\mathbf{S}_{\text{PEH}}(2,2)}, \tag{B.29}$$

$$\frac{\boldsymbol{B}_{\text{in}}}{\boldsymbol{A}_{\text{in}}} = \frac{\boldsymbol{A}_{\text{out}}}{\boldsymbol{A}_{\text{in}}} = \mathbf{S}_{\text{PEH}}(1,1) - \frac{\mathbf{S}_{\text{PEH}}(1,2)\mathbf{S}_{\text{PEH}}(2,1)}{\mathbf{S}_{\text{PEH}}(2,2)} = \frac{1}{\mathbf{S}_{\text{PEH}}(2,2)}, \tag{B.30}$$

where the determinant of $\mathbf{S}_{\text{PEH}}$ should be zero since the system is reciprocal. Now, it is required to obtain the amplitudes $\boldsymbol{A}_{\text{eff}}$ and $\boldsymbol{B}_{\text{eff}}$ of the displacement fields of $\boldsymbol{u}_{\text{eff}}=\boldsymbol{A}_{\text{eff}}e^{i(\omega t-k_{\text{eff}}x)}+\boldsymbol{B}_{\text{eff}}e^{i(\omega t+k_{\text{eff}}x)}$ in the effective medium in terms of the reflection coefficient $\boldsymbol{B}_{\text{in}}/\boldsymbol{A}_{\text{in}}$ and/or the transmission coefficient $\boldsymbol{A}_{\text{out}}/\boldsymbol{A}_{\text{in}}$. Equation (B.27) deals with the relationship between the input mechanical energy and output responses in a system called a PnC with a piezoelectric defect. Likewise, for a small system called a bunch of unit cells before a defect where PEH devices are attached, the relationship between the input mechanical energy and output responses can be obtained. In this case, the output responses become the amplitudes $\boldsymbol{A}_{\text{eff}}$ and $\boldsymbol{B}_{\text{eff}}$ in the effective medium. Indeed, the relationship can be expressed as

$$\begin{bmatrix} \boldsymbol{A}_{\text{eff}} \\ \boldsymbol{B}_{\text{eff}} \end{bmatrix} = \mathbf{P}_{\text{l}}^{-1}\mathbf{T}_{\text{d}}\mathbf{T}_{\text{M}}\left(\mathbf{T}_{\text{m}}\mathbf{T}_{\text{M}}\right)^{K-2}\mathbf{P}_{\text{m}}\begin{bmatrix} \boldsymbol{A}_{\text{in}} \\ \boldsymbol{B}_{\text{in}} \end{bmatrix}. \tag{B.31}$$

Finally, substituting the calculated displacement amplitudes $\boldsymbol{A}_{\text{eff}}$ and $\boldsymbol{B}_{\text{eff}}$ into $\boldsymbol{A}$ and $\boldsymbol{B}$ in Equation (B.16), respectively, enables calculation of the output voltage amplitude $\boldsymbol{V}(\omega)$. Further, the output electric power can be calculated by Ohm's law.

B.4 Evaluation of Model Predictive Capability

This section presents the predictive capability evaluation of the proposed electroelastically coupled analytical model of a PnC with a piezoelectric defect. Section B.4.1 deals with evaluation planning such as values of system parameters and validation method. Section B.4.2 demonstrates how inertia, stiffness, and electroelastic coupling of PEH devices affect the defect bands from viewpoint of frequencies and defect mode shapes. In harmonic analysis, Sections B.4.3 and B.4.4 presents energy localization and PEH performances, respectively.

B.4.1 Evaluation Planning

In this research, we considered a situation in which the host medium and embedded medium consisted of aluminum and steel, respectively. Five unit cells (N=5) are arranged in the x-direction and the steel stack in the third unit cell (K=3) is replaced with an aluminum stack. PZT-5H (lead zirconate titanate, $Pb(Zr_xTi_{1-x})O_3$) is used as the piezoelectric material. Geometric dimensions of the unit cell and PEH device are summarized in Table B-1. Mechanical properties of the aluminum and steel that are used in the unit cell are listed in Table A-1. Mechanical and electrical properties of PZT-5H are summarized in Table B-2. The lengths l_m and l_M are set to be the quarter wavelengths of longitudinal waves at 20 kHz in the aluminum and steel stacks, respectively. In the previous work [33], it was shown that a quarter-wave stack had abilities to match a target frequency with a center of a band gap. The length l_{defect} of the defect is equal to 190.4 mm. The length and height of the PEH device (l_p and h_p) are the half and quarter of those of the defect, respectively. Considering the material

of the last stack of the PnC is equal to that of the attached infinite bars, there are nine layers in the PnC-based PEH system with the defect.

In this study, a commercially available FEM software, COMSOL Multiphysics 5.4 is used to evaluate the predictive capability of the proposed electroelastically coupled analytical model of a PnC with a piezoelectric defect. It has been shown throughout the published literature that COMSOL Multiphysics is a highly predictive for PEH performance of PnCs [43, 66, 78, 79, 81]. In FEM setting, perfectly matched layers are applied at the ends of the system to assume the infinite domain [172, 173]. Here, mesh elements of the whole structure are constituted with rectangles. The maximum mesh size is considered to be one-fifth of the wavelength of the longitudinal elastic waves at 20 kHz. Longitudinal elastic waves are excited with a prescribed velocity of 1.20π mm/s, irrespective of frequency. The corresponding displacement at 20 kHz is 30 nm. To consider the mechanical loss in the system, a loss factor η of 0.001 is introduced.

Table B-1 Geometric dimensions of the unit cell and PEH device.

Unit cell	Aluminum stack	Length, l_m	63.65 mm
		Height, h_m	5.00 mm
		Width, w_m	5.00 mm
	Steel stack	Length, l_M	63.09 mm
		Height, h_M	5.00 mm
		Width, w_M	5.00 mm
PEH device (PZT-5H)		Length, l_p	95.19 mm
		Height, h_p	1.25 mm
		Width, w_p	5.00 mm

Table B-2 Mechanical and electrical properties of PZT-5H.

Mechanical properties	Density	ρ_p	7500 kg m^{-3}
	Compliances matrix	s_{11}^E	16.5 pm^2 N^{-1}
		s_{12}^E	-4.78 pm^2 N^{-1}
		s_{13}^E	-8.45 pm^2 N^{-1}
		s_{33}^E	20.7 pm^2 N^{-1}
		s_{55}^E	43.5 pm^2 N^{-1}
		s_{66}^E	42.6 pm^2 N^{-1}
Electrical properties	Piezoelectric strain coefficient	d_{31}	-274 pm V^{-1}
	Piezoelectric constant	e_{31}	-16.6 C m^{-2}
	Absolute permittivity	ε_0	8.85 pF m^{-1}
	Dielectric permittivity at constant stress	ε_{33}^T	30.09 nF m^{-1}
	Dielectric permittivity at constant strain	ε_{33}^S	25.55 nF m^{-1}
	Relative permittivity	ε_r	3400

B.4.2 Band Structure Evaluation

Figure B-2 describes the dispersion curves calculated by Equation (B.26). As mentioned in Appendix A, in the case of the supercell calculation that is based on multiple unit cells, the passbands are folded depending on the number of unit cells. However, since the main concern of this appendix is defect bands, the band gap analysis is performed at a unit cell level. The sky-blue box indicates a band gap, ranging from 13.56 kHz to 26.44 kHz. When inducing longitudinal elastic waves within the band gap, the PnC without defects oscillates with a form of evanescent elastic waves whose amplitudes exponentially decay along the propagating direction with a complex-value (not real) wavenumber.

Figure B-2 also presents defect bands formed within the band gap for the three cases: (1) a PnC without PEH devices (Case I, solid blue lines); (2) the PnC with the

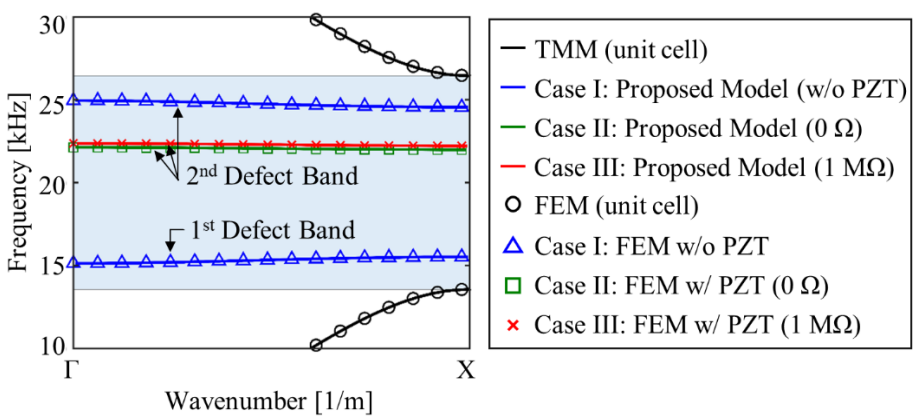

Figure B-2 Formation of defect bands within the band gap for the three cases (Cases I, II, and III).

piezoelectric defect shown in Figure B-1 (a) under the external electrical resistance of 0 Ω (Case II, solid green lines); and (3) the same PnC under the external electrical resistance of 1 MΩ (Case III, solid red lines). Here, external electrical resistances of 0 Ω and 1 MΩ are considered as the short-circuit and open-circuit conditions, respectively. The short-circuit condition means that the host structure and PEH devices are only mechanically coupled, while the open-circuit condition means that they are electroelastically coupled and the maximum output voltage is generated. It can be seen that the results of the proposed electroelastically coupled analytical model (solid blue lines, solid green lines, and solid red lines) are in very good agreement with those of FEM (blue triangle dots, green square dots, and red cross dots).

In the absence of the PEH devices (Case I), two defect bands are observed; defect band frequencies are 15.20 kHz and 24.89 kHz. The corresponding defect mode shapes (normalized strain fields) of the PnC are presented in Figure B-3: the 1st defect mode shape (Figure B-3 (a)) at 15.20 kHz and the 2nd defect mode shape (Figure B-3 (b)) at 24.89 kHz. Normalized strain fields near the defect in the PnC are visualized on the top of the figures; these results are obtained from FEM. The center of the defect is set to an origin. At one of defect band frequencies, the defect and neighboring unit cells oscillate with the corresponding defect mode shape. Hence, the strain amplitude of evanescent elastic waves inside the defect can be highly amplified. Here, when the normalized strain fields are calculated from the defect mode shapes (normalized displacement fields) in Figure A-3 (b) and Figure A-3 (c), it should be noted that they are similar to Figure B-3 (a) and Figure B-3 (b). From this, the theoretical approach related to the formation of defect bands in

Appendix A is sufficiently valid. Therefore, it can be seen that the normal modes of a finite string, which is bounded by fixed-fixed conditions, are considerably similar to defect mode shapes in Figure B-3.

When envisaging that PEH devices are attached to the center of the defect, there is a very important issue that should be taken into account. In the field of PVEH, it is known that the output voltage is proportional to strains, which means that tensile (compressive) strains yield the positive (negative) output voltage. If the piezoelectric patch possesses strain nodal lines, the different sign of strains within the piezoelectric patch would result in dramatically decreasing the output voltage. This is so-called voltage cancellation. This is an interesting physical phenomenon that occurs in vibrations, but it can be expected that such voltage cancellation may appear in our engineering situations since it was revealed in Appendix A that the defect modes in the domain of waves can be regarded as vibrations. For instance, the 1st defect mode (Figure B-3 (a)) will possess different signs of mechanical strains in PEH devices, thus resulting in serious voltage cancellation. The 1st defect mode shape causes the right-hand side of Equation (B.14) to be nearly zero; the output voltage should also be nearly zero. On the other hand, the 2nd defect mode (Figure B-3 (b)) will possess the same signs as the mechanical strains in the PEH devices. The 2nd defect mode shape causes the right-hand side of Equation (B.14) to be non-zero. Therefore, the attached PEH devices can harvest a certain value of output voltage. Therefore, when selecting a target defect mode shape, it should be emphasized that the 2nd defect mode is proper for highly dense PEH from viewpoint of avoiding voltage cancellation.

The results show that the attachment of the PEH devices significantly decreases

the 2nd defect band frequency from 24.89 kHz (Case I) to 22.08 kHz (Case II). On the other hand, it should be noted that the 1st defect band frequency has shifted out of the band gap, due to the attachment of the PEH devices. This implies that even if a certain defect mode shape is observed before attaching the PEH devices, energy localization by the corresponding defect mode may not occur due to the inertia and stiffness effects of the PEH devices.

It is worth pointing out that the normalized strain field (Figure B-3 (c)) of the PnC with the PEH devices at 22.08 kHz (Case II) is different from that (Figure B-3 (b)) without the PEH devices at 24.89 kHz (Case I). In particular, it is intriguing that the positions of the strain nodes are considerably shifted. The distance between the strain nodes without the PEH devices is calculated as 102.3 mm, which is larger than the length of the PEH devices. However, the distance between the strain nodes is calculated as 89.26 mm, which is smaller than the length of the PEH devices. This implies that the PEH devices possess strain nodes, thus resulting in voltage cancellation, even though the PnC before attaching the PEH devices does not. These observations lead to an important design-related rationale that a change in the position of strain nodes – as well as the defect band frequency due to the inertia and stiffness effects of the piezoelectric defect – should be taken into consideration when designing a PnC-based PEH system with a defect.

Moreover, as shown in Figure B-2, it is found that the 2nd defect band frequency increases from 22.08 kHz (Case II) to 22.32 kHz (Case III) when switching the electrical boundary conditions from the external electrical resistances of 0 Ω (short-circuit) to 1 MΩ (open-circuit). To thoroughly investigate how the defect band frequency is affected by the electroelastic coupling, Figure B-4 depicts

the relationship between the 2nd defect band frequency and the external electrical resistance, ranging from the external electrical resistances of 0 Ω (short-circuit) to 1 MΩ (open-circuit). From the results, it can be confirmed that the 2nd defect band frequency asymptotically increases as the external electrical resistance increases. These results are attributed to the fact that the effective stiffness of a piezoceramic material increases due to electroelastic coupling effects [19-21]. These observations are analogous to those presented in previous studies [20, 174], in which the resonance frequency increases as the external electrical resistance increases. If models consider only the inertia and stiffness effects of PEH devices, a serious error can be made that the peak values of PEH performance will be obtained at a defect band frequency corresponding to the short-circuit condition, regardless of the external electrical resistance. On the other hand, it is worth pointing out that the proposed electroelastically coupled analytical model can completely demonstrate the defect band frequency shift that arises from the electroelastic coupling through considering both forward and backward coupling in the electrical circuit equation (Equation (B.12)) and equation of motions (Equation (B.7)), respectively. Note that the normalized strain field of the PnC at 22.32 kHz (Case III, Figure B-3 (d)) does not exhibit significant differences, as compared with that at 22.08 kHz (Case II, Figure B-3 (c)).

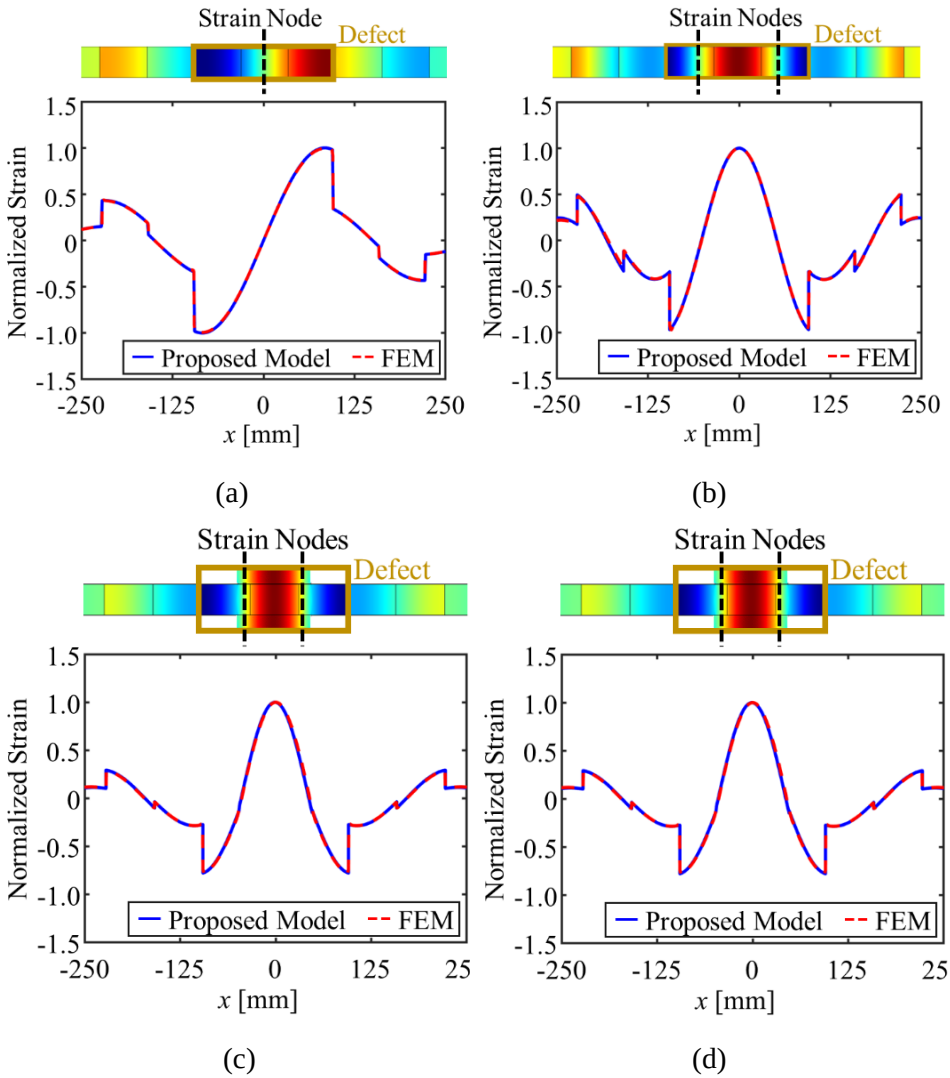

Figure B-3 Defect mode shapes (normalized strain fields): (a) the 1st defect mode shape at 15.20 kHz (Case I); the 2nd defect mode shape (b) at 24.89 kHz (Case I), (c) at 22.08 kHz (Case II), and at 22.32 kHz (Case III).

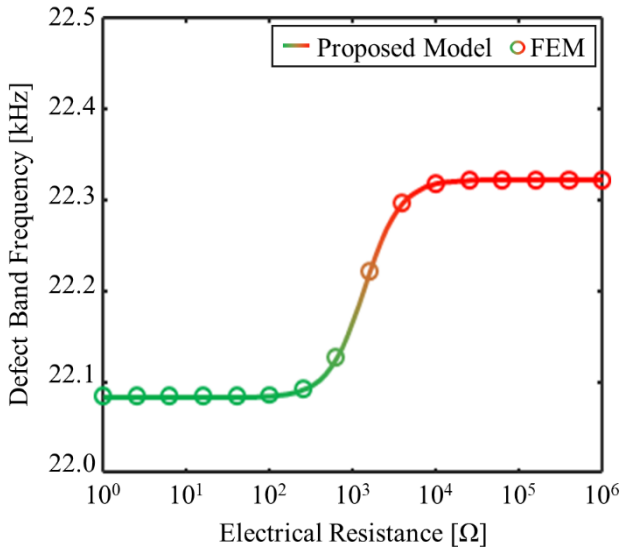

Figure B-4 Effects of the external electrical resistance on the 2nd defect band frequency.

B.4.3 Energy Localization Performance Evaluation

When longitudinal elastic waves enter a PnC with a piezoelectric defect from the left end in Figure B-1 (a) with a prescribed velocity of 1.20π mm/s at 22.08 kHz (Case II), the energy localization phenomenon of a PnC with a piezoelectric defect is investigated. To observe operating deflection shapes (strain fields) in and out of the PnC, we must calculate the amplitudes $\boldsymbol{A}_s$ and $\boldsymbol{B}_s$ of displacement fields $\boldsymbol{u}_s = \boldsymbol{A}_s e^{i(\omega t - k_s x)} + \boldsymbol{B}_s e^{i(\omega t + k_s x)}$ in each layer (i.e., two attached infinite aluminum bars, aluminum and copper stacks in unit cells, two remaining aluminum stacks in the defect, and the effective medium). Here, the displacement amplitudes of the attached aluminum bar in the incident wave domain can be obtained from the input wave amplitude and the reflection coefficient $\boldsymbol{B}_{in}/\boldsymbol{A}_{in}$ (Equation (B-27)). Similarly, those of the aluminum bar

in the transmitted wave domain can be obtained from the transmission coefficient $\boldsymbol{A}_{out}/\boldsymbol{A}_{in}$ (Equation (B-28)); in addition, due to the radiation, $\boldsymbol{B}_{out}$ should be zero. With the help of the continuity conditions at interfaces of each stack, displacement amplitudes for a certain stack in the PnC can be obtained from relationships between the vector of the amplitudes in the stack and the vector of the amplitudes in the attached aluminum bar in the incident wave domain. The relationships can be expressed as multiplication of several transfer matrices (e.g., $\mathbf{T}_m$, $\mathbf{T}_M$, $\mathbf{T}_{rem}$, or $\mathbf{T}_{eff}$) and other matrices (e.g., $\mathbf{P}_m$, $\mathbf{P}_M$, $\mathbf{P}_l$, or $\mathbf{P}_r$). Followed by the similar procedure that is shown in Equation (B-29), the calculated reflection coefficient and transmission coefficient finally provide the displacement amplitudes for a certain stack in the PnC.

Figure B-5 illustrates the results of strain fields in and out of the PnC. In addition, to investigate the energy localization phenomenon, Figure B-5 also depicts the strain fields of the aluminum structure in the absence of the PnC. Here, it should be noted that the incident waves unidirectionally propagate without reflection and the amplitude of the strain field is calculated as 0.74 μm/m. For each case, normalized strain fields in and out of the defect in the PnC are visualized on the top of the figure. These results are obtained from FEM. Since the strain fields vary with time, the results for the time when the maximum strain is observed at the center of the piezoelectric defect are presented. Locations of strain nodes are fixed in space in operating deflection shapes, whereas they change with time in the case of propagating waves. It can be found that the results of the proposed analytical model (solid blue lines) agree well with those of FEM (dashed red lines).

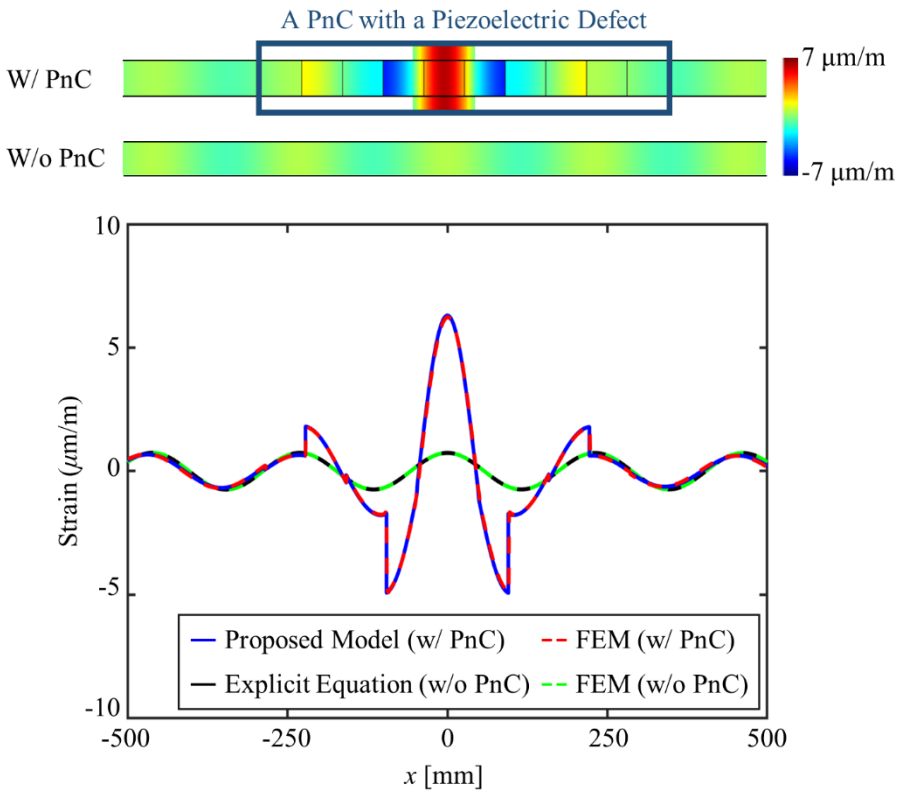

Figure B-5 Operating deflection shapes (strain fields) in and out of the PnC having the piezoelectric defect at 22.08 kHz (Case II).

It is worth pointing out that the strain fields within the defect are highly amplified, while exhibiting the defect mode shape (Figure B-3 (c)) at 22.08 kHz. The amplitude of the strain at the center of the defect is amplified 8.5 times larger than that without the PnC. These results illustrate the defect-mode-enabled energy localization phenomenon. From the results so far, it can be seen that there are two advantages when incorporating the defect-mode-enabled energy localization into

PEH under elastic waves as follow. First, with the help of mechanical resonance, the mechanical energy inside and in the vicinity of the defect is highly amplified, thereby enabling the dramatic improvement in the output performance of the PEH. Second, the strain nodes or nodal lines of defect mode shapes, which are fixed in space, help to readily design PEH devices. Note that the strain fields of the PnC at 22.32 kHz (Case III) do not exhibit significant differences from those at 22.08 kHz (Case II); thus, the results at 22.32 kHz (Case III) are not shown.

B.4.4 Electrical Output Performance Evaluation

Figure B-6 illustrates output performance of PEH, calculated by Equations (B.16), (B.27) - (B.29). Figures B-6 (a) to B-6 (c) present FRFs for output electric power, voltage, and current across various external electrical resistances of 50 Ω, 436 Ω, 4,571 Ω, and 50,000 Ω, respectively. It can be found that the results of the proposed electroelastically coupled analytical model (solid black lines, solid blue lines, solid red lines, and solid dark red lines) are in very good agreement with those of FEM (black circle dots, blue triangle dots, green square dots, and red cross dots).

Since the external electrical resistances of 50 Ω and 50,000 Ω are close to short-circuit and open-circuit conditions, respectively, their peak frequencies of 22.08 kHz and 22.32 kHz are equal to defect band frequencies under the external electrical resistances of 0 Ω (short-circuit) and 1 MΩ (open-circuit), respectively. These results can be also observed in Figure B-4. One of the important aspects of the electrical circuit configuration for PEH is the impedance matching between the PEH devices and electrical regulation [125]. From the output response contours of the electric

power in terms of the frequency and the external electrical resistance, the optimal external electrical resistances for the maximum output electric power are obtained as 436 Ω and 4,571 Ω. Corresponding two peak frequencies are obtained as 22.10 kHz and 22.30 kHz, respectively. Both frequencies deviate by 0.02 kHz from the peak frequencies under the external electrical resistances of (short-circuit) and 1 MΩ (open-circuit). In the field of PVEH, the maximum output electric power can be achieved across the optimal external electrical resistances at the peak frequencies in the FRFs for the output voltage near the short-circuit and open-circuit conditions, respectively [29, 30, 125]. In the meantime, their magnitudes are the same. In Figure B-6 (a), the maximum output electric power at 22.10 kHz and 22.30 kHz are almost the same. Its magnitude is approximately 2.09 mW. It can be confirmed that the existing considerations obtained in PVEH can be also observed in PnC-based PEH system that leverages the defect mode. As a reference, the maximum output electric power in the absence of the PnC is calculated as 0.26 mW at 22.10 kHz and 22.30 kHz. Thus, the maximum output electric power of the presented PnC-based PEH system is amplified about 8.13 times greater than that in the case without the PnC. Here, it should be noted that the maximum mechanical power of longitudinal elastic waves that transferred to the cross-section of the host medium by the excitation is calculated as 4.88 mW, regardless of a frequency [175].

In Figure B-6 (b), the output voltage at the peak frequency gradually increases, as the external electrical resistance increases. It is well known that the output voltage asymptotically converges to a certain value, as the external electrical resistance increases. The maximum output voltage is approximately 5.55 V at 22.32 kHz under the open-circuit condition. As a reference, the maximum output voltage in the

absence of the PnC is calculated as 0.90 V at 22.32 kHz. The maximum output voltage of the presented PnC-based PEH system is amplified about 5.62 times greater than the case without the PnC. Even though the wavelength in the host medium without the PnC is longer than the length of the PEH devices, it needs to be mentioned that voltage cancellation may or may not repetitively occur repeatedly over time since strain nodes cannot be defined.

As compared with Figure B-6 (b), the opposite results are observed in the case of the output current. In Figure B-6 (c), the output current at the peak frequency gradually decreases, as the external electrical resistance increases. It is well known that the output current asymptotically converges to a certain value, as the external electrical resistance decreases. The maximum output current is approximately 3.77 mA at 22.08 kHz when the external electrical resistance converge to the exact short-circuit condition (0 Ω). As a reference, the maximum output current in the absence of the PnC is calculated as 0.61 mA at 22.08 kHz. The maximum output current of the presented PnC-based PEH system is amplified about 6.18 times greater than the case without the PnC.

Even though the magnitudes of the maximum output power at 22.10 kHz (436 Ω) and 22.30 kHz (4,571 Ω) are the same, the output voltage at 22.30 kHz (4,571 Ω) is higher than that at 22.10 kHz (436 Ω) while the output current at 22.10 kHz (436 Ω) is higher than that at 22.30 kHz (4,571 Ω). Therefore, when designing a PnC-based PEH system with a defect, it is of importance to consider which peak frequency should match the operating frequency by investigating the electric voltage and the current requirement of potential applications such as wireless sensors.

Through these in-depth investigations, it can be concluded that the proposed electroelastically coupled analytical model can elucidate the effects of the inertia, stiffness, and electroelastic coupling in both defect band analysis and PEH performance analysis with high predictive capability.

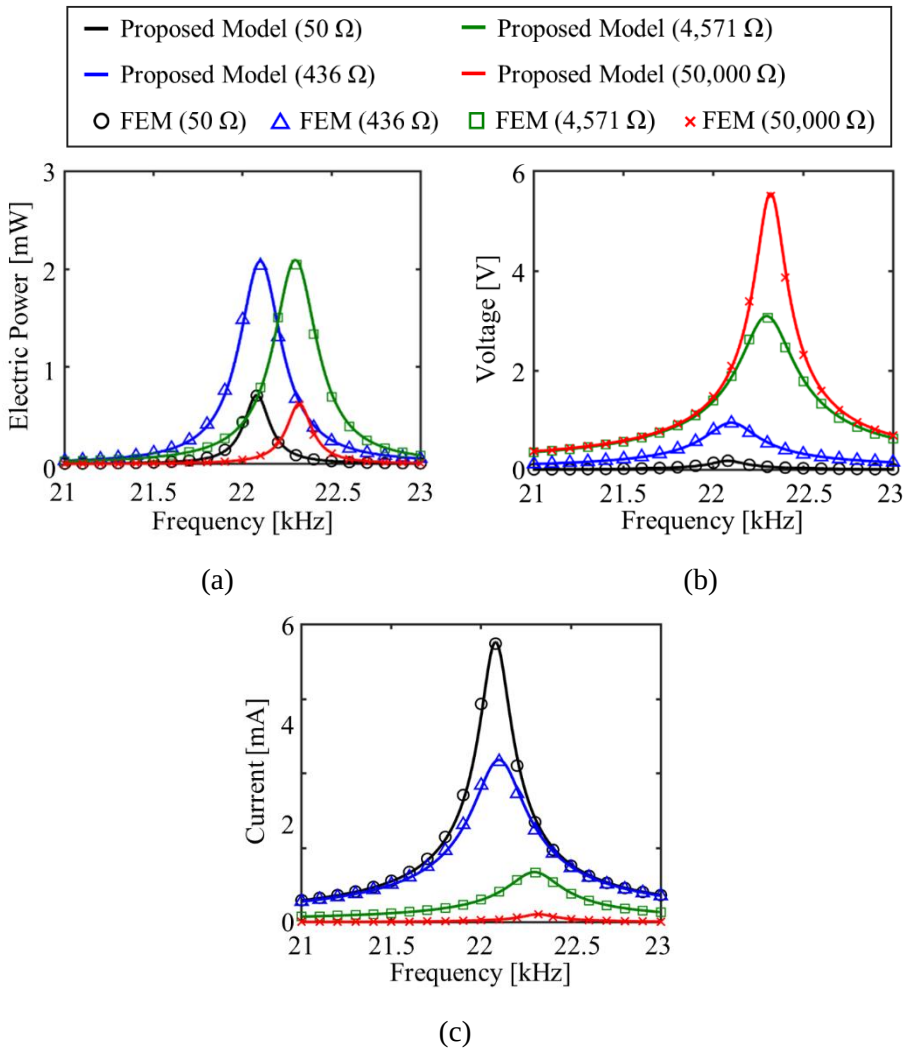

(a) (b)

(c)

Figure B-6 PEH performance FRFs across various external electrical resistances of 50 Ω, 436 Ω, 4,571 Ω, and 50,000 Ω: (a) output electric power, (b) output voltage, and (c) output current.

B.5 Application of the Proposed Model: Design Optimization of a Phononic Crystal for Maximizing Output Electric Power at a Target Frequency

This section is dedicated to demonstrating a potential application of the proposed model: design optimization of a PnC for matching a defect band frequency with a target frequency while maximizing the output electric power. Since design optimization requires iterative calculation, the proposed electroelastically coupled analytical model can be useful in a cost-effective manner. Section B.5.1 describes the design optimization formulation and procedure. The results and discussion are provided in Section B.5.2.

B.5.1 Design Optimization Formulation and Procedure

Design optimization of a PnC-based PEH system with a defect can be formulated as follows:

$$\begin{aligned}
&\text{Maximize } P\left(\mathbf{d}, f_{\text{target}}\right) \\
&\text{Subject to } f_{\text{bandgap,lower}} - f_{\text{target}} < 0 \\
&\qquad f_{\text{target}} - f_{\text{bandgap,lower}} < 0 \\
&\qquad \left| f_{\text{peak}} - f_{\text{target}} \right| - 0.005\, f_{\text{target}} < 0 \\
&\qquad \left| f_{\text{res,open}} - f_{\text{peak}} \right| - \left| f_{\text{res,short}} - f_{\text{peak}} \right| < 0 \\
&\qquad 2l_{\text{m}} + l_{\text{s}} - l_{\text{p}} < 0 \\
&\qquad \mathbf{d}_{\text{L}} \le \mathbf{d} \le \mathbf{d}_{\text{U}} \text{ where } \mathbf{d} = \left(l_{\text{m}}, l_{\text{M}}, l_{\text{p}}, h_{\text{p}}, R_{\text{load}}\right)
\end{aligned}, \tag{B.32}$$

where $P(\mathbf{d}, f_{target})$ is the calculated output electric power at a target frequency f_{target} for a particular design vector $\mathbf{d}$. $f_{bandgap,lower}$ and $f_{bandgap,upper}$ are lower and upper frequencies of the calculated band gap. f_{peak} is a peak frequency corresponding to a peak value of the output electric power across a certain external resistance R_{load}. $f_{res,short}$ and $f_{res,open}$ are short-circuit and open-circuit resonance frequencies, respectively. $\mathbf{d}_L$ and $\mathbf{d}_U$ are the lower and upper bounds of the design variables, respectively. There are five design variables, including lengths (l_m and l_M) of the aluminum and steel stacks, length and height (l_p and h_p) of the bimorph PEH devices, and external electrical resistance R_{load} connected to the PEH devices. The width and height of both stacks are fixed to 5 mm. In addition, the width of the PEH devices is set to 5 mm.

In the design optimization formulation, the objective function is to maximize the output electric power at a target frequency f_{target} of 20 kHz. In this study, six inequality constraints are under consideration. The first and second design constraints indicate that the target frequency f_{target} should be within the band gap since the prerequisite for defect-mode-enabled energy localization is that a PnC should possess the band gap. Third, a small tolerance is allowed between the peak frequency f_{peak} and the target frequency f_{target}. The tolerance was selected as 0.1 kHz, 0.5% of the target frequency f_{target} of 20 kHz. Fourth, the absolute difference between the open-circuit resonance frequency $f_{res,open}$ and the peak frequency f_{peak} is less than that between the short-circuit resonance frequency $f_{res,short}$ and the peak frequency f_{peak}. When the peak frequency f_{peak} is closer to the open-circuit resonance frequency $f_{res,open}$, the optimal external electrical resistance would be larger, thereby resulting in higher output voltage. The fifth constraint is that the length l_p of the PEH devices

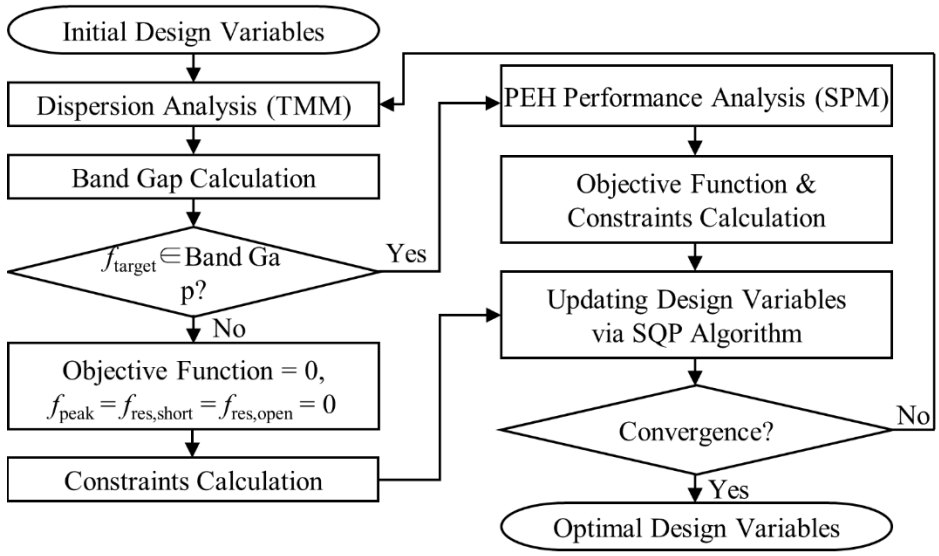

Figure B-7 The flowchart of design optimization of a PnC with a piezoelectric defect for target frequency matching.

should be less than the length $2l_m+l_M$ of the defect. If the length l_p is larger than the length $2l_m+l_M$ (Figures B-3 (c) and (d)), voltage cancellation should occur as strain nodal lines can be generated in the PEH devices; thereby worsening the PEH performance. Last, the design variables are bounded.

It is worth pointing out that the range of each design variable is diverse. Lengths of the unit cell and PEH devices (l_m, l_M, and l_p) range from tens of mm to hundreds of mm, while the height h_p of the PEH devices is from hundreds of μm to several mm. The external electrical resistance R_{load} ranges from ones of Ω to ones of MΩ. It is thus required to modify the design variables having a similar range. Otherwise, there are possibilities that the calculated solution may likely converge to an infeasible point. Besides, for the design optimization problem with multiple

constraints, the calculated design variables may likely converge to an infeasible local optimum depending on the initial design variable. Hence, it is desirable to reduce the number of constraints as much as possible. Motivated by this issue, we modify the design variables as

$$\mathbf{d}_{\mathbf{re}} = \left(\frac{l_{\mathrm{m}}}{\lambda_{\mathrm{m,target}}}, \frac{l_{\mathrm{M}}}{\lambda_{\mathrm{M,target}}}, \frac{l_{\mathrm{p}}}{2l_{\mathrm{m}} + l_{\mathrm{M}}}, \frac{h_{\mathrm{p}}}{h_{\mathrm{m}}}, \frac{1}{7}\log\left(R_{\mathrm{load}}\right) \right), \tag{B.33}$$

where $\lambda_{\mathrm{m,target}}$ and $\lambda_{\mathrm{M,target}}$ are wavelengths of the aluminum and steel stacks at a target frequency f_{target} of 20 kHz. If the upper bound of the modified design variable $l_{\mathrm{p}}/2l_{\mathrm{m}}+l_{\mathrm{M}}$ is set to one, it can replace the fifth geometric constraint in Equation (B.32). The design optimization formulation in Equation (B.32) can be thus rewritten as

$$\begin{aligned} &\text{Maximize } P\left(\mathbf{d}_{\mathbf{re}}, f_{\mathrm{target}}\right) \\ &\text{Subject to } f_{\mathrm{bandgap,lower}} - f_{\mathrm{target}} < 0 \\ &\qquad f_{\mathrm{target}} - f_{\mathrm{bandgap,lower}} < 0 \\ &\qquad \left| f_{\mathrm{peak}} - f_{\mathrm{target}} \right| - 0.005\, f_{\mathrm{target}} < 0 \\ &\qquad \left| f_{\mathrm{res,open}} - f_{\mathrm{peak}} \right| - \left| f_{\mathrm{res,short}} - f_{\mathrm{peak}} \right| < 0 \\ &\qquad \mathbf{d}_{\mathrm{re,L}} \le \mathbf{d}_{\mathrm{re}} \le \mathbf{d}_{\mathrm{re,U}} \end{aligned} \quad , \tag{B.34}$$

where $\mathbf{d}_{\mathrm{re,L}}$ and $\mathbf{d}_{\mathrm{re,U}}$ are the lower and upper bounds of the modified design variables, respectively. The lower bounds of them are set to 0.1. The upper bounds of the modified design variables, associated with lengths l_{m}, l_{M}, and the height h_{p}, are set to 0.5. On the other hand, those of the remaining modified design variables are set to be one. Table B-3 summarizes the initial, lower, and upper bounds of the modified design variables.

In this study, the sequential quadratic programming (SQP) method is used as an optimizer. The design optimization procedure consists of two sequentially-executed processes. The first step is to calculate dispersion curves using TMM in order to investigate whether the target frequency f_{target} of 20 kHz is within the band gap or not for a particular design vector $\mathbf{d_{re}}$. Unless the band gap does include the target frequency f_{target}, defect-mode-enabled energy localization cannot happen at the target frequency f_{target}. Therefore, the objective function and some crucial frequencies are set to zero since they have meaningless values in this case. If the target frequency f_{target} is included, it goes to the next step. The second step is to carry out PEH performance analysis using SPM for calculating (1) output electric power at the target frequency f_{target} of 20 kHz (objective function), (2) a peak frequency f_{peak}, (3) a short-circuit resonance frequency $f_{res,short}$, and (4) an open-circuit resonance frequency $f_{res,open}$. Then, the objective function and inequality constraints can be calculated. The gradients of the objective function and constraints can be evaluated from the finite-difference of design variables. One may state that the sensitivity analysis needs to be performed through the explicit form of sensitivities for ensuring accuracy and reducing time consumption. Since the advantages of the proposed model is that it takes very less computation time and predicts the output responses for high resolution, the above-mentioned issues will not occur. Finally, after sequentially updating the design variables via the SQP algorithm until satisfying the constraints and given tolerances of the objective function, the optimal design variables are obtained. Figure B-7 depicts the flowchart of design optimization of a PnC with a piezoelectric defect for target frequency matching.

B.5.2 Design Optimization Results

Table B-4 summarizes the design optimization results. Compared with the initial design variables, all geometric variables increase, except for aluminum stack's length l_m that decreases from 63.65 mm to 56.80 mm. Besides, the external electrical resistance R_{load} decreases from 3.16 kΩ to 2.29 kΩ. Figures B-8 (a) and (b) present the results of the band gap and the output electric power FRFs for the initial and optimal designs, respectively. Lines with green-solid and magenta-solid indicate the results obtained from TMM (dispersion analysis) and SPM (PEH performance analysis) for the initial and optimal designs, respectively. Dots with green-square and green-triangle indicate the results obtained from the FEM to validate the effectiveness of the proposed electroelastically coupled analytical model. First, the results obtained from TMM and SPM are in excellent agreement with those from the FEM for both designs. These results support that the proposed analytical model can be applied to arbitrary geometric variables and external electrical resistance if the modeling assumptions are satisfied. Second, it is worth pointing out the design optimization takes only 4 min 26 sec, which is much less than evaluating the PEH performance only once using the FEM. The number of iterations was 35, and the calculated number of the objective function was 338. Considering that the required times to perform band gap analysis and PEH performance analysis using FEM are 59 sec and 31 min 53 sec for the final optimal design, respectively. It can be concluded that the proposed electroelastically coupled analytical model can help to execute design optimization while guaranteeing high accuracy efficiently.

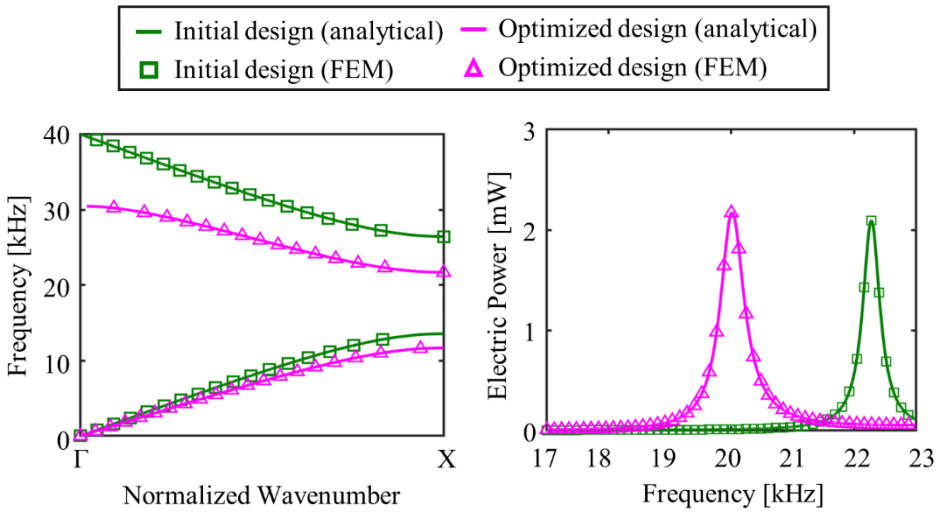

(a) (b)

Figure B-8 Comparison of initial and optimal designs: (a) band gap and (b) output electric power FRFs.

In Figure B-8 (a), the band gap ranges from 13.56 kHz to 26.44 kHz for the initial design, while it ranges from 11.69 kHz to 21.70 kHz for the optimal design. Since the lattice constant of the unit cell increases from 126.7 mm to 149.5 mm, the band gap's lower and upper bounds are slightly decreased due to the decreased stiffness and increased mass of the unit cell. The target frequency f_{target} of 20 kHz is included in the band gap for the optimal design. Figure B-8 (b) shows that the peak frequency f_{peak} and the corresponding output electric power are calculated as 22.31 kHz and 2.09 mW for the initial design. The output electric power at the target frequency f_{target} of 20 kHz is 0.014 mW. Therefore, the PnC-based PEH system for the initial design cannot play a role in localizing and harvesting the elastic wave

energy at 20 kHz. The peak frequency f_{peak} and the corresponding output electric power are calculated as 20.01 kHz and 2.18 mW for the optimal design. The output electric power at the target frequency f_{target} of 20 kHz is 2.17 mW. Note that the length $2l_m+l_M$ of the defect increases from 190.4 mm to 206.3 mm and the length l_p of the PEH devices increases from 95.20 mm to 97.1 mm. The defect band frequency is slightly decreased due to the decreased stiffness and increased mass of the defect where PEH devices are attached. Thereby, the optimal design enables to amplify the output electric power at the target frequency remarkably.

Table B-3 Information about design variables of the one-dimensional PnC with the piezoelectric defect.

Design variables	Initial value	Lower bound	Upper bound
Length of the aluminum stack, l_m/ $\lambda_{m,target}$	0.25	0.1	0.5
Length of the steel stack, l_M/ $\lambda_{M,target}$	0.25	0.1	0.5
Length of the PEH devices, $l_p/2l_m+l_M$	0.5	0.1	1
Height of the PEH devices, h_p/h_M	0.25	0.1	0.5
External electrical resistance, $\log(R_{load})/7$	0.5	0.1	1

Table B-4 Design optimization results of the one-dimensional PnC with the piezoelectric defect.

Category		Initial design	Optimal design
Design variables	Length of the aluminum stack, l_m	63.50 mm	56.80 mm
	Length of the steel stack, l_M	63.09 mm	92.70 mm
	Length of the PEH devices, l_p	95.20 mm	97.10 mm
	Height of the PEH devices, h_p	1.25 mm	1.20 mm
	External electrical resistance, R_{load}	3.16 kΩ	2.29 kΩ
Physical quantities	Band gap	13.56 kHz - 26.44 kHz	11.69 kHz - 21.70 kHz
	Peak frequency, f_{peak}	22.31 kHz	20.01 kHz
	Output electric power at f_{peak}	2.09 mW	2.18 mW
	Output electric power at f_{target}	0.014 mW	2.17 mW

B.6 Summary and Discussion

Even though several previous studies have demonstrated the successful enhancement of output performance of PEH by leveraging a defect mode of a PnC, most of them have focused on numerical models, such as FEM, to calculate the output electric power and the defect bands. Little research effort has been made to date to develop an electroelastically coupled analytical model of a PnC with a piezoelectric defect for PEH. This appendix thus proposed an electroelastically coupled analytical model of a PnC with a piezoelectric defect under longitudinal elastic waves.

First, an electroelastically coupled transfer matrix was derived. Newton's 2nd law and constitutive relations of linear piezoelectricity were used to derive a mechanical equation of motions. Gauss's law and Kirchhoff's law were used to derive an electrical circuit equation. Under an assumption of harmonic motions, an electroelastically coupled transfer matrix was explicitly derived by simultaneously solving the mechanical equation of motions and electrical circuit equation with the help of Green's function. Second, using the derived electroelastically coupled transfer matrix, the defect band frequencies and output electric power generated by the PEH devices were calculated based on TMM and SPM, respectively. Results of the band structure and PEH performance analyses confirmed that the proposed electroelastically coupled analytical model is able to elucidate the effects of the inertia, stiffness, and electroelastic coupling of the PEH device attached to the defect.

To the best of the authors' knowledge, the unique contributions of this study are two-fold. First, this work is the first attempt to propose an electroelastically coupled analytical model of a PnC with a piezoelectric defect for energy harvesting.

Second, an electroelastically coupled transfer matrix is parameterized in an explicit manner for a structure to which PEH devices are attached while considering both the forward and backward electroelastic coupling.

Compared with the FEM, the proposed analytical model has two primary advantages. First, it requires much less computation time to execute both defect band and PEH performance analyses. For example, the proposed analytical model takes 2.2 sec and 1.2 sec to complete one simulation in defect band and PEH performance analyses, respectively, while the FEM takes 7 min and 9 min, respectively. The proposed analytical model can be thus used for uncertainty propagation analysis with an affordable computation cost. Second, the proposed analytical model can provide a theoretical basis to enhance the output electric power, since it is expressed in a mathematical and explicit form.

Sections of this appendix have been published or submitted as the following journal articles:

1) **Soo-Ho Jo**, Heonjun Yoon, Yong Chang Shin, and Byeng D. Youn, "An Analytical Model of a Phononic Crystal with a Piezoelectric Defect for Energy Harvesting Using an Electroelastically Coupled Transfer Matrix," *International Journal of Mechanical Sciences*, Vol. 193, pp. 106160, 2021.

References

[1] Y.-W. Kuo, C.-L. Li, J.-H. Jhang, S. Lin, Design of a wireless sensor network-based IoT platform for wide area and heterogeneous applications, IEEE Sensors Journal, 18 (2018) 5187-5197.

[2] R. Piyare, S.R. Lee, Towards internet of things (iots): Integration of wireless sensor network to cloud services for data collection and sharing, arXiv preprint arXiv:1310.2095, (2013).

[3] S.R. Anton, H.A. Sodano, A review of power harvesting using piezoelectric materials (2003–2006), Smart Materials and Structures, 16 (2007) R1.

[4] H.S. Kim, J.-H. Kim, J. Kim, A review of piezoelectric energy harvesting based on vibration, International Journal of Precision Engineering and Manufacturing, 12 (2011) 1129-1141.

[5] S. Beeby, M. Tudor, R. Torah, S. Roberts, T. O'Donnell, S. Roy, Experimental comparison of macro and micro scale electromagnetic vibration powered generators, Microsystem Technologies, 13 (2007) 1647-1653.

[6] S.P. Beeby, R.N. Torah, M.J. Tudor, P. Glynne-Jones, T. O'Donnell, C.R. Saha, S. Roy, A micro electromagnetic generator for vibration energy

harvesting, Journal of Micromechanics and Microengineering, 17 (2007) 1257-1265.

[7] E.O. Torres, G.A. Rincón-Mora, Electrostatic energy-harvesting and battery-charging CMOS system prototype, Circuits and Systems I: Regular Papers, IEEE Transactions on, 56 (2009) 1938-1948.

[8] M. Lallart, S. Pruvost, D. Guyomar, Electrostatic energy harvesting enhancement using variable equivalent permittivity, Physics Letters A, 375 (2011) 3921-3924.

[9] L. Wang, F. Yuan, Vibration energy harvesting by magnetostrictive material, Smart Materials and Structures, 17 (2008) 045009.

[10] A. Adly, D. Davino, A. Giustiniani, C. Visone, Experimental tests of a magnetostrictive energy harvesting device toward its modeling, Journal of Applied Physics, 107 (2010) 09A935-909A935-933.

[11] J. Cui, H. Yoon, B.D. Youn, An omnidirectional biomechanical energy harvesting (OBEH) sidewalk block for a self-generative power grid in a smart city, International Journal of Precision Engineering and Manufacturing-Green Technology, 5 (2018) 507-517.

[12] M. Safaei, H.A. Sodano, S.R. Anton, A review of energy harvesting using piezoelectric materials: state-of-the-art a decade later (2008–2018), Smart Materials and Structures, 28 (2019) 113001.

[13] H. Yoon, M. Kim, C.-S. Park, B.D. Youn, Time-varying output

performances of piezoelectric vibration energy harvesting under nonstationary random vibrations, Smart Materials and Structures, 27 (2017) 015004.

[14] K. Yang, J. Wang, D. Yurchenko, A double-beam piezo-magneto-elastic wind energy harvester for improving the galloping-based energy harvesting, Applied Physics Letters, 115 (2019) 193901.

[15] B. Wang, S. Yang, P. Sharma, Flexoelectricity as a universal mechanism for energy harvesting from crumpling of thin sheets, Physical Review B, 100 (2019) 035438.

[16] S.F. Nabavi, A. Farshidianfar, A. Afsharfard, H.H. Khodaparast, An ocean wave-based piezoelectric energy harvesting system using breaking wave force, International Journal of Mechanical Sciences, 151 (2019) 498-507.

[17] Q. Deng, M. Kammoun, A. Erturk, P. Sharma, Nanoscale flexoelectric energy harvesting, International Journal of Solids and Structures, 51 (2014) 3218-3225.

[18] J. Wang, S. Zhou, Z. Zhang, D. Yurchenko, High-performance piezoelectric wind energy harvester with Y-shaped attachments, Energy Conversion and Management, 181 (2019) 645-652.

[19] M. Kim, M. Hoegen, J. Dugundji, B.L. Wardle, Modeling and experimental verification of proof mass effects on vibration energy harvester performance, Smart Materials and Structures, 19 (2010) 045023.

[20] A. Erturk, D.J. Inman, Piezoelectric Energy Harvesting, John Wiley & Sons, 2011.

[21] H. Yoon, B.D. Youn, Stochastic quantification of the electric power generated by a piezoelectric energy harvester using a time–frequency analysis under non-stationary random vibrations, Smart Materials and Structures, 23 (2014) 045035.

[22] G.K. Ottman, H.F. Hofmann, A.C. Bhatt, G.A. Lesieutre, Adaptive piezoelectric energy harvesting circuit for wireless remote power supply, IEEE Transactions on Power Electronics, 17 (2002) 669-676.

[23] S. Priya, H.-C. Song, Y. Zhou, R. Varghese, A. Chopra, S.-G. Kim, I. Kanno, L. Wu, D.S. Ha, J. Ryu, A review on piezoelectric energy harvesting: materials, methods, and circuits, Energy Harvesting and Systems, 4 (2019) 3-39.

[24] S. Du, Y. Jia, C. Zhao, G.A. Amaratunga, A.A. Seshia, A fully integrated split-electrode SSHC rectifier for piezoelectric energy harvesting, IEEE Journal of Solid-State Circuits, 54 (2019) 1733-1743.

[25] J.H. Lee, K.Y. Lee, M.K. Gupta, T.Y. Kim, D.Y. Lee, J. Oh, C. Ryu, W.J. Yoo, C.Y. Kang, S.J. Yoon, Highly stretchable piezoelectric-pyroelectric hybrid nanogenerator, Advanced Materials, 26 (2014) 765-769.

[26] C. Bowen, H. Kim, P. Weaver, S. Dunn, Piezoelectric and ferroelectric materials and structures for energy harvesting applications, Energy &

Environmental Science, 7 (2014) 25-44.

[27] G.K. Ottman, H.F. Hofmann, G.A. Lesieutre, Optimized piezoelectric energy harvesting circuit using step-down converter in discontinuous conduction mode, IEEE Transactions on Power Electronics, 18 (2003) 696-703.

[28] Y.K. Ramadass, A.P. Chandrakasan, An efficient piezoelectric energy harvesting interface circuit using a bias-flip rectifier and shared inductor, IEEE Journal of Solid-State Circuits, 45 (2010) 189-204.

[29] A. Erturk, D.J. Inman, An experimentally validated bimorph cantilever model for piezoelectric energy harvesting from base excitations, Smart Materials and Structures, 18 (2009) 025009.

[30] A. Erturk, D.J. Inman, A distributed parameter electromechanical model for cantilevered piezoelectric energy harvesters, Journal of Vibration and Acoustics, 130 (2008) 041002.

[31] S. Lee, B.D. Youn, A design and experimental verification methodology for an energy harvester skin structure, Smart Materials and Structures, 20 (2011) 057001.

[32] S. Lee, B.D. Youn, B.C. Jung, Robust segment-type energy harvester and its application to a wireless sensor, Smart Materials and Structures, 18 (2009) 095021.

[33] Y .C. Shin, H. Yoon, S.-H. Jo, W. Choi, C.-S. Park, M. Kim, B.D. Youn,

Phononic band gap of a quarter-wave stack for enhanced piezoelectric energy harvesting, International Journal of Mechanical Sciences, 192 (2020) 106003.

[34] L. Shen, J.H. Wu, S. Zhang, Z. Liu, J. Li, Low-frequency vibration energy harvesting using a locally resonant phononic crystal plate with spiral beams, Modern Physics Letters B, 29 (2015) 1450259.

[35] C. Sugino, A. Erturk, Analysis of multifunctional piezoelectric metastructures for low-frequency bandgap formation and energy harvesting, Journal of Physics D: Applied Physics, 51 (2018) 215103.

[36] Z. Chen, B. Guo, Y. Yang, C. Cheng, Metamaterials-based enhanced energy harvesting: A review, Physica B: Condensed Matter, 438 (2014) 1-8.

[37] S. Gonella, A.C. To, W.K. Liu, Interplay between phononic bandgaps and piezoelectric microstructures for energy harvesting, Journal of the Mechanics and Physics of Solids, 57 (2009) 621-633.

[38] A. Colombi, P. Roux, S. Guenneau, M. Rupin, Directional cloaking of flexural waves in a plate with a locally resonant metamaterial, The Journal of the Acoustical Society of America, 137 (2015) 1783-1789.

[39] Y. Jin, B. Djafari-Rouhani, D. Torrent, Gradient index phononic crystals and metamaterials, Nanophotonics, 8 (2019) 685-701.

[40] S.-H. Jo, Y. Xia, A.G. Moura, H. Yoon, Y.C. Shin, A. Erturk, B.D. Youn,

Experimentally validated broadband self-collimation of elastic waves, International Journal of Mechanical Sciences, 192 (2021) 106131.

[41] H. Ruiz, C. Claeys, E. Deckers, W. Desmet, Numerical and experimental study of the effect of microslits on the normal absorption of structural metamaterials, Mechanical Systems and Signal Processing, 70 (2016) 904-918.

[42] X. Cui, J. Zhao, O. Boyko, B. Bonello, Z. Zhong, Multi-branch subwavelength focusing of the lowest-order antisymmetric Lamb mode in a gradient-index phononic crystal, International Journal of Mechanical Sciences, 157 (2019) 677-683.

[43] S. Tol, F. Degertekin, A. Erturk, Phononic crystal Luneburg lens for omnidirectional elastic wave focusing and energy harvesting, Applied Physics Letters, 111 (2017) 013503.

[44] J. Qu, M. Kadic, M. Wegener, Three-dimensional poroelastic metamaterials with extremely negative or positive effective static volume compressibility, Extreme Mechanics Letters, 22 (2018) 165-171.

[45] J. Zhu, H. Chen, B. Wu, W. Chen, O. Balogun, Tunable band gaps and transmission behavior of SH waves with oblique incident angle in periodic dielectric elastomer laminates, International Journal of Mechanical Sciences, 146 (2018) 81-90.

[46] V.F. Dal Poggetto, A.L. Serpa, Elastic wave band gaps in a three-

dimensional periodic metamaterial using the plane wave expansion method, International Journal of Mechanical Sciences, (2020) 105841.

[47] W. Zhou, W. Chen, M. Destrade, C. Lim, Actively controllable topological phase transition in phononic beam systems, International Journal of Mechanical Sciences, (2020) 105668.

[48] D. Garcia-Pablos, M. Sigalas, F.M. De Espinosa, M. Torres, M. Kafesaki, N. Garcia, Theory and experiments on elastic band gaps, Physical Review Letters, 84 (2000) 4349.

[49] E. Rohan, B. Miara, F. Seifrt, Numerical simulation of acoustic band gaps in homogenized elastic composites, International Journal of Engineering Science, 47 (2009) 573-594.

[50] M. Carrara, M. Cacan, J. Toussaint, M. Leamy, M. Ruzzene, A. Erturk, Metamaterial-inspired structures and concepts for elastoacoustic wave energy harvesting, Smart Materials and Structures, 22 (2013) 065004.

[51] Y.-C. Zhao, Y.-B. Wu, L.-B. Yuan, Characteristics of the localized modes in 2D phononic crystal with heterostructure point defect, Physica Scripta, 80 (2009) 065401.

[52] F. Wu, Z. Hou, Z. Liu, Y. Liu, Point defect states in two-dimensional phononic crystals, Physics Letters A, 292 (2001) 198-202.

[53] Y. Li, T. Chen, X. Wang, T. Ma, P. Jiang, Acoustic confinement and waveguiding in two-dimensional phononic crystals with material defect

states, Journal of Applied Physics, 116 (2014) 024904.

[54] Y. Li, L. Zhu, T. Chen, Q. Ye, Elastic wave confinement and absorption in a dissipative metamaterial, Indian Journal of Pure & Applied Physics (IJPAP), 56 (2018) 158-163.

[55] K.-C. Chuang, Z.-Q. Zhang, H.-X. Wang, Experimental study on slow flexural waves around the defect modes in a phononic crystal beam using fiber Bragg gratings, Physics Letters A, 380 (2016) 3963-3969.

[56] C. Gu, F. Jin, Research on the tunability of point defect modes in a two-dimensional magneto-elastic phononic crystal, Journal of Physics D: Applied Physics, 49 (2016) 175103.

[57] V. Romero-García, J. Sánchez-Pérez, L. Garcia-Raffi, Propagating and evanescent properties of double-point defects in sonic crystals, New Journal of Physics, 12 (2010) 083024.

[58] X. Li, Z. Liu, Coupling of cavity modes and guiding modes in two-dimensional phononic crystals, Solid State Communications, 133 (2005) 397-402.

[59] Y.-C. Zhao, L.-B. Yuan, Characteristics of multi-point defect modes in 2D phononic crystals, Journal of Physics D: Applied Physics, 42 (2008) 015403.

[60] A. Khelif, A. Choujaa, B. Djafari-Rouhani, M. Wilm, S. Ballandras, V. Laude, Trapping and guiding of acoustic waves by defect modes in a full-

band-gap ultrasonic crystal, Physical Review B, 68 (2003) 214301.

[61] K.F. Graff, Wave Motion in Elastic Solids, Ohio State University Press, 1975.

[62] S.E. Lima, O. Frazão, R.G. Farias, F.M. Araújo, L.A. Ferreira, J.L. Santos, V. Miranda, Mandrel-based fiber-optic sensors for acoustic detection of partial discharges—A proof of concept, IEEE Transactions on Power Delivery, 25 (2010) 2526-2534.

[63] T. Toutountzakis, C.K. Tan, D. Mba, Application of acoustic emission to seeded gear fault detection, NDT & E International, 38 (2005) 27-36.

[64] Y. Zhu, S.R. Moheimani, M.R. Yuce, A 2-DOF MEMS ultrasonic energy harvester, IEEE Sensors Journal, 11 (2010) 155-161.

[65] Q. Shi, T. Wang, C. Lee, MEMS based broadband piezoelectric ultrasonic energy harvester (PUEH) for enabling self-powered implantable biomedical devices, Scientific Reports, 6 (2016) 24946.

[66] C.-S. Park, Y.C. Shin, S.-H. Jo, H. Yoon, W. Choi, B.D. Youn, M. Kim, Two-dimensional octagonal phononic crystals for highly dense piezoelectric energy harvesting, Nano Energy, 57 (2019) 327-337.

[67] T.-G. Lee, S.-H. Jo, H.M. Seung, S.-W. Kim, E.-J. Kim, B.D. Youn, S. Nahm, M. Kim, Enhanced energy transfer and conversion for high performance phononic crystal-assisted elastic wave energy harvesting, Nano Energy, 78 (2020) 105226.

[68] S. Qi, M. Oudich, Y. Li, B. Assouar, Acoustic energy harvesting based on a planar acoustic metamaterial, Applied Physics Letters, 108 (2016) 263501.

[69] M. Oudich, Y. Li, Tunable sub-wavelength acoustic energy harvesting with a metamaterial plate, Journal of Physics D: Applied Physics, 50 (2017) 315104.

[70] L.-Y. Wu, L.-W. Chen, C.-M. Liu, Acoustic energy harvesting using resonant cavity of a sonic crystal, Applied Physics Letters, 95 (2009) 013506.

[71] A.H. Aly, A. Nagaty, Z. Khalifa, A. Mehaney, The significance of temperature dependence on the piezoelectric energy harvesting by using a phononic crystal, Journal of Applied Physics, 123 (2018) 185102.

[72] T. Deng, S. Zhang, Y. Gao, Tunability of band gaps and energy harvesting based on the point defect in a magneto-elastic acoustic metamaterial plate, Applied Physics Express, 13 (2019) 015503.

[73] Q. Geng, T. Cai, Y. Li, Flexural wave manipulation and energy harvesting characteristics of a defect phononic crystal beam with thermal effects, Journal of Applied Physics, 125 (2019) 035103.

[74] X.-F. Lv, X. Fang, Z.-Q. Zhang, Z.-L. Huang, K.-C. Chuang, Highly localized and efficient energy harvesting in a phononic crystal beam: Defect placement and experimental validation, Crystals, 9 (2019) 391.

[75] H. Lv, X. Tian, M.Y. Wang, D. Li, Vibration energy harvesting using a phononic crystal with point defect states, Applied Physics Letters, 102 (2013) 034103.

[76] T.-X. Ma, Q.-S. Fan, Z.-Y. Li, C. Zhang, Y.-S. Wang, Flexural wave energy harvesting by multi-mode elastic metamaterial cavities, Extreme Mechanics Letters, 41 (2020) 101073.

[77] T. Deng, S. Zhang, Y. Gao, A magnetic-dependent vibration energy harvester based on the tunable point defect in 2D magneto-elastic phononic crystals, Crystals, 9 (2019) 261.

[78] R.U. Ahmed, S. Banerjee, Low frequency energy scavenging using sub-wave length scale acousto-elastic metamaterial, AIP Advances, 4 (2014) 117114.

[79] S. Tol, F. Degertekin, A. Erturk, Gradient-index phononic crystal lens-based enhancement of elastic wave energy harvesting, Applied Physics Letters, 109 (2016) 063902.

[80] Z. Chen, J. He, G. Wang, Vibration bandgaps of piezoelectric metamaterial plate with local resonators for vibration energy harvesting, Shock and Vibration, 2019 (2019) 1397123.

[81] J. Hyun, W. Choi, M. Kim, Gradient-index phononic crystals for highly dense flexural energy harvesting, Applied Physics Letters, 115 (2019) 173901.

[82] H. Lee, J.H. Oh, H.M. Seung, S.H. Cho, Y.Y. Kim, Extreme stiffness hyperbolic elastic metamaterial for total transmission subwavelength imaging, Scientific Reports, 6 (2016) 24026.

[83] Y.K. Ahn, H.J. Lee, Y.Y. Kim, Conical refraction of elastic waves by anisotropic metamaterials and application for parallel translation of elastic waves, Scientific Reports, 7 (2017) 10072.

[84] S. Alan, A. Allam, A. Erturk, Programmable mode conversion and bandgap formation for surface acoustic waves using piezoelectric metamaterials, Applied Physics Letters, 115 (2019) 093502.

[85] A.H. Aly, A. Nagaty, Z. Khalifa, Propagation of acoustic waves in 2D periodic and quasiperiodic phononic crystals, International Journal of Modern Physics B, 31 (2017) 1750147.

[86] J. Hyun, W. Choi, S. Wang, C.-s. Park, M. Kim, Systematic realization of double-zero-index phononic crystals with hard inclusions, Scientific Reports, 8 (2018) 7288.

[87] F. Wu, Z. Liu, Y. Liu, Splitting and tuning characteristics of the point defect modes in two-dimensional phononic crystals, Physical Review E, 69 (2004) 066609.

[88] Z. Yan, Y. Wang, C. Zhang, Wavelet method for calculating the defect states of two-dimensional phononic crystals, Acta Mechanica Solida Sinica, 21 (2008) 104-109.

[89] Z.-J. Yao, G.-L. Yu, Y.-S. Wang, Z.-F. Shi, Propagation of bending waves in phononic crystal thin plates with a point defect, International Journal of Solids and Structures, 46 (2009) 2571-2576.

[90] V. Romero-García, J. Sánchez-Pérez, S. Castiñeira-Ibáñez, L. Garcia-Raffi, Evidences of evanescent Bloch waves in phononic crystals, Applied Physics Letters, 96 (2010) 124102.

[91] M. Sangster, A. Hussain, The supercell method for calculating responses in defective lattices, Physica B+C, 131 (1985) 119-125.

[92] M.J. Puska, S. Pöykkö, M. Pesola, R.M. Nieminen, Convergence of supercell calculations for point defects in semiconductors: Vacancy in silicon, Physical Review B, 58 (1998) 1318.

[93] L.-Y. Wu, L.-W. Chen, Propagation of acoustic waves in the woodpile sonic crystal with a defect, Applied Acoustics, 73 (2012) 312-322.

[94] H. Yang, G. Yun, Y. Cao, Coupling characteristics of point defects modes in two-dimensional magnonic crystals, Journal of Applied Physics, 112 (2012) 103911.

[95] M.S. Kushwaha, P. Halevi, G. Martinez, L. Dobrzynski, B. Djafari-Rouhani, Theory of acoustic band structure of periodic elastic composites, Physical Review B, 49 (1994) 2313.

[96] E.J.P. Miranda Jr, J.M.C. Dos Santos, Band structure in carbon nanostructure phononic crystals, Materials Research, 20 (2017) 555-571.

[97] G. Yi, Y.C. Shin, H. Yoon, S.-H. Jo, B.D. Youn, Topology optimization for phononic band gap maximization considering a target driving frequency, JMST Advances, (2019) 1-7.

[98] F.-L. Li, Y.-S. Wang, C. Zhang, A BEM for band structure and elastic wave transmission analysis of 2D phononic crystals with different interface conditions, International Journal of Mechanical Sciences, 144 (2018) 110-117.

[99] F. Wu, Z. Liu, Y. Liu, Acoustic band gaps in 2D liquid phononic crystals of rectangular structure, Journal of Physics D: Applied Physics, 35 (2002) 162.

[100] Y. Wang, F. Li, Y. Wang, K. Kishimoto, W. Huang, Tuning of band gaps for a two-dimensional piezoelectric phononic crystal with a rectangular lattice, Acta Mechanica Sinica, 25 (2009) 65-71.

[101] H. Zhong, F. Wu, X. Zhang, Y. Liu, Localized defect modes of water waves through two-dimensional periodic bottoms with point defects, Physics Letters A, 339 (2005) 478-487.

[102] H. Zhu, F. Semperlotti, Metamaterial based embedded acoustic filters for structural applications, AIP Advances, 3 (2013) 092121.

[103] Y. Pennec, B. Djafari-Rouhani, H. Larabi, J. Vasseur, A. Hladky-Hennion, Low-frequency gaps in a phononic crystal constituted of cylindrical dots deposited on a thin homogeneous plate, Physical Review B, 78 (2008)

104105.

[104] B.A. Auld, Acoustic Fields and Waves in Solids, John Wiley & Sons, 1973.

[105] A. Erturk, P.A. Tarazaga, J.R. Farmer, D.J. Inman, Effect of strain nodes and electrode configuration on piezoelectric energy harvesting from cantilevered beams, Journal of Vibration and Acoustics, 131 (2009) 011010.

[106] D. Zizys, R. Gaidys, R. Dauksevicius, V. Ostasevicius, V. Daniulaitis, Segmentation of a vibro-shock cantilever-type piezoelectric energy harvester operating in higher transverse vibration modes, Sensors, 16 (2016) 11.

[107] J. Miklowitz, The theory of elastic waves and waveguides, Elsevier, 2012.

[108] A. Korovin, Y. Pennec, B. Djafari-Rouhani, Strong coupling of phononic cavity modes in one-dimensional corrugated nanobeam structures, Physical Review B, 96 (2017) 184302.

[109] B. Ahn, H. Lee, J.S. Lee, Y.Y. Kim, Topology optimization of metasurfaces for anomalous reflection of longitudinal elastic waves, Computer Methods in Applied Mechanics and Engineering, 357 (2019) 112582.

[110] B. Ahn, H.J. Lee, Y.Y. Kim, Topology optimization of anisotropic metamaterials tracing the target EFC and field polarization, Computer Methods in Applied Mechanics and Engineering, 333 (2018) 176-196.

[111] X. Yang, M. Kweun, Y.Y. Kim, Monolayer metamaterial for full mode-

converting transmission of elastic waves, Applied Physics Letters, 115 (2019) 071901.

[112] V. Romero-García, J.V. Sánchez-Pérez, L.M. Garcia-Raffi, Evanescent modes in sonic crystals: Complex dispersion relation and supercell approximation, Journal of Applied Physics, 108 (2010) 044907.

[113] V. Romero-García, J.V. Sánchez-Pérez, L. Garcia-Raffi, Propagating and evanescent properties of double-point defects in sonic crystals, New Journal of Physics, 12 (2010) 083024.

[114] B.C. Jung, H. Yoon, H. Oh, G. Lee, M. Yoo, B.D. Youn, Y.C. Huh, Hierarchical model calibration for designing piezoelectric energy harvester in the presence of variability in material properties and geometry, Structural and Multidisciplinary Optimization, 53 (2016) 161-173.

[115] H. Yoon, B.D. Youn, System reliability analysis of piezoelectric vibration energy harvesting considering multiple safety events under physical uncertainty, Smart Materials and Structures, 28 (2018) 025010.

[116] G. Lee, W. Kim, H. Oh, B.D. Youn, N.H. Kim, Review of statistical model calibration and validation—from the perspective of uncertainty structures, Structural and Multidisciplinary Optimization, (2019) 1-26.

[117] T. Kim, G. Lee, B.D. Youn, Uncertainty characterization under measurement errors using maximum likelihood estimation: cantilever beam end-to-end UQ test problem, Structural and Multidisciplinary

Optimization, 59 (2019) 323-333.

[118] Y. Guo, M. Hettich, T. Dekorsy, Guiding of elastic waves in a two-dimensional graded phononic crystal plate, New Journal of Physics, 19 (2017) 013029.

[119] J.M. De Ponti, A. Colombi, R. Ardito, F. Braghin, A. Corigliano, R.V. Craster, Graded elastic metasurface for enhanced energy harvesting, New Journal of Physics, 22 (2020) 013013.

[120] X.-Z. Zhou, Y.-S. Wang, C. Zhang, Effects of material parameters on elastic band gaps of two-dimensional solid phononic crystals, Journal of Applied Physics, 106 (2009) 014903.

[121] P. Wang, T.-N. Chen, K.-P. Yu, X.-P. Wang, Lamb wave band gaps in a double-sided phononic plate, Journal of Applied Physics, 113 (2013) 053509.

[122] Z.-j. Yao, G.-l. Yu, Y.-s. Wang, Z.-f. Shi, J.-b. Li, Propagation of flexural waves in phononic crystal thin plates with linear defects, Journal of Zhejiang University-SCIENCE A, 11 (2010) 827-834.

[123] Y.-H. Kim, Sound Propagation: An Impedance Based Approach, John Wiley & Sons, 2010.

[124] B. Schlicht, K.F. Wall, R.K. Chang, P.W. Barber, Light scattering by two parallel glass fibers, Journal of the Optical Society of America A, 4 (1987) 800-809.

[125] H. Yoon, B.D. Youn, H.S. Kim, Kirchhoff plate theory-based electromechanically-coupled analytical model considering inertia and stiffness effects of a surface-bonded piezoelectric patch, Smart Materials and Structures, 25 (2016) 025017.

[126] S. Ali, M. Friswell, S. Adhikari, Piezoelectric energy harvesting with parametric uncertainty, Smart Materials and Structures, 19 (2010) 105010.

[127] A.T. Eshghi, S. Lee, M.K. Sadoughi, C. Hu, Y.-C. Kim, J.-H. Seo, Design optimization under uncertainty and speed variability for a piezoelectric energy harvester powering a tire pressure monitoring sensor, Smart Materials and Structures, 26 (2017) 105037.

[128] J. Banerjee, A. Ananthapuvirajah, An exact dynamic stiffness matrix for a beam incorporating Rayleigh–Love and Timoshenko theories, International Journal of Mechanical Sciences, 150 (2019) 337-347.

[129] J.-B. Han, S.-Y. Hong, J.-H. Song, H.-W. Kwon, Vibrational energy flow models for the Rayleigh–Love and Rayleigh–Bishop rods, Journal of Sound and Vibration, 333 (2014) 520-540.

[130] L. Han, Y. Zhang, Z.-Q. Ni, Z.-M. Zhang, L.-H. Jiang, A modified transfer matrix method for the study of the bending vibration band structure in phononic crystal Euler beams, Physica B: Condensed Matter, 407 (2012) 4579-4583.

[131] Y. Zhang, Z.-Q. Ni, L.-H. Jiang, L. Han, X.-W. Kang, Study of the bending

vibration characteristic of phononic crystals beam-foundation structures by Timoshenko beam theory, International Journal of Modern Physics B, 29 (2015) 1550136.

[132] A. Hu, X. Zhang, F. Wu, Y. Yao, C. Cheng, P. Huang, Temperature effects on the defect states in two-dimensional phononic crystals, Physics Letters A, 378 (2014) 2239-2244.

[133] X. Zhou, Y. Xu, L. Wang, Tuning flexural elastic wave propagation in electroactive phononic crystals, Journal of Applied Physics, 123 (2018) 225103.

[134] Z.-G. Huang, Silicon-based filters, resonators and acoustic channels with phononic crystal structures, Journal of Physics D: Applied Physics, 44 (2011) 245406.

[135] K.H. Matlack, M. Serra-Garcia, A. Palermo, S.D. Huber, C. Daraio, Designing perturbative metamaterials from discrete models, Nature Materials, 17 (2018) 323-328.

[136] H.J. Lee, J.K. Lee, Y.Y. Kim, Elastic metamaterial-based impedance-varying phononic bandgap structures for bandpass filters, Journal of Sound and Vibration, 353 (2015) 58-74.

[137] Y.-F. Wang, A.A. Maznev, V. Laude, Formation of Bragg band gaps in anisotropic phononic crystals analyzed with the empty lattice model, Crystals, 6 (2016) 52.

[138] J.S. Jensen, Phononic band gaps and vibrations in one-and two-dimensional mass–spring structures, Journal of Sound and Vibration, 266 (2003) 1053-1078.

[139] Z.-B. Cheng, Z.-F. Shi, Multi-mass-spring model and energy transmission of one-dimensional periodic structures, IEEE Transactions on Ultrasonics, Ferroelectrics, and Frequency Control, 61 (2014) 739-746.

[140] J.-L. Tsai, H.-H. Huang, C. Sun, Multi-displacement continuum model for discrete systems, International Journal of Mechanical Sciences, 52 (2010) 1767-1771.

[141] Y. Liu, X. Su, C. Sun, Broadband elastic metamaterial with single negativity by mimicking lattice systems, Journal of the Mechanics and Physics of Solids, 74 (2015) 158-174.

[142] H.B. Al Ba'ba'a, M. Nouh, Mechanics of longitudinal and flexural locally resonant elastic metamaterials using a structural power flow approach, International Journal of Mechanical Sciences, 122 (2017) 341-354.

[143] S. Yao, X. Zhou, G. Hu, Experimental study on negative effective mass in a 1D mass–spring system, New Journal of Physics, 10 (2008) 043020.

[144] C. Yuan, L. Jing, Z. Jingdong, H. Tao, Z. Minggang, Y.D. Yuan, Phononic first band gap of quaternary layered periodic structure with the lumped-mass method, Shock and Vibration, 2014 (2014).

[145] J.H. Oh, S.J. Choi, J.K. Lee, Y.Y. Kim, Zero-frequency Bragg gap by spin-

harnessed metamaterial, New Journal of Physics, 20 (2018) 083035.

[146] P. Deymier, K. Runge, One-dimensional mass-spring chains supporting elastic waves with non-conventional topology, Crystals, 6 (2016) 44.

[147] L. Wu, F. Zhuang, S. He, Degeneracy analysis for a supercell of a photonic crystal and its application to the creation of band gaps, Physical Review E, 67 (2003) 026612.

[148] A. Cerjan, S. Fan, Complete photonic band gaps in supercell photonic crystals, Physical Review A, 96 (2017) 051802.

[149] Y.K. Ahn, J.H. Oh, P.S. Ma, Y.Y. Kim, Dispersion analysis with 45°-rotated augmented supercells and applications in phononic crystal design, Wave Motion, 61 (2016) 63-72.

[150] I .A. Veres, T. Berer, O. Matsuda, Complex band structures of two dimensional phononic crystals: Analysis by the finite element method, Journal of Applied Physics, 114 (2013) 083519.

[151] G. Yi, Y.C. Shin, H. Yoon, S.-H. Jo, B.D. Youn, Topology optimization for phononic band gap maximization considering a target driving frequency, JMST Advances, 1 (2019) 153-159.

[152] H. Huang, C. Sun, G. Huang, On the negative effective mass density in acoustic metamaterials, International Journal of Engineering Science, 47 (2009) 610-617.

[153] G.F. Assis, D. Beli, E.J. de Miranda Jr, J.F. Camino, J.M.C. Dos Santos, J.R.F. Arruda, Computing the complex wave and dynamic behavior of one-dimensional phononic systems using a state-space formulation, International Journal of Mechanical Sciences, 163 (2019) 105088.

[154] V. Laude, Y. Achaoui, S. Benchabane, A. Khelif, Evanescent Bloch waves and the complex band structure of phononic crystals, Physical Review B, 80 (2009) 092301.

[155] Y. Chen, J. Shi, T. Liu, J. Dong, Q. Zhu, W. Chen, Study on the propagation mechanism of evanescent waves in one-dimensional periodic photonic crystal, Physics Letters A, 379 (2015) 2257-2260.

[156] L. Brillouin, Wave propagation in periodic structures: electric filters and crystal lattices, Courier Corporation, 2003.

[157] P.A. Deymier, Acoustic metamaterials and phononic crystals, Springer Science & Business Media, 2013.

[158] A.H. Aly, A. Nagaty, Z. Khalifa, Piezoelectric material and one-dimensional phononic crystal, Surface Review and Letters, 26 (2019) 1850144.

[159] R.F. Gibson, Principles of Composite Material Mechanics, CRC press, 2016.

[160] C. Shengbing, W. Jihong, W. Gang, Y. Dianlong, W. Xisen, Improved modeling of rods with periodic arrays of shunted piezoelectric patches,

Journal of Intelligent Material Systems and Structures, 23 (2012) 1613-1621.

[161] S. Jiang, L. Dai, H. Chen, H. Hu, W. Jiang, X. Chen, Folding beam-type piezoelectric phononic crystal with low-frequency and broad band gap, Applied Mathematics and Mechanics, 38 (2017) 411-422.

[162] R. Basutkar, Analytical modelling of a nanoscale series-connected bimorph piezoelectric energy harvester incorporating the flexoelectric effect, International Journal of Engineering Science, 139 (2019) 42-61.

[163] G. Wang, J. Wang, S. Chen, J. Wen, Vibration attenuations induced by periodic arrays of piezoelectric patches connected by enhanced resonant shunting circuits, Smart Materials and Structures, 20 (2011) 125019.

[164] O. Thorp, M. Ruzzene, A. Baz, Attenuation and localization of wave propagation in rods with periodic shunted piezoelectric patches, Smart Materials and Structures, 10 (2001) 979.

[165] W. Jian-Wei, W. Gang, C. Sheng-Bing, W. Ji-Hong, Broadband attenuation in Phononic Beams induced by periodic arrays of feedback shunted piezoelectric patches, Chinese Physics Letters, 29 (2012) 064302.

[166] J. Xu, X. Zhang, R. Yan, Coupled piezoelectric phononic crystal for adaptive broadband wave attenuation by destructive interference, Journal of Applied Mechanics, 87 (2020).

[167] H. Lee, J.K. Lee, H.M. Seung, Y.Y. Kim, Mass-Stiffness substructuring of

an elastic metasurface for full transmission beam steering, Journal of the Mechanics and Physics of Solids, 112 (2018) 577-593.

[168] J.W. Lee, J.Y. Lee, Free vibration analysis of functionally graded Bernoulli-Euler beams using an exact transfer matrix expression, International Journal of Mechanical Sciences, 122 (2017) 1-17.

[169] W. Zhou, C. Lim, Topological edge modeling and localization of protected interface modes in 1D phononic crystals for longitudinal and bending elastic waves, International Journal of Mechanical Sciences, 159 (2019) 359-372.

[170] H.J. Lee, H.S. Lee, P.S. Ma, Y.Y. Kim, Effective material parameter retrieval of anisotropic elastic metamaterials with inherent nonlocality, Journal of Applied Physics, 120 (2016) 104902.

[171] D. Smith, S. Schultz, P. Markoš, C. Soukoulis, Determination of effective permittivity and permeability of metamaterials from reflection and transmission coefficients, Physical Review B, 65 (2002) 195104.

[172] X. Zhu, X. Zou, B. Liang, J. Cheng, One-way mode transmission in one-dimensional phononic crystal plates, Journal of Applied Physics, 108 (2010) 124909.

[173] J.M. Kweun, H.J. Lee, J.H. Oh, H.M. Seung, Y.Y. Kim, Transmodal Fabry-Pérot resonance: theory and realization with elastic metamaterials, Physical Review Letters, 118 (2017) 205901.

[174] S. Lin, Effect of electric load impedances on the performance of sandwich piezoelectric transducers, IEEE Transactions on Ultrasonics, Ferroelectrics, and Frequency Control, 51 (2004) 1280-1286.

[175] D.T. Blackstock, Fundamentals of physical acoustics, in, Acoustical Society of America, 2001.

국문 초록

광대역 에너지 국부화 및 수확을 위한 압전 결함 인가 음향양자 결정의 모델링 및 설계

서울대학교 대학원

기계항공공학부

조 수 호

우리 주변에서 버려진 에너지를 재 수집하여 전력 원으로 활용하는 에너지 수확 기술은 궁극적으로 무선 센서 네트워크 내 화학적 배터리를 대체할 수 있는 수단으로 많은 주목을 받고 있다. 에너지원과 변환 메커니즘에 따라, 풍력, 태양열, 발열 및 기계적 에너지 수확을 포함한 광범위한 기술이 활발하게 연구되었다. 그 중 압전 에너지 수확은 에너지 밀도가 높고 무선 센서 네트워크에 활용할 수 있도록 소형화가 용이하다는 장점 덕분에 실현 가능성이 높은 유망할 기술로 알려져 있다.

최근에는 압전 소자에 전달되는 파동 에너지 밀도를 증폭함으로써 압전 에너지 수확 성능을 향상시키는 음향양자 결정 기반 에너지 수확 기술이 새로운 연구 분야로 떠오르고 있다. 음향양자 결정은 단위

격자를 주기적으로 배열하여 파동 특이현상을 구현하도록 설계된 인공 구조체를 뜻하며, 밴드 갭과 같이 자연계에 존재하지 않는 파동 특이현상을 가진다. 이 때 밴드 갭을 가지는 음향양자 결정 내에 국부적인 주기성을 파괴하는 단일 혹은 다중 결함을 인가할 시, 밴드 갭 내에 결함 밴드가 생성된다. 결함 밴드에 상응하는 주파수로 파동을 인가하면 파동 에너지가 결함 부근에 국부화되며, 궁극적으로 압전 에너지 수확 성능의 획기적인 향상을 가능케 한다.

고체 매체와 고체 압전 소자 간의 기계적 임피던스 불일치를 줄이는 측면에서 음향파보다는 탄성파 하에 음향양자 결정을 설계하는 것이 유리하다. 따라서, 탄성파 영역에서의 몇몇 연구가 보고 되고 있지만 대부분의 연구는 에너지 수확 성능이 향상되는 현상 자체에만 초점을 두고 있다. 시스템의 해석과 설계 관점에서 다음과 같이 두 가지 중요한 이슈가 존재한다. 첫 번째로, 고밀도 에너지 수확을 위한 단일 혹은 다중 결함 인가 음향양자 결정에 대한 설계적 근거가 전무하다. 두 번째로, 결함 모드 기반 에너지 국부화 및 수확은 본연적으로 협대역 특성을 가지고 있다. 이에 본 박사학위논문에서는 (1) 압전 결함 인가 음향양자 결정의 구조 및 전기 회로 설계에 대한 매개 변수 연구와 (2) 광대역 에너지 수확을 구현하기 위한 새로운 개념의 음향양자 결정 설계의 연구를 제안한다. 덧붙여, 결함 밴드 형성 및 분리를 물리적으로 고찰하기 위한 압전 결함 인가 음향양자 결정의 수학적 해석 모델 개발을 부록에 제시한다.

첫 번째 연구에서는 단일 혹은 이중 압전 결함이 인가된 2차원 음향양자 결함을 설계할 시, 수확 가능 전력을 극대화하기 위한 주요 설계 변수에 대한 지침과 이론적 근거를 제공하는 것을 목표로 한다. 여기서 설계 변수는 기계적 도메인에서의 슈퍼셀 크기, 결함 위치, 이중

결함 사이 상대적 위치(예: 거리 및 배열 방향)와 전기 도메인에서의 이중 결함 간의 전기 회로 연결을 뜻한다. 첫 번째로, 전압 상쇄 회피 관점에서 목표 결함 모드 형상 선택에 대해 설명하였다. 두 번째로, (1) 결함 위치가 고정된 채 다양한 슈퍼셀 크기를 가지거나 (2) 슈퍼셀 크기가 고정된 채 다양한 결함 위치를 가지는 단일 압전 결함 인가 2차원 음향양자 결정의 기계적 및 전기적 응답을 분석하였다. 끝으로, (1) 각 결함에 독립적으로 회로가 연결되었을 시 결함 간 다양한 거리 및 배열 방향을 가지거나 (2) 결함 간 거리 및 배열 방향이 고정될 시 5가지의 전기 회로 연결 유형(독립적인 연결, 두 가지의 직렬 연결, 두 가지의 병렬 연결)을 가지는 이중 압전 결함 인가 2차원 음향양자 결정의 기계적 및 전기적 응답을 분석하였다.

두 번째 연구에서는 결함 모드 기반 에너지 국부화의 고유한 협대역 특성으로 인해, 광대역 에너지 수확을 실현하기 위한 압전 결함 인가 음향양자 결정의 새로운 설계 안들을 제안한다. 하나는 L형으로 배열된 삼중 결함 인가 2차원 음향양자 결정이다. 본 설계 안은 단일 결함 인가 음향양자 결정과 이중 결함 인가 음향양자 결정을 중첩하여 각 시스템의 장점을 모두 활용하는 데 핵심적인 역할을 수행하였다. 단일 결함 인가 음향양자 결정은 좁은 대역폭의 특정 결함 밴드 주파수 근처에서 고출력 전력을 수확할 수 있는 반면, 이중 결함 인가 음향양자 결정은 비교적 넓은 대역폭에서 분리된 이중 결함 밴드 주파수 근처에서 저출력 전력을 수확할 수 있다. 따라서 두 시스템을 중첩시킴으로써 광대역 에너지 수확이 가능케된다. 다른 하나는 탈동조화된 이중 결함 인가 구배형 음향양자 결정이다. 결함 밴드 주파수는 관련 결함을 둘러싼 격자들의 질량과 강성에 따라 결정되기 때문에 탈동조화 및 구배형 특성을 융합함으로써 각 이중 결함에 해당하는 결함 밴드 주파수를 개별적으로

설계할 수 있다. 이는 설계된 다른 결함 밴드 주파수에 각 결함 부근에 탄성파를 국부화할 수 있으며, 성공적으로 광대역 에너지 수확을 가능케한다.

끝으로, 압전 결함 인가 음향양자 결정의 수학적 해석 모델 개발로써 다음의 두 가지 주제로 구성된다. 하나는 결함 밴드 형성 및 분리를 고찰하기 위한 단일 혹은 이중 결함 인가 1차원 음향양자 결정의 집중 파라미터 모델(예: 다자유도계 질량-강성 시스템) 개발을 목표로 한다. 점근적 해석을 결함 밴드 해석에 접목할 시, 결함 밴드 및 해당 결함 모드 형상의 극한적 거동은 밴드 갭이 왜 결함 모드 기반 에너지 국부화 구현을 위한 전제인가? 라는 질문에 해답을 제공한다. 다른 하나는 결함 밴드 및 에너지 수확 성능을 예측하기 위한 단일 결함 인가 1차원 음향양자 결정의 전기-탄성 연성 수학적 해석 모델 개발을 목표로 한다. Newton의 제 2법칙과 Gauss 법칙으로부터 각각 기계 운동방정식과 전기 회로 방정식을 유도하였다. Green 함수를 통해 상기된 전기-탄성 연성 방정식을 해결함으로써, 수학적 형태의 전기-탄성 연성 전달 행렬을 유도하였으며, 전달행렬법과 S-파라미터 기법으로부터 결함 밴드와 출력 전력 예측 모델을 개발하였다.

주요어: 압전 에너지 수확
자율 전원 무선 센서 네트워크
음향양자 결정
밴드 갭
결함 모드
에너지 국부화

학 번: 2016-20715